Author:
Teece, Lisa Joanne

Title:
Controlling the collapse of weak colloid-polymer gels

Controlling the collapse of weak colloid-polymer gels

Lisa Teece
Joanne

A dissertation submitted to the University of Bristol in accordance with the requirements of the degree of Doctor of Philosophy in the Faculty of Science, Department of Chemistry.

46,408 words

Abstract

Colloidal gels which are formed as the result of weak depletion attractions exhibit a two stage settling behaviour under gravity. Initially the space spanning network displays solid like behaviour and is resistant to gravitational effects. This structure persists for a finite period of time defined as the delay time τ_D . When the age of the gel exceeds its characteristic τ_D the structural integrity of the network is lost and it begins to rapidly collapse. The microscopic processes which are responsible for this sudden collapse have yet to be established and a better understanding is imperative because a quantitative prediction of gel stability has great implications in the formulation of many commercial products. In this thesis a detailed experimental study of the collapse of emulsion gels is presented.

An oil-in-water emulsion system is studied where gelation is induced by the addition of a non-adsorbing polymer, which has a polymer-colloid size ratio of 0.62. Comparison of the measured phase diagram with generalised free volume theory shows that the system behaves as an ideal mixture of hard spheres and non-adsorbing polymer. Research in this area is usually focused on short range attractive systems where the dynamics of phase separation become arrested resulting in an arrested gel network. In contrast, measurements show that there is no period of kinetic arrest in long range attractive systems. Instead, phase separation occurs via a spinodal-like decomposition process until such time that the gel network fails. The gels have a characteristic domain radius R_c which grows as the sample ages and obeys the approximate power law $\mathrm{R} \sim t^{\alpha}$, where α is a strong function of quench depth. The mechanism of phase separation therefore differs from the classical spinodal decomposition of binary liquids, where α is independent of the quench depth.

A combination of confocal microscopy, rheology and time lapse video imaging is used to fully explore the collapse of transient gels. Confocal microscopy reveals that network restructuring is continuously occurring during the initial stable period, however there is no large scale restructuring of the network or formation of channels which have been attributed by previous workers to the cause of sudden collapse. The ageing process is microscopically different depending upon whether the initial height (h_0) of the sample is large or small (where 'large' is defined as $>\approx$ 12 mm). When $h_0 > 12$ mm the ageing of the network does not occur uniformly throughout the full height of the network, rather, some areas of the network coarsen at a slightly increased rate resulting in inhomogeneities in the size of R_c . Contrary to this when h_0 is small the network ages homogeneously throughout the entire height.

Time lapse video imaging has revealed that there are two height dependant collapse processes occurring. The network reduces in height at a rate which is well described by the expression $h(t-\tau_D)/h(0) \sim \exp\left((t-\tau_D)/\tau_C\right)^{\beta}$. Provided h_0 remains above $\approx$ 12 mm $\beta \approx 1.5$ and the rate of collapse is a constant independent the height. When h_0 is small $\beta \approx 1$ which is reminiscent of the collapse of strong gels. The delay time is completely independent of h_0 in both instances. It is surmised that these results originate from internal stresses being generated by particles moving to more favourable positions in an attempt to reduce the interaction energy. These movements occur at the expense of particles with fewer nearest neighbours. As the network connectivity is reduced beyond some critical level, the gel starts to collapse. The stress inhomogeneities are not found in small h_0 samples. The phenomenon of network collapse has been widely observed in systems with short range attractions. The measurements reported here provide a framework to quantitatively describe the physical processes which result in the sudden collapse of transient gel networks with long range attractions. When this process is fully understood then the formulation of commercial products can be adjusted accordingly in order to increase the shelf life of products, and maximise financial benefit.

Acknowledgments

I would like to thank my supervisor Paul Bartlett for all his support, encouragement and guidance throughout my PhD. I am sure that he has found the experience as challenging as I have! Special thanks goes to Malcolm Faers for his support, and and experimental assistance. I would also like to thank my fellow students Roger, Rodrigo, Juan, Leila, Sam and Humphrey for their valuable support throughout this thesis. Finally, I would like to thank the Engineering and Physical Sciences Research council and Bayer CropScience for funding this research.

Declaration

I declare that the work in this dissertation was carried out in accordance with the Regulations of the University of Bristol. The work is original except where indicated by special reference in the text and no part of the dissertation has been submitted for any other degree. Any views expressed in the dissertation are those of the author and in no way represent those of the University of Bristol. The dissertation has not been presented to any other University for examination either in the United Kingdom or overseas.

SIGNED: ..... DATE: 9/01/2013

Contents

List of Figures

List of Tables

Notation

A	Hamaker constant
A_{fv}	free volume coefficient
a	particle radius
B_{fv}	free volume coefficient
C_{fv}	free volume coefficient
CP	crystal phase
c*	polymer overlap concentration
C_p	polymer weight concentration
D	diffusion constant
D_f	fractal dimension of a cluster
D_0	diffusion co-efficient
D_N	Deborah number
D_s	short time self diffusion constant
d	diameter
E_{bond}	bond energy in units of k_BT
e	elementary charge
F	Helmholtz free energy
f	fluid phase
f	free energy density
G	Gibbs free energy
G*	complex modulus
G'	elastic modulus
G"	viscous modulus
g	acceleration due to gravity
g^2	autocorrelation function
H	particle surface separation
h	particle centre-centre separation
h(t)	height of colloid rich phase at time, t
h(0)	initial height of sample

I	intensity
J	compliance
k'	Mark-Houwink constant
k_0	permeability
k_BT	Boltzmann constant
L*	effective polymer length
l_c	critical length
l_{cap}	capillary length
M	mass of a cluster
M_L	mass per unit contour length
M_p	mass of polymer
M_w	polymer molecular weight
N	number of spheres
N_A	Avogadro's constant
N_p	number of depletion polymer coils
N_{ran}	random number between 0 and 1
n	number of bonds
n_{ion}	concentration of monovalent ions
$n_p^{(R)}$	number density of polymer in a reservoir in osmotic equilibrium with a system
q	wave vector
q_{max}	position of structure factor peak
q_p	persistence length
q_R	depletion layer thickness in dilute solutions
q_s	δ/a, relative thickness of depletion zone around a sphere
$\langle R^2 \rangle$	mean squared end to end distance
$\langle r^2 \rangle$	mean squared displacement
R_c	radius of a fractal cluster
R_c	characteristic domain radius
$\langle R \rangle$	root mean squared end to end distance
r_h	hydrodynamic radius

$r(\phi_0)$	dimensionless hydrodynamic interaction parameter
r_g	polymer radius of gyration
$\langle S^2 \rangle$	mean square radius gyration
T	absolute temperature
T_{eff}	effective temperature
t	time
t_0	time zero
t_1	solvent efflux time
t_2	polymer solution efflux time
U_0	colloid pair potential at contact
U_{max}	maximum value of U_T
U_R	repulsive potential
U_T	sum of attractive and repulsive potentials
U_{vdW}	van der Waals attractive potential
u_0	sedimentation velocity of an isolated particle
V	total volume
V*	free volume available to polymer
V_{dep}	depletion volume
v_s	initial settling velocity
y	reduced polymer concentration, $C_p / C_p *$
Z	particle charge

Π	osmotic pressure
Π_p	polymer osmotic pressure
β	power exponent
γ	interfacial tension
γ_0	strain amplitude
γ_G	de Gennes exponent
γ_s	shear rate
δ_{dep}	thickness of depletion zone around a sphere
δ	lag phase
δ_u	degree of deformation
ϵ_0	permittivity of free space

ϵ_m relative dielectric constant

ζ zeta potential

η viscosity

η_0 solvent viscosity

η_i instantaneous viscosity

η_{red} reduced viscosity

η_r relative viscosity

η_{sp} specific viscosity

κ inverse screening length

κ^{-1} Debye length

λ_p de Broglie thermal wavelength of a polymer

λ^{-1} Kuhn statistical segment length

μ_p chemical potential of polymer

ξ colloid-polymer size ratio

ρ density

σ polydispersity

σ_0 stress amplitude

σ_g gravitational stress

σ_s shear stress

τ_c fundamental collapse time

τ_D delay time

τ_{diff} characteristic diffusion time

τ_{esc} Kraemers escape time

τ_{mD} microscopic delay time

ϕ volume fraction

ϕ_0 initial volume fraction

ϕ_p^{free} volume fraction of polymer in free volume

ϕ_{RCP} random close packing volume fraction

$\phi_c^{\otimes}$ minimum colloid volume fraction required for gelation

ω angular frequency

Chapter 1

Introduction

1.1 Colloidal dispersions

Colloidal dispersions are ubiquitous, from food products such as ice-cream where fat droplets are suspended within an aqueous medium, to paints where solid pigments are dispersed within a solvent. Colloidal particles are very small and usually have a particle radius, a, in the approximate range 1nm to 500nm. The main disadvantage of colloidal systems is that the particles will settle under gravity and either sediment or cream to form a dense layer which cannot easily be redispersed.

In an attempt to stabilise particles against sedimentation, a colloidal gel network is formed where pairs of colloids experience an effective attraction termed a 'depletion attraction'. This describes how an effective attraction between two particles is induced in the presence of a non-adsorbing polymer. The attraction is relatively weak and the bonds are constantly breaking and reforming in a process known as ageing. Colloidal gels which are formed as a result of weak depletion attractions exhibit a two stage settling behaviour under gravity. Initially the space spanning network displays solid like behaviour and is resistant to gravitational effects. This structure persists for a finite period of time defined as the delay time τ_D . When the age of the gel exceeds its characteristic τ_D the structural integrity of the network is lost and it begins to rapidly collapse.

The aim of this investigation is to study network ageing during the delay period, and the collapse of the network, in an attempt to further understand the processes which cause the network to collapse. The literature so far has focused predominantly on systems with short range attractions. The attractive range is determined by the size of the depletion polymer, where smaller polymers results in colloids having to be in closer proximity in order to experience an attraction. However far less research has been conducted on systems with long range attractions. In this thesis a detailed experimental study of the collapse of emulsion gels with long range attractions is presented.

1.2 Colloids

A colloidal system is formed when a small particle of one material is suspended within another material. The two materials can be any combination of a solid, liquid or gas but a colloidal dispersion cannot be formed from two gases since mixtures of gases are completely miscible. Conventionally it is normally assumed that a colloidal dispersion must have a particle radius, a, in the approximate range 1nm to 500nm. There exists a total of eight colloid combinations as follows:

1. liquid aerosol (a liquid dispersed in a gas eg mist)
2. solid aerosol (a solid dispersed in a gas eg smoke)
3. Foam (a gas dispersed in a liquid eg whipped cream)
4. Emulsion (a liquid dispersed in a liquid eg milk)
5. Sol (a solid dispersed in a liquid eg pigmented ink)
6. Solid foam (a gas dispersed in a solid eg styrofoam)
7. Gel (a liquid dispersed in a solid eg agar)
8. Solid sol (a solid dispersed in a solid eg stained glass)

There are many examples of colloidal systems which are common in every day life. They may be naturally occurring such as milk, or man made such as personal care products, paints and agrochemicals. A significant amount of research on colloidal systems is therefore undertaken due to their industrial importance. A second feature of colloidal systems is that they are small enough that their dynamics are dominated by their thermal energy, k_BT . The slow dynamics and large length scales of colloidal suspensions makes them ideal models for atomic systems, since they are larger than the wavelength of visible light and can be individually resolved.

Colloids are small enough that their movements are not dominated by gravitational effects, they instead move in a random fashion. This random movement is referred to as Brownian motion since it was first observed by Robert Brown in 1827 when observing pollen grains in water [1]. Brown studied other similar sized particles and witnessed the same random movements and deduced that these movements were a characteristic of the particles, but was unable to explain the their origins. It was not until 1905 that Einstein was able to determine that the movements of this particular size range of particles was due to thermal molecular motions, where particles were being bombarded by the molecules of the suspending solvent. Since the particles are equally likely to move in any direction the mean of all movements would be zero which suggests that the particle has not moved from its original position. A more useful measure is the mean square displacement $\langle r^2 \rangle$ in which the magnitude of each particle movement is squared and then the mean of all squared displacement values is determined. The value of $\langle r^2 \rangle$ is dependent upon both time t and the diffusion coefficient D_0 as follows:

$$\langle r^2 \rangle = 6D_0 t \tag{1.1}$$

The diffusion coefficient can be calculated from the Stokes-Einstein equation:

$$D_0 = \frac{k_B T}{6\pi\eta a} \tag{1.2}$$

where k_B is the Boltzmann constant, T is the absolute temperature, η is the viscosity of the suspending phase, and a is the particle radius. This equation demonstrates how particle radius plays a vital role in determining the diffusion coefficient. For example, a particle with radius of 1nm suspended in water has a diffusion coefficient of $\approx 2 \times 10^{-10}$ m^2s^{-1} whereas a particle with a radius of 500nm suspended in water has a diffusion coefficient of $\approx 5 \times 10^{-13}$ m^2s^{-1} which shows a decrease by a factor of 500.

1.3 Colloidal Stabilisation

Colloidal dispersions are not thermodynamically stable, except in rare cases such as a microemulsion. Interactions between colloids can cause them to aggregate which is often an undesirable occurrence. All colloidal particles are attracted to each other due to short ranged attractions called van der Waals attractions. The origin of the van der Waals attractions lies in the instantaneous dipole generated by the fluctuation of the electron cloud surrounding the nucleus of electrically neutral atom. The strength and range of this interaction between two particles of radius a can be defined with respect to a small particle surface separation, H, using the Hamaker equation:

$$U_{vdW}(H) = \frac{-Aa}{12H} \tag{1.3}$$

where A is the Hamaker constant. The Hamaker constant is a material property, with the dimensions of energy, dependent on the polarisablity of the particles and the solvent and can be defined for a van der Waals body-body interaction as follows:

$$A = \pi^2 C \rho_1 \rho_2 \tag{1.4}$$

where ρ_1 and ρ_2 are the number of atoms per unit volume of two interacting bodies, and C is the coefficient in the atom-atome pair interaction. The attractive

Hamaker force is strong but relatively short ranged. Under the influence of this attractive interaction potential a colloidal suspension is unstable and therefore needs to be stabilised to prevent the particles approaching close enough to experience this attraction. This is done by introducing a repulsive component to a colloidal suspension that acts as a barrier to coagulation. This repulsive component can be achieved either through electrostatic or steric stabilisation, which rely on electrical charges and polymer configurational entropy respectively.

1.3.1 Electrostatic Stabilisation

When an interface is created within a highly polar medium the interface can gain a charge. There are a number of mechanisms responsible for the development of the surface charge, which are dissociation of surface groups, adsorption of charged species such as an ionic surfactant, or isomorphous substitution. Once a surface charge has developed it encourages counter-ions of an equal magnitude from the bulk solution to balance the charge, resulting in two forms of layers. The counter-ions closest to the surface form the Stern layer which is an immobile monolayer of ions. Beyond the Stern layer the remaining counter- ions exist as a diffuse cloud of ions where the concentration of the ions decreases with distance from the particle surface. The diffuse cloud is formed as a result of competition between electrostatic attractive forces of the surface charge and thermal forces distributing the ions homogenously by diffusion. The Stern layer and the diffuse ion cloud are termed the electrical double layer (EDL, see figure 1.1). The formation of the double layer causes an electric potential between the surface and any point in the bulk of the suspending medium. The electrical potential ψ_0 of the charged particle decreases linearly across the Stern layer. The potential then decreases exponentially from the shear plane into the bulk solution. The shear plane is an imaginary layer which coincides with the start of the diffuse ion cloud. The value of the potential between the shear plane and the bulk is conventionally termed the electrokinetic or zeta (ζ) potential [2].

Charged colloidal particles are stabilised by electrostatic repulsive interactions.

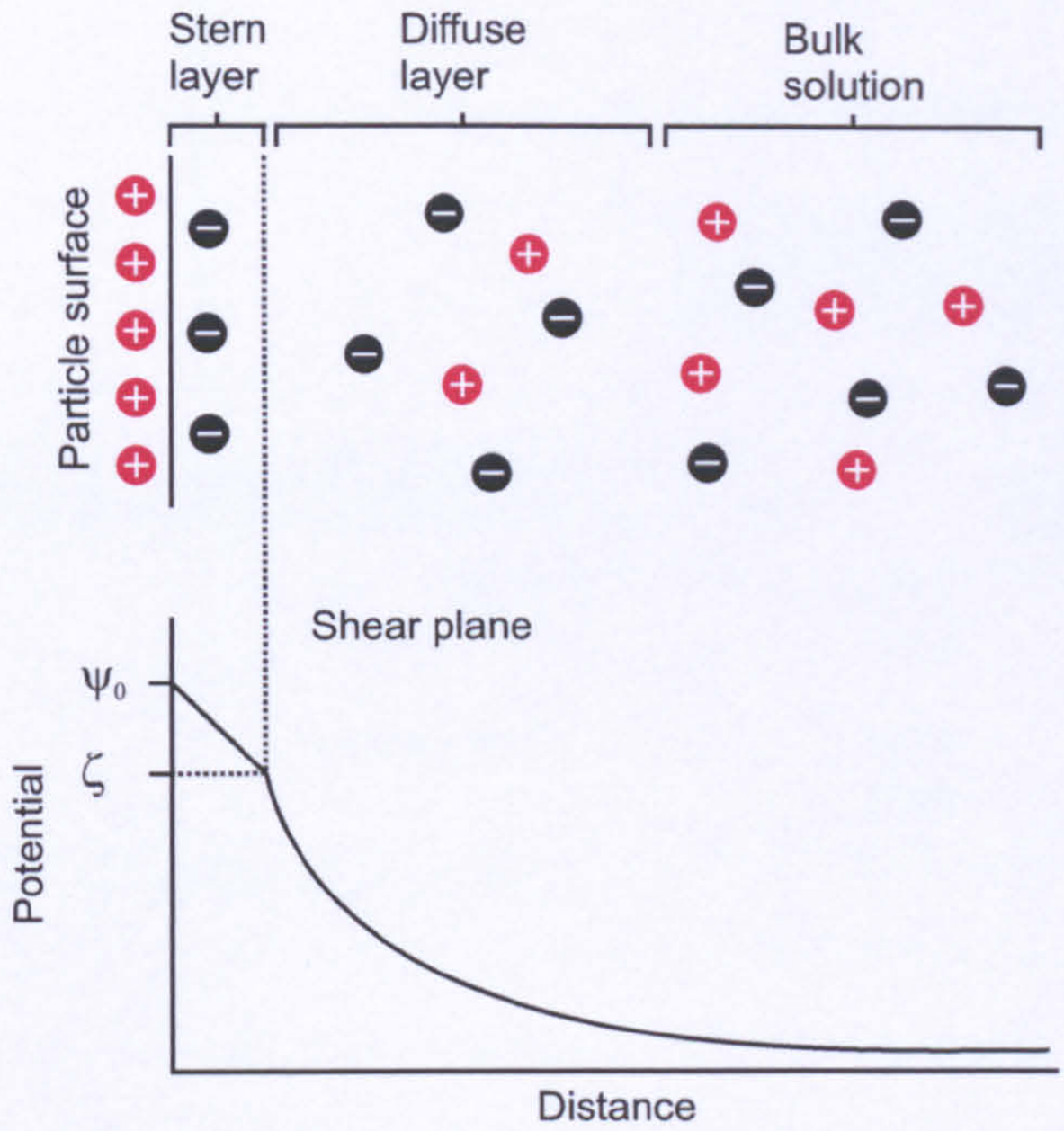

Figure 1.1: The electrical double layer. Schematic representation of the potential and ion distribution at a positively charged interface, where the surface potential(ζ) decreases linearly across the Stern layer. The potential then decreases exponentially from the shear plane through the diffuse layer to the bulk.

When the electric double layer of each particle begins to overlap the result is a repulsive interaction. The electrostatic repulsive potential ($U_R(D)$) experienced by a pair of charged colloids can be calculated as:

$$U_R(D) = z^2 \lambda_B \left(\frac{\exp(\kappa a)}{1 + \kappa a} \right)^2 \frac{\exp(-\kappa r)}{r} \tag{1.5}$$

where Z is the particle surface charge, a is the particle radius, r is the center to center distance, λ_B is the Bjerrum length, and κ is the inverse screening length. The Debye length, κ^{-1}, is the scale over which mobile charge carriers screen out electric fields in polar medium and is given by:

$$\kappa^{-1} = \sqrt{\frac{\epsilon_m \epsilon_0 k_B T}{e^2 n_{ion}}} \tag{1.6}$$

where n_{ion} is the concentration of monovalent ions of identical size. The Debye screening length is a good approximation of the diffuse layer thickness. The thickness of the diffuse layer can be adjusted by controlling the ion concentration since it is clear from equation 1.6 that the screening length is inversely proportional to the square root of the ion concentration. The high dielectric constant required for separation and solvation of the ions dictates that charge stabilisation will generally only occur in aqueous medium.

A theory was developed by Derjaguin and Landau [3] and separately by Verwey and Overbeek [4] which described the total interaction potential U_T between two charged particles, which is referred to as the DLVO theory, where U_T is the sum of the van der Waals attractive potential U_{vdW} and the repulsive potential U_R from the overlap of the double layers. Figure 1.2 shows a sketch of the summation of the attractive and repulsive potentials. The sum of the two potentials U_T shows a positive barrier of height U_{max}. If the barrier is significantly greater than a few k_BT , particles are prevented from approaching to within a distance over which the attractive forces are felt and the dispersion remains stable.

1.3.2 Steric Stabilisation

Steric stabilisation is an important mechanism for colloid stabilisation and involves covering the colloid in a layer of polymer which gives rise to repulsions between colloids. The most simple method to achieve this is to allow a polymer to be adsorbed from solution, but there is usually a configurational entropy cost when a polymer adsorbs from solution onto a surface. If two colloids, each coated with a polymer layer approach each other beyond the point of contact between the two polymers layers, there are two possible scenarios which will occur. The polymer layers may overlap and interpenetrate, or the layers may compress rather than interpenetrate as demonstrated by figure 1.3. In reality it is likely that a scenario which lies between these two extremes may occur, and the adsorbed polymers layers will experience both interpenetration and compression [5].

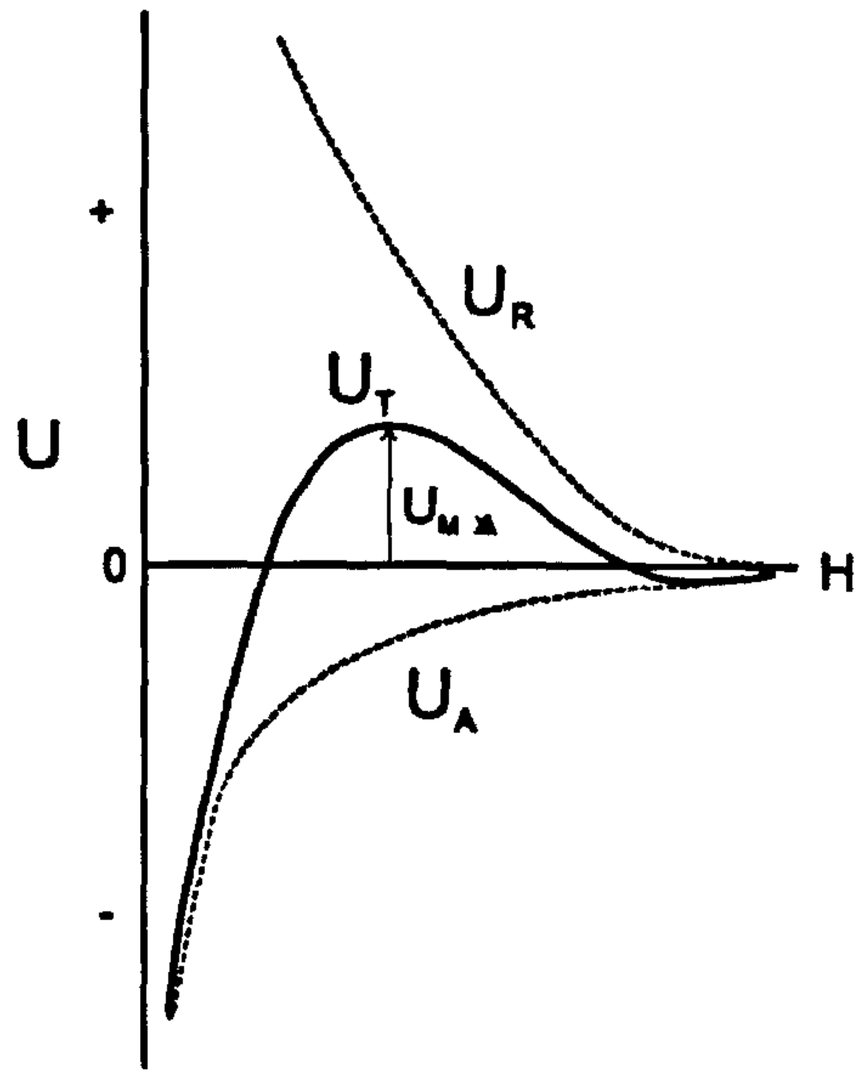

Figure 1.2: A schematic representation of the particle pair potential, U for a charge stabilised system. The total potential U_T is the sum of the attractive component due to van der Waals forces U_A, and the repulsive component U_R due to the overlap of electrical double layers. Stability is achieved when U_{max} is significantly greater than k_BT .

When polymers are in a good solvent interactions between polymer segments and solvent molecules are energetically favorable, causing polymer coils to expand. When in a poor solvent, polymer self-interactions are preferred, and the polymer coils will contract. The quality of the solvent depends on both the chemical compositions of the polymer and solvent molecules and the solution temperature. Provided the polymer layers are in a good solvent then the local increase in polymer segment density will result in a strong repulsion between the polymer layers. This repulsion is due to two main effects. Firstly, in the polymer layer overlap area there is an increase in the osmotic pressure due to unfavourable mixing of the polymer chains in good solvent. Secondly the overlapping polymer layers experience a decrease in the configurational entropy as a result of a decrease in the volume available to the polymers when the polymers either interpenetrate or compress.

If the polymers are in a poor solvent then it is possible that an attraction may actually result from the interaction, and so solvent selection is crucial.

For steric stabilisation to be completely effective, the adsorbed polymer layer should completely cover the particle surface as any bare patches may allow for aggregation. The polymer must also be anchored strongly to the surface to avoid being displaced by approaching polymer coils, and the layer thickness must be sufficiently thick ($\approx>$ 10nm) to prevent weak flocculation. The range of this potential is equivalent to the length of the polymer chains that extend from the colloid surface into the dispersing medium. The range of this interaction can therefore be controlled by carefully selecting the molecular weight of the polymer. Block co-polymers are useful for steric stabilisation as component block types can be selected for their physical properties, where one is able to adsorb preferentially to the particle surface while the second block type shows good interactions with the solvent and extends out from the particle surface to its maximum capacity. Steric stabilisation is equally effective in polar (high dielectric constant) and non-polar (low dielectric constant) solvents, but is typically used in non-polar solvents as charge stabilisation tends to be more difficult to control in such media.

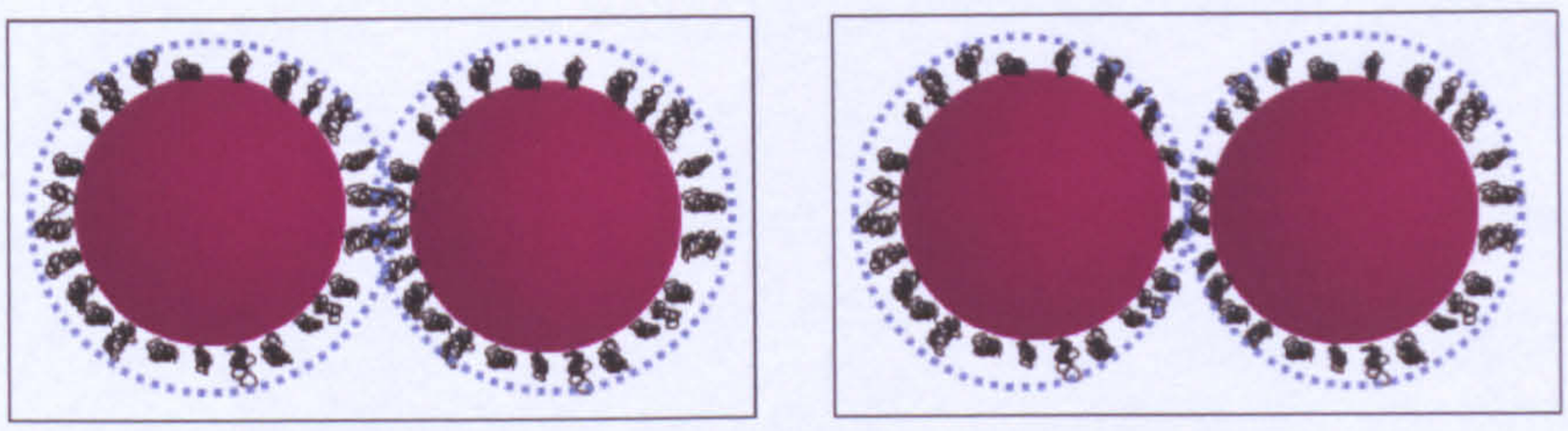

Figure 1.3: Schematic representation of the result of two adsorbed polymer layers coming in to contact. The left image shows interpenetration of the layers and the image on the right shows compression of the two layers which do not interpenetrate.

1.4 Colloid polymer mixtures

The addition of a non-adsorbing polymer to a colloidal dispersion can cause phase separation, with a variety of equilibrium and nonequilibrium behaviour being observed [6]. The first theoretical interpretation of the phase separation induced by non-adsorbing polymer was offered by Asakura and Oosawa [7] and also by Vrij at a later date [8] which they referred to as the depletion mechanism. The destabilization is a result of the expulsion of polymer from the interstitial spaces between approaching particles because of volume restriction and osmotic effects.

1.4.1 The depletion mechanism

The depletion mechanism describes the phase behaviour of a suspension of large spherical colloids with added non-adsorbing polymer. The polymer coils and colloidal particles were modelled as mutually impenetrable spheres. As a result the polymer centre of mass is excluded from a region around each colloidal particle creating a layer around the colloid which is devoid of polymer. This layer is equal in thickness to the polymer radius of gyration, r_g as shown by (figure 1.4). This excluded region is termed the depletion zone. The polymer coils are only free to move within the volume which is not occupied by the colloidal particles or their depletion zone. This volume is termed the free volume. When the separation between two large colloidal particles in solution is less than the $2r_g$, exclusion or depletion of the smaller non-adsorbing polymer occurs. The consequences of this depletion can be understood in both mechanical and thermodynamic terms.

An isolated colloidal particle in solution experiences an osmotic pressure acting normal to its surface. When the particle is entirely surrounded by polymer the pressure exerted by the polymer is uniform over its entire surface area. When two or more colloidal particles are in close enough proximity to enable their depletion layers to overlap and give rise to an excluded volume, there is a decrease in the osmotic pressure exerted on the particle from this area. This leads to anisotropy of the local pressure which gives rise to an attractive depletion force between the

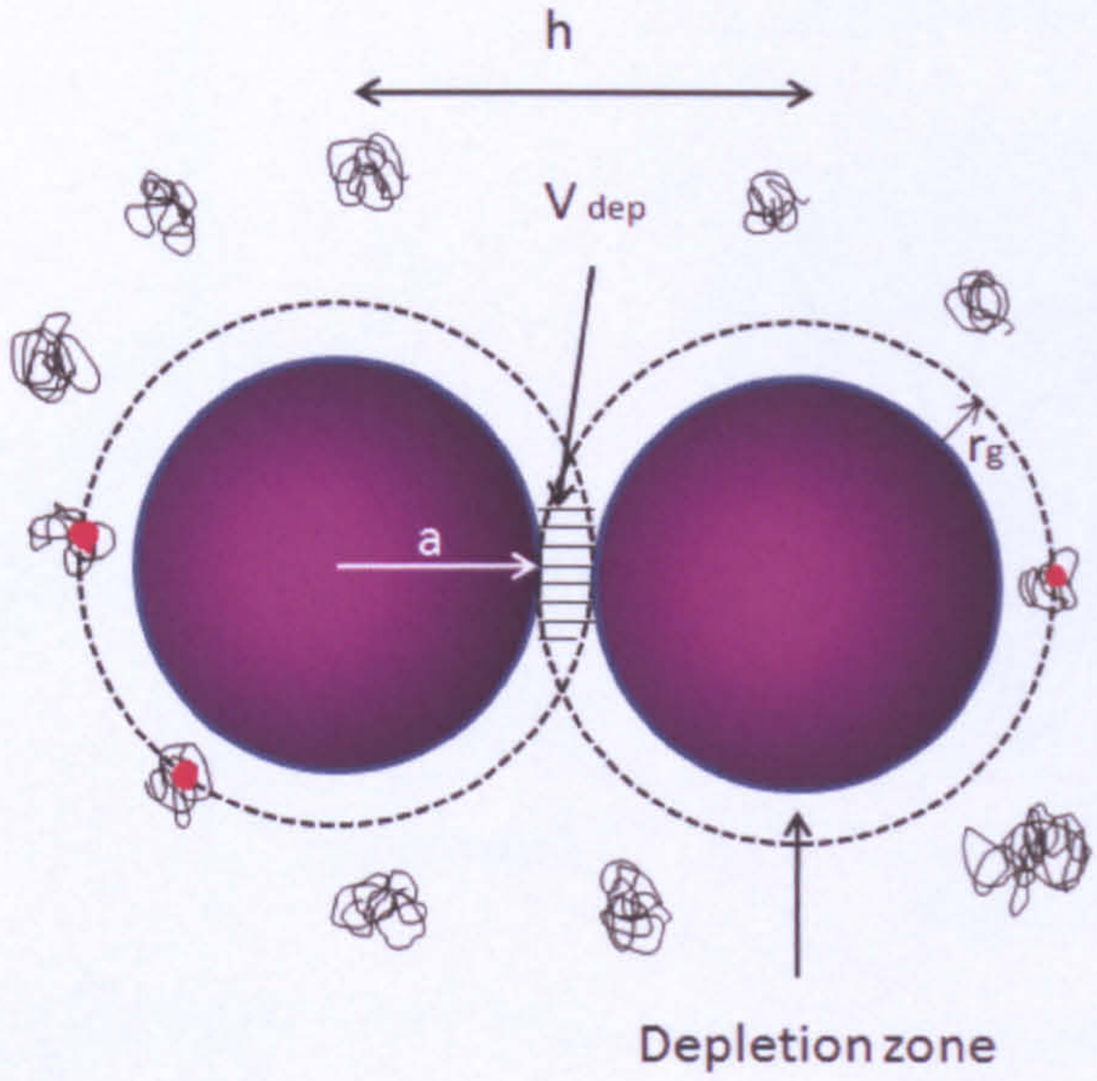

Figure 1.4: The polymer exclusion zone. The centres of mass of the polymer coils are excluded from a region around the surface of each particle - the depletion zone. The depletion layer thickness is equal to r_g and when the depletion zones of two particles overlap, an unbalanced osmotic force pushes the two particles together. The force is modelled as an effective attractive pair potential.

particles (figure 1.5).

Thermodynamically, the overlap of two depletion zones releases a volume of solvent which increases the entropy of the polymer and hence reduces the Helmholtz free energy

1.4.2 The depletion potential

An attractive force with a range of r_g can be achieved when a non-adsorbing polymer is added to a colloidal suspension. This attraction can be modelled in the form of an attractive pair potential, U_{dep} where:

$$U_{dep} = \left\{ \begin{array}{cc} +\infty & h \leq d \\ -\Pi_p V_{dep} & d < h \leq d + 2r_g \\ 0 & h > d + 2r_g \end{array} \right\} \tag{1.7}$$

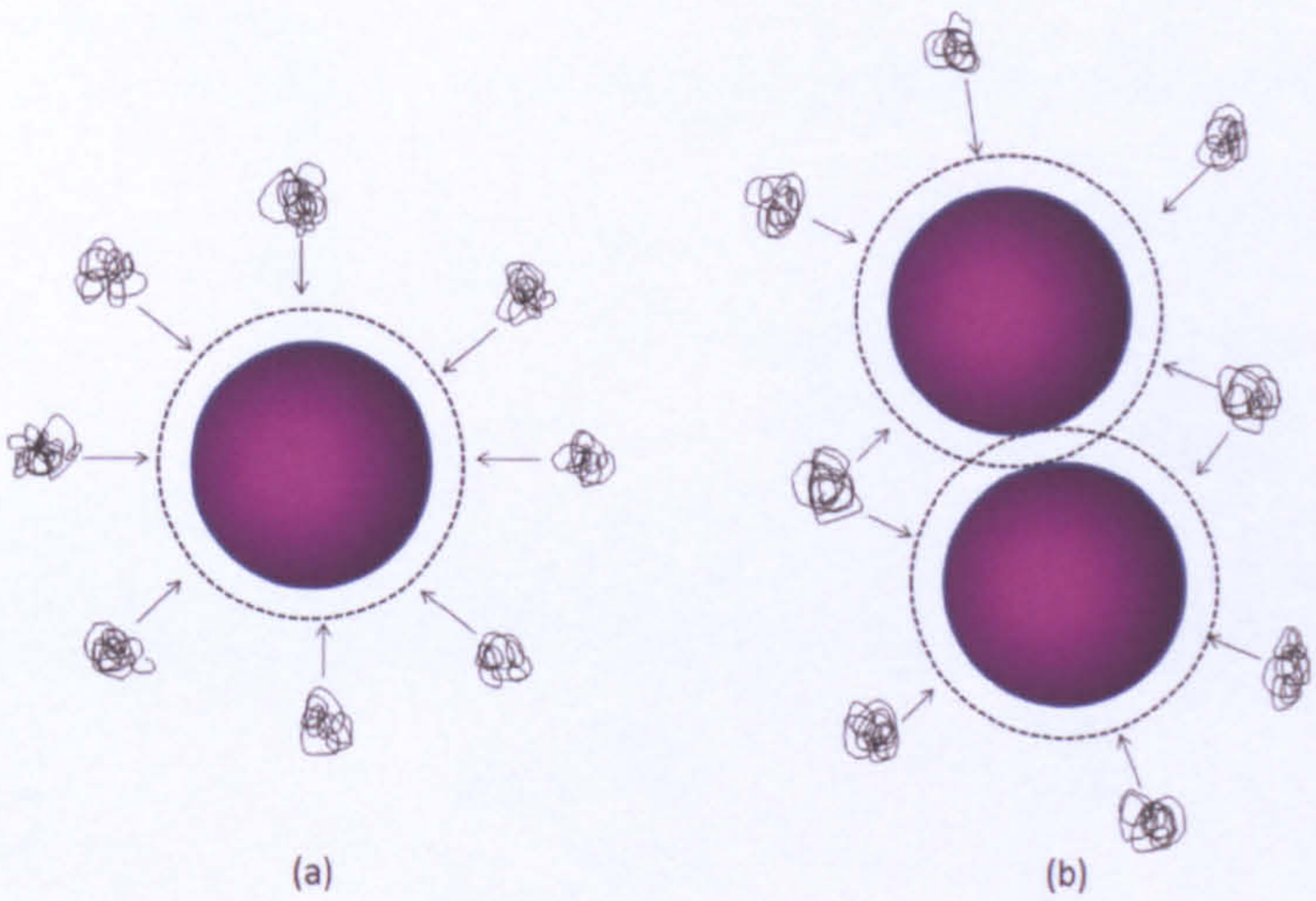

Figure 1.5: Schematic representation of (a) isotropy of osmotic pressure and (b) anisotropy of osmotic pressure in a colloidal suspension with non-adsorbing polymer. The arrows are indicative of the pressure exerted by the non-adsorbing polymer

where d is the particle diameter, Π_p is the polymer osmotic pressure and h the particle center-to-center separation. The volume of the overlapping depletion zones between two particles at a separation h is calculated from:

$$V_{dep} = \left(1 - \frac{3h}{2d(1+\xi)} + \frac{1}{2}\left[\frac{h}{d(1+\xi)}\right]^3\right)\frac{\pi}{6}d^3(1+\xi)^3 \tag{1.8}$$

where ξ is the ratio of the polymer radius of gyration to the particle radius, r_g/a.

In a colloidal suspension where the concentration of polymer coils is dilute, the osmotic pressure, Π_p of the polymer solution can be modelled as an ideal gas and expressed using vant Hoffs equation:

$$\Pi_p = \frac{N_p K_B T}{V^*} \tag{1.9}$$

where N_p is the total number of depletion polymer coils V^* is the free volume available to the polymer coils in which to freely move. The polymer weight con-

centration, C_p , can be related to the osmotic pressure by:

$$\frac{\prod_p}{k_B T} = \frac{N_p}{\alpha V} = \frac{M_p}{\alpha V} \cdot \frac{N_A}{M_w} = \frac{N_A}{M_w} \cdot \frac{c_p}{\alpha} \tag{1.10}$$

where M_p is the mass of polymer, M_w is the polymer molecular weight and N_A is Avogadros constant. C_p can also be related to the volume fraction of polymer in the free volume by:

$$\phi_p^{free} = \frac{N_A}{M_w} \cdot \frac{c_p}{\alpha} \cdot \frac{4}{3}\pi r_g^3 \tag{1.11}$$

Since C_p is proportional to $\prod_p$, the strength of the depletion interaction may be increased by increasing the concentration of non-adsorbing polymer which will ultimately lead to phase separation or aggregation.

1.4.3 Bridging flocculation

Particle aggregation can also be induced by adsorbing macromolecules in a process which is known as bridging flocculation. It arises when a polymer in the suspension adsorbs onto a particle surface. The rate at which the particle adsorption occurs is usually very slow compared to the rate of particle collisions. Under these conditions it is possible for a polymer to be co−adsorbed, that is, adsorbed to more than one colloidal particle which causes a polymer bridge to be formed between the two particles. The final amount of adsorbed polymer will be much less than the amount of polymer required to completely cover the particle surface. This is a necessary requirement as polymer bridges which are initially formed may be disrupted by the adsorption of further polymer chains. Bridging flocculation occurs on a rapid timescale, which is dependent upon the initial particle concentration and it leads to reasonably strong flocs.

1.5 Phase behaviour

Colloid-polymer mixtures exhibit a wide range of equilibrium and non-equilibrium behaviour and such systems are of industrial relevance since they are common in many commercial products. Phase transitions can be induced in an otherwise stable colloidal suspension by the addition of non-adsorbing polymer, via the depletion mechanism. At low polymer concentrations the suspension will remain as a single phase fluid where the particles are randomly and uniformly dispersed. Once the polymer concentration exceeds a critical value the colloidal system separates into a colloid rich and colloid poor phase, which are in equilibrium with each other. Two phases are in equilibrium when they have identical Gibbs free energies and pressures, even though their structures may be different. Increasing the polymer concentration serves to deplete the colloid poor phase further of colloids and increase the colloid number in the colloid rich phase. Predicting the phase behaviour is not a simple task since it is dependant upon the colloid volume fraction, the concentration of polymer in the system and the polymer–colloid size ratio. The hard sphere model for colloidal interactions is a simplistic model which describes the phase behaviour of a model system in which only the colloid volume fraction dictates the resulting phase, and is a useful starting point when considering phase behaviour.

1.5.1 The hard sphere model

The hard sphere model is the most simple colloidal model in which colloids do not attract or repel one another over distances greater than their diameter, and cannot interpenetrate. Two hard sphere particles of radius a will have an infinite repulsion if the separation of their centers is less than $2a$. This potential can therefore be described by:

$$U(h \leq 2a) = \infty \tag{1.12}$$

$$U(h > 2a) = 0 \tag{1.13}$$

The only control parameter which can be altered is the overall density of spheres, which can be expressed as the colloid volume fraction. The systems can therefore be characterised by the number density of particles alone. This is more commonly expressed as the colloid volume fraction ϕ which for a collection of N spheres of radius a, in a system volume V is given by:

$$\phi = \frac{4}{3}\pi a^3 \frac{N}{V} \tag{1.14}$$

where N is the number of spheres of radius a in a system with a total volume,V.

The phase behaviour of hard sphere colloids with increasing ϕ has been predicted by computer simulations and is shown in figure 1.6[9]. A colloidal fluid is observed when the volume fraction is less than 0.494, where each particle is free to explore all of the available volume through diffusion. There will only be a short ranged particle order at any one time. As the volume fraction is increased beyond 0.545 a crystal phase can be observed with a more compact crystalline structure forming as the colloid volume fraction is increased further up to a maximum close packing volume fraction of $\phi = 0.74$. Between the volume fractions of 0.494 and 0.545 lies the fluid-crystal co-existence regime, where the system phase separates into coexisting fluid and crystalline phases. As the volume fraction is increased within this regime the volume fraction of the liquid phase is decreased as more crystal forms until at the melting volume fraction ($\phi = 0.545$), the system becomes fully crystalline. Quenching the hard sphere volume fraction rapidly to $\phi = 0.58$ forces the system into a non-equilibrium state, where the particles are trapped in an amorphous fluid-like arrangement known as a glass. The equilibrium state of the glass is still a crystal, but suppression of the long time diffusion by caging effects prevents the equilibrium stage from ever being reached. Maximum packing density of the

random close packed structure is reached at $\phi = 0.64$.

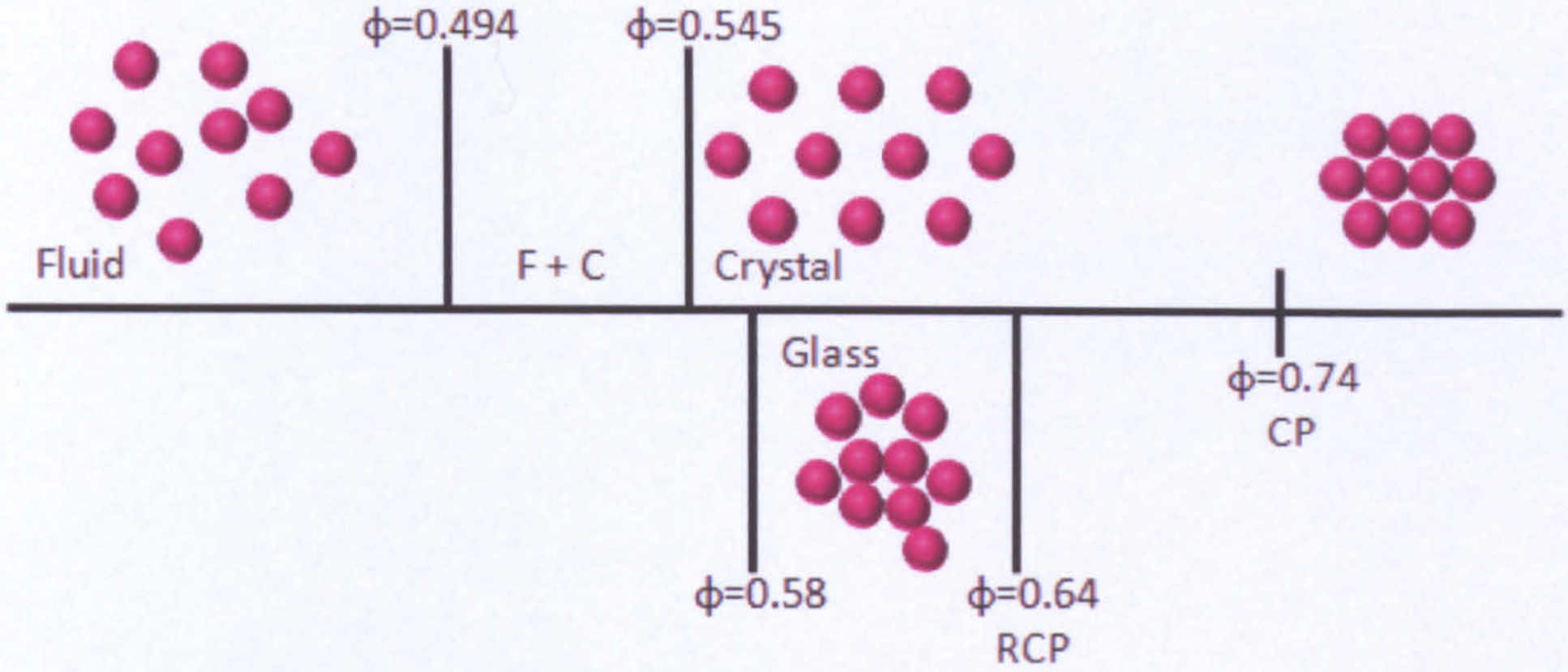

Figure 1.6: Phase behaviour of hard sphere model colloids as predicted by computer simulations.

The formation of colloidal crystals is purely entropic, where the competition between configurational entropy and free-volume entropy may be used to rationalize the formation of crystalline phase. When the ratio of the particles to the free volume is increased, there is less space for the particles to move and the particles rearrange in an effort to try to maximize their space. There arises a competition between trying to maximize the free volume per particle and wanting to remain in the disordered state favoured by the configurational entropy, as demonstrated in figure 1.7 . There are two boxes in figure 1.7 each with 8 spheres. In the first box the spheres are packed in a random arrangement which has a high configurational entropy. However, each sphere is relatively restricted in its movement and the free volume entropy is low. The second box shows how the spheres are arranged in a highly ordered state resulting in a low configurational entropy, but it has a high free volume entropy as each sphere is now free to move about its average position. Crystallisation of a suspension of hard-sphere occurs when the entropy gained by creating more free volume for each particle exceeds that lost by having an ordered arrangement.

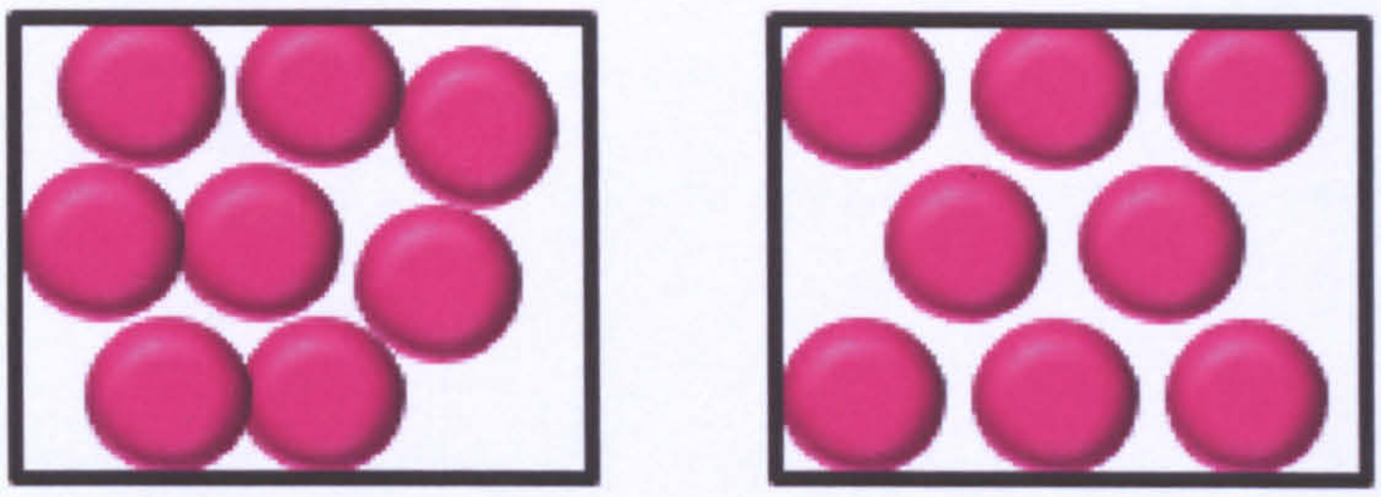

Figure 1.7: A schematic representation of the two configurations of a group of eight spheres. The left box shows a system with high configurational entropy but low free volume entropy and the right box shows a system with low configurational entropy and high free volume entropy.

1.5.2 Polymer partitioning

The hard sphere model predicts colloidal arrangements for a colloidal suspension of ideal monodisperse spheres as the colloid volume fraction is varied. The phase behaviour of colloid-polymer mixtures depends upon both the colloid volume fraction and the polymer concentration, and the theoretical predictions shall now be discussed. The theoretical statistical mechanical work of Gast et al was able to predict the destabilization of nonaqueous colloidal suspensions due to nonadsorbing polymer [10]. They used perturbation theory to predict the equilibrium phase behaviour which involves calculating the osmotic pressure $\prod$ and Gibbs free energy G as a function of ϕ for both the fluid and solid states at fixed values of C_p . On a plot of G against $\prod$ the intersection of the two lines denotes the disorder-order transition. Should more than one co−existence point emerge then the point with the lower free energy determines the equilibrium phase. They they showed that the resulting phase diagrams also depend upon the size ratio of the polymer and colloid. When ξ is small ($\approx < 0.3$) the fluid-crystal coexistence region widens as polymer is added to the colloidal suspension. When ξ is large a three phase coexistence of a colloidal gas, solid and liquid are formed.

As shown previously, each particle is surrounded by a depletion layer which is devoid of polymer, and the total volume available to the polymer is then decreased

by the volume of the depletion layers. This description was limited in that it did not take into account the differences in polymer concentration within the colloid rich and colloid poor phases.

Generalised Free Volume Theory

Lekkerkerker and co adopted a statistical mechanical approach which was used in determining the phase behaviour, by minimizing the Helmholtz free energy F [6]. This was an extension of the depletion potential theory of Asakura and Oosawa which accounted for the partitioning of the polymer within the various phases of the suspension. In this approach the free energy density, f = F/V of a colloid-polymer mixture is considered as a function of the colloid volume fraction, ϕ_c, and the chemical potential of the polymer, μ_p so that F=f(μ_p, ϕ_c). At fixed temperature, μ_p is a function only of the number density of polymers in the free volume,

$$n_p^* = \frac{N_p}{V^*} \tag{1.15}$$

which in turn is related to the polymer free volume fraction and polymer concentration.

The Free Volume Theory of Lekkerkerker et al predicts the phase behaviour of colloid-polymer mixes as well as the polymer partitioning at phase separation in the colloid rich and colloid poor phases. The actual C_p in each sample can be calculated from the total C_p with the expression $C_p^{tot} = V^* \; C_p$, where V* is the free volume which is available to the polymer and can be calculated using the standard scaled particle result:

$$V* = (1-\phi)\exp(-A_{fv}f - B_{fv}f^2 - C_{fv}f^3) \tag{1.16}$$

where:

$$f = \phi/(1-\phi) \tag{1.17}$$

and the coefficients are:

$$A_{fv} = (1+q_s)^3 - 1 \tag{1.18}$$

$$B_{fv} = 3q_s^3(q_s + 3/2) \tag{1.19}$$

$$C_{fv} = 3q_s^3 \tag{1.20}$$

Here $q_s = \delta_{dep}/a$ which is the relative thickness of the depletion zone (δ_{dep}) around a sphere of radius a. The width of the depletion layer decreases with increasing polymer from a value of q_R in dilute solutions to a value of ξ/a in semi-dilute solutions where $\xi \sim C_p{}^{-\gamma_G}$ is the polymer blob size. For excluded-volume polymer chains the de Gennes exponent γ_G is equal to 0.77.

The phase diagrams arising as a result of Free Volume Theory by Lekkerkerker et al also show a dependence of the phase diagram on the range of the attractive potential. At $\xi \leq 0.32$ the region of liquid-crystal coexistence is broadened noticeably with increasing polymer, and in the case of a larger attractive potential where $\xi \geq 0.32$ there emerges critical and triple points in the phase diagram (figure 1.8). For $\xi \leq 0.32$ there is a simple fluid-solid coexistence which has marked partitioning of polymer between the phases. For $\xi \geq 0.32$ the triple point (as shown in figure 1.9(b) expands into a region of three-phase coexistence (gas-liquid-solid) surrounded by three distinct two-phase regions (G–L, G–C, L–C) due to polymer partitioning.

The more recently published Generalised Free Volume Theory of Fleer and Tuinier [11]is an extension of the FVT of Lekkerkerker et al. The benefit of GFVT is that it improves the accuracy at large ξ of the free-volume theory of Lekkerkerker et al by taking into account the compression of the depletion zone around each particle in

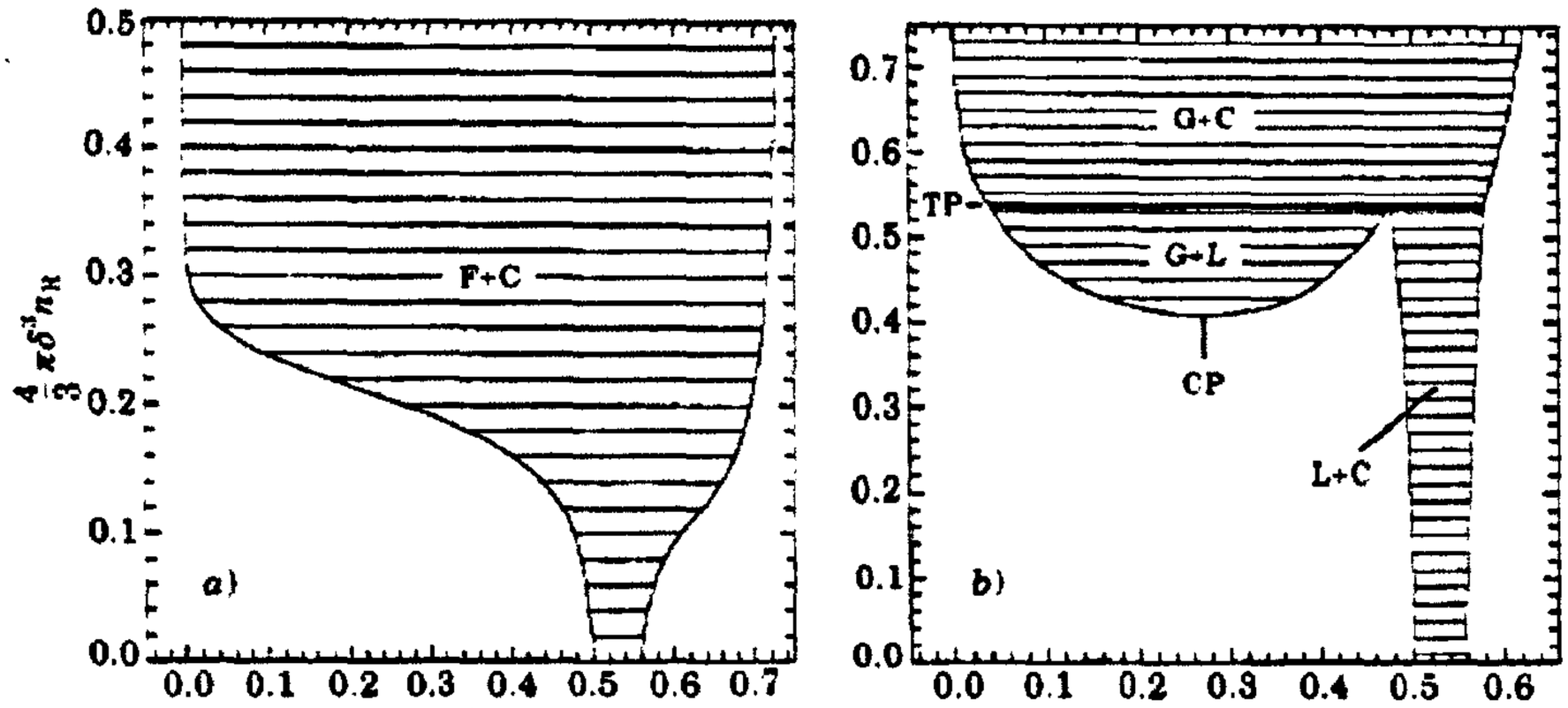

Figure 1.8: Phase diagrams of colloid − polymer mixtures showing colloid volume fraction ϕ against dimensionless polymer reservoir concentration $(4/3)\pi\delta^3 n_R$, for $\delta/a = 0.1$ (a) and 0.4 (b). The tie lines are shown in the two phase regions, whose composition is indicated as colloidal fluid (F), colloidal gas (G), colloidal liquid(L) or colloidal crystal (C). In (b) the critical point (CP) and triple point (bold line marked TP) are also indicated. Phase diagrams reproduced from [6]

a semi-dilute solution and by incorporating non-ideal contributions to the polymer osmotic pressure. Fleer and Tuinier have shown that the concentration-dependent cross-over between the dilute and semi-dilute limits is captured by the expression:

$$q_s = 0.865 q_R^{0.88}(1 + 3.95 y^{2\gamma_G})^{-0.44} \tag{1.21}$$

where y is the reduced polymer concentration and is equal to $C_p\ / C_p\ ^*$.

The strength of the depletion potential is quoted as the strength of the depletion potential at contact, expressed in units of $k_B T$. Fleer and Tuinier have calculated that a colloid pair potential at contact has the strength U_0 which can be calculated from:

$$-U_0/k_B T = q_s^2(q_s + \frac{3}{2}) q_R^{-3} y(1 + 3.77 y^{1.31}) \tag{1.22}$$

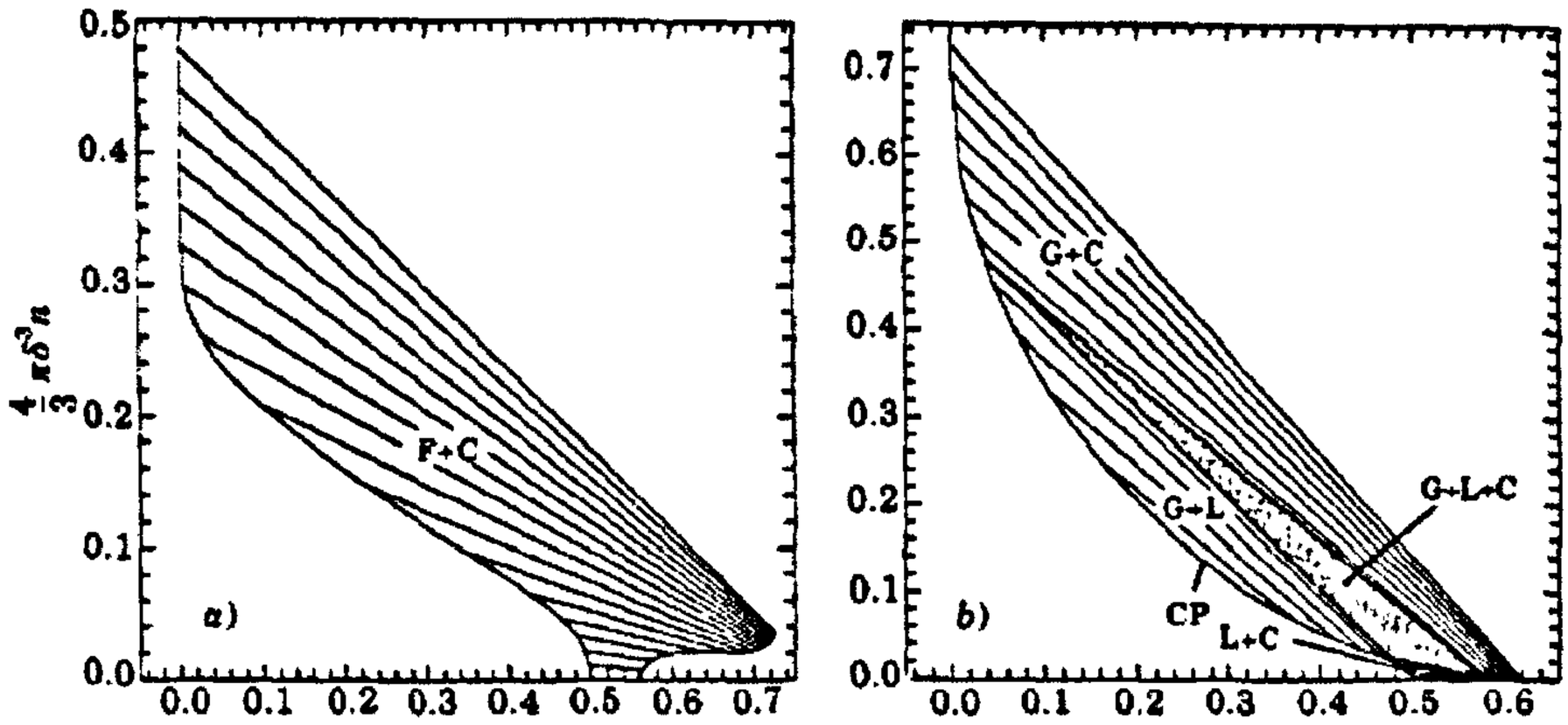

Figure 1.9: Phase diagrams of colloid − mixtures as functions of colloid volume fraction ϕ against dimensionless polymer concentration $(4/3)\pi\delta^3 n$. The notation is the same as in figure 1.8. Note that the oblique tie lines imply considerable polymer partitioning among the phases. In the (ϕ, n) plane the triple point observed in (b) becomes the region of three phase co−existence (gas−liquid−crystal) shown shaded in (b). Phase diagrams reproduced from [6]

1.5.3 Predicting phase behaviour

A van der Waals mean field approach can be used to calculate the free energy density for two ensembles of polymer and colloid at a fixed polymer chemical potential, μ_p and varying ϕ_c (colloid volume fraction) where μ_p is given by:

$$\mu_p = k_B T \ln\left(n_p^{(R)} \lambda_p^3\right) \tag{1.23}$$

where $n_p^{(R)}$ is the number density of the polymer in a reservoir in osmotic equilibrium with the system and λ_p is de Broglie thermal wavelength of the polymer. $n_p^{(R)}$ can also be related to the polymer free volume fraction by:

$$\phi_p^{V*} = \frac{4}{3}\pi R_g^3 n_p^{(R)} \tag{1.24}$$

Firstly, the free energy of a disordered arrangement of colloids and polymers (the

fluid branch) is calculated. Secondly, the free energy of an ordered arrangement of colloids with polymers randomly dispersed, (the crystal branch) is calculated. Curves of the Free energy against ϕ_c for the fluid and crystal branches can then be plotted. Figure 1.10 illustrates the free energy curves for a low μ_p (which is equivalent to low ϕ_c). An initially homogeneous fluid with concentration ϕ_i, has a higher free energy than the minima of the two free energy branches. In order for the fluid to reduce its free energy, it separates into coexisting fluid and crystal phases. The volume fractions of the two coexisting phases can be determined via the common tangent construction. Figure 1.10 shows a tangent drawn between the fluid and crystal branches. The points where the tangent touches the fluid and crystal branches gives the volume fraction of the fluid and crystal phases. At these two points the coexisting phases have equal particle and polymer chemical potentials and pressures and the two phases are in equilibrium. To build up a complete phase diagram this procedure is repeated for a range of depletion potentials. The phase behaviour can therefore be predicted as a function of colloid volume fraction and free polymer concentration.

Polymer – colloid size ratio

The statistical mechanical work of Gast et al [10] show that for a suspension of hard spheres in an ideal solvent for the polymer, the phase boundaries depend upon the polymer–colloid size ratio, ξ, as shown in figure 1.11. In cases of low ξ, (0.1 to 0.2) a fluid – solid rather than a fluid – fluid phase transition is observed. This means that the colloid –rich phase shows long range order and that there is no critical point. The attractive potential becomes weaker but longer in range as ξ increases resulting in a greater polymer concentration being required to induce the phase transition, and the resulting solid phase is less densely packed. At the highest ξ of 0.4 a fluid-fluid transition appears between $0.39 < \phi_c < 0.41$ in addition to the fluid-solid transition.

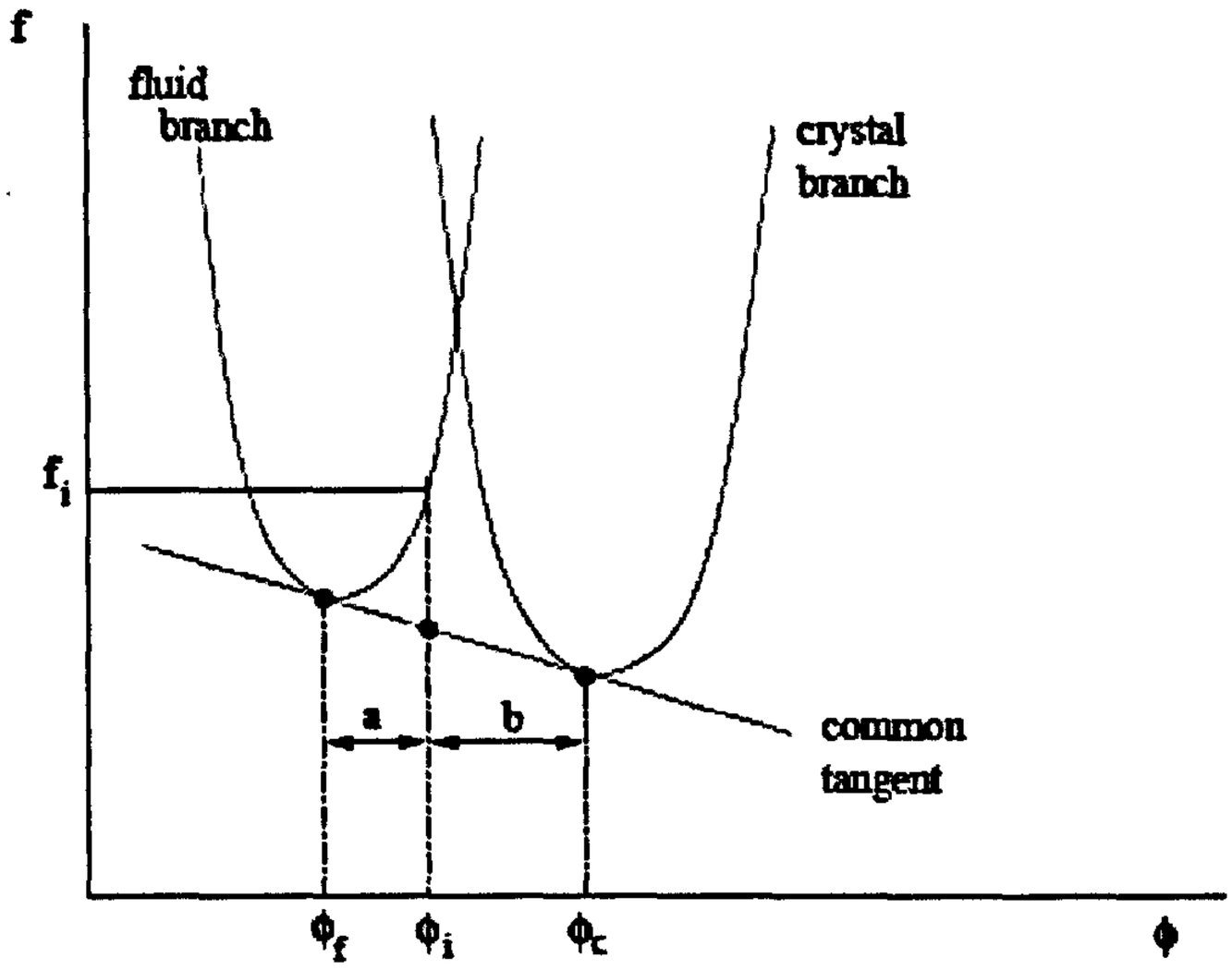

Figure 1.10: Schematic diagram of the free energy density (f) as a function of colloid volume fraction ϕ at a fixed free volume polymer concentration. The figure shows how the common tangent construction is used to determine the concentrations of the two coexisting phases.

1.5.4 Polydispersity

The hard sphere model and the AO model assume that the colloids and depletion polymer are monodisperse in size. In reality it is likely that there will exist a size distribution for both the colloid and depletion polymer which can have some interesting effects on the observed phase behaviour.

Colloid polydispersity

The polydispersity of a particle is given by:

$$\sigma = \sqrt{\frac{\langle a^2 \rangle}{\langle a \rangle^2} - 1} \tag{1.25}$$

where a is the particle radius. The hard sphere model describes how a colloidal crystal structure is formed above colloidal volume fractions $\phi > 0.545$ (see figure 1.6). Increasing the colloid polydispersity will have an effect on the phase

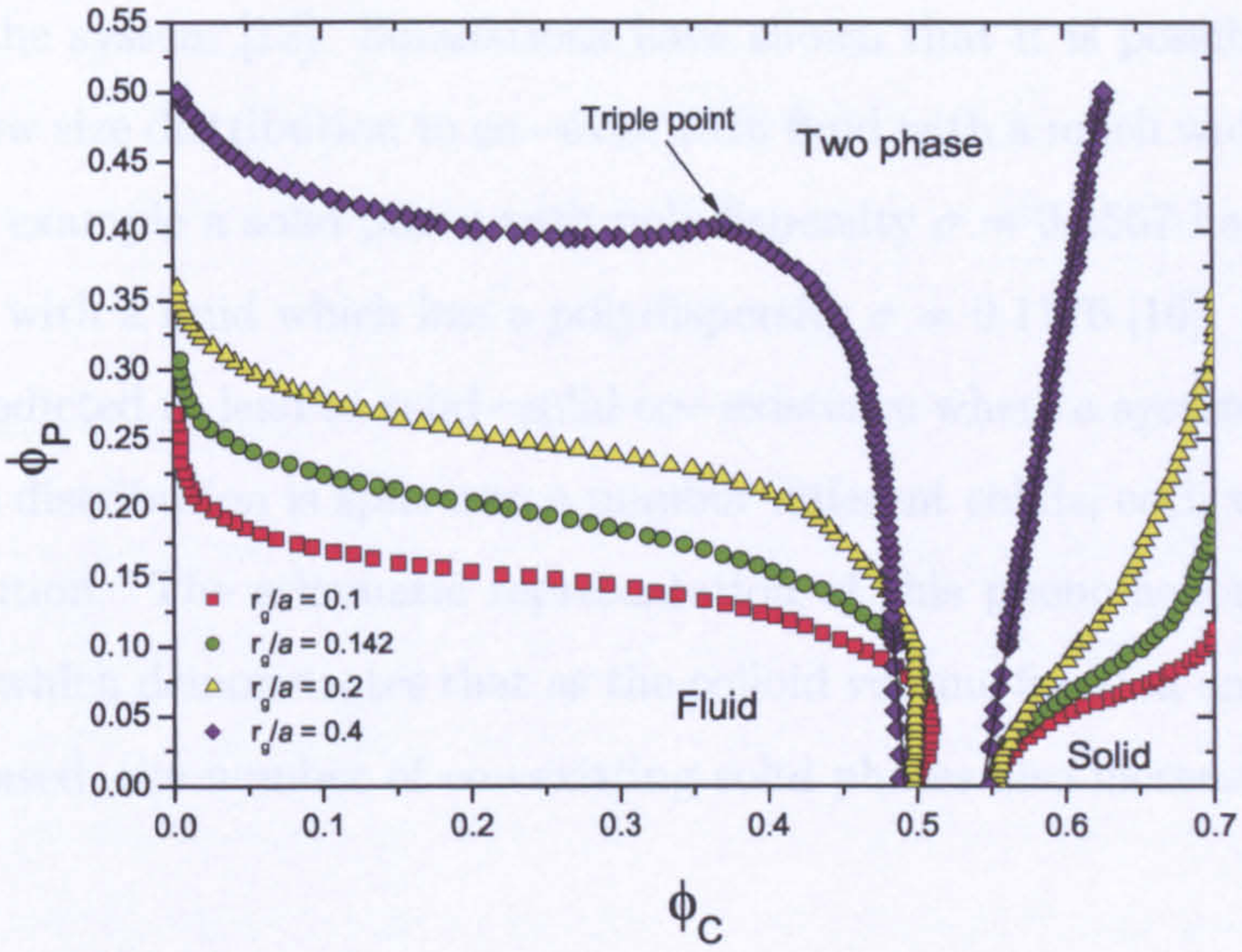

Figure 1.11: Phase diagram of polymer volume fraction against colloid volume fraction showing the fluid and solid co−existence lines for a range of ξ. Figure reproduced from [10]

behaviour [12, 13]. It is easy to imagine that once there is a significant colloid size distribution that there will be difficulty accommodating the particles in a lattice structure and so the crystal structure will become destabilised with increasing polydispersity. Experiments have been performed which show that crystallisation is indeed suppressed above a polydispersity of ≈ 0.12, which is referred to as the *terminal polydispersity* [14, 15]. In a system with low σ of 0.075 a fluid − crystal transition was observed whereas in a suspension which was chemically identical but with an increase in polydispersity to $\sigma \approx 0.12$ there was no evidence of crystal formation even after several months. Theoretical work suggests that the terminal polydispersity value arises from a progressive narrowing of the fluid − solid coexistence region with increasing σ, with the phase boundaries meeting at the terminal polydispersity value in a point of equal concentration.

The colloid polydispersity will cause fractionation of the colloids, where two co-

existing phases can have different size distributions in an attempt to decrease the entropy of the system [12]. Simulations have shown that it is possible for a solid with a narrow size distribution to co−exist with fluid with a much wider size distribution. For example a solid phase with polydispersity $\sigma = 0.0567$ has been shown to co−exist with a fluid which has a polydispersity $\sigma = 0.1176$ [16]. Fractionation has been predicted to lead to solid−solid co−existence where a system with a large particle size distribution is split into a number different solids, each with a narrow size distribution. The schematic representation of this phenomenon is shown in figure 1.12, which demonstrates that as the colloid volume fraction and polydispersity is increased, the number of co−existing solid phases also increases [17].

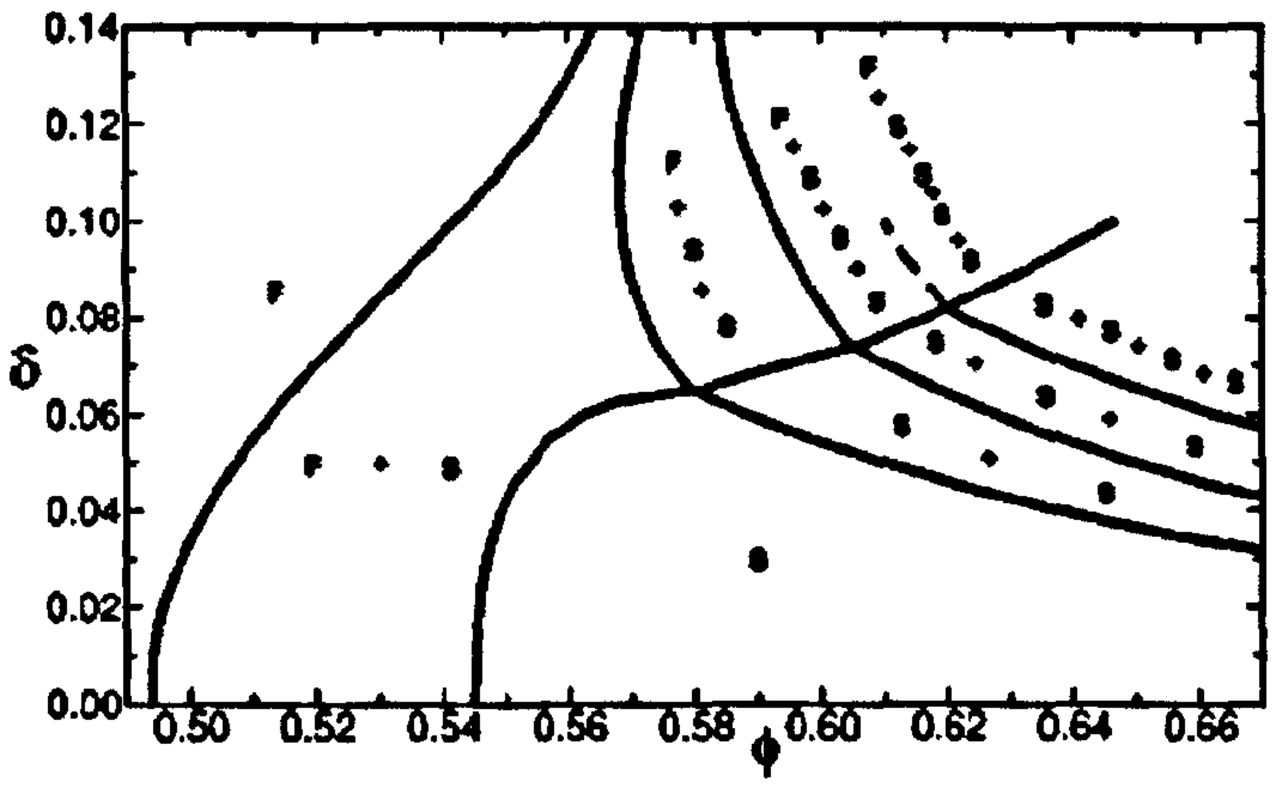

Figure 1.12: Schematic representation of fluid (F) and multiple solid (S) phase co−existence in polydisperse hard spheres. Approximate phase boundaries are plotted as polydispersity δ against volume fraction ϕ. For sufficiently large δ and ϕ, co−existence of several solids is predicted. Figure reproduced from [17].

Another intuitive effect is that as the colloidal σ increases, so does the random close packing volume fraction, ϕ_{RCP} since the smaller colloids are able to fill the spaces between larger colloids and so produce a more dense phase. The simulation work of Schaertl and Sillescu show just that and their observations can be seen in table 1.1 [18].

Table 1.1: Calculated random close packing fractions as particle polydispersity is increased [18].

σ	0.00	0.02	0.05	0.075	0.10	0.15	0.20	0.25	0.30	0.35	0.40
ϕ_{RCP}	0.64	0.65	0.66	0.66	0.67	0.68	0.68	0.69	0.71	0.74	0.78

Polymer polydispersity

It is rare that a depletion polymer will be uniform in size, particularly in commercial formulations [19] and the effect of this size distribution has been investigated [20, 21]. Lieter-Santos et al report that even a small size distribution in the depletion polymer can markedly alter the behaviour, where phase separation can be observed at low values of C_p where phase separation would not usually be expected to occur, and with lesser depletion potentials. This phenomenon is attributed to the presence of polymer coils which are much larger than the mean polymer size inducing an attraction over much larger distances. The lesser number of these larger polymer coils results in a weaker depletion potential until particles are able to move within close enough proximity that the effect of the majority of the polymer coils is felt.

1.5.5 Non equilibrium phase behaviour

The hard sphere model shows how a colloidal system can form a glass by rapidly quenching the system beyond $\phi = 0.58$ causing a non equilibrium state to be formed in which particles are trapped in an amorphous fluid–like arrangement. The previous section has also discussed the phase behaviour of colloid – polymer systems where the separating phases are in equilibrium with each other and therefore co–exist. There does exist a further scenario in which a colloidal system separates into phases which are unable to obtain their equilibrium states, and they become temporarily trapped in states which are not in equilibrium with each other. Colloid polydispersity has been shown to suppress crystallisation, however, Poon et al have shown that crystallisation can also be suppressed in a colloidal hard sphere system by the addition of high enough concentrations of depletion polymer [22]. By using small angle light scattering they show evidence for three different types

of non-equilibrium behaviour in a system with small ξ of 0.08 which emerge as the polymer concentration is increased, which are nucleation−like, spinodal−like and transient gelation. Nucleation occurs immediately beyond the the non-equilibrium boundary. Microscopic observation shows the formation of disconnected aggregates which are reminiscent of nucleation of droplets in classical fluids. Spinodal decomposition occurs just above the non-equilibrium boundary at moderate values of ϕ and microscopic observations show the formation of interconnected domains. Transient gelation occurs at yet marginally higher values of ϕ and C_p and shows a temporarily stable network of particles which then collapses to form a dense layer.

Poon et al proposed that non-equilibrium behaviours were a result of the competition between the rates of thermal rearrangement of aggregates and the process of aggregation. At high polymer concentrations the depletion potential is large enough to slow the rate of thermal rearrangement, allowing aggregation to dominate and resulting in the formation of a gel.

1.6 The onset of non equilibrium behaviour

There exists a boundary between the homogenous nucleation of the coexisting fluid−crystal phases, and the non−equilibrium aggregation which is highly reproducible. In an attempt to explain this Poon and co [23] utilised a thermodynamic approach where the Helmholtz free energy of a colloidal suspension is calculated as a function of ϕ_c and Π_p for a fluid and crystal branch. Energy curves analogous to those seen in figure 1.10 are obtained at low polymer concentrations, with the minima representing points on the the fluid−crystal co-existing phase boundary. At higher polymer concentrations however, a double minimum is seen in the fluid branch, as shown by figure 1.13.

From the free energy curves shown in figure 1.13 tangents can be drawn between minima. The first can be drawn between lowest minimum of the fluid branch and the minimum of the crystal branch, which generates points along the fluid-crystal

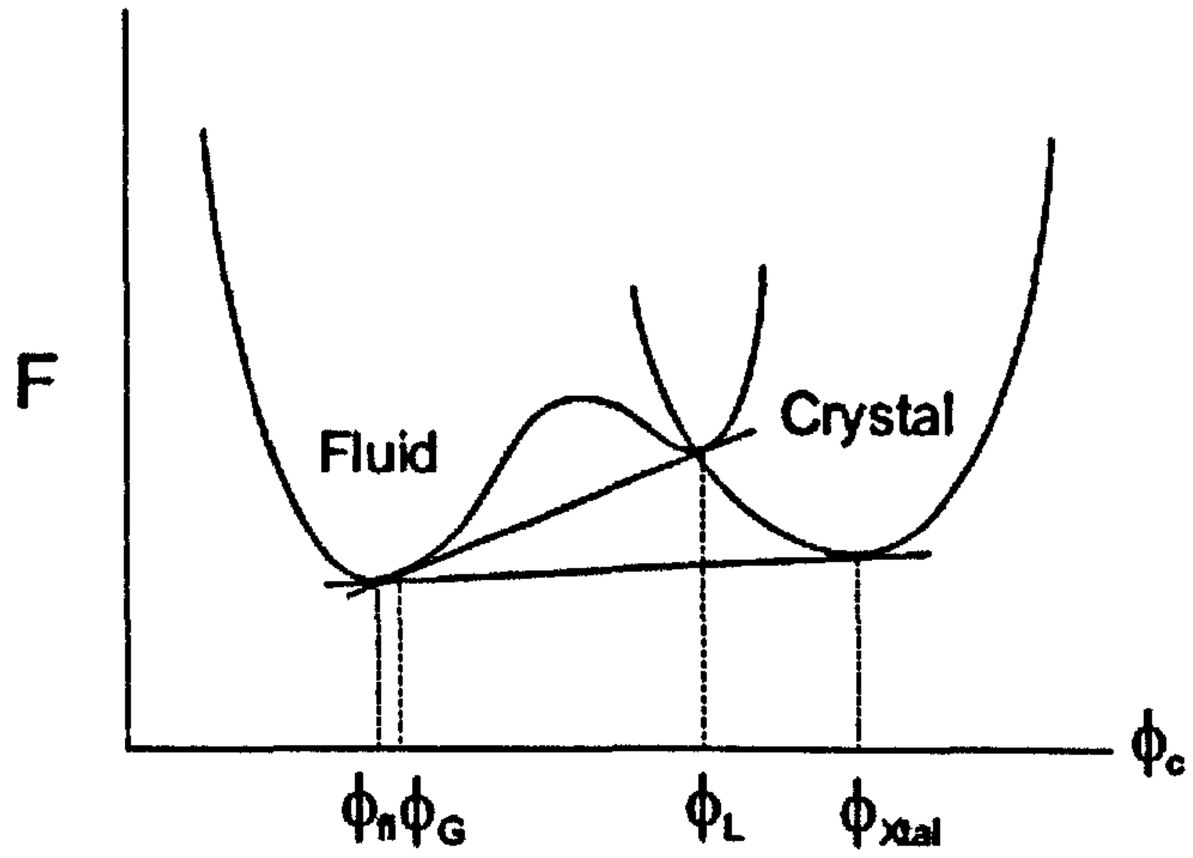

Figure 1.13: The fluid and crystal free energy branches for a high polymer concentration colloid-polymer mixture. There is a double minima evident in the fluid branch, leading to a hidden gas–liquid binodal in the fluid–crystal co–existence region

phase boundary. The second tangent can be drawn between the two minima of the fluid branch which generate points along a gas–liquid binodal. In cases where $\xi > 0.3$, this would appear as a gas–liquid co–existence region in the phase diagram, but in cases where $\xi \sim 0.1$ the gas-liquid binodal is hidden within the fluid-crystal co-existence region. Poon suggests that it is the crossing of the hidden gas–liquid binodal that instigates the non-equilibrium behaviour.

If the appearance of non–equilibrium phase behaviour was a genuine result of crossing the hidden gas–liquid binodal, Poon argued that the initial behaviour of a homogeneous fluid system above the non-equilibrium polymer concentration would be similar to simple fluids undergoing phase separation. Close to the binodal it is expected to observe nucleation, followed by spinodal decomposition at a deeper quench and a cross–over from spinodal decomposition to transient gelation at an even deeper quench.

1.6.1 Gravitational effects on the transient gel boundary

The effect of gravity on the position of the gel line was discussed using a simple model by Allain et al [24] who reported that gravity can hinder gelation in colloidal suspensions and that the volume fraction of colloid required for gelation can be considerably larger than expected. In order for a network to be formed the individual clusters formed must not grow to a large size, or they will become dominated by gravitational effects and begin to sediment and a gel will not form. This implies a threshold particle volume fraction which is required in order for gelation to occur, $\phi_c^{\otimes}$. Assuming infinite particle bond energy so that no thermal restructuring takes place, the minimum particle volume fraction at which gelation will occur, $\phi_c^{\otimes}$, is given by:

$$\phi_c^{\otimes} = \left(\frac{9k_BT}{2\pi\Delta\rho g a^4}\right)^{\frac{D_f-3}{D_f+1}} \tag{1.26}$$

where $\Delta\rho$ is the difference in density between the particles and dispersion medium, g is the gravitational acceleration constant and D_f is the fractal dimension of the clusters ($D_f = 1.78$ for DLCA clusters, see next section). In the absence of gravity (which can be achieved by matching the density of the colloids to the suspension medium) a gel phase should be observed above the underlying dynamic percolation threshold (thin dashed line). With the increasing effect of gravity gelation occurs at higher $\phi_c^{\otimes}$ [25](see figure 1.14).

1.7 Particle aggregation routes

Understanding the mesoscopic structure of the transient gel has been attempted with the aid of computer models and simulations. Typically, experimental data from an aggregated system is compared to data from a simulated structure to infer structural information about the experimental system. Probably the first breakthrough on the process of particle aggregation was made by Witten and Sander who proposed the diffusion limited aggregation (DLA) model [26]. In the DLA model,

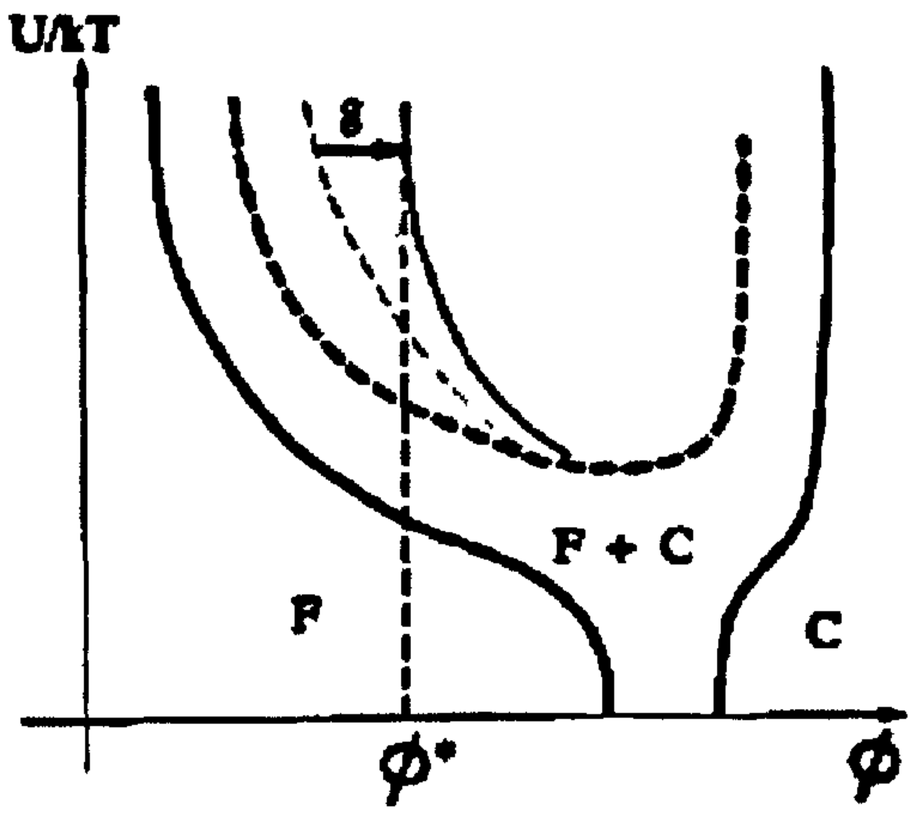

Figure 1.14: The effect of gravity on the transient gel boundary. In the absence of gravity the gel boundary can be found just above the dynamic percolation threshold (dashed line). Under the influence of gravity the boundary moves to higher $\phi_c^{\otimes}$ values. The hidden gas–liquid binodal is represented by the bold dashed line.

a seed particle is fixed at the centre of a simulation box and a particle is released from the edge of a simulation box and allowed to diffuse following a random walk path. The released particle will either enter a position along side the seed particle in which case it is assumed that there is irreversible aggregation, or the particle will move out of the simulation box. A ramified (non-compact) cluster is built up with intricate branched structures as the process is repeated [27]. Weitz and coworkers showed that the DLA model could be used to interpret the structure of real particle aggregates [28]. Modifications to the DLA model have been undertaken which has led to the diffusion limited cluster aggregation model (DLCA model).

In the DLCA model a finite volume fraction ϕ_0 of particles (in either two or three-dimensions) are allowed to freely diffuse via a random walk. When the two particles occupy neighbouring positions they form an irreversible bond and a cluster is formed. The newly formed cluster is free to diffuse and can aggregate with additional particles or clusters as it diffuses. Multiple numbers of clusters and particles can simultaneously diffuse throughout the system which makes the DLCA model more applicable to experimental systems. The expanding DLCA clusters are found

to be fractal, with the mass of a cluster M (which is proportional to the number of particles, N) scaling with its radius of gyration r_g as:

$$M \sim N \sim r_g^{D_f} \tag{1.27}$$

where D_f is the fractal dimension and is less than the corresponding spatial dimension D.

Due to the fractal dimension D_f being less than the spatial dimension (the size of the region originally containing its constituent particles), the density of the fractal structure decreases as it grows. This results in the size of the growing aggregate increasing faster than the embedding space until the fractal clusters come into contact each other and a percolating gel is formed (see figure 1.15) . The radius R_c of the fractal cluster at this gel point can be found from:

$$R_c = a\phi_c^{\frac{1}{D_f-3}} \tag{1.28}$$

where ϕ_c is the volume fraction of particles. The equation indicates that fractal clusters become smaller as ϕ_c is increased which implies that at some limiting ϕ_c clusters can no longer be fractal.

The DLCA model makes a number of assumptions [22]. Firstly, that all particles will eventually become part of an aggregate. It is also assumed that aggregates grow at identical rates and therefore aggregates will contain the same number of particles at any given time. This is more acceptable when ϕ_c is low . The final assumption is that the aggregates grow independently of each other. At volume fractions close to the transient gelation boundary, aggregates will be in close proximity and compete for material. As a result of this competition equation 1.28 is thought to only hold true for $\phi_c < 0.1$ [22].

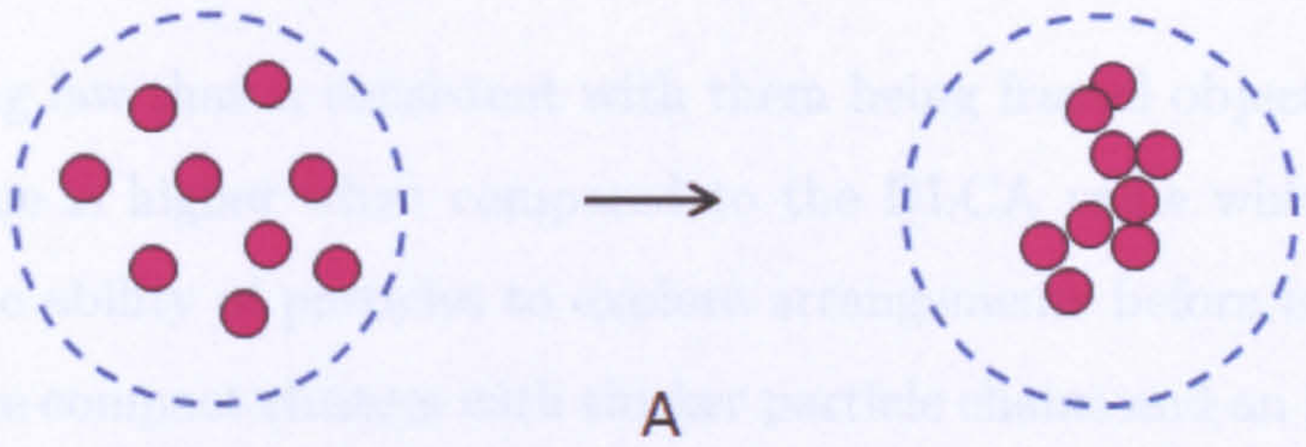

Figure 1.15: Schematic representation of the fractal growth and formation of a percolating network. The dashed line represents the embedded space of the particles prior to aggregation. In A the aggregate formed is smaller than the embedded space, whereas the fractal structure in B is as large as the embedded space due to it growing faster than the embedding space.

The DLCA model only accounts for the formation of particle bonds due to strong van der Waals attractions, which limits the model to systems which have an infinitely short ranged attraction of depth $>> k_BT$. Experimentally, it is more acceptable to assume that there are numerous particle−particle contacts occurring before an actual bond is formed and this type of particle interaction is known as reaction limited cluster aggregation (RLCA)[29, 30]. Although many particle−particle contacts may occur, a bond is permanent from the instant it is formed.

Numerical simulations [29] and experiments [31] have shown the clusters obtained

follow a scaling law that is consistent with them being fractal objects where $D_f \approx 2.1$. This value is higher when compared to the DLCA value which may be attributed to the ability of particles to explore arrangements before bonding, which allows for more compact clusters with thicker particle chains and an increased fractal dimension.

Induced colloidal attractions due to the addition of non−adsorbing polymer will occur provided the strength of the depletion potential is large in comparison to the thermal energy of the system. In situations where the strength of the depletion potential is comparable to the thermal energy, it is possible for particle bonds to break and re−form so that clusters can restructure. In this situation the reversible−DLCA model is more applicable [32]. In this model a finite bond energy is assigned to a particle such that once bonded to its neighbour there exists a non-zero probability of the particle escaping. After each time step in the simulation, particles are examined to determine if there are bond breakages. If the condition:

$$N_{ran} < e^{(-nE_{bond})} \tag{1.29}$$

where N_{ran} is a random number between 0 and 1, n is the number of bonds and E_{bond} is the bond energy in units of k_BT , is satisfied the particle breaks its bonds and escapes. By introducing a finite bond energy the competition between thermally induced rearrangement and diffusion limited aggregation is modified.

1.7.1 The effect of polymer concentration

In colloid-polymer systems at high C_p values (or at low temperatures) the particles form bonds due to the presence of an attractive interaction. At very high C_p the lifetime of the bond will increase dramatically resulting in a fractal structure that follows the pure DLCA model. A decrease in C_p will result in an increase in thermal fluctuations and a structure that does not span the available space. However, increasing colloid volume fraction at lower C_p can eventually give rise to structural

arrest.

In a plot of T against ϕ_c for attractive colloids, Coniglio et al suggested that there will be two lines: a percolation line close to which a fractal gel occurs and, at higher volume fractions a second line corresponding to structural arrest (see figure 1.16) [33]. At low C_p the presence of the percolation line becomes less and less detectable as clusters are not long living enough for observation. At very high C_p the two lines become indistinguishable as structural arrest is expected to combine features of gelation and glass transition [33]. Structural arrest is accompanied by a change from ergodic to non-ergodic behaviour.

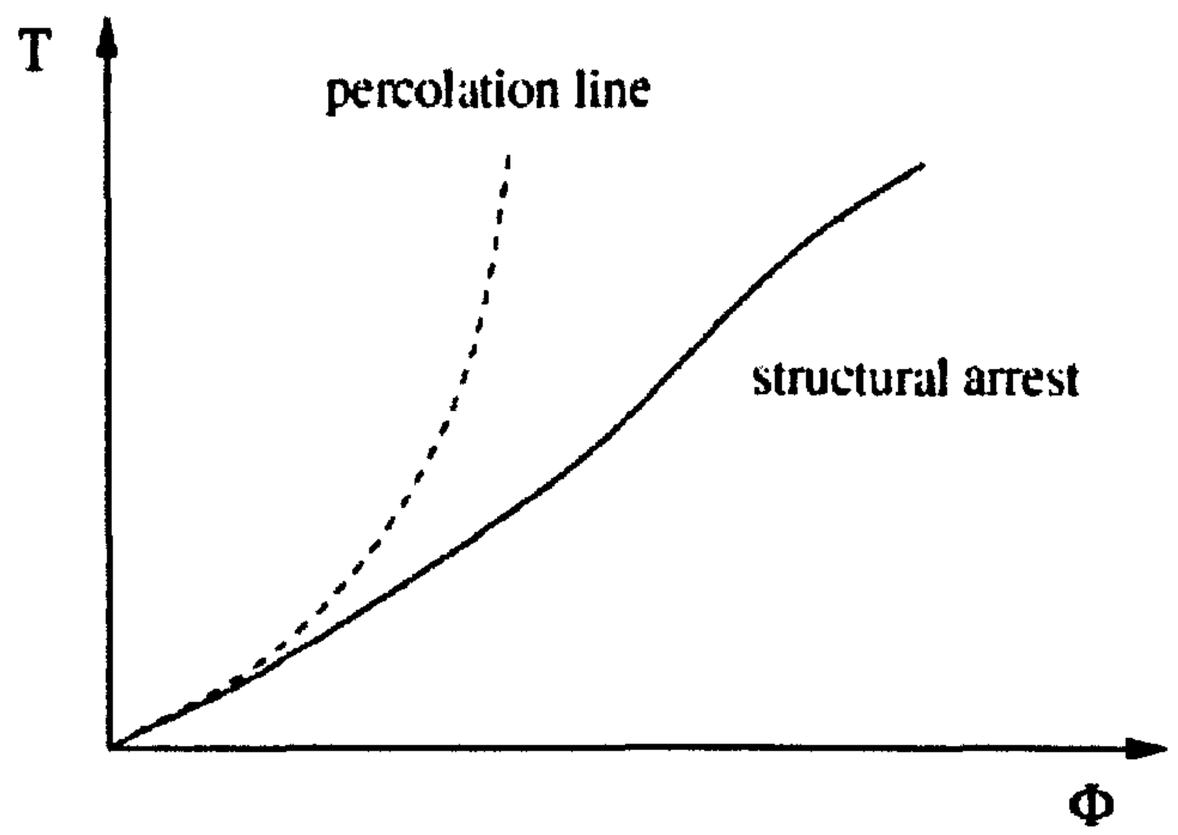

Figure 1.16: Schematic phase diagram showing the existence of two lines in a plot of temperature, T, against colloid volume fraction ϕ_c. An increase in temperature is equivalent to a decrease in C_p . Figure reproduced from [33]

Chapter 2

Colloidal glasses and gels

2.1 Colloidal glasses

In the hard sphere model discussed in chapter one, a glass is formed at a colloidal volume fraction of 0.58 and when the particles are in a disordered configuration. Here the phase behaviour depends solely upon ϕ. When an attractive interaction is added, the phase behaviour becomes more diverse. The new key parameters introduced into the phase diagram are the strength of the attraction and the range of the attraction, resulting in a three-dimensional phase space. For simplicity phase diagrams are often considered at fixed colloid-polymer size ratios, ξ. The regions of high volume fraction within the phase space are dominated by crowding effects, as in the hard sphere model, and attractive colloids form glasses at high volume fractions [34–36].

2.1.1 Attractive and repulsive glasses

When an inter-particle attraction is added to the hard sphere model, it is possible to produce a second glassy state known as an attractive glass. The hard sphere glass also known as a repulsive glass, is formed at a volume fraction of 0.58 where particles become trapped within cages of surrounding particles. This process is driven by entropy. For an attractive glass however the particles are trapped within

local positions due to the attractive bonds shared with its nearest neighbours, rather than a physical overcrowding and is a process which is driven by energy. An experimental study investigating the dynamics of repulsive and attractive glasses found that particles in repulsive glasses exhibit cage rattling and escape, while those in attractive glasses are nearly static while caged but are able to undergo large displacements upon cage escape, although this number of cage escapes was not large [37]. The average mean squared displacement is a measure of the average distance travelled by the particles and therefore provides an estimate of the size of the cage. In the case of the hard sphere repulsive glass, each particle can only rattle within its own cage, usually travelling no further than an average distance of $\approx 0.1\ d$ where d is the particle diameter. In the case of attractive glasses, provided the range of the attraction, ξ, is smaller than $\approx 0.1\ d$ the particles will become much closer together, resulting in a reduced cage size and a more inhomogeneous distribution of the empty space.

Between these two glassy extremes lie a a re-entrant pocket of liquid states, which exists at higher higher volume fractions with respect to the hard sphere glass [38]. It occurs when the range of the attraction is less than 0.1 d. This phenomenon is due to the short range attractive potential between particles allowing particles to become much closer together and therefore liberating additional free volume in which the particles can move, and the glass begins to melt. A representative phase diagram is shown in figure 2.1.

2.1.2 Ageing in colloidal glasses

As the concentration of a colloidal suspension is increased, the motion of a colloidal particle becomes increasingly slowed as a result of particle crowding. There comes a point when the particle motion is no longer diffusive on long time scales, and it is at this point that the glass transition is considered to occur [39]. The ageing of glasses is the phenomenon that lowers the potential energy of the system with time by means of a slow structural evolution. In a system in which there may

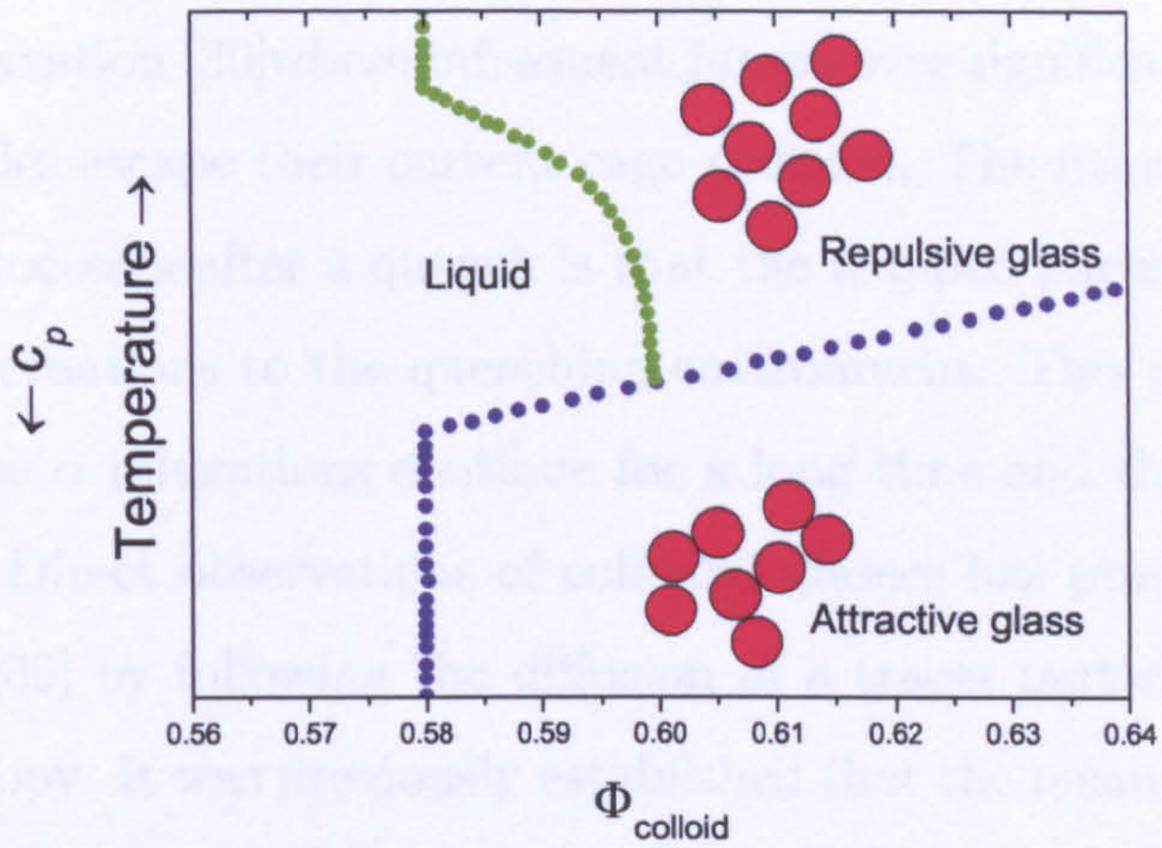

Figure 2.1: Schematic phase diagram showing both the repulsive and attractive glasses. The diagram represents hard spheres with short-range square-well attraction at high volume fraction, and shows the three distinct phases: re-entrant liquid, repulsive glass and attractive glass. Figure reproduced from [38]

be limited large scale particle movement, the mean squared displacement provides good quantitative information regarding the ageing process, and the application of Mode Coupling Theory (MCT) for predicting the colloidal glass transition has proven to be very useful [34].

There has been much interest in trying to understand the ageing of colloidal glasses, particularly as a model system for understanding the glass transition in simple liquids. As a glass ages in an attempt to restore equilibrium its properties changes accordingly and the particle dynamics slow with time and metastable states become increasingly more stable. As the overall energy of the system decreases with time the ageing process can be understood as a walk through an energy landscape with many local minima. This means that on long timescales, a glass may appear as though it is arrested when in actuality the dynamics are occurring far too slowly to follow. The age of the glass (time since glass formation) is important when consid-

ering experimental observations. The ageing of colloidal glasses is thought to be due to the slow α relaxation [30]where infrequent jumps over significant energy barriers occur and particles escape their current cage position. The microscopic picture of the relaxation processes after a quench is that the trapped particles quickly adapt their rattling fluctuations to the quenching environment. This is referred to as β relaxation. These α relaxations continue for a long time and therefore constitute itself as ageing. Direct observations of colloidal glasses has provided evidence for this arguement [39] by following the diffusion of a tracer particle with the aid of confocal microscopy. It was previously established that the mean-squared displacement of these tracer particles shows an increase at long delay times which is related to cage escape. The study shows that ageing increases the cage escape time, while the cage size remains unchanged, and that there is a decrease of the cage escape rate with sample age.

Experimentally, the ageing process is usually followed by means of dynamic light scattering. However, the slow ageing of a colloidal glass has shown this to be a time consuming method, and so multispeckle dynamic light scattering was developed [40]. This method consists of averaging the autocorrelation function over time, but also over a large number of different speckles. The correlation functions for thousands of different speckles can be calculated in parallel and then averaged which drastically cuts the required measurement time. A second method for the measurement of ageing is by direct visualization using fast scanning confocal microscopy [39], which enables the path travelled by tracer particles to be followed.

2.2 Spinodal Decomposition

Within the unstable region of the phase diagram where phase separation is observed, there are two types of separation that can occur: binodal and spinodal decomposition. During binodal decomposition phase separation occurs via a nucleation and growth mechanism, where particles begin to cluster around nucleation

sites throughout the system. In contrast to this, spinodal decomposition occurs uniformly throughout the sample where two distinct regions appear and grow in size until phase separation is complete. Figure 2.2 shows a representation of a two component system which is undergoing spinodal decomposition. As the system is quenched into the two phase region on the phase diagram, it first crosses the binodal line. Further quenching then allows the system to cross the spinodal line which lies within the binodal region (see figure 2.3). The point at which the two curves meet is the critical point.

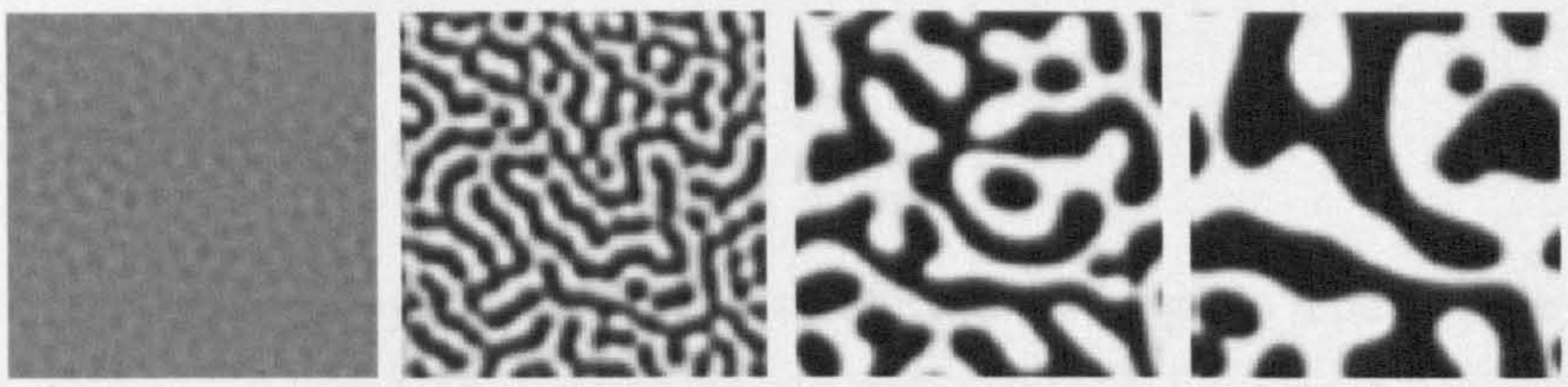

Figure 2.2: Representation of a two component system undergoing spinodal decomposition. The images (left to right) are shown as a function of time. At the earliest time there is a very fine network which gradually coarsens until two very distinct domains are apparent. Image reproduced from [41]

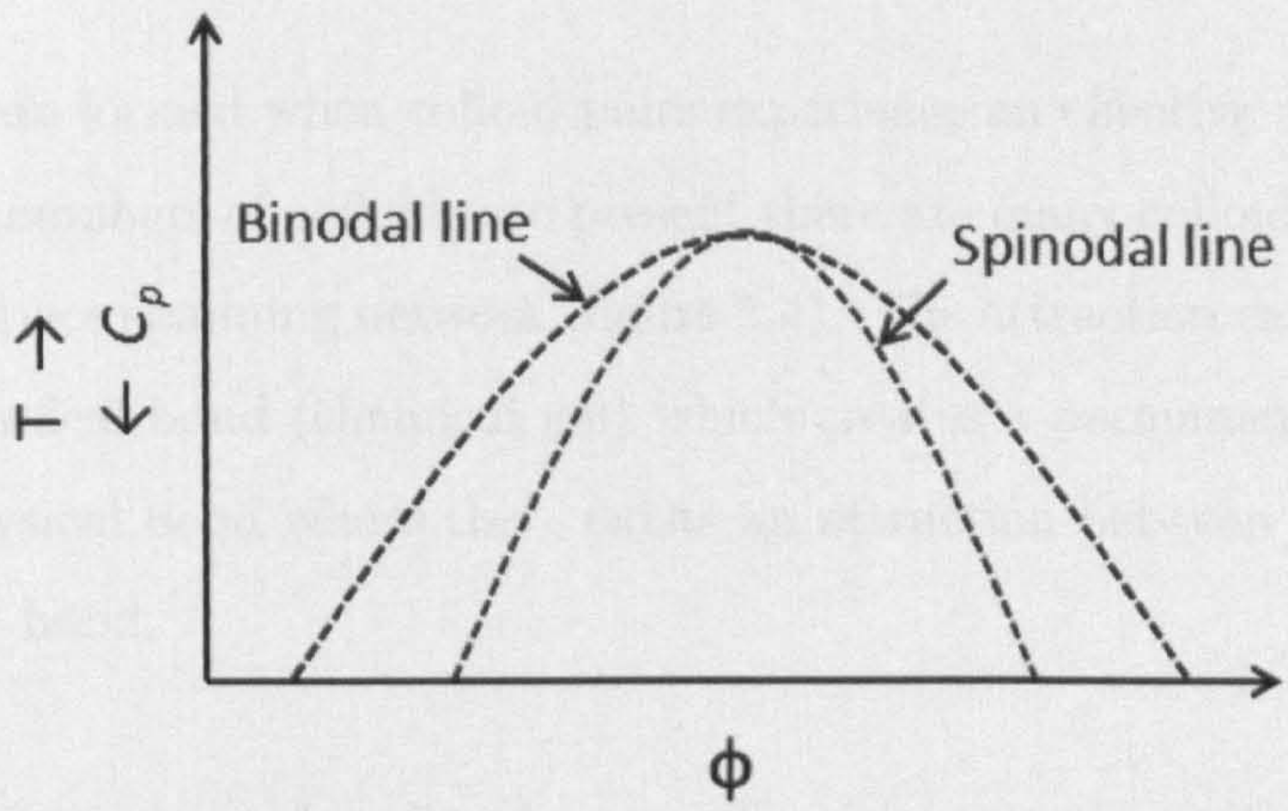

Figure 2.3: Schematic phase diagram showing the location of the binodal and spinodal line within the unstable region of a gas-liquid transition.

There are three stages of spinodal decomposition: early or linear stage, intermediate

stage, and late or flow stage. The early stage can be characterised by the Cahn-Hillard theory which predicts a maximum peak in the structure factor occurring at a constant q position (q_{max}), where the peak displays an increasing intensity [42]. The fixed position of the structure factor peak represents a fixed characteristic domain radius size, R_c . During the intermediate stage R_c increases as R_c (t) $\sim$ $R_0 t^{\theta}$ where $\theta = \frac{1}{3}$ in a purely diffusive system, and in the final stage viscous flow results in $\theta = 1$. However it has been suggested that the growth exponents in colloid-polymer mixtures may be somewhat different [43].

2.3 Colloidal gels

There are two types of systems which are referred to as gels. The first is a simple gel which has a cross linked network throughout solution. A hydrogel consists of a polymer dispersed throughout an aqueous solution, and an organogel comprises an organic solution containing a cross linked network [44]. The second gel type is a colloidal gel, where the cross linked network consists of colloidal particles rather than polymers, suspended throughout a continuous medium (which may be aqueous or organic). It is this type of gel which is the focus of this study.

Colloidal gels are formed when colloid pairs experience an effective attraction, and when multiple numbers of colloids are present there are many colloidal interactions resulting in a space spanning network (figure 2.4). The attraction can be either the result of a chemical bond (chemical gel) which creates a permanent structure, or it can be a physical bond where there exists an attraction between colloids rather than an actual bond.

The depletion interaction describes how an effective attraction between two particles can be induced in the presence of a non-adsorbing polymer. The characteristics of the resulting networks are dependant upon system components and so a wide range of behaviours are observed in colloidal gels. For example, the concentration of depletion polymer dictates the strength of the attraction, where higher concen-

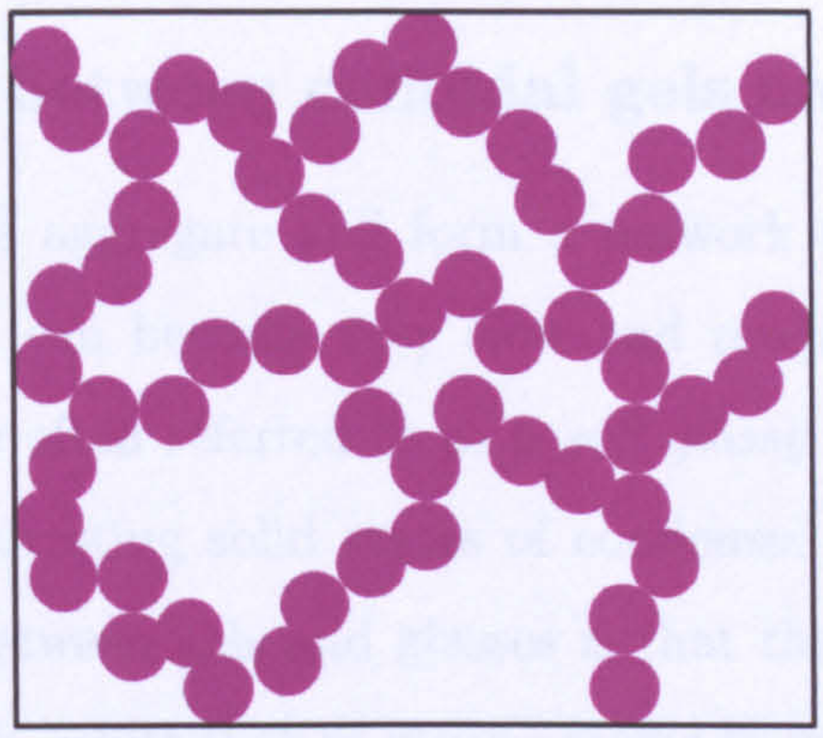

Figure 2.4: Representation of a space spanning colloidal network. In both physical and chemical gels the interaction between colloidal pairs causes a space spanning network to form, with interlinked chains of colloids.

trations result in stronger attractions. It is useful to discuss the strength of the colloidal attraction in terms of the thermal energy, U/k_BT as it allows data to be directly compared. In the limit of high polymer concentrations where $U/k_BT \gg 10$, the resulting attractions are so strong and long lived that they are considered to have formed a permanent bond. Colloidal gels do not generally exist in the opposite limit since there is a system-dependent minimum polymer concentration at which gelation occurs. Between these two extremes lie colloidal gels which have an attractive strength comparable to thermal energy, where U/k_BT <10. The induced attraction between colloidal pairs is relatively weak and of a short lived nature. It is for this reason that weakly attractive gels are referred to as 'transient' since the attractions are constantly breaking and reforming.

In the following sections the collapse of the gel network is discussed in general terms, followed by a presentation of the key publications regarding network collapse. The publications present both theoretical and experimental work, and the differences between the collapse of strongly attractive and transient gels are discussed.

2.3.1 Similarity between colloidal gels and glasses

When colloidal particles aggregate and form a network the local colloid density is high. The dynamics can become very slow and resemble that of a glass. A colloidal gel is therefore often referred to as a *soft glassy material.* Both colloidal gels and glasses are interesting solid states of condensed matter with some elasticity. The difference between gels and glasses is that the elasticity of gels is due to a percolating network, while that of glasses stems from caging effects [45]. The process of liquid-glass transition is called ageing and can be governed by either attractive or repulsive interactions between particles (depending on whether an attractive or repulsive glass is formed), while that of gelation is dominated by attractive interactions. During ageing, a system explores the energy landscape by thermally overcoming barriers in order to lower the total energy. The more the system is aged, the higher the barriers are that it must overcome. This is why there is a slowing down of the kinetics observed during ageing. Eventually, the system falls into a steep valley, from which it can no longer escape and thus becomes nonergodic. During gelation a percolated network is formed. Towards this percolation transition, the characteristic relaxation time of the system diverges, reflecting the growth of the clusters with time. Both processes can be characterized as an ergodic-to-nonergodic transition and by the resulting appearance of elasticity. Because of this, the similarity between glasses and gels is emphasized in the literature [36, 39, 40, 45–47]. A crucial difference between gels and glasses is that a gel is inhomogeneous over the characteristic length scale of the network and exhibits a structural organization, while a glass is homogeneous for inter-particle distances of order a few radii.

2.4 The collapse of the colloidal network

Except in cases where permanent chemical bonds are formed between colloidal pairs, the network follows an ageing pattern, the route and rate of which is governed by system characteristics. A colloidal system is not thermodynamically stable

and is constantly attempting to phase separate into its component parts in cases where the free energies of the separate component parts is less than the free energy of the homogenous mixture. Except for the case of permanent gels, colloidal networks are constantly rearranging until such a time that a dense close packed colloidal layer is formed. There is a range of forces acting on and from within the network which contribute to the collapse process, such as gravity. The rearranging of colloidal particles which results in the collapse of the network is also dependant upon the strength of the attraction, where strong gels and transient gels exhibit different behaviours.

The simplest way in which to observe the collapse of the colloidal network is by observing the bulk sample by eye. When a colloidal network is compressing, a layer of supernatant forms which is virtually free from colloids and a clear boundary can be observed between the colloid rich phase and the supernatant (figures 2.5 and 2.6). Recording the height of the colloid rich phase, $h(t)$, as a function of time allows a sedimentation (or creaming in cases where the particles are less dense than the continuous phase) profile to be plotted.

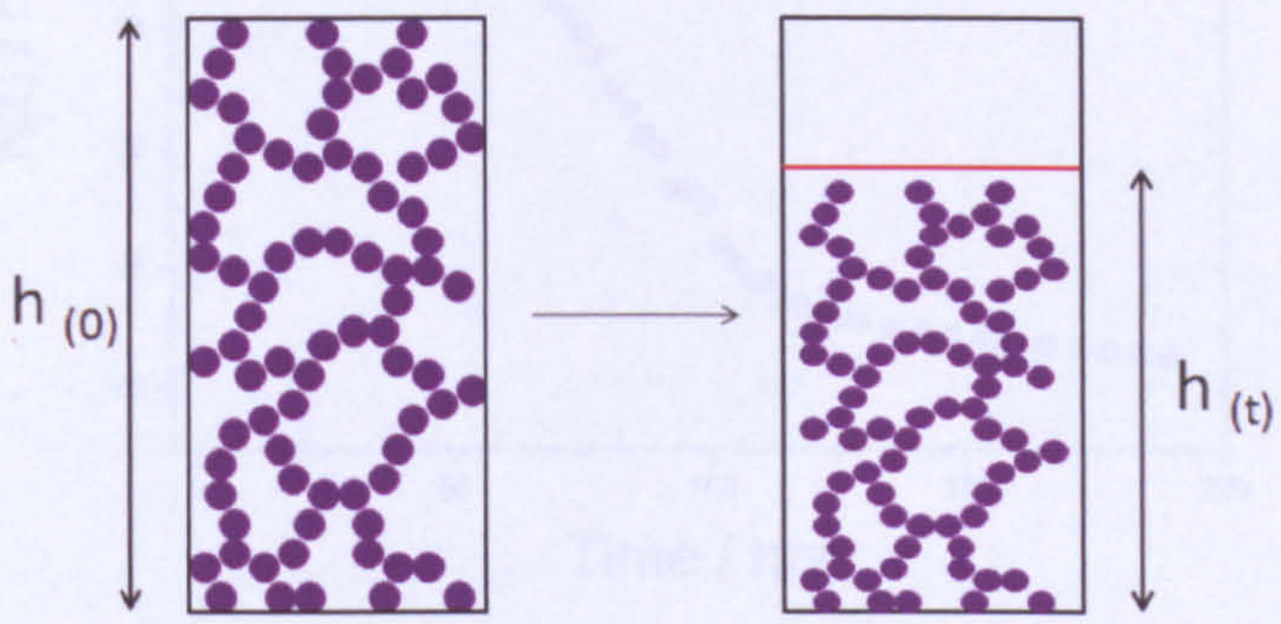

Figure 2.5: Representation of the compression, or collapse of a space spanning colloidal network. The figure on the left shows the initial space spanning network formed. The figure on the right shows compression of the network. Here the particles are sedimenting due to them being heavier than the continuous phase, resulting in a colloid rich phase and a colloid poor supernatant.

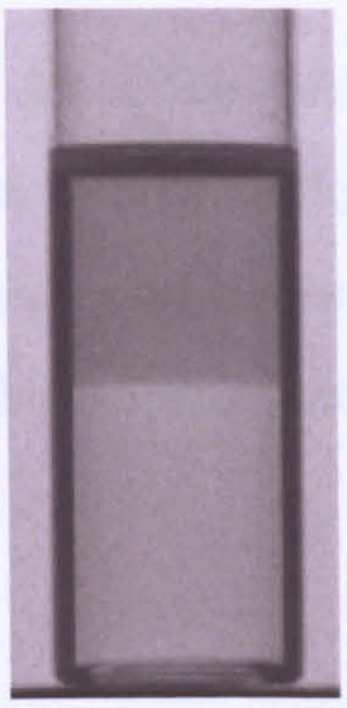

Figure 2.6: Photograph in which a colloid network has already collapsed into a dense colloidal layer. The colloid rich phase (dark upper layer) and the colloid poor supernatant (light lower layer) can be clearly observed. The system is an oil−in−water emulsion and so the colloids are creaming as a result of gravity due to their density being less than that of the continuous phase. The boundary between the two layers is distinct.

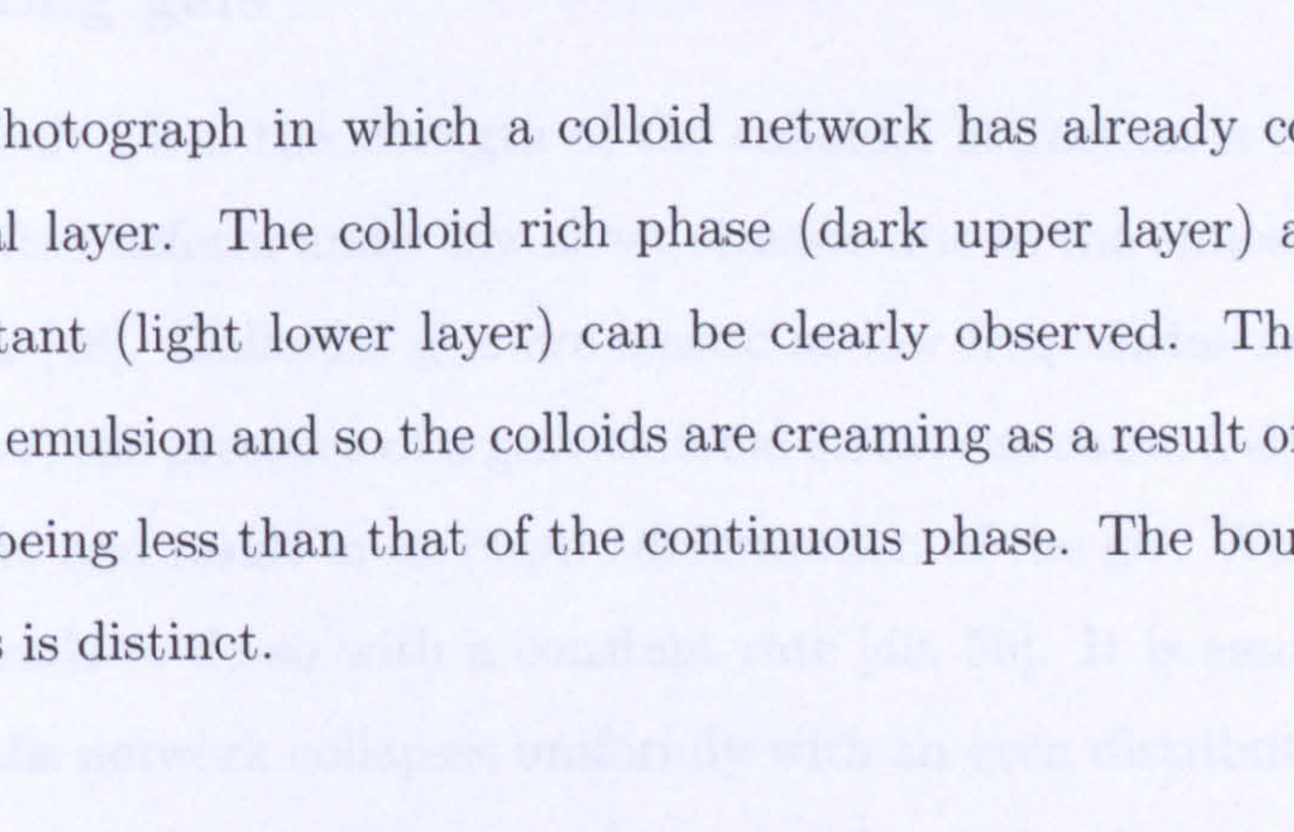

Figure 2.7: Example of a sedimentation profile, where the height of the colloid rich phase is shown as a function of time. The sample in this example had an initial height of 46.5mm.

Figure 2.7 shows an example of a sedimentation plot, where there is a period of

time where the network is stable. After this period of time the network begins to shrink with what appears to be an almost uniform rate until such a point that a dense colloidal layer is formed which undergoes a slow densification period. The effect of a range of variables on the collapse rate can be investigated in this way with relative ease.

2.4.1 Strong gels

Strong gels result when the strength of the colloidal attraction is of order $U/k_BT \gg 10$. They often deform under low shear stresses due to the almost brittle nature of the network [48]. Colloidal gels are elastic at low frequencies and can support stress. However, the presence of a gravitational stress can cause a slow compression of the structure and result in an elastic deformation of the gel. When a strong gel collapses, it tends to do so with a constant rate [49, 50]. It is assumed that once formed, that the network collapses uniformly with an even distribution of particles throughout the sedimenting portion of the sample, with a layer of sediment that simultaneously grows in height (2.8).

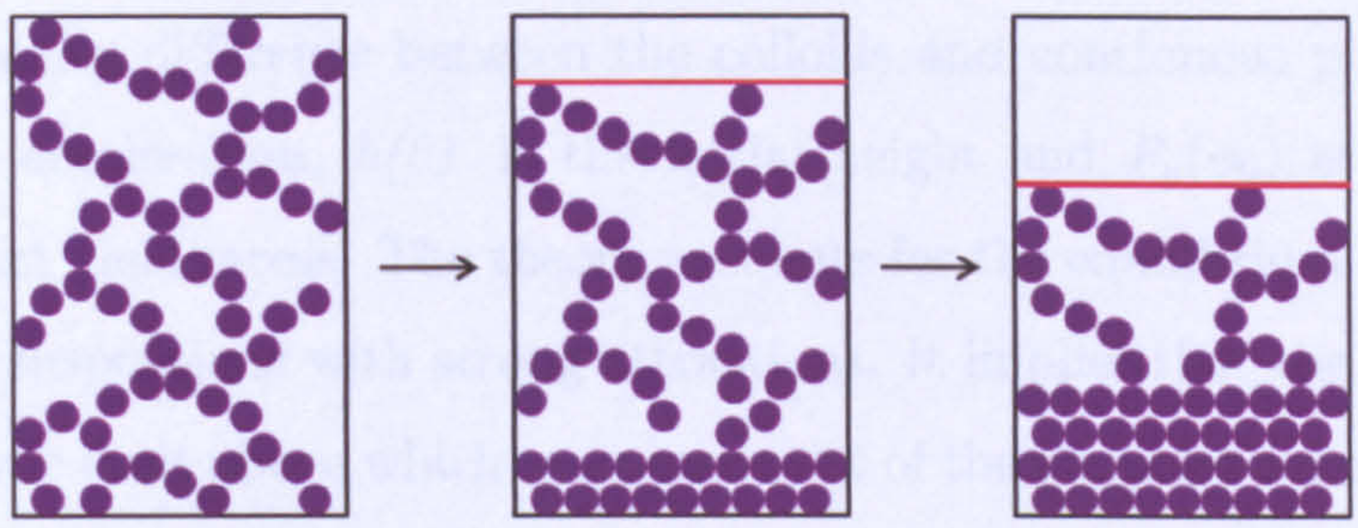

Figure 2.8: Schematic representation of the compression of a colloidal gel with strong attractions. The left hand schematic shows a space spanning network which has not yet started to sediment. In the centre picture some sedimentation has occurred and a dense sediment is beginning to form at the bottom of the sample. The red line represents the boundary between the colloid rich phase and the supernatant. In the right had schematic, the network has sedimented even further and the height of the sediment has increased.

The consolidation or compression of colloidal gels occurs poroelastically [51–54], and has been a subject of much study in the last 30 years. A theoretical approach to the consolidation of concentrated suspension was proposed by Buscall and White [55] where the rate and extent of consolidation depends upon the balance of three forces. Within this model, the gravitational stress is balanced by the sum of a frictional stress (from the fluid flow through the particle network), and the elastic stress of the gel. The initial rate of change of sediment height with time in a uniform gravitational or centrifugal field is approximately given by:

$$\frac{dh}{dt} = -\frac{(1-\phi_0)\,u_0}{r\,(\phi_0)}\left[1-\frac{1}{B}\right] \text{ when } B > 1 \tag{2.1}$$

where:

$$B = \Delta\rho g \phi_0 h(0)/P_y\,(\phi_0) \tag{2.2}$$

u_0 is the sedimentation velocity of an isolated particle, ϕ_0 is the initial volume fraction of colloids, $r(\phi_0)$ is a dimensionless hydrodynamic interaction parameter, $\Delta\rho$ is the density difference between the colloids and continuous phase, g is the gravitational acceleration, $h(0)$ is the initial height and $P_y(\phi_0)$ is a concentration dependant yield stress. The theory accounts for the equilibrium consolidation behaviour of suspensions with strong attractions. It implies that the network possesses an elastic limit above which rearrangement of the particles occurs to produce a more concentrated structure. No consolidation will be observed in samples where the forces acting upon the network do not exceed the yield stress.

Experimental study of strong gels

A range of experimental data regarding the collapse of strong gels is also available [49, 51, 56]. The majority of these studies involve observing the bulk sample rather than performing a microscopic analysis. The collapse of strong gels has been stud-

ied by Derec et al [48] where the strong attraction was a result of Van der Waals attractions. A CCD camera was used to record images of the sedimenting samples, and a single pixel vertical line was extracted from each image and displayed as a function of time, the results of which can be seen in figure 2.9. There are three regimes evident on the profile, an initial slow settling or creep regime, a period of more rapid collapse, and finally a period of densification.

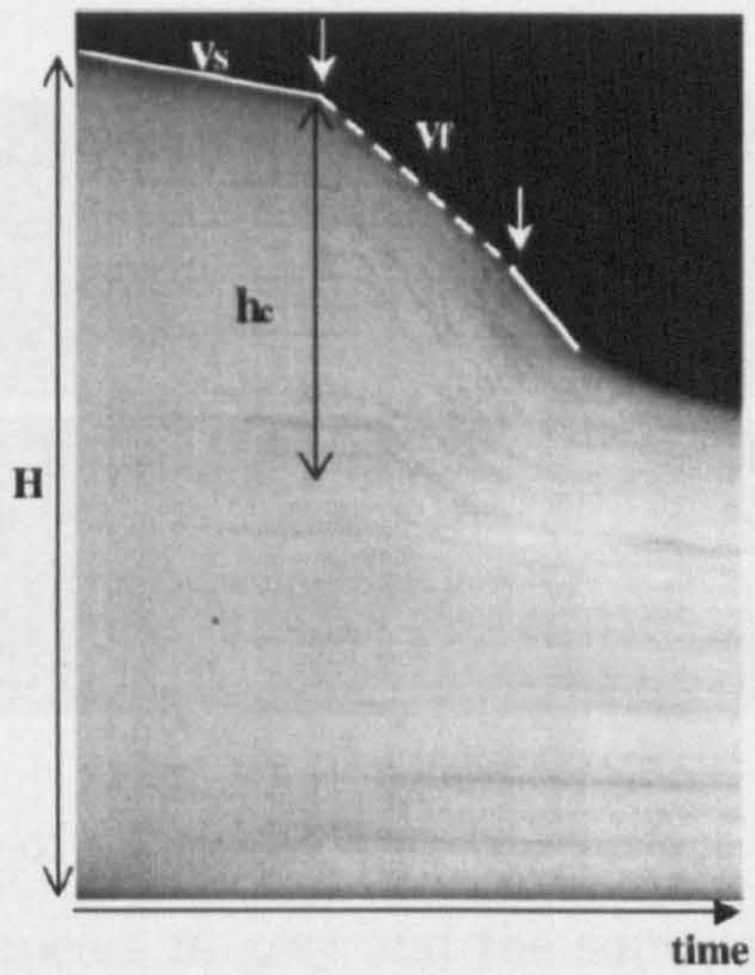

Figure 2.9: Space v's time diagram of a settling gel. The X axis spans a total of 1770 seconds, and the Y axis spans 74mm. The boundary between the dark and white zones corresponds to the water−gel interface position as a function of time. It is enhanced by a white line in the first and second settling regime. The white arrows represent the occurrence of eruptions at the surface of the gel. (Figure reproduced from [48]).

The initial settling velocity was found to be dependant upon the colloid volume fraction, such that

$$v_s \sim \phi^{(1-D_f)/(3-D_f)} \tag{2.3}$$

where D_f is the fractal dimension of the aggregates, which has been shown to

vary with the volume fraction of colloids. At the point between the early settling and rapid collapsing behaviour, surprisingly, eruptions were witnessed at the colloid−supernatant boundary which were evident in all samples. The eruptions correspond to fractures within the gel which open up and allow solvent to pass through the network with more ease, and in the process particles and aggregates are eroded from the channel and carried to the boundary forming the observed volcano pattern (figure 2.10).

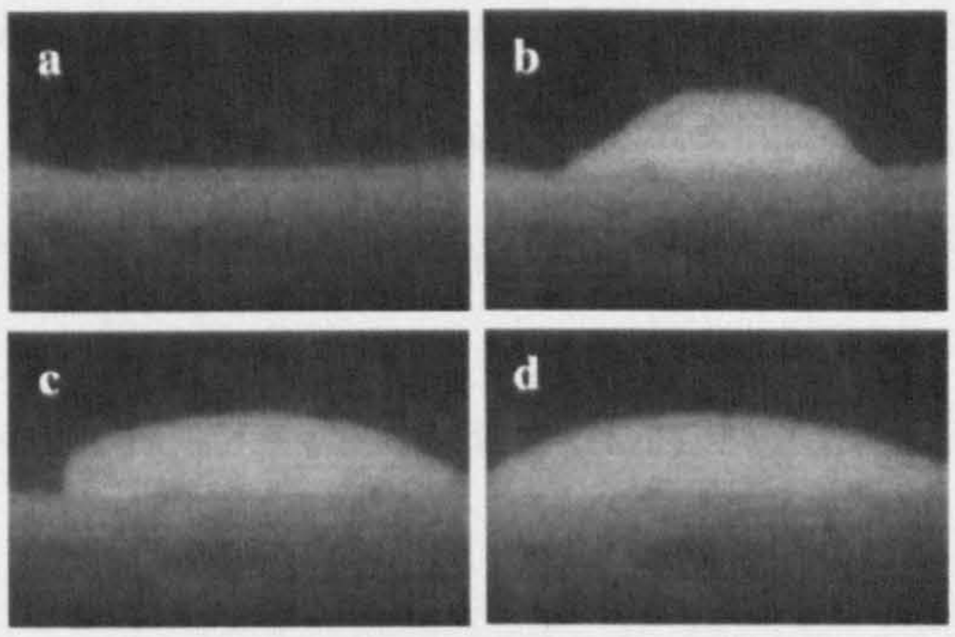

Figure 2.10: Close view of an eruption at the surface of the settling gel, at different times. The gel appears in grey and the supernatant in black. The width of the photograph corresponds to 7.5mm and the time interval between successive photographs is 4 seconds. (Figure reproduced from [48]).

Both the permeability and elasticity of a colloidal network have been calculated using the rate of collapse under gravity by Manley et al [51]. They investigate a range of samples where the gravitational stress is either lower or higher than the network yield stress. The initial theory of Buscall et al states that a network will only collapse once the sum of the forces acting upon the network exceed its yield stress [55]. However, more recent works concentrate on the balance of the gravitational and yield stress [51, 52]. In cases where the gravitational stress is less than the network yield stress, the networks are observed to collapse poroelastically. The gravitational stress is altered by varying the initial height of the sample and the colloid volume fraction, but in all instances there is a strong attraction between colloidal pairs.

For gels formed at small initial heights and with high ϕ, the height of the network decreases at a rate which decays exponentially with time, until it reaches a final equilibrium height, which is determined by the balance between the network elastic stress and the gravitational stress. For networks formed with large initial heights, and with lower ϕ, gels initially exhibit the same behaviour which is then followed by a rapid, catastrophic collapse, which occurs because the network is ultimately unable to bear its own weight. At short times, the two cases are indistinguishable, and the rate of collapse of the gel is limited by the backflow of the solvent through the solid network. The initial rate of collapse decreases with increasing ϕ, in a manner which is comparable with Darcy flow which describes the flow of fluid through porous media. At short times, the gel is uncompressed and the elastic stress negligible, and so the permeability is hypothesised to be calculated as follows [51]:

$$k_0 = -\frac{\eta}{\Delta\rho g\phi}\frac{\partial w}{\partial t} \tag{2.4}$$

where $\frac{\partial w}{\partial t}$ is the displacement of solid as a function of time, and $\Delta\rho$ is the density difference between the particles and solvent. This hypothesis is found to be accurate by comparing the results to the permeability value which is calculated using the initial velocity of the interface. Using this method of calculation, the permeability is found to be set by the largest length scale in the system, which is the cluster size R_c so that:

$$k_0 \sim \frac{a^2}{\phi^{2/(3-D_f)}} \tag{2.5}$$

where D_f is the fractal dimension of the aggregates and a is the particle radius [51].

The gravitational collapse of colloidal gels has also been the focus of research by Lietor-Santos et al [53], where the particle volume fraction was measured as a function of height at any experimental time. The intensity of light transmitted through

a sample is a measure of the colloid volume fraction, and high intensities correspond to a low volume fraction. Samples were prepared with varying C_p and the resulting sedimentation plots can be seen in figure 2.11. During the compression of the network the colloid volume fraction was shown to change almost linearly along the height of the network, with the volume fraction being close to 0.5 at the top of the colloid rich phase and close the initial colloid volume fraction at the bottom (in a system which is creaming rather than sedimenting). This is represented in figure 2.12. The network therefore does not remain uniform under compression and a dense layer is formed. The prediction of the poroelastic model for the long time volume fraction profile is consistent with the experimental observations and is represented in figure 2.12 by the drawn solid line.

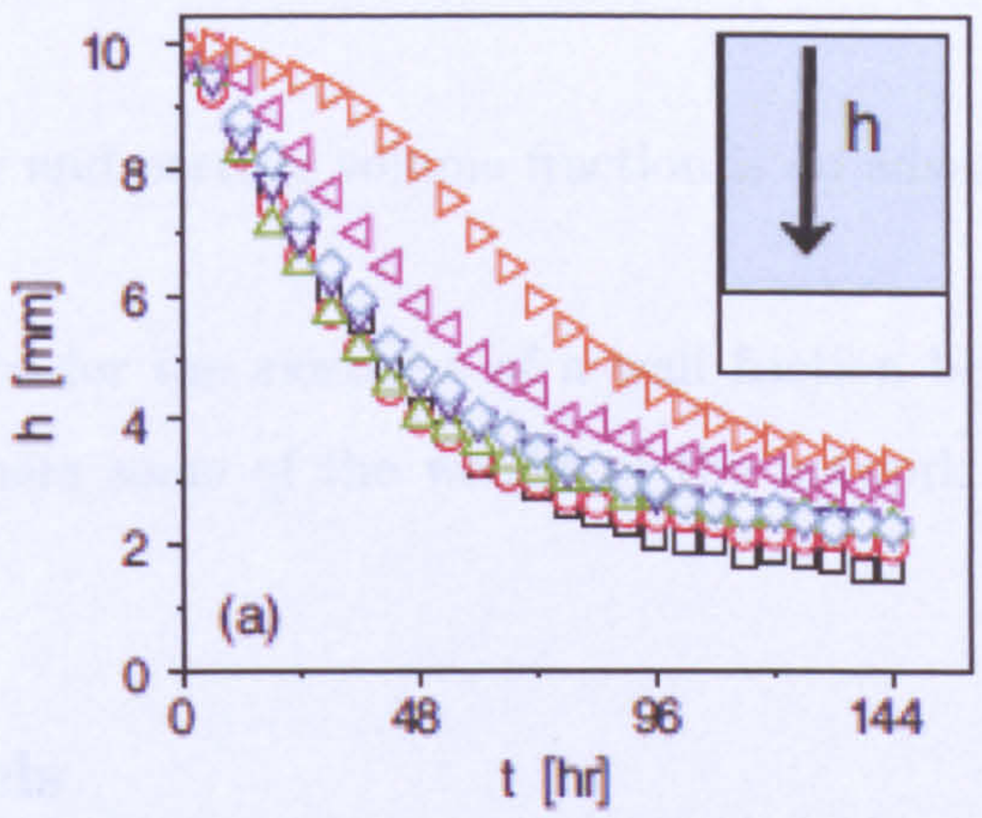

Figure 2.11: Interface height, h, as a function of time for different polymer concentrations. □:1.45 gL^{-1} , ○:1.60 gL^{-1} , △: 1.82 gL^{-1} , ▽: 1.94 gL^{-1} , ◇: 2.15 gL^{-1} , ◁; 2.33 gL^{-1} , ▷: 2.44 gL^{-1} . Figure reproduced from [53]

Recently the slow compression or settling of a colloidal gel has been investigated by Brambilla et al [54] using a light scattering technique where the intensity of depolarised light is related to the particle volume fraction. The time and height dependance of the local colloid volume fraction throughout a settling sample was accurately recorded as well as the settling velocity, by averaging the CCD signal over horizontal rows of pixels. The ability of this analytical technique to obtain

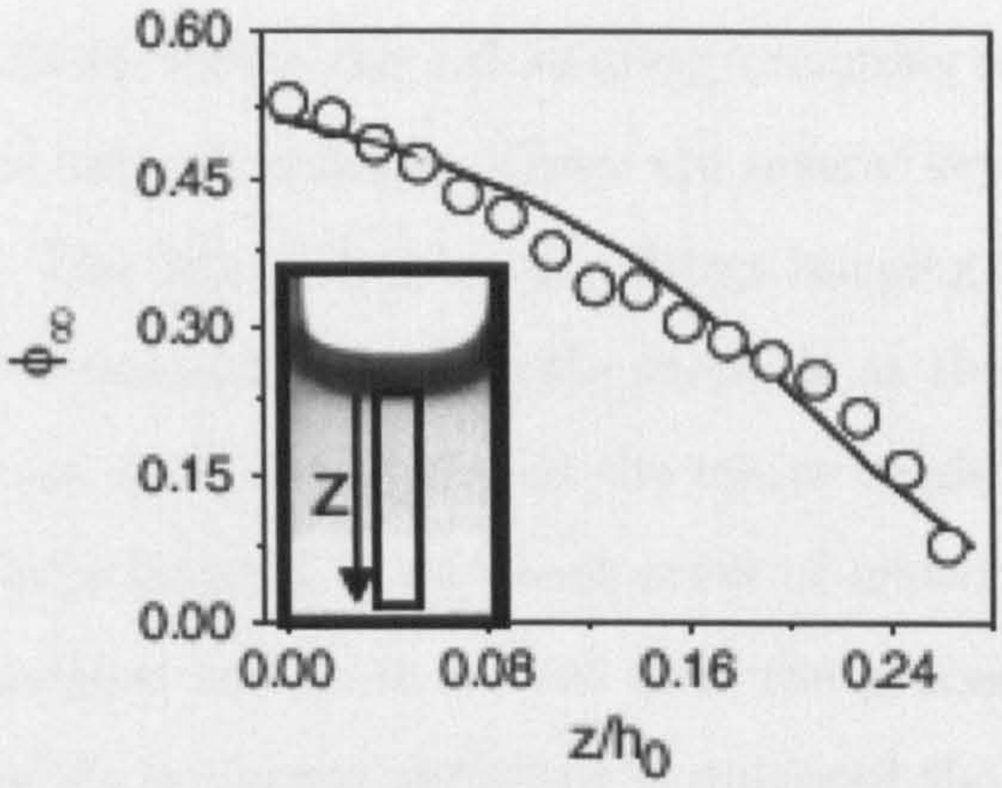

Figure 2.12: Varying colloid volume fraction as a function of height throughout the collapsing network, where $C_p = 2.15$ gL^{-1} . The line shows the best fit based on the predictions of the poroelastic model. The inset shows the slice considered when obtaining the intensity grey scale. Figure reproduced from [53].

both settling velocity and particle volume fraction is an advantageous feature.

There is also evidence for the existence of a wall friction between cell walls and networks [49, 57] where some of the weight of the network is supported by the containing walls.

2.4.2 Weak gels

Weak gels result when the strength of the colloidal attraction is of order $U/\ k_BT < 10$. The low strength of the attraction means that the 'bonds' are not permanent and are subject to fluctuations. It is for this reason that these gels are often referred to as transient gels. What is most striking about transient gels in comparison to strong gels is that collapse process occurs extremely suddenly, often after an initial period of stability [47, 58, 59]. The collapse also does not tend to occur in a linear fashion as predicted by the poroelastic model.

A detailed experimental study of weak gels has been undertaken by Starrs et al [58], who utilised a number of different analytical techniques which allowed the concen-

tration profiles of colloids within the sedimenting/creaming sample to be obtained, as well as the rate of network collapse. There are several key findings which result from their research. The first is that using a direct imaging technique, it was possible to observe the formation of large scale channels at the edges of the sample, which increased in size until they spanned the entire height of the network. The bright regions shown in figure 2.13 represent areas of network which have become broken up, or fragmented and so it is clear that the processes which govern the collapse of a weak gel do not occur uniformly throughout the entire network. From the darkfield images in figure 2.13 it is clear that there are considerable changes occuring within the network even before the onset of rapid collapse, and that this point appears to coincide with the channels spanning the full height of the sample. When a channel breaks through the surface of the suspension, small volcano-like structures are observed as colloidal material carried by the channel is deposited, similar to the structures observed by Derec et al [48]. The growth rate of the channels was found to be comparable to that of the sedimentation speed during rapid collapse. Small cracks were also observed to appear that generally originated from the edges of the sample and grew both inwards and upwards, and which did not allow for the transport of material.

An interesting feature of the study is that at the highest polymer concentrations the suspension continuously settles at a rate comparable to the initial slow settling rate of gels exhibiting delayed sedimentation, and does not undergo a rapidly sedimenting stage [58]. This is referred to as creeping collapse. The sedimentation profile resembles that of a strong gel, and yet the strength of the attraction is $U/k_BT < 10$. Concentration profiles were measured for samples which show creeping collapse and also for a transient gel sample which exhibits a true delay time (see figures 2.14 and 2.15). The transient gel suspension is initially homogeneous at a volume fraction of 0.2 and remains homogenous throughout the delay period. The formation of a sharp interface between colloid and supernatant at the very top of the sample before the onset of rapid collapse, indicates that the network has already settled slightly before the onset of rapid collapse. At 28.8 hrs (after the

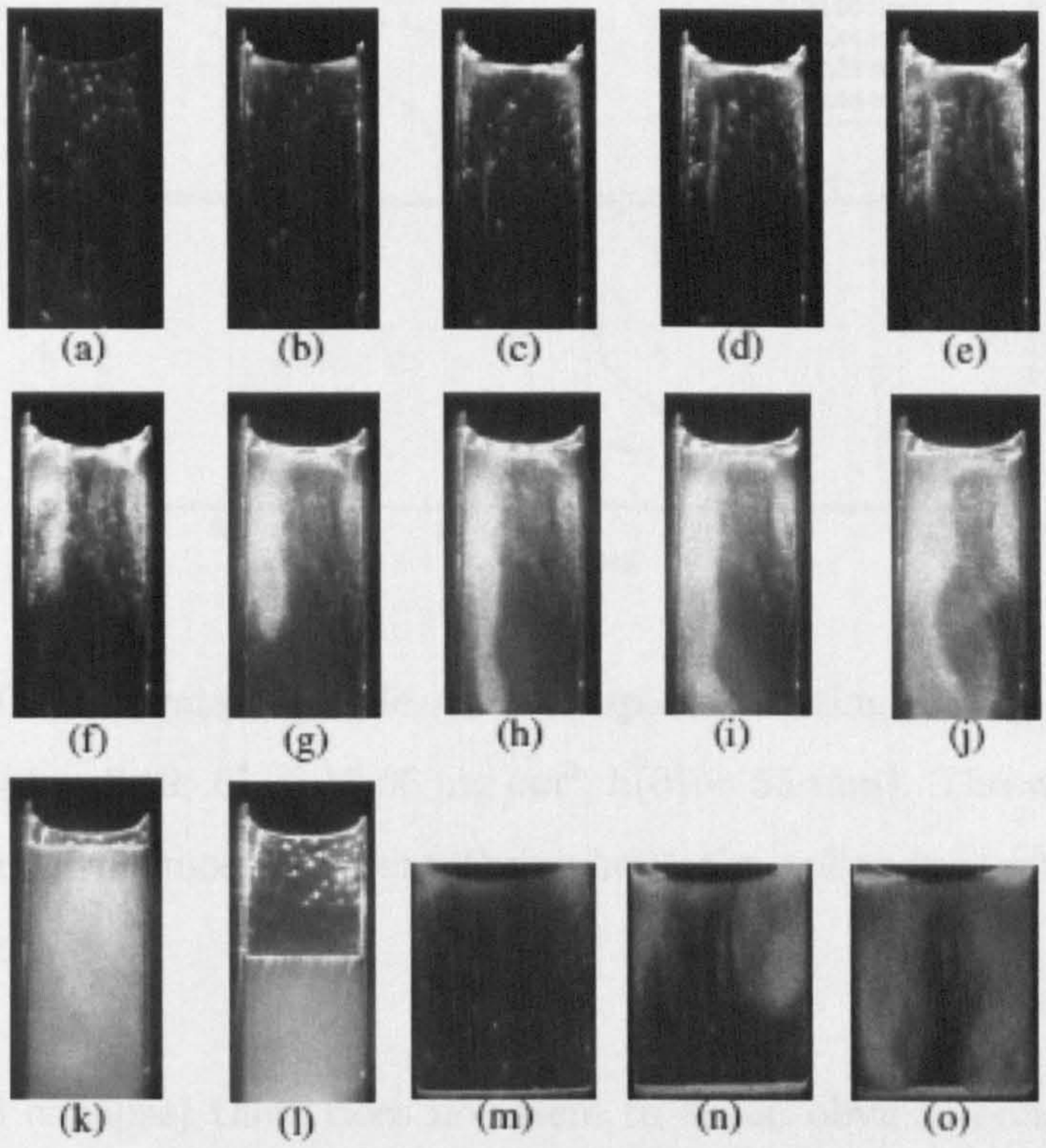

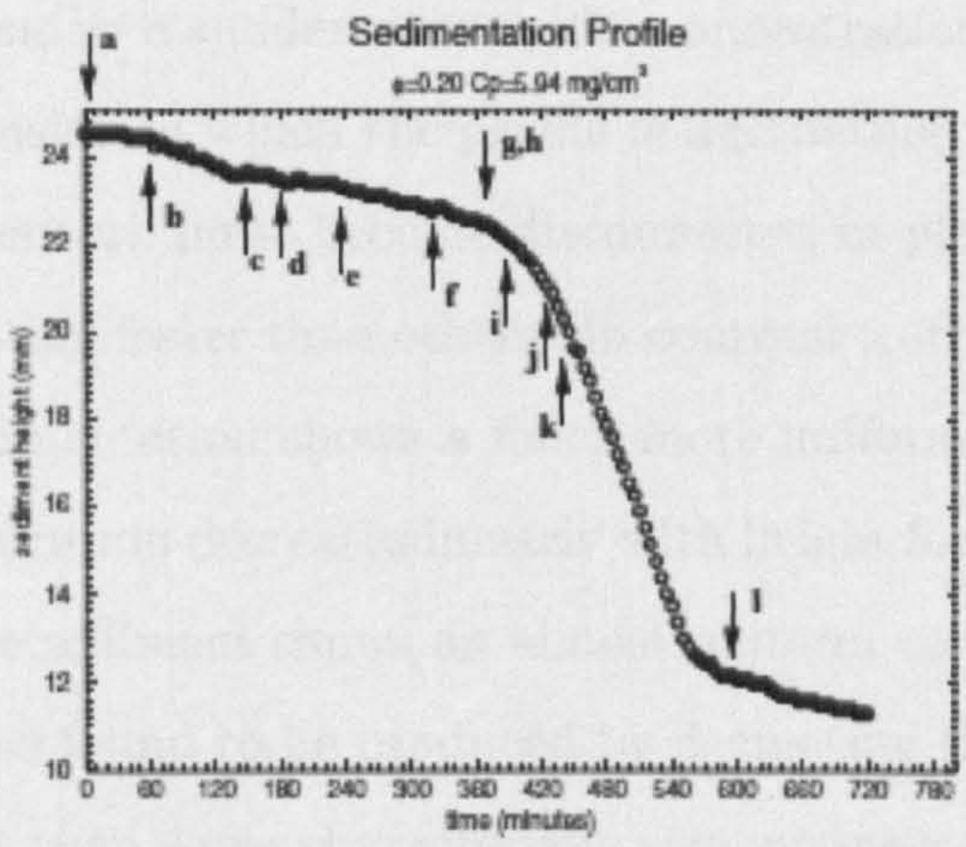

Figure 2.13: Dark-field images of a gel undergoing delayed sedimentation with a latency time of 420 min. For images (a)−(l) the time at which each image was captured is shown in the h(t) plot for this sample. Figure reproduced from [58].

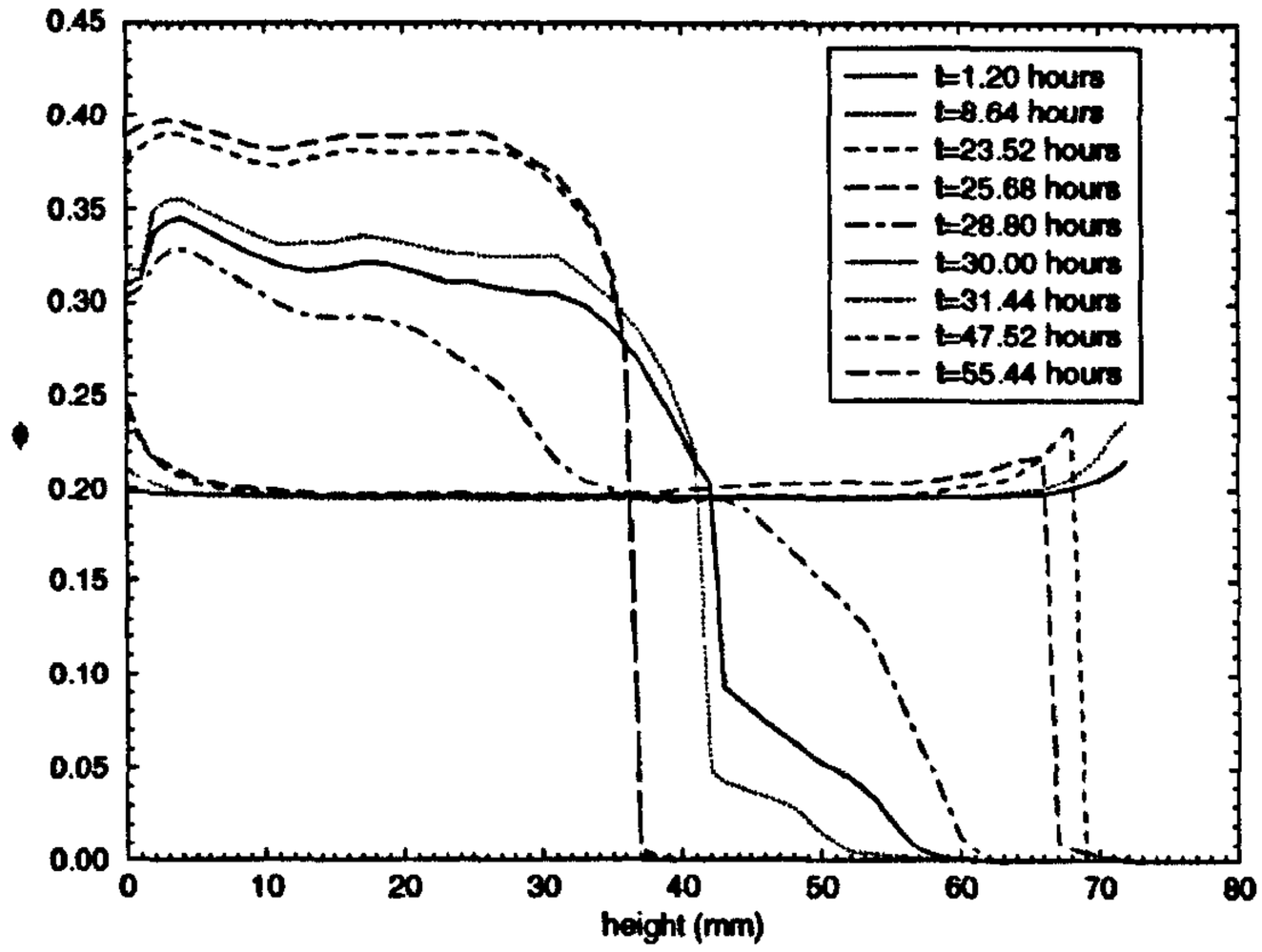

Figure 2.14: Concentration profiles of a sample exhibiting a long delay time, of order 25 hrs. ($\phi = 0.19$, $C_p = 10.66$ mg cm^3, h(0) = 55 mm). The volume fraction of colloids remains almost constant throughout the collapsing network. Figure reproduced from [58].

onset of rapid collapse) there does not seem to be an obvious boundary present, which would be evident by a sudden drop in the concentration profile. Instead, the profile shows a suspension in which the profile is fluctuating throughout its height indicating that the network must become disconnected in places, since some areas appear to be sedimenting faster than others. In contrast to this, the profile of a gel showing creeping sedimentation shows a much more uniform concentration gradient, where the concentration decreases linearly with height for a period, after which the top portion of the sediment shows an almost uniform concentration. Creeping sedimentation was also found to be produced by decreasing the sample dimensions until they are smaller than some characteristic size intrinsic to the gel.

A study of the factors which affect the delay time has been carried out by Gopalakrishnam et al [60] where the delay time is studied as a function of the attractive range, the colloid volume fraction, and the concentration of depletion polymer. It has already been shown how the delay time increases with polymer concentration, but Gopalakrishnam et al show how it also increases with colloid volume fraction,

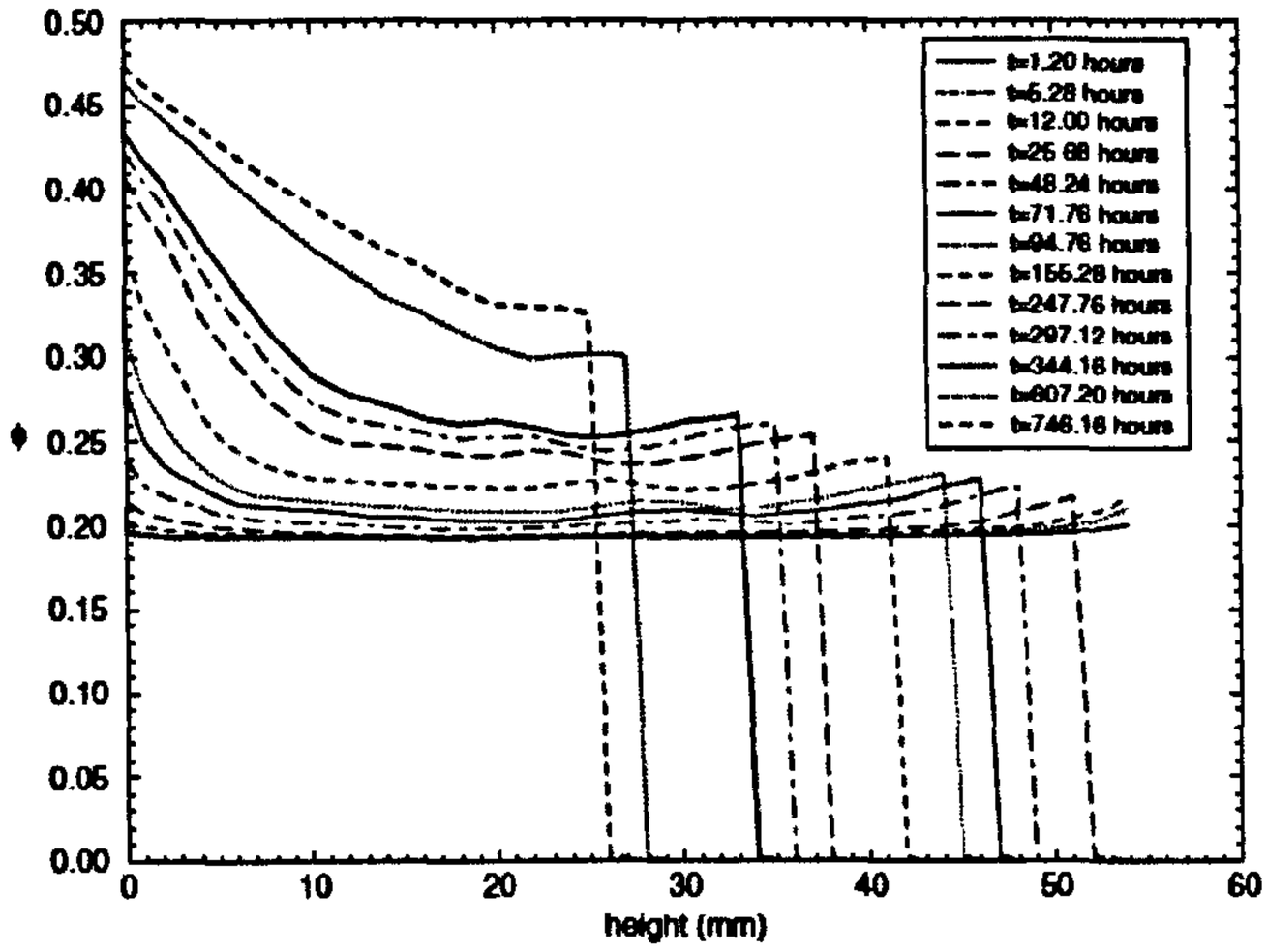

Figure 2.15: Concentration profiles of a gel exhibiting creeping sedimentation (ϕ = 0.19, C_p = 10.66 gL^{-1} , h(0) = 71 mm).There is a concentration gradient of colloids throughout the collapsing network. Figure reproduced from [58].

and an increase in the attractive range.

The boundary between weak and strong gels is not clearly defined, it is a generally accepted value of $U/k_BT \approx 10$. It is clear that gel samples which fall under the general classification of weak gels, as dictated by the strength of the attraction, can exhibit characteristics of a strong gel such as homogenous collapse and no observable delay period [58]. Therefore factors other than the strength of the attraction must dictate the type of collapse behaviour observed.

Network size dependence

Following on from the experimental research of Starrs et al [58], the sedimentation of gels toward the base of a tall container, both far from its walls and close to its walls has been modelled by Evans et al [59]. The concept of a stress transmission length was introduced, and it is shown how the ratio to the dimensions of the container controls the sedimentation. At distances beyond this length the

transmission of stress via the network does not occur. This manifests itself as a characteristic length-scale above which the gels do not have self-supporting structures, but sediment at their terminal velocity, supported predominantly or entirely by drag. These are the samples whose lifetime is independent of the container size. By contrast, gels with inter-particle attractions sufficiently strong that the percolating network can transmit a stress right across the container, support some of their own weight as they sediment. These gels collapse at a time that depends on the container size or, in the limit of very strong attractions, exhibit no sudden collapse at all.

Experimentally, the effect of altering the container size on the collapse of the network is nicely shown by the work of Weitz et al [61], where sedimentation profiles of samples with identical composition were prepared, but with each sample having a different initial height *h(0)*. The sedimentation profiles shown in figure 2.16 clearly show the two different collapse regimes, where for small *h(0)* there is no delay time and the height of the network with time decreases linearly with time, and at larger *h(0)* there is a period of slow collapse followed by a rapid collapse. The lines in the right hand inset of figure 2.16 represent the values obtained using the non linear poroelastic model as discussed in the previous section. No description is offered for the delayed collapse.

The effect of altering container size on the collapse process has be examined theoretically by Tanaka [62], where the phase separation of the network is modelled as a viscoelastic process. The colloidal system is regarded as a binary liquid mixture in which one of the liquids (the colloidal network) is able to support stress. The key feature of this phase separation is that it is a result of dynamic asymmetry within the system resulting from the different sizes in component particles (fluid and colloid). A key point is that Tanaka states that there are two different types of network ageing, which depends upon the size of the gel. When it is so small that a characteristic diffusion time, τ_{diff}=L^2/D (where D is a diffusion constant, and L is the system size) is shorter than the bulk mechanical relaxation time, then the

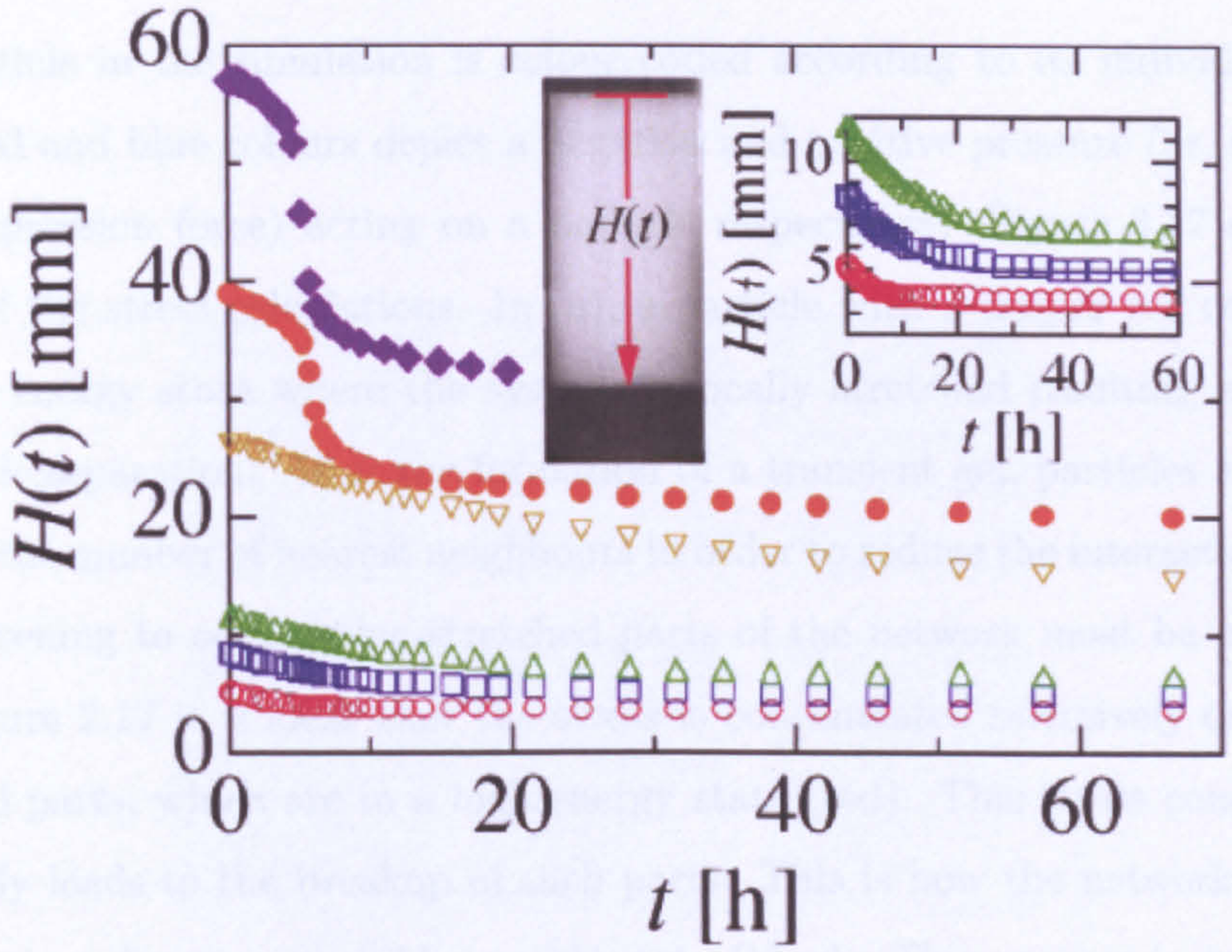

Figure 2.16: Time evolution of the heights of an emulsion gel with various initial height but the same composition, ϕ 0:2, and C_p 0.06 gL^{-1} . The initial heights are 5, 9, 12, 26, 39 and 57 mm from bottom to top, respectively. Left inset: Picture of a sample. Right inset: Measured $h(t)$ compared with the values calculated with the nonlinear poroelastic model for the samples that do not exhibit a delayed collapse. Figure reproduced from [61].

network shrinks homogeneously. Where τ_{diff} is longer than the bulk mechanical relaxation time then the network shrinks inhomogeneously under the influence of mechanical stress. Tanaka argues that the local stretching caused by the shrinking of a gel leads to a stress concentration on the stretched part of a domain, causing it to break up, which further enhances the inhomogeneous stress distribution. A detailed review of viscoelastic phase separation has been prepared by Tanaka [41].

When studying the collapse of gels the process is usually considered in terms of the balance of external stress as a result of gravity, and the network yield stress. However, Tanaka has introduced the concept of an additional stress which builds within the network and is self generated [63]. Simulations are used to study the stresses within the network. The stress experienced by each particle is calculated and then

each particle in the simulation is colour coded according to its individual stress level. Red and blue colours depict a negative and positive pressure (or, stretching and compression force) acting on a particle respectively. Figure 2.17 shows the results of the stress calculations. In (a), a particle with a deeper red colour is in a higher energy state where the system is locally stretched resulting a large interparticle separation. After the formation of a transient gel, particles attempt to increase the number of nearest neighbours in order to reduce the interaction energy. For coarsening to occur some stretched parts of the network must be broken up. From figure 2.17 it is clear that the stress is concentrated selectively on the thin stretched parts, which are in a high-energy state (red). This stress concentration eventually leads to the breakup of such parts. This is how the network structure relaxes into a lower metastable energy state (blue). This process is repeated to allow for further relaxation, and is apparent by the coarsening of the network.

The previous section discussed how it is usually believed that particles experiencing strong inter-particle attractions are essentially permanently connected. Contrary to this common belief, however, the internal stress mechanism of Tanaka can lead to successive breakage of the stress-bearing backbone as far as the self-generated stress is strong enough to break up the backbone, which is indeed the case for a system with long-range interactions. The mechanical coarsening of a network is presented as an alternative to the idea of coarsening due to thermal activation, although this process is more relevant for systems with long range attractions, where the range of interaction is long enough for a system to experience some particle motion leading to a reduction of the interaction energy.

2.5 The significance of transient gels

The phase diagrams of colloid-polymer mixtures show a rich phase behaviour which can be exploited in order to dramatically change the properties of a material. A colloidal system can behave as a liquid at low C_p but a small increase in C_p can

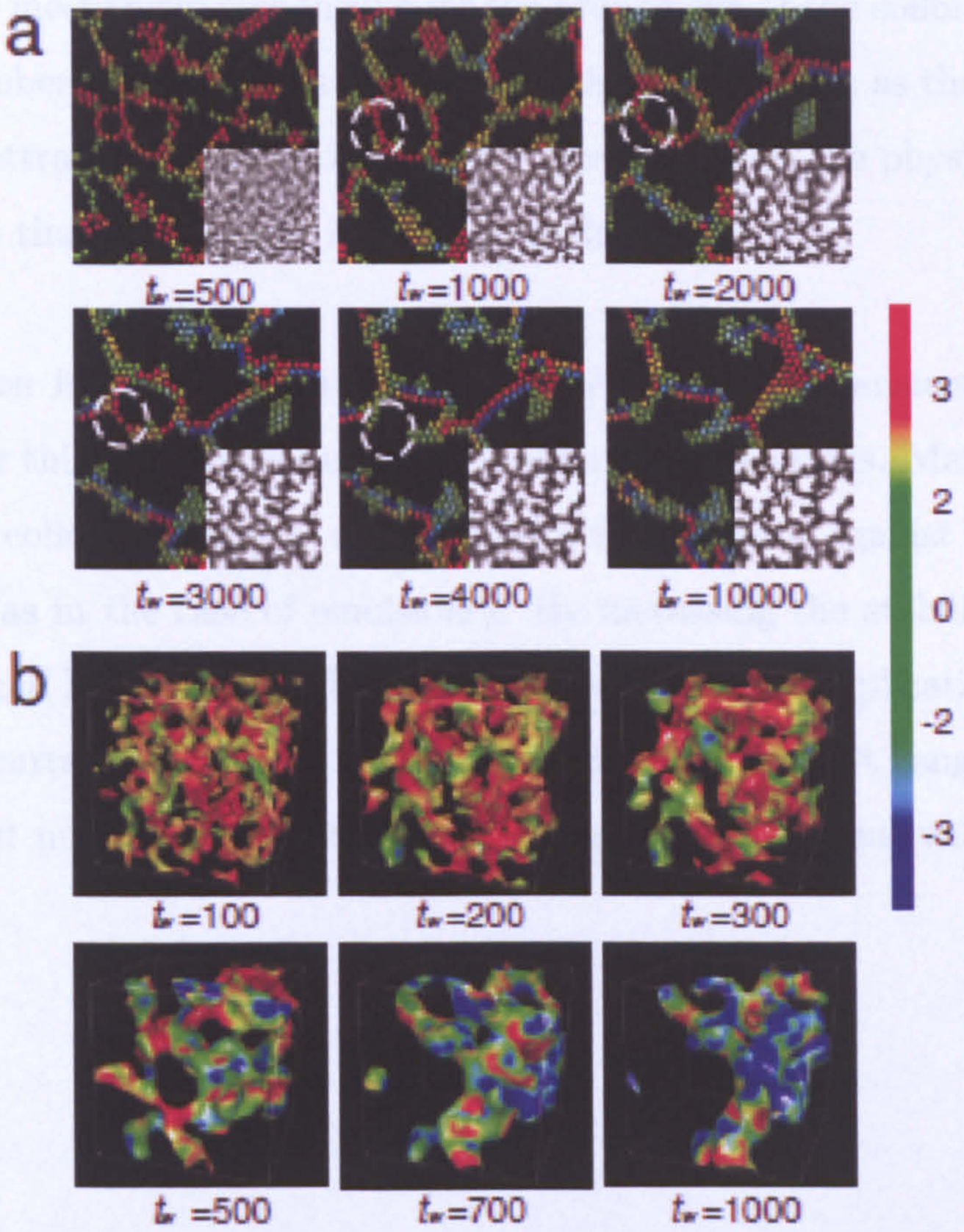

Figure 2.17: Phase-separation process in colloidal suspensions. (a) 2D pattern evolution. The insets show the evolution of the overall structure, whereas the figures show a fraction of the network with the stored stress, which is expressed by the colour of each particle. (b) 3D pattern evolution showing network stress. The red areas represent areas of the network which are under negative pressure, or being stretched, and blue areas represent areas under positive pressure, which are being compressed. Figure reproduced from [63].

cause a space spanning network to form resulting in a colloidal system with a degree of elasticity. The route of phase separation in these systems has been well researched, although a unified view has yet to emerge. There has also been much interest in the mechanism responsible for the breakdown of the colloidal structures. The large number of parameters involved in this process, such as the strength and range of the attraction, the colloid-polymer size ratio, and the physical size of the sample means that this process is far from understood.

The motivation for understanding the collapse process of transient gels and the motivation for this research is due to its industrial applications. Many commercial products are colloidal systems which require stabilisation against sedimentation (or creaming as in the case of emulsions). By increasing the stability period of a product its shelf life is increased which has great financial implications. However, much of the current research is focused on systems with short ranged attractions whereas a vast number of industrial applications utilise systems with long ranged attractions.

Chapter 3

Experimental Methods

3.1 Confocal microscopy

Confocal microscopy is an optical imaging technique used to obtain a micrograph with increased optical resolution and contrast by using point illumination, and a spatial pinhole to eliminate out-of-focus light in specimens that are thicker than the focal plane. The confocal microscope allows the construction of 3-d images to be obtained from analysis of a series of micrographs. The principle of confocal imaging was first presented by Marvin Minsky, and was termed the 'double focusing stage scanning microscope'[64]. Sadly, Minsky's invention was commercially unfeasible due to lack of technology at the time and as a result his invention went largely unnoticed for nearly three decades. It was not until 1987 when technology had advanced considerably that the first prototype of the confocal microscope was constructed by biologists Amos,White and Fordham [65]. Their aim was to combat the usual image blur present when using a conventional epiflourescence microscope by combining the technologies of the laser, the computer and microelectronics.

In a conventional fluorescence microscope the entire specimen is evenly illuminated by a light source. All parts of the specimen in the optical path are illuminated at the same time and the resulting fluorescence is detected by the microscope's photodetector or camera, including a large part of the out of focus background. In comparison, a confocal microscope uses point illumination and a pinhole in front

of the detector to eliminate out-of-focus signal. As only light produced by fluorescence very close to the focal plane can be detected the image optical resolution is much better than that of traditional wide-field microscopes. Figure 3.1 shows a schematic representation of the confocal microscope (recreated from the user manual) and demonstrates how the pinhole eliminates fluorescence from everywhere except the focal plane. One disadvantage of this technique is that the signal is greatly reduced given that much of the sample light is blocked by the pinhole, resulting in the requirement for increased exposure times.

One point in the sample is illuminated at a time and so in order to produce 2D or 3D micrographs scanning over a regular raster (a rectangular pattern of parallel scanning lines) in the sample is required. The thickness of the focal plane is predominantly defined by the wavelength of the illumination light divided by the numerical aperture of the objective lens. Confocal microscopy is especially useful for producing 3D images and for surface profiling due to the thin optical sectioning which is possible to achieve. The key feature of confocal microscopy is its ability to acquire micrographs at precise depths within the sample, a process known as optical sectioning.

The detection pinhole in confocal microscopy functions as a point light detector and suppresses light from outside of the focal plane. When the diameter of the pinhole is large, light from sources other than the focal plane can be allowed to pass through to the detector resulting in an undefined and noisy image. However, when the diameter of the detection pinhole is small, the amount of light reaching the detector is limited resulting in more defined images. However, this also reduces the intensity of the detection signal and so a compromise has to be found between maximum detection signal and minimum optical sectioning.

Due to the nature of light, diffraction occurs when light passes through a lens. The resulting diffraction pattern has a bright region in the center, known as the Airy disk which is surrounded by a series of concentric bright rings called the Airy

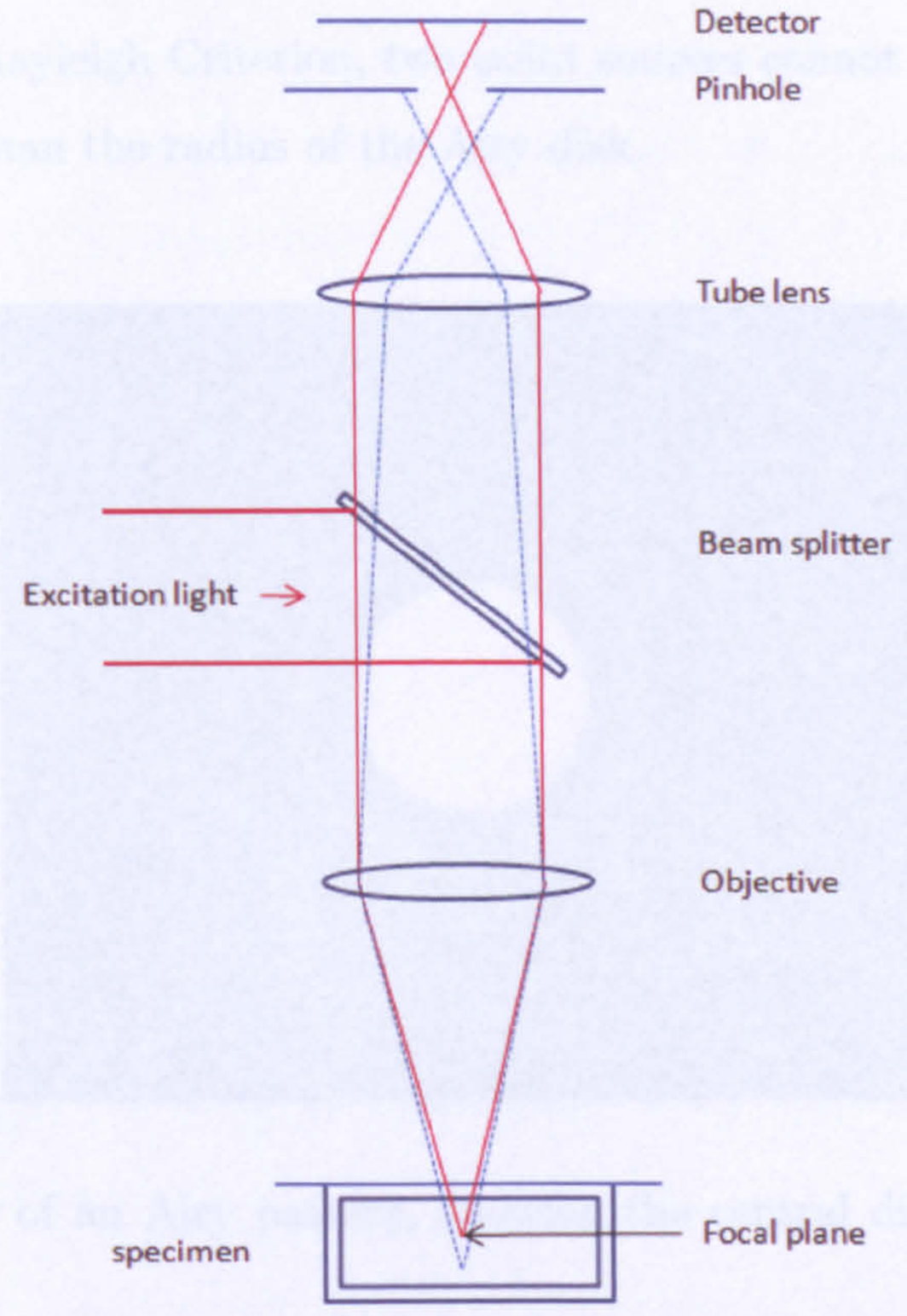

Figure 3.1: Schematic diagram of the confocal microscope. The fine red lines represent laser light which is focused by the beam splitter onto the focal plane, and is then reflected through the pinhole and on to the detector. The blue lines represents laser light which is reflected from an area of sample outside of the focal plane, which is unable to pass through the pinhole and so is not detected.

pattern (figure 3.2), named after George Biddell Airy. As a result of diffraction, the smallest point to which a lens can focus a beam of light is the size of the Airy disk. When the resolution is no longer limited by imperfections in the lenses but only by diffraction, it is said to be diffraction limited. In this situation the radius of the Airy disc is given by:

$$D \sin\theta = 1.22\lambda \tag{3.1}$$

where D is the diameter of the aperture and λ is the wavelength of the light source.

According to the Rayleigh Criterion, two point sources cannot be resolved if their separation is less than the radius of the Airy disk.

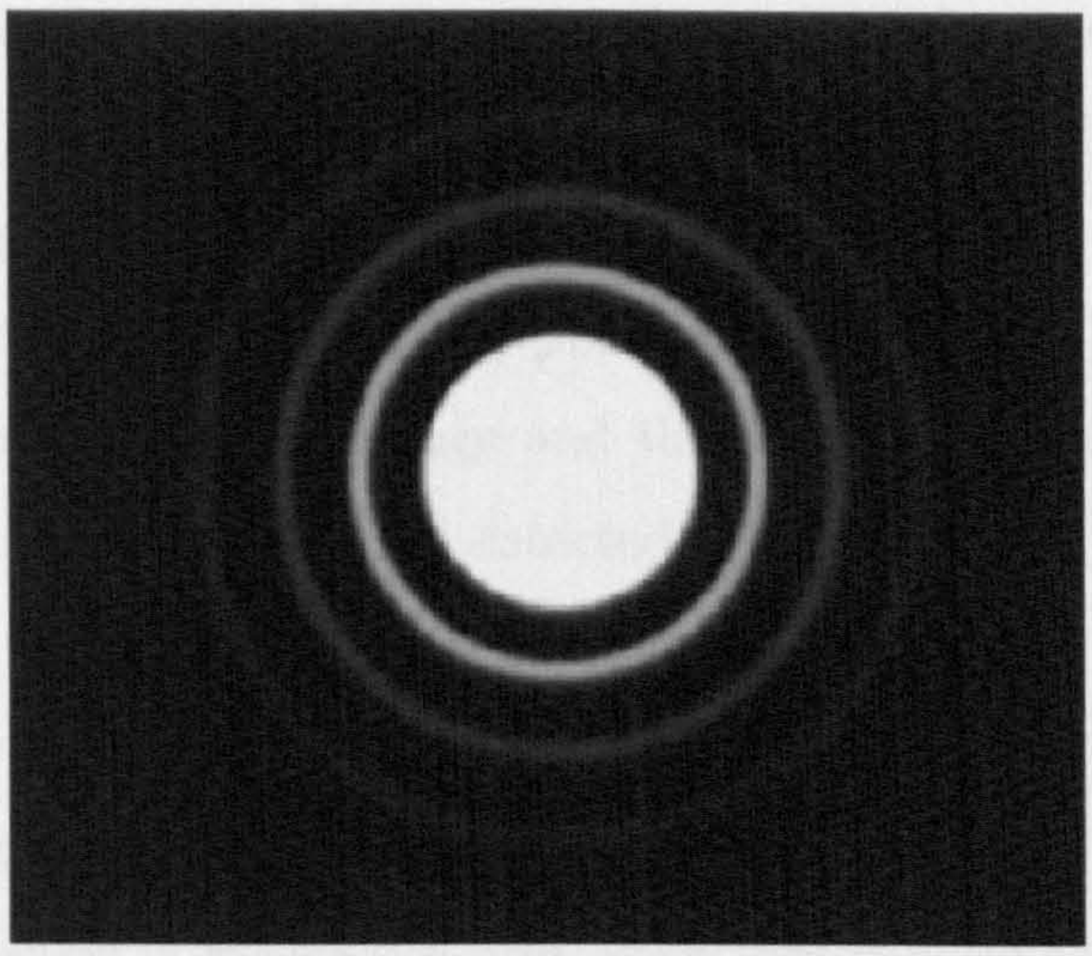

Figure 3.2: Image of an Airy pattern, showing the central disc and surrounding rings.

3.1.1 The Laser Scanning Confocal Microscope

The LSCM has several main components (see figure 3.3). Firstly, there is a microscope unit which is also acts as a standard light microscope (Zeiss Axiovert S 100). Secondly, there is a scan module which is attached to the microscope and finally is a laser module (He-Ne laser, 543 nm λ). A laser beam is produced in the laser module in which the light rays are almost parallel. The laser beam is said to be collimated. The collimated laser beam passes through a dichromatic mirror (a mirror with significantly different reflection or transmission properties at two different wavelengths) and on to oscillating scanning mirrors where it is reflected. The light from the laser is then projected through a high numerical aperture objective (Zeiss Plan NEOFLUAR 100X NA 1.3) and focussed to a diffraction limited spot within the specimen. The reflected laser light and fluorescence light produced are collected by the same objective and passed back up the microscope to be de-scanned by the scanning mirrors. When using fluorescent microscopy, any reflected laser light is

reflected 90^0 by the dichroic mirror, while the fluorescent light passes through the dichroic mirror and is projected onto a variable pinhole diaphragm. Light which reaches the detector, a photomultiplier tube (PMT), is converted into a voltage signal, which is then converted into a digital signal using an analogue to digital (A/D) converter incorporated into the system. The laser position is controlled by motorised scanning mirrors which allows the laser to scan over the specified area, and a whole image is obtained pixel-by-pixel and line-by-line. The detected light represents one pixel in the final image and the brightness of an image pixel corresponds to the relative intensity of detected light. The scan speed can usually be varied. Slower scans provide a better signal-to-noise ratio, resulting in better contrast and higher resolution. Images can be collected at different focal planes by raising or lowering the microscope stage or objective lens. As the image is being constructed, each pixel is assigned a grey value which is dependant upon the intensity of the signal received.

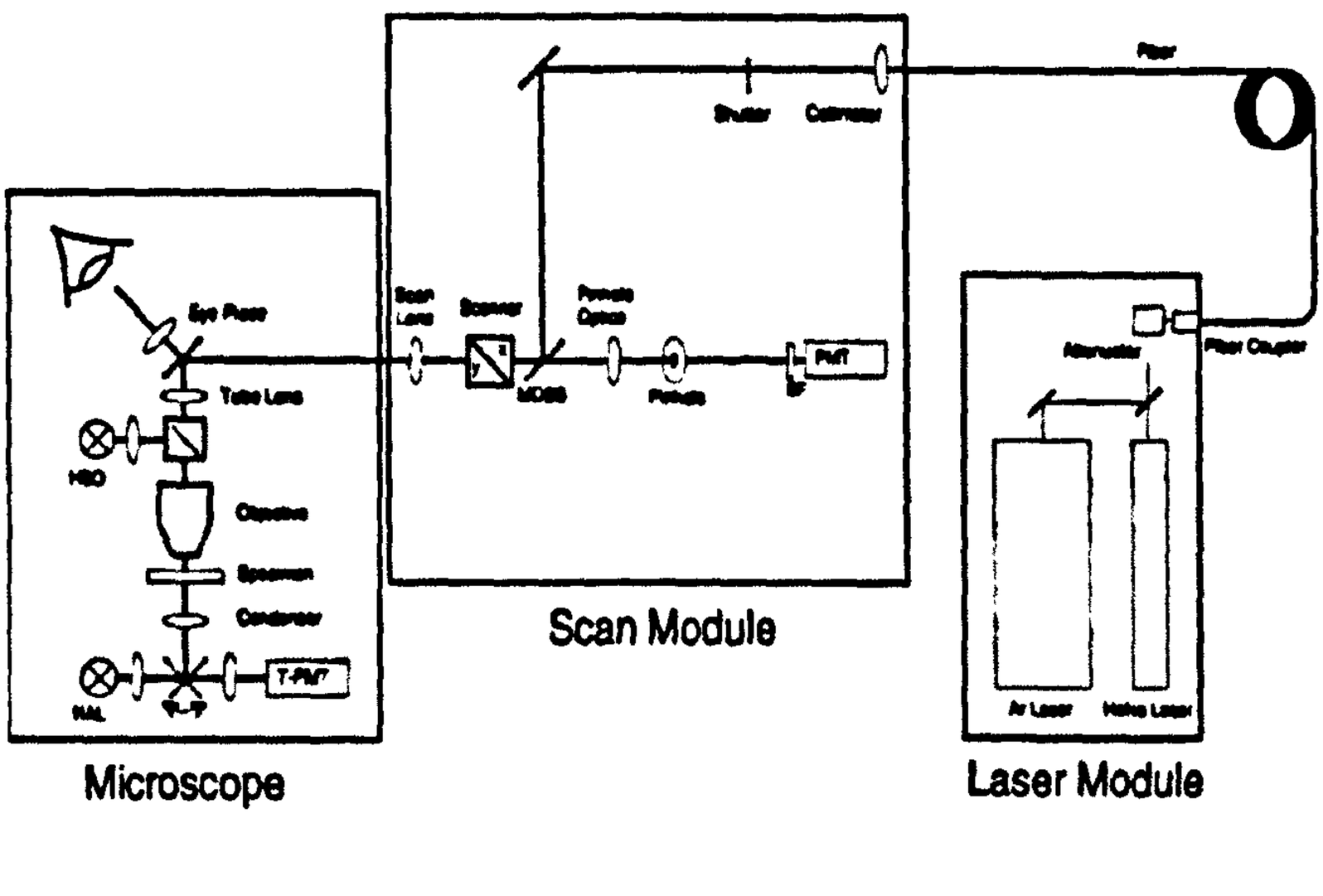

Figure 3.3: Schematic diagram of the confocal microscope, scan module and laser module (recreated from the LSCM manual).

3.1.2 Imaging perpendicular to gravity

In order to study the time evolution of the gel structure, confocal microscopy images were initially obtained from samples which were contained within a glass circular cell, with a diameter of 17mm, and a height of 0.8mm. The structure showed very little change and there was doubt as to whether the images were representative of the full height of the sample. Limitations as to the sample depth that can be imaged when using the 63x oil immersion objective on the LSCM meant that it was impossible to observe structural changes occurring within the depths of the sample. Therefore, a supporting frame was constructed for the microscope, which allowed the microscope to be rotated by 90 degrees. The emulsion samples creamed in the direction of gravity, but now single images were able to be obtained in the YZ axis, rather than XY axis where the Z axis represents the direction of gravity. The original microscope stage was removed, and replaced with a low profile manual translation stage, which was mounted to a metal plate and secured to the microscope. The translation stage allowed the full height of a sample to be imaged. Sample cells as shown in Figure 3.4 were constructed which allowed bulky samples (up to 6ml) to be imaged. The cells were square with an internal width and depth of 13mm and a height of 30mm. A large coverslip made up the front wall of the cell, and a hole in the top allowed the sample to be added to the cell.

An example of the micrographs obtained using this method is shown in figure 3.5. Each micrograph has a resolution of 1024 x 1024 pixels and dimensions of 146 x 146 μm . Gravity acts in a downward direction and so creaming emulsion drops can be observed moving in an upward direction. In this image the colloid network is clearly visible, but individual particles can not be observed due to the mean particle size being smaller than the microscope resolution limit. The fluorescent aqueous continuous phase is shown by the green areas and the colloidal network which results from depletion attractions is shown by the dark areas. The green colour which shows the fluorescent areas is the colour selected via the computer software and is not significant to the sample. There is a small area with extremely high levels of fluorescence near the bottom of the micrograph. It is most likely that

this is the result of a dye crystal forming.

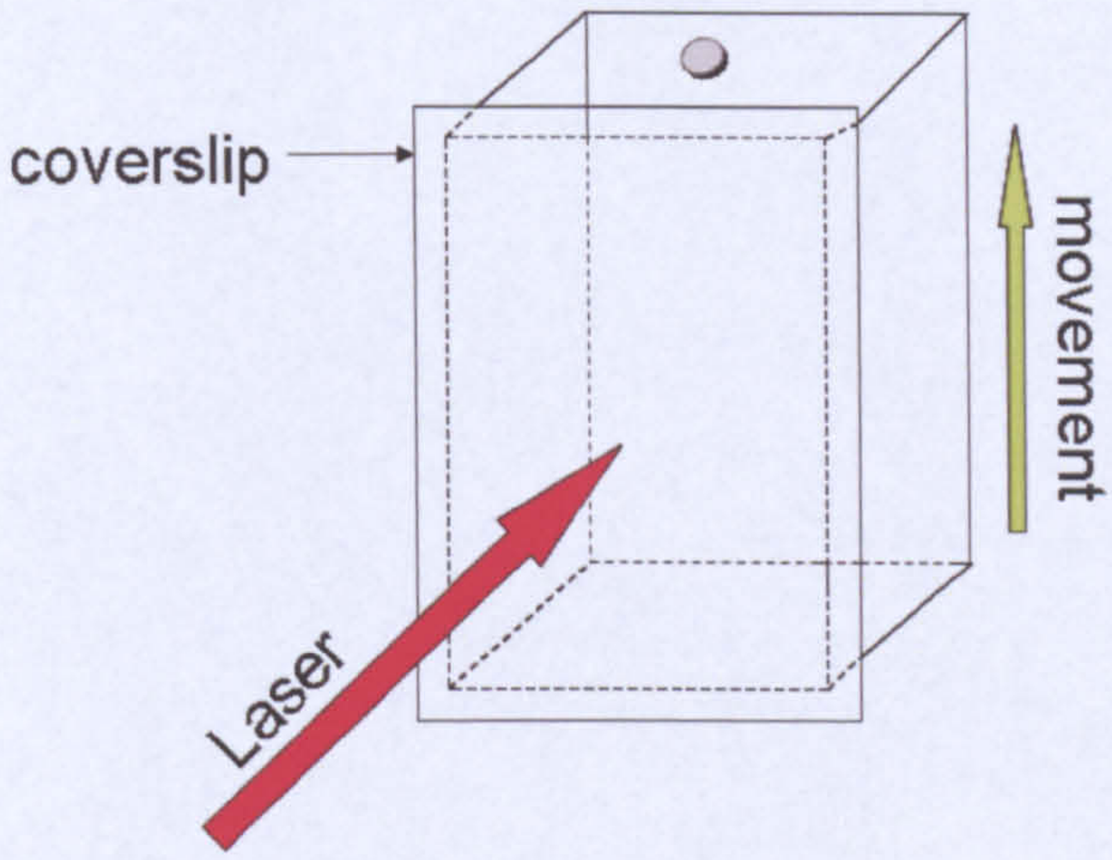

Figure 3.4: Sample cell constructed for imaging in the YZ plane. The sample is added to the cell using a syringe via the hole at the top. The front vertical wall comprises a coverslip through which the laser light is able to pass. The emulsion particles move upwards with gravity, and the cell is able to be moved along the vertical axis with the aid of a linear translation stage.

3.1.3 Analysis of confocal microscopy images

In order to accurately detail any coarsening of the network it is essential that a quantitative analysis is possible. The degree of network growth, or coarsening, can be quantified by determining the radially averaged structure factor *S(q,t)* of each micrograph,

$$S(q,t) = \frac{1}{2\pi q \Delta q} \int_{q \leq |\mathbf{q}'| \leq q+\Delta q} d\mathbf{q}' \left\langle \tilde{I}(\mathbf{q},t)\tilde{I}(-\mathbf{q}',t) \right\rangle \tag{3.2}$$

where $I(\mathbf{q},t)$ is the 2D Fourier-transform of the image intensity *I(r, t)* recorded from a sample of age t and $\Delta \mathrm{q} = 2\pi/L$ where L is the width of the image. The 2D Fourier-transform displays a ring of high intensity which corresponds to the presence of a large characteristic length scale. Figure 3.6 is an example of a 2D Fourier-transform obtained, and clearly shows the high intensity ring.

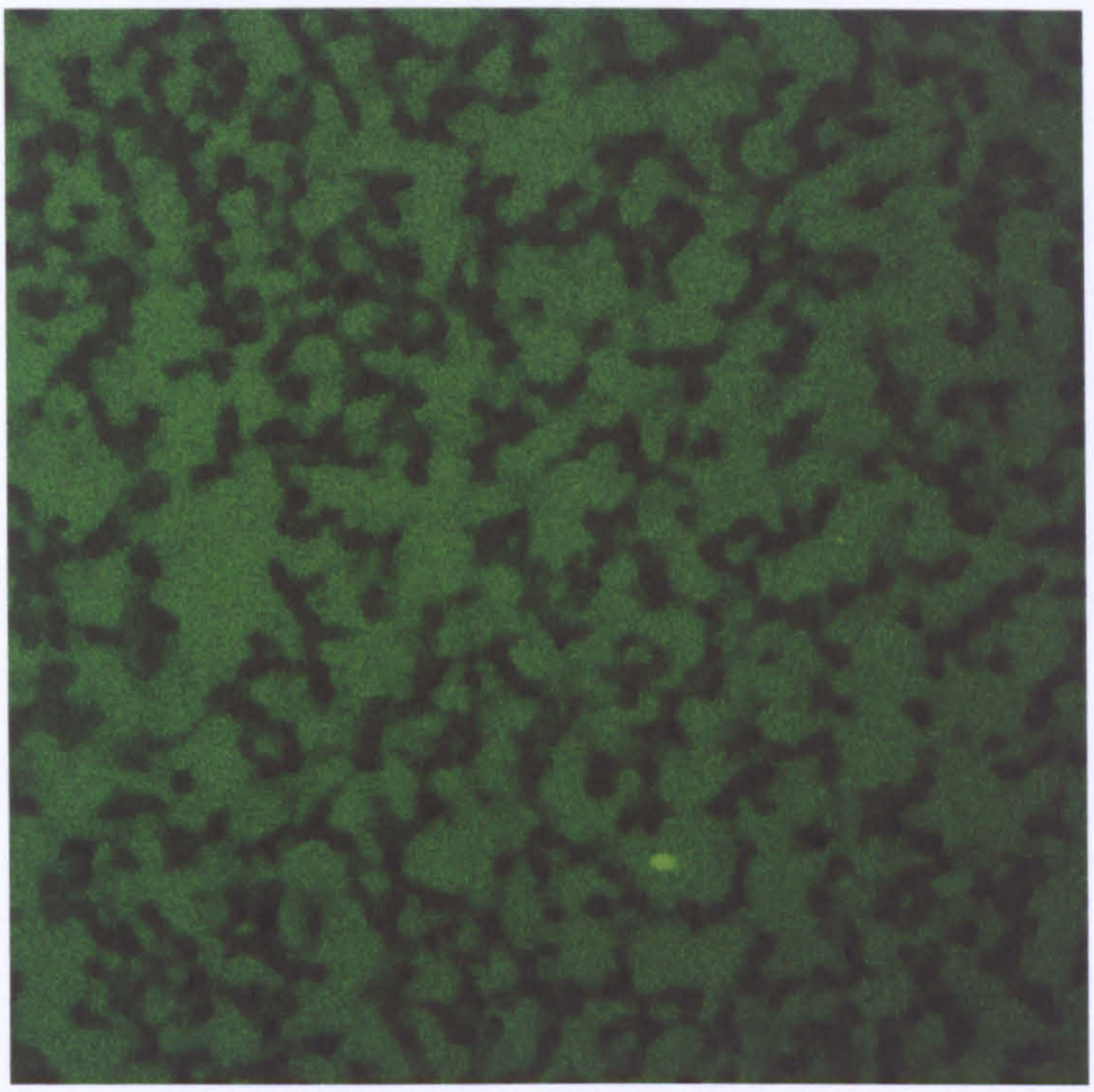

Figure 3.5: Example of a micrograph obtained in the YZ plane ($\phi = 0.2$, $C_p = 0.6$ gL^{-1} xanthan, *h(0)* 15mm, sample age = 2 hours). The green areas represent the fluorescent continuous phase, and the dark areas represent the colloid network. The dimensions of the micrograph are 146 x 146 μm , and the colloids move upwards against gravity. The very bright object near the bottom of the micrograph is most likely a dye crystal.

The calculated structure factor, *S(q,t)* is rather noisy because of a lack of statistics, so the average wavenumber is characterised by calculating the first moment $\langle q(t) \rangle$ of the scattered intensity,

$$\langle q(t) \rangle = \frac{1}{I_t} \int_{q_1}^{q_2} dq' q S(q't)) \tag{3.3}$$

where

$$I_t = \int_{q_1}^{q_2} dq' S(q't) \tag{3.4}$$

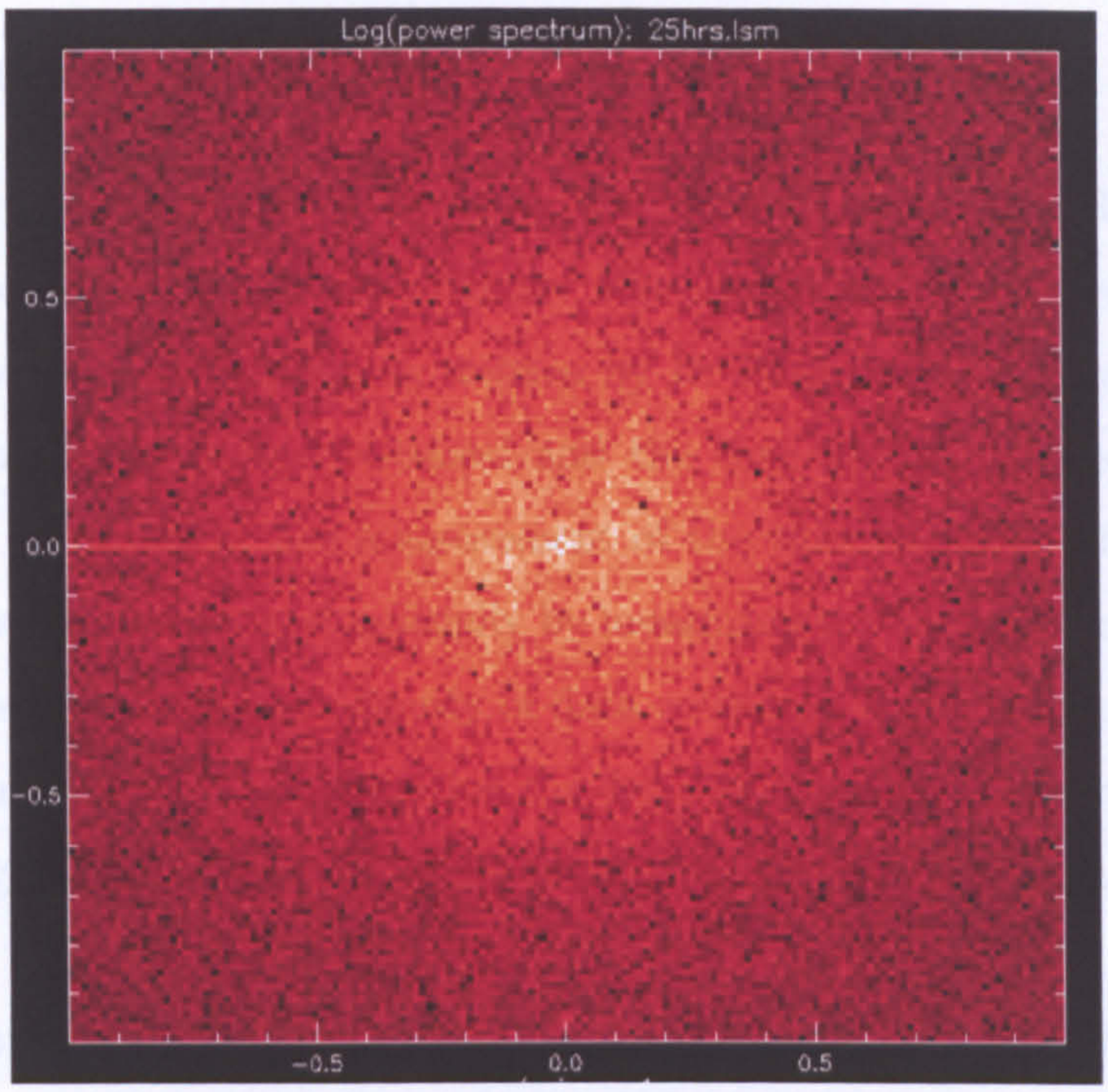

Figure 3.6: 2D Fourier transform of a micrograph taken of a sample with 0.6 gL^{-1} xanthan and an initial height of 5mm after 25 hours. The micrograph was obtained within the delay time.

The integration was performed over the finite interval $q_1 \leq q \leq q_2$ with $q_1 = 0.02$ μm^{-1} and $q_2 = 0.4$ μm^{-1}. The wavenumber $q(t)$ can then be used to calculate the characteristic domain radius $(R_c(t))$ from the expression:

$$R_c(t) = \pi / \langle q(t) \rangle \tag{3.5}$$

The time evolution of the characteristic length scale can be determined from the confocal micrographs obtained for each sample, therefore providing a quantitative analysis of the coarsening process of the colloidal network as a function of time. Software was kindly written by Dr Paul Bartlett which automatically performed this process for individual micrographs.

3.2 Video microscopy

A charge coupled device (CCD) camera was used to obtain time lapse 'videos' of samples experiencing network collapse. The camera was controlled by purpose written software which was kindly written by Dr Paul Bartlett. The software allowed the number of images obtained and the time interval between images to be specified. Historically, the measurement of the time evolution of the network boundary has been performed manually by measuring the height of the colloid rich phase with calipers and so continuity of data collection depended on the presence of the experimentalist. By automating the data collection, it is ensured that there are no time gaps in the data, therefore producing detailed sedimentation profiles.

An AVT Guppy F-080B firewire CCD camera with a resolution of 1034 x 778, a 12mm focal lens, and a red filter was used to obtain images of samples. The samples contained Rhodamine B fluorescent dye which gives the samples a cerise or red colour, depending on the concentration used. The filter allowed the red hues of the colour spectrum to pass through to the camera and blocked out other colours, resulting in the boundary position being more clearly observed in images compared to when looking at the samples by eye. The camera was then attached to a mounting block which was secured to a vertical translation stage, allowing the height of the camera to be altered. A spirit level was used to ensure that the camera was level. Even illumination of the samples was created by using an A3 size light box obtained from Glowlite which was placed directly behind the samples.

3.2.1 Imaging network collapse

The camera position and settings must be optimised in order to obtain good quality images. Firstly the height of the camera was adjusted so that the base of the sample holder was at the center point of the image. Once positioned at the correct height, the front edge of the base of the sample holder was used to focus the camera. By zooming in to the image to such an extent that each pixel is clearly visible, the focus can be precisely controlled. The final step is to alter the diameter

of the camera pinhole. If too little or too much light is allowed to pass through the pinhole then the boundary between the colloid rich phase and the supernatant will be difficult to determine.

Once a sample was prepared, it was added to the cells which were then secured within a sample holder, which was mounted to a floating table. An A4 sized back light ensured bright, even illumination of the samples and figure 3.7 shows an example of the images obtained. All experiments were carried out using glass circular cells with an internal diameter of 17mm, unless otherwise stated.

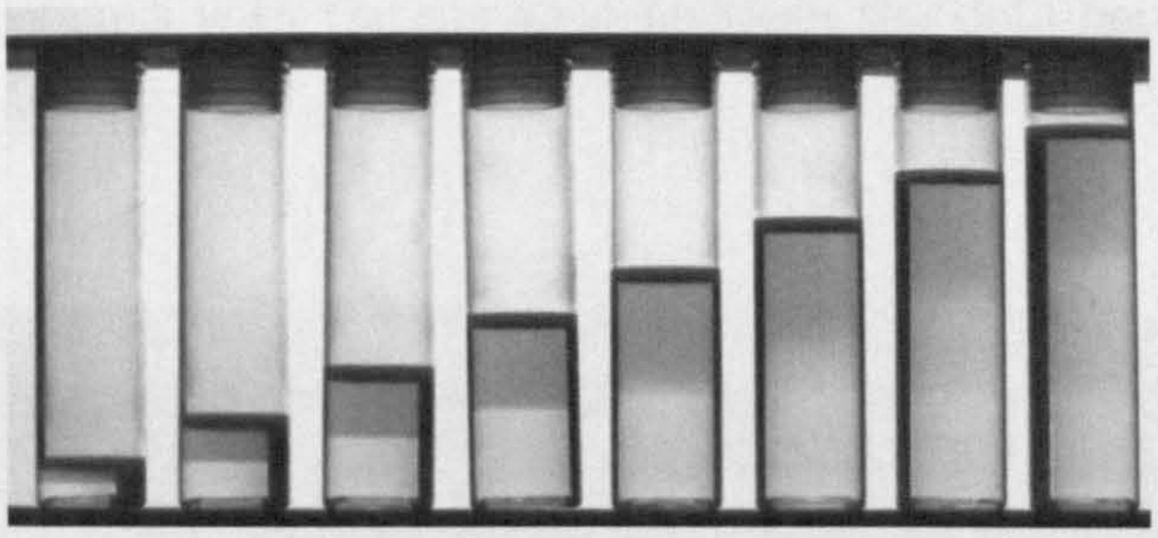

Figure 3.7: Image of creaming samples. The concentration of these samples was fixed at 0.9 gL^{-1} xanthan and the initial heights of the samples were in the range 5mm to 62mm. This image was obtained once creaming was complete in the smallest height samples. The dark layer visible at the top of each sample is the creamed emulsion particles. In the smallest height samples where creaming is complete the boundary between the creaming phase and supernatant is clearly defined. The larger height samples are still undergoing the collapse process which is obvious from the non-uniform colouring of the colloid rich phase and a less defined boundary.

3.2.2 Calibration of images

Images were calibrated before measurements were obtained from them to ensure that there was no distortion, and to enable real world measurements to be taken directly from the images of creaming samples. Images were calibrated and analysed using National Instruments Vision Assistant software. A grid of dots was printed

onto a clear acetate sheet, which was then mounted onto a pane of glass in order to support the acetate. The glass sheet was placed in the precise location that samples were to be imaged, taking care to ensure that it was completely vertical and an image of the grid was then taken with the CCD camera.

To perform the calibration in the software, the 'image calibration' function is selected, followed by the 'non-linear' function, and the grid image is loaded into the software. The software then allows for the grid threshold to be altered, where the aim is to highlight the dots from its background. Each dot must be of diameter between 6 and 10 pixels with the distance between the dots being approximately 30 pixels (see figure 3.8).

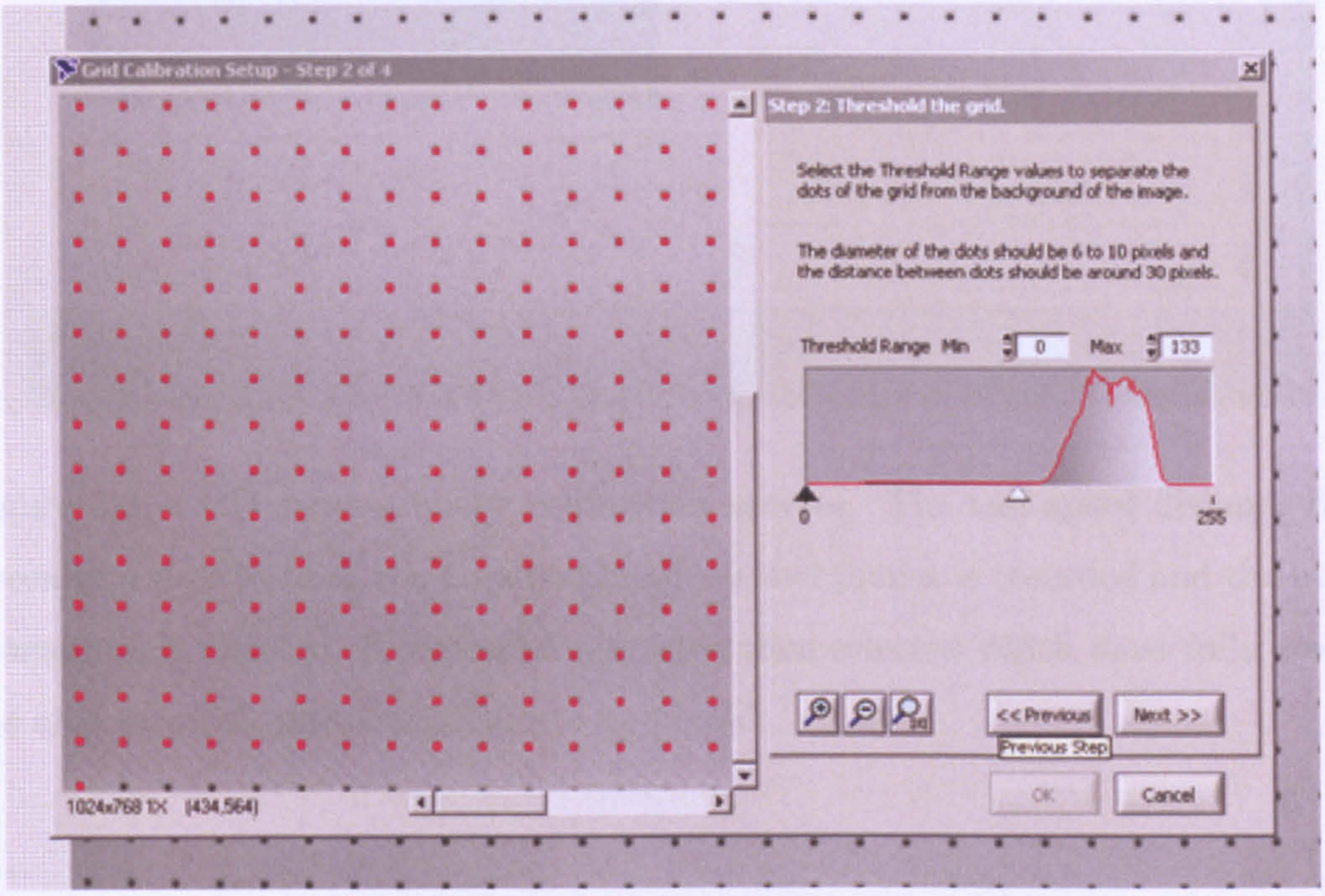

Figure 3.8: CCD camera image calibration process. The threshold of a grid of dots is altered in order to separate the dots from the background.

Once the dots have been separated from the background, the real space distance between the centers of the dots is detailed and the unit of measure is selected from a list. There is the option to have different spacing between dots in the horizontal

and vertical planes. A region of interest is then selected which must completely contain the sample imaging area (green rectangle shown in figure 3.9). The calibration is now complete, and must be saved for future use.

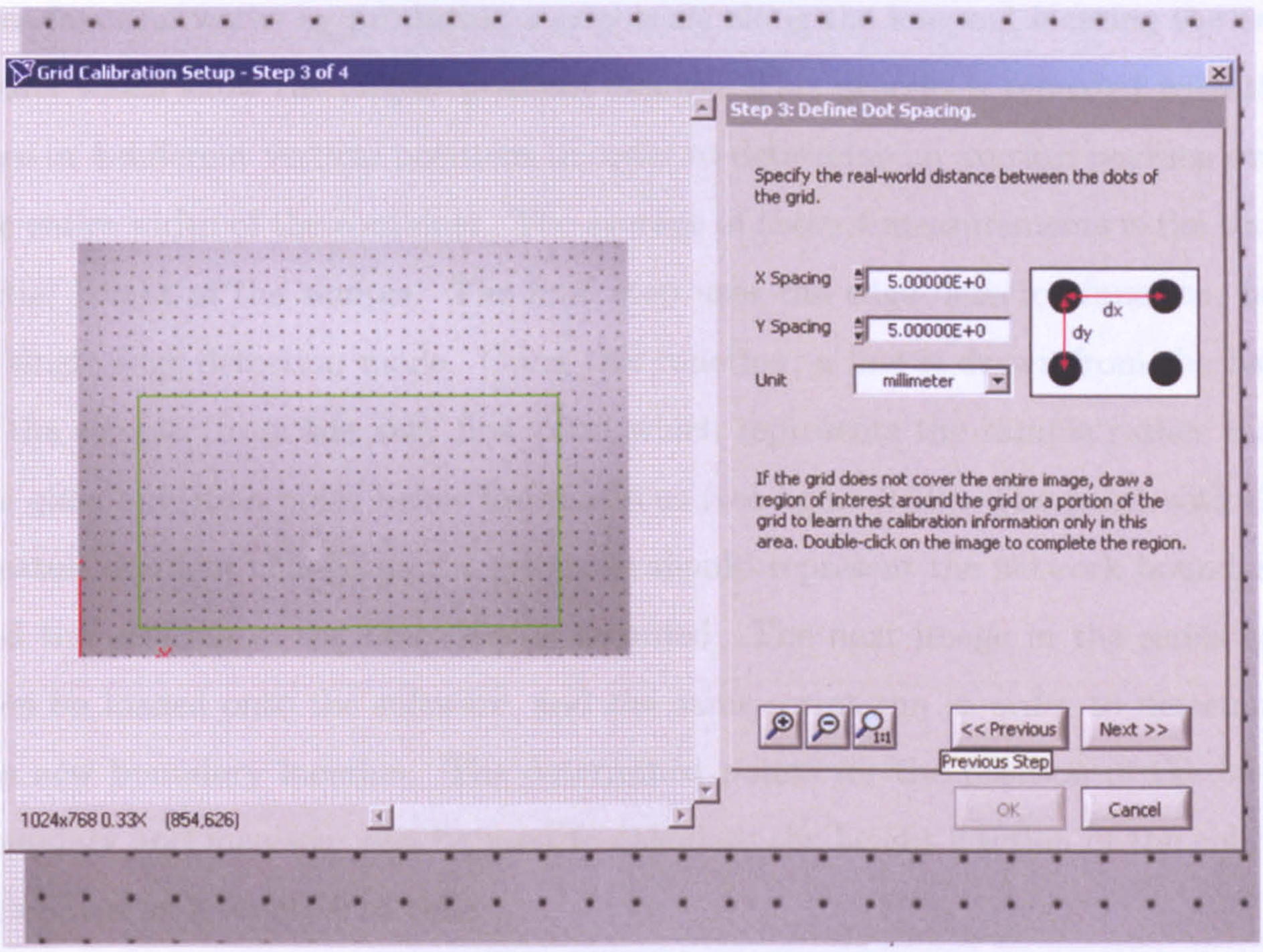

Figure 3.9: CCD camera image calibration process. The real space distance between grid dots in both the horizontal and vertical planes is recorded and the unit of measure is selected. A region of interest is then selected which must fully cover the area in which the samples are to be placed.

3.2.3 Image analysis

Once the calibration is carried out and the data collection is complete, analysis of the images can be carried out using Vision Assistant software. The first image from a series is selected and then a script is prepared for each sample within the image. A script is a series of commands which details how the image is to be treated. The first function in each script performs the calibration as described previously.

Secondly the Edge Detector function is used to determine the exact location of the base and the top of the sample. By selecting the 'find first and last' edge function, and drawing a vertical line which runs from the bottom of the cell to a point above the meniscus, the exact location of the base and meniscus is located. This function works by producing a grey scale along the line and locating the two points which show the largest gradient change. This process is repeated with the lines in 4 different vertical positions in order to determine an average position over the entire width of the container. The average of these 4 measurements is the total initial height of the sample. The final step uses the edge detector function, but in single edge detection mode. Using this function, a line is drawn from the base of the sample (from the very first pixel which represents the sample rather than the glass base)to a point below the meniscus (see figure 3.10). The point with the greatest gradient change on the greyscale should represent the network boundary, and the position of the boundary is recorded. The next image in the series can then be loaded onto the software, and the same script run in order to determine the new boundary location. The determined points for the position of the base, boundary and meniscus can be used to calculate the height fraction of the colloid rich phase as a function of time.

3.3 Dynamic Light Scattering

Dynamic Light scattering (DLS)which is also known as photon correlation spectroscopy and quasi-elastic light scattering, is a non-invasive analytical technique that is often used to determine the average size and size distribution of a particles in a suspension, and polymers in solution. The technique is based upon the displacement of particles or polymers as they undergo Brownian motion.

3.3.1 Dynamic Light Scattering Theory

When light is directed at a particle which is smaller than the wavelength of light, it is reflected in all directions by the particle (Raleigh scattering). A laser is assumed to be monochromatic (very narrow frequency) and coherent (each wave is identical

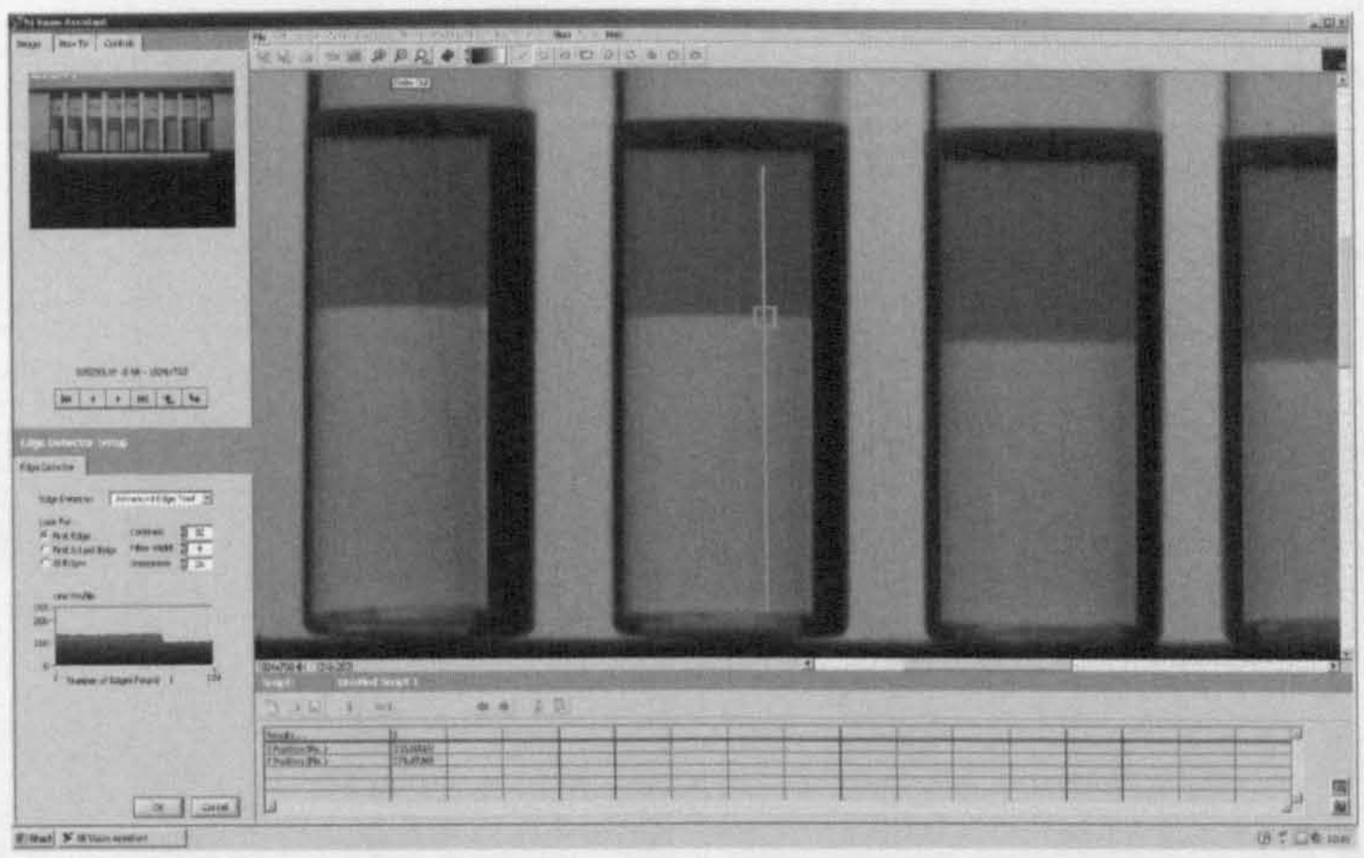

Figure 3.10: Determining the network boundary. A line is drawn over the sample using the edge detector function (green line). They greyscale along this line is determined and the boundary position is located by identifying the point with the largest gradient change along the line.

and can allow for maximum constructive interference) and when used as the light source in DLS there is a time dependence fluctuation in the scattering intensity. This fluctuation is a result of the molecules in solution undergoing Brownian motion and creating differences in the distances between scattering particles. Once light has been scattered by a particle it can overlap with light waves scattered by another particle resulting in either constructive or destructive interference. Constructive interference occurs when two waves are completely in phase with one another and is results an increase in the light intensity. Destructive interference occurs when two waves combine which are out of phase resulting in a decrease in the total intensity (see figure 3.11).

It is within these combined waves that information is held about the timescale on which the scattering particles move. The light reflected at any given angle is received by the detector, which records the intensity of light received. Figure 3.12 shows a schematic representation of the component arrangement in DLS. The measured intensity is used to generate a second order autocorrelation curve using:

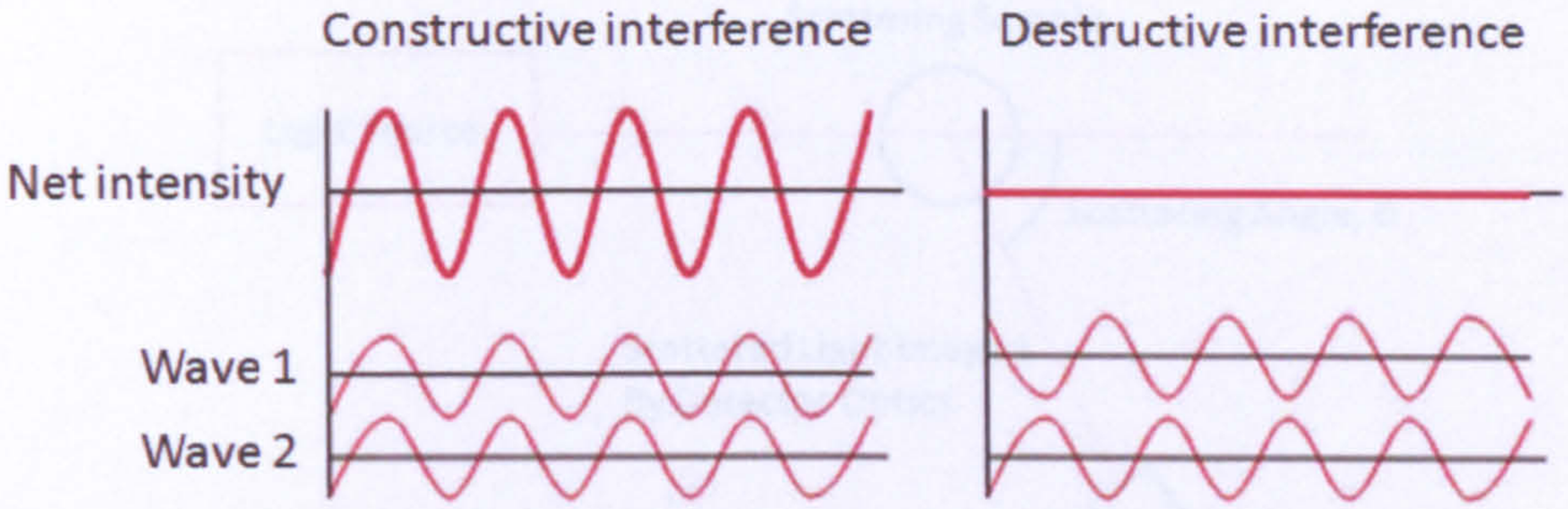

Figure 3.11: Diagram showing the result of combining two light waves. The image on the left demonstrates constructive interference where upon addition of the two waves which are **in phase**, the intensity is doubled. The image on the right demonstrates constructive interference where upon the addition of the two waves which are 180^0 **out of phase** the overall intensity is zero.

$$g^2(q;\tau) = \frac{\langle I(t)I(t+\tau)\rangle}{\langle I(t)\rangle^2} \tag{3.6}$$

where $g^2(q;\tau)$ is the autocorrelation function at a given wave vector, q, and waiting time, τ, where I is the measured intensity. q may be obtained at a single angle, or through a range of angles from:

$$q = \frac{4\pi n_0}{\lambda} sin\left(\frac{\theta}{2}\right) \tag{3.7}$$

where n_0 is the refractive index of the sample and θ is the angle at which the detector is located in relation to the sample, and λ is the laser wavelength.

3.3.2 Data Interpretation

An autocorrelation function compares a signal with its original signal after a waiting time so that differences can be observed. If the waiting time is relatively small then it is expected that the correlation will be high since the particles have had little time in which to move to new positions. As the waiting time is increased the correlation between two points will decrease exponentially, meaning that after a

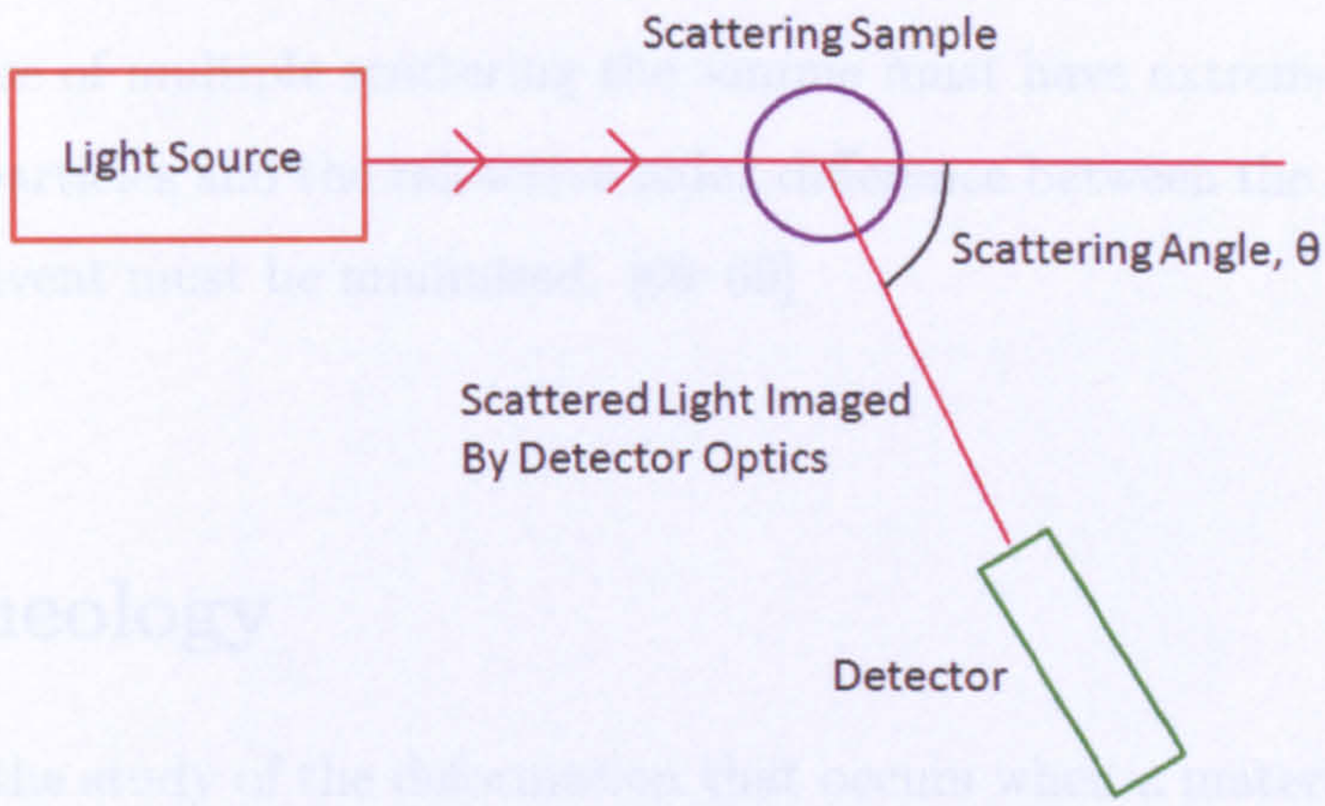

Figure 3.12: Schematic representation of the arrangement of the separate components of a Dynamic Light Scattering system.

very long waiting time that there is no correlation between the two points. Once the autocorrelation data has been obtained, a mathematical interpretation of the data can be carried out. The exponential decay observed in the autocorrelation data is related to the diffusion coefficient (D_0) of the particles and in samples where the particles are monodisperse the decay is a single exponential. It allows the size of the particle to be calculated since the diffusion coefficient depends upon the size of the particle as shown in the Stokes-Einstein equation:

$$D_0 = \frac{k_B T}{6\pi\eta a} \tag{3.8}$$

where k_B is the Boltzmann constant, T is the absolute temperature, η is the solvent viscosity and a is the particle radius. When the particle moves it has a layer of solvent surrounding it which also moves with the particle. It is therefore the size of the particle together with its associated solvent layer which is being measured, r_h, the *hydrodynamic radius.*

DLS is only effective when light photons are only scattered once (singly scattered). Multiple scattering occurs when light photons are reflected by more than one particle before being detected making data interpretation difficult. In order to reduce

the occurrence of multiple scattering the sample must have extremely low volume fractions of particles and the refractive index difference between the scattering particles and solvent must be minimised. [66–69]

3.4 Rheology

Rheology is the study of the deformation that occurs when a material is subjected to an external stress. The stress can be applied in a number of different ways: as a compression, tension or a shearing process. There are two extremes of rheological behaviour: Solid materials exhibit elastic behaviour where any deformation reverses spontaneously when the applied force is removed: energy is stored by the system and then released. The opposite extreme is viscous (or plastic) behaviour where any deformation caused by the applied stress is irreversible. Energy performs work on the material. A measurement of a materials response to stress can be described by the Deborah number, D_N, where D_N = relaxation time of material / time of observation. A material where $D_N \to 0$ behaves as a fluid, and where $D_N \to \infty$ it behaves as a solid. Between these two extremes lies a wealth of materials which can exhibit both of these characteristics. Measurements at high colloid volume fractions or on very short time scales may reveal evidence of solid like behaviour in something that appears to be a liquid. Such materials are called visco-elastic and depending upon which characteristic is dominant, they may be intrinsically either solid or liquid.

3.4.1 Introduction to rheology

There are different types of measurements which can be obtained using a rheometer which are dependant upon variations in the way that the force is applied. If a constant force is applied to the top surface of a cube and it deforms to a new position, the material behaves as an ideal solid. This type of deformation is called *shear deformation*, where the base of the cube is fixed, and only the upper part is

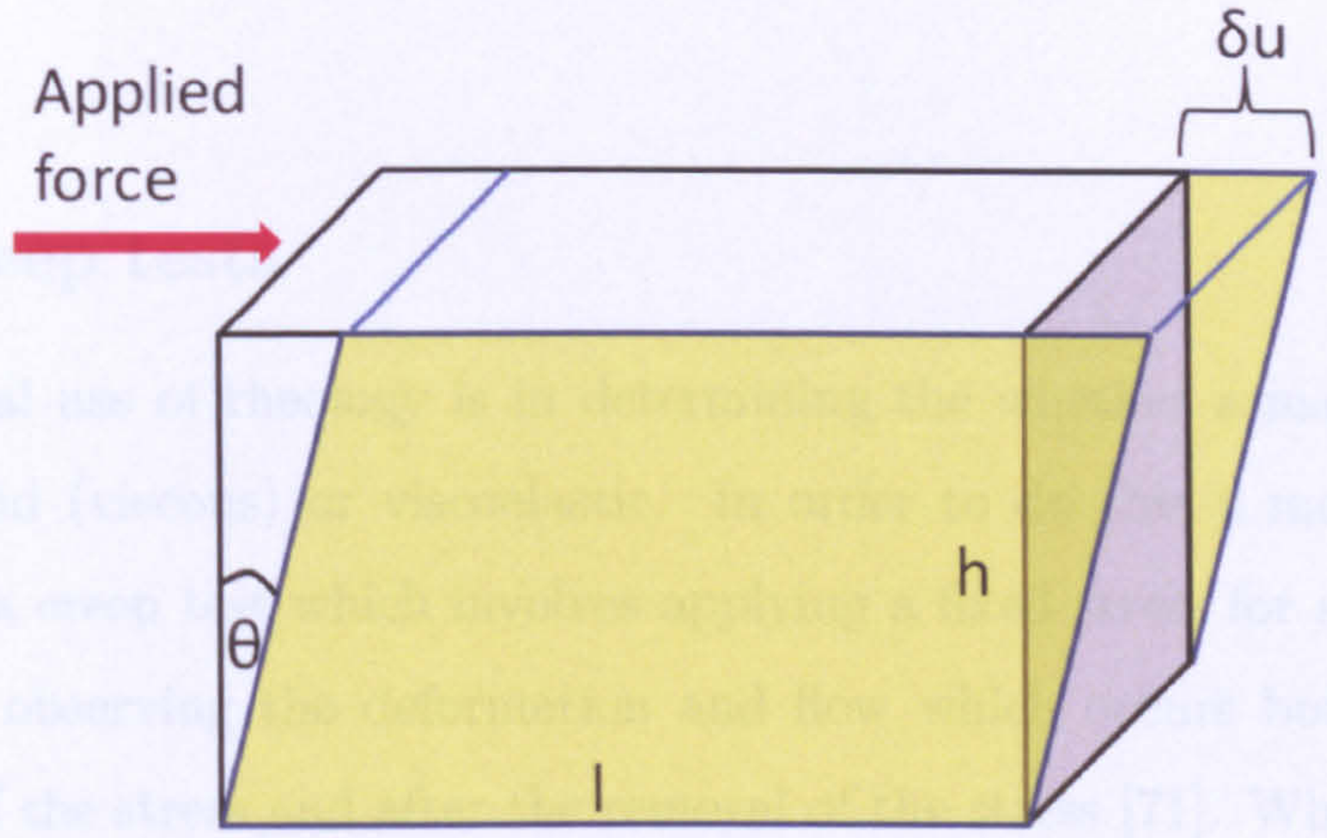

Figure 3.13: Cube showing how ideal solids deform under an applied stress.

moving as shown in figure 3.13 [70].

The degree of deformation, δu, and h define the *shear strain* as δu/h. The *shear stress* is related to the amount of force applied (F) and is defined as F/A where A is the area of the upper surface of the cube. The shear stress unit is the Pascal (N/m^2, or Pa) and is usually denoted by the symbol σ_s. In a purely elastic material the stress is proportional to the strain (Hookes law) multiplied by a constant G, the *shear modulus*. A linear response is observed if doubling the stress results in a doubling of the strain [68].

In the case of a material that behaves as an ideal fluid, when a shear stress (force) is applied the material will deform continually, at a constant rate. The rate of change of shear strain as a function of time is referred to as the *shear strain rate*, or *shear rate* $\dot{\gamma}$. The shear rate obtained is dependant upon the materials shear viscosity, η, where:

$$\eta = \frac{\sigma_s}{\dot{\gamma}} \tag{3.9}$$

The viscosity is purely the ratio of shear stress and shear rate, and has units of $Nm^{-2}s$, known as Pascal Seconds (Pa.s).

3.4.2 Creep tests

A fundamental use of rheology is in determining the whether a material is solid (elastic), liquid (viscous) or viscoelastic. In order to do this a material can be subjected to a creep test which involves applying a fixed stress for a finite period of time, and observing the deformation and flow which occurs both during the application of the stress and after the removal of the stress [71]. When a constant stress is applied to an elastic material, deformation occurs instantly and remains constant until such a time that the stress is removed and the deformation is reversed. However, when a constant stress is applied to a viscous material the strain increases linearly with time and there is no recovery once the stress is removed. A viscoelastic material will display a combination of these two types of behaviours. There is initially a non linear response to stress, and when the stress is removed there is the ability for partial recovery. A representation of this can be seen in figure 3.14. The results of a creep test are usually expressed in terms of the creep compliance $J = \gamma_s/\sigma_s$ and has units 1/Pa [71].

3.4.3 Stress relaxation tests

A stress relaxation test is the reverse of a creep test, and it is used to describe the way viscoelastic materials relax over time. A constant strain is applied to the system and the stress required to keep the strain at a constant is recorded. As the system rearranges and flows with time, less stress is required in order to maintain the deformation and a lower energy structure is formed. This is termed stress relaxation. The deformation will become permanent over long timescales with complete relaxation of the structure [72].

3.4.4 Oscillatory tests

During an Oscillatory test, the measuring geometry oscillates around the rotation axis instead of moving constantly in a single direction. This allows the both the

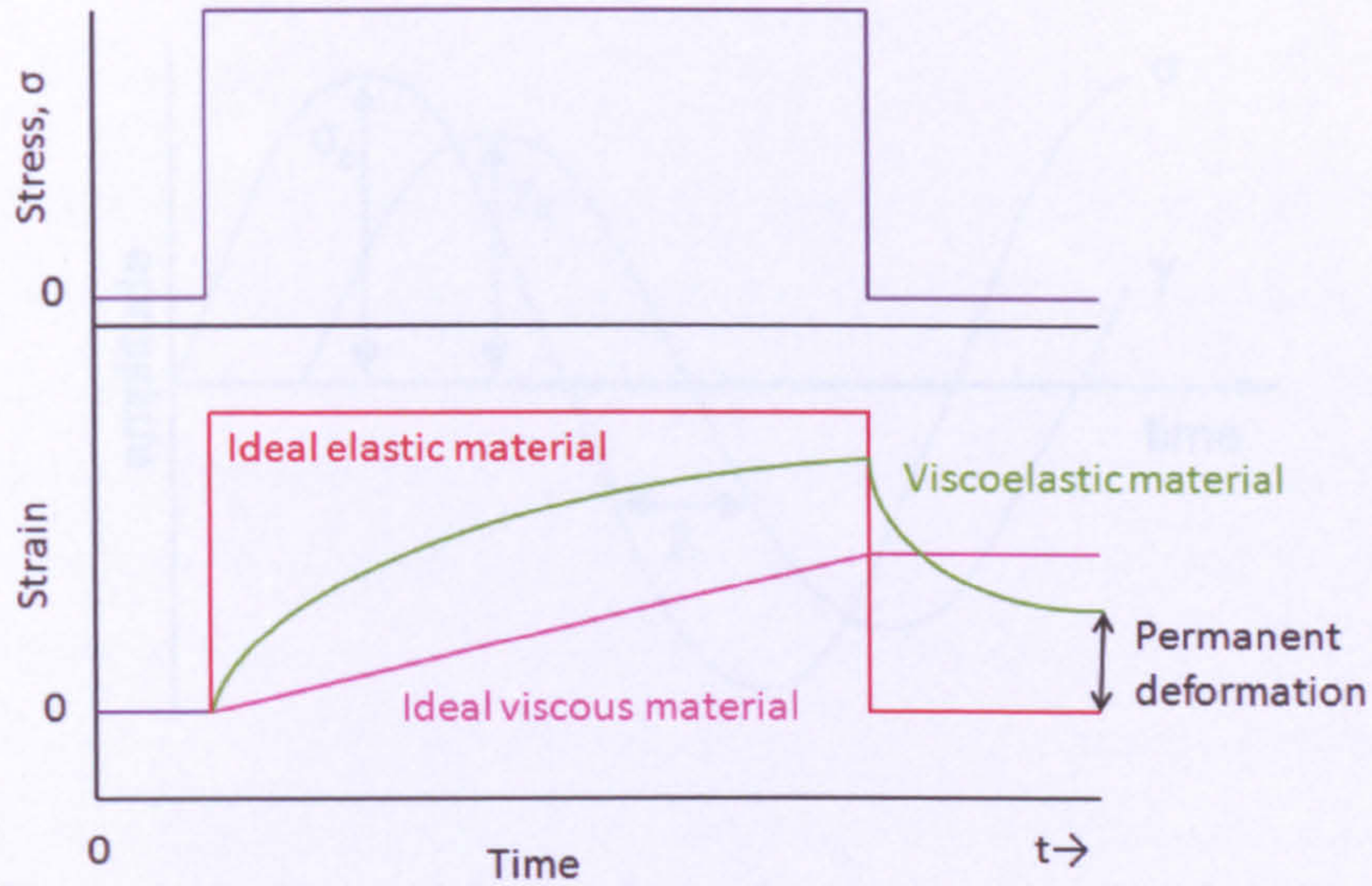

Figure 3.14: Creep and recovery curves for an ideal elastic material (red line), ideal viscous material (pink line), and a viscoelastic material (green line). The upper plot represents the stress applied to the material, which is applied instantaneously and at a fixed value for a finite period of time. The lower plot represents the resulting strain for an elastic, viscous and viscoelastic material. Figure reproduced from [71]

viscous behaviour as well as the elasticity of the material to be determined. The difficulty with Oscillatory tests is that they have a lower level of reproducibility when compared to standard rotational tests.

In a typical oscillation experiment, the applied stress (σ) and resulting strain (γ) wave forms can be described by:

$$\sigma_s = \sigma_0 \cos \omega t \tag{3.10}$$

and

$$\gamma_s = \gamma_0 \cos (\omega t - \delta) \tag{3.11}$$

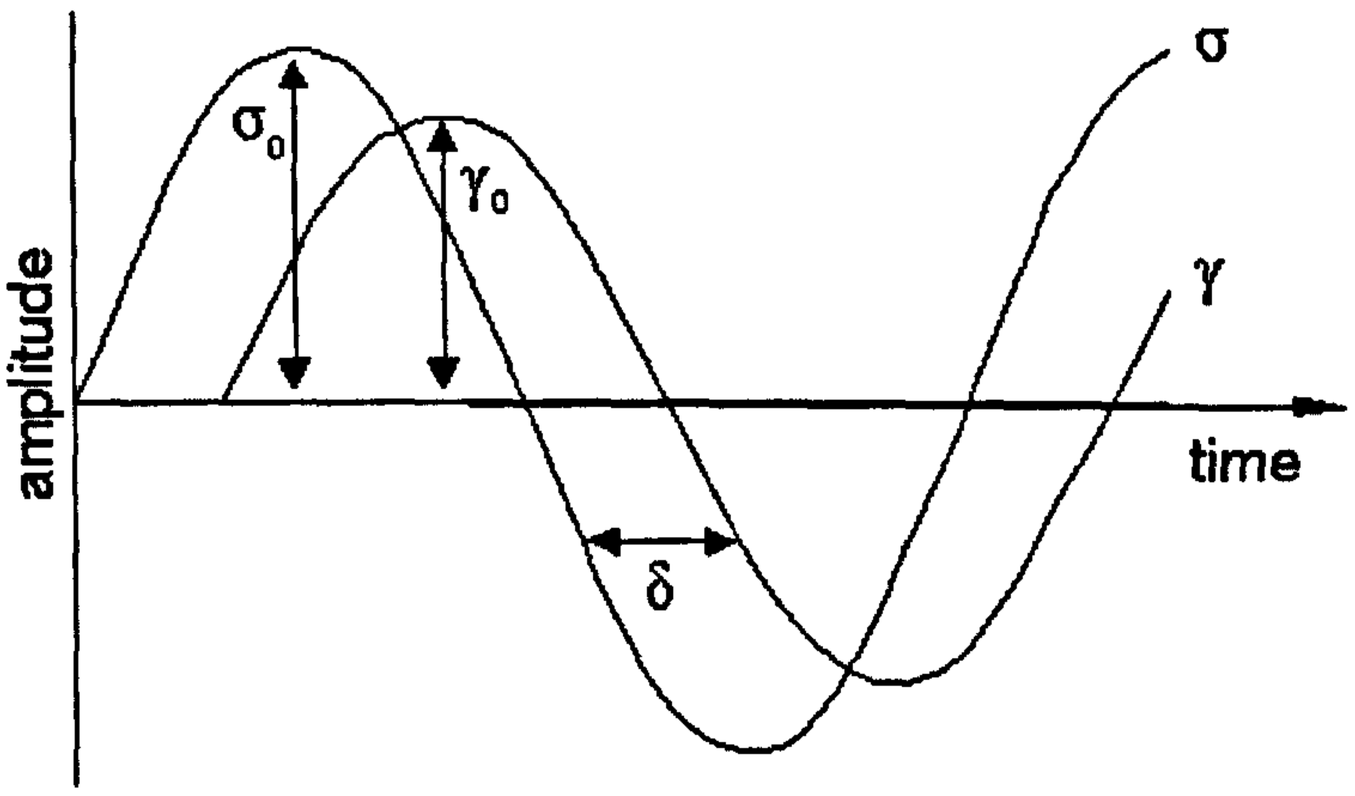

Figure 3.15: Sinusoidal wave forms for stress and strain functions.

where σ_0 is the stress amplitude, γ_0 is the strain amplitude, $\omega = 2\pi f$ and is the angular frequency, t is time, and δ is the phase lag, or loss angle. These terms are represented in figure 3.15. The phase lag of an ideal solid is δ=0^0 which represents a purely elastic response, whereas for a purely viscous fluid the phase lag is δ=90^0. The complex modulus G*,is the overall resistance of a material to deformation, regardless of whether the deformation is reversible or not and is a combination of the shear storage modulus and shear loss modulus.

The shear storage modulus, G' represents the elastic (in phase) component where:

$$G' = \frac{\sigma_0}{\gamma_0} \cos \delta \tag{3.12}$$

and the shear loss modulus, G'' represents the viscous component of the material where:

$$G'' = \frac{\sigma_0}{\gamma_0} \sin \delta \tag{3.13}$$

3.4.5 Vane rheology

There are a number of different apparatus available for carrying out rheological measurements, which are referred to as geometries. The standard geometries are the cup and bob, cone and plate, and parallel plate [73]. Each geometry has its own advantages and disadvantages. The cone and plate only requires small amounts of material and can be used on low viscosity materials. The cone is available in a variety of angles where smaller cone angles result in greater errors in gap setting, but at larger cone angles the shear rate across the gap varies more. The parallel plate also requires only a small volume of material, but the main disadvantage is that the shear rate produced varies across the sample, and so an average value of shear is usually obtained. The cup and bob is available is three different styles: the coaxial cylinder, the double gap, and the mooney cell. Cup and bob measuring geometries require large volumes of material, but they are mostly used because their large surface area allows for good data to be obtained at low shear rates and viscosities.

A further type of measuring geometry which has not yet been mentioned is the vane, and it is this type of geometry which is used for each measurement carried out throughout the course of this research. A vane consists of a number of identical paddles (usually 4) arranged around a rotating spindle, as shown in figure 3.16. The three types of measuring geometries previously mentioned are all prone to wall slip, where a thin layer of material is able to adhere to surfaces and act as a lubricating layer, allowing the bulk of the material to 'slip' over this layer at low shear. This phenomenon results in inaccurate measurements being obtained [70]. Wall slip is able to be minimised by using a vane, and a further advantage of this method is that sample disturbance is minimal as the vane is lowered into the sample. The stress is calculated from the rheometer torque, T as follows:

$$\sigma = \frac{2T}{\pi D^3} \frac{1}{\frac{H}{D} + \frac{1}{3}} \tag{3.14}$$

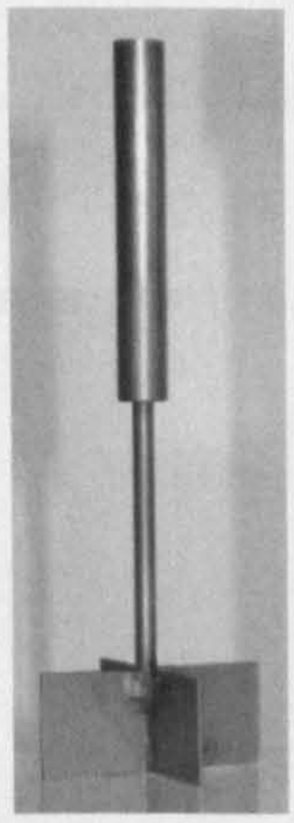

Figure 3.16: Example of a vane measuring geometry.

where D is the vane diameter, and H is the height [74–76].

Constructing a new vane

In order to probe the rheological properties of an ageing gel network, it is essential that network disturbance is kept to a minimum. In order to achieve this a vane geometry was specially constructed for the rheometer (Bohlin HR Nano, Malvern Instruments) which consisted of four blades. The total width of the geometry was 22.7 mm with a height of 10mm and each blade was constructed with the thinnest material possible providing a small end profile when compared to other vane geometries. This meant that sample displacement as the vane was lowered into the sample was kept to a minimum.

Samples were prepared in clear polycarbonate vials with internal diameter of 25.5 mm at the top of the vial and 24.5 mm at the base, and a total height of 65mm. The clear vials allowed the interface height to be followed as a function of time, whilst simultaneously performing rheological measurements. Since the continuous phase of the samples is an aqueous mix, a thin later of silicone oil was added to the surface of each sample in order to minimise evaporation. The vane geometry was lowered into the sample by the rheometer, so that the top of the blades were positioned 10

mm beneath the top of the sample. Provided that any disturbances to the sample remain within the linear viscoelastic range for deformation, measurements should be possible which correspond to the unperturbed state of the samples.

Chapter 4

Experimental Materials

4.1 Requirements of a model system

Colloidal systems have proven to be beneficial in the field of soft matter physics by acting as atomic models. Atoms are difficult to study due to their small size, and so model colloidal systems are used since the colloids are small enough that they are still greatly affected by Brownian motion and large enough that they can be readily studied with a microscope and light scattering techniques. Alternatively, a colloidal system can model real life colloidal dispersions such as salad dressing or paint.

The aim of this investigation is to create a model of an oil-in-water emulsion crop protection formulation in which the colloidal particles contain organic active compounds and the suspension is stabilised against creaming by the addition of a non-adsorbing polymer, creating a colloidal particle network. Coalescence of the emulsion drops is prevented by the addition of surfactants, which orientate themselves and the oil/water interface and reduce the interfacial tension. When preparing a model colloidal system it is often a requirement that the colloids are monodisperse, or at least have an extremely low size distribution in order to decrease the number of variables within a system. The analytical methods used impart some restrictions on the model system. The use of Laser Scanning Confocal Microscopy dictates that in order for colloids deep within the sample to be clearly imaged, they must be sus-

pended within a continuous phase which has an identical refractive index to that of the colloids. This refractive index matching of the continuous phase and suspended particles also removes any interactions which arise as a result of Van der Waals attractions. A fluorescent dye must be incorporated into the system which has an excitation wavelength identical to one of the available lasers, and either the continuous phase or the colloids can be fluorescently labelled. Many fluorescent dyes are prone to photobleaching, where continued excitation by a laser drastically reduces the level of fluorescence observed. This characteristic must not be present in the selected dye as samples will be required to undergo imaging for prolonged periods of time. The particles must also be density matched as closely as possible to the continuous phase so that the particles do not cream out of the focal plane of the microscope where they can no longer be observed. Density matching will also slow down the rate of creaming to such an extent that the rate of creaming in bulk samples can be accurately determined by eye over long periods of time. Since large quantities of material are going to be utilised, it is essential that a preparation technique is selected which allows for large scale production of the materials.

4.2 Formulating a model system

In the model system the oil phase is represented by poly(dimethylsiloxane) which is a well characterised silicon oil. The refractive index matching of the aqueous phase to the PDMS is achieved by combining the continuous water phase with a second liquid which has a higher refractive index than that of the colloids. By matching the refractive index of the continuous phase and the colloids the amount of scattering from the laser is reduced, which allows for the working depth of the microscope to be increased. The liquid chosen to be combined with water was 1,2-ethane diol as it is a low molecular weight molecule which is completely miscible with water, and has a high refractive index. The required ratio of water and 1,2-ethane diol for index matching also provides a very close density match to the particles. The organic actives contained within the oil droplets in the real life system can be excluded here

since they are not relevant for this study and should not alter the behaviour of the particles in any way, therefore simplifying the model system. Although particle monodispersity is desirable, it is not feasible to produce a monodisperse particle system for this study since it is difficult to prepare large quantities of monodisperse material. Also, since industrial formulations are produced by high shear mixers in large quantities, there is always some degree of particle size distribution and so a monodisperse system will not be truly representative of the real life formulation. This allows production using a high shear mixer where it is possible to produce material volumes of order 2L. The attraction between colloids is induced by adding a depletion polymer. The biopolymer xanthan is commonly used in a wide number of formulations as both a stabiliser and viscosity enhancer, as well as in the real life formulation and so is used in the model system. The model colloids are stabilised against coalescence by the addition of a combination of surfactants which are used in the real life formulation. A combination of two non-ionic surfactants is used as well as an ionic surfactant which gives the particles a slight negative charge, increasing particle repulsion. Finally, a fluorescent dye is added to the aqueous continuous phase as this procedure is much simpler than trying to incorporate a dye into the oil droplets. The dye selected is Rhodamine B since it is water soluble, and tests by previous researchers show that there is little photobleaching of the dye after prolonged periods of imaging.

4.2.1 Poly(dimethylsiloxane)

Poly(dimethylsiloxane) (PDMS) is an organosilicon compound with the chemical formula $CH_3[Si(CH_3)_2O]_nSi(CH_3)_3$. Its structure is shown in figure 4.1, and it is also referred to as dimethicone or the additive E900. It is optically clear and considered to be inert, non-toxic and non-flammable. Synthesis of the PDMS occurs via several steps. Firstly dimethyldichlorosilane is formed from a reaction between methyl chloride and silicon (3.10). Secondly, in the presence of water the dimethyldichlorosilane undergoes a nucleophilic attack (HCl) to form dimethyldisilanol, which is unstable and quickly condenses to form linear oligomers (3.11). The net reactions are summarised below:

$$2(CH_3Cl) + Si \rightarrow Si(CH_3)_2Cl_2 \tag{4.1}$$

$$2Si(CH_3)_2Cl_2 + H_2O \rightarrow [Si(CH_3)_2O] + 2HCl \tag{4.2}$$

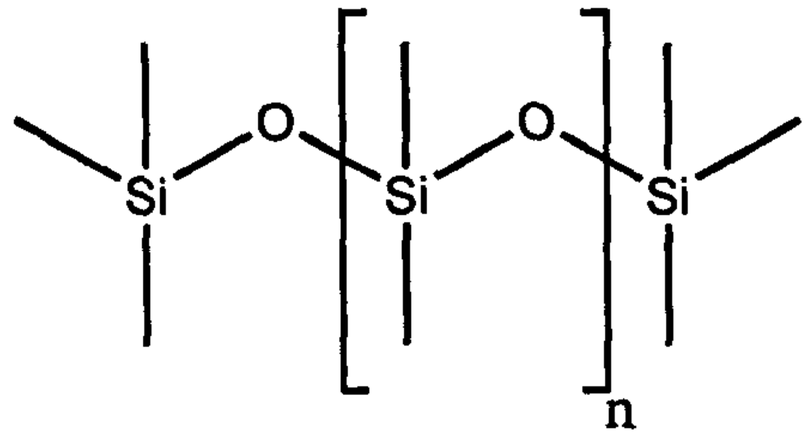

Figure 4.1: Structure of poly(dimethylsiloxane).

PDMS has strong chemical bonds which are not easily broken due to their polarity [77] and it requires either a strong acid or strong base to depolymerise the siloxane chain. As a result, the PDMS is not very susceptible to oxidation or thermal degradation and it can be sterilised by heat. PDMS is hydrophobic as the methyl groups shield the polar Si-O-Si backbone, and the surface energy and surface tension is decreased by exposing a maximum number of methyl groups [78].

Emulsions are unstable and do not tend to occur spontaneously. This can be demonstrated by equation 4.3:

$$\Delta G = \Delta A_{int} \cdot \gamma - T\Delta S_{disp} \tag{4.3}$$

Where ΔG is the change in Gibbs free energy, ΔA_{int} is the change in the interfacial area, γ is the interfacial tension, and ΔS_{disp} is the entropy change associated with the droplet dispersion. When a colloidal system is generated from two immiscible liquids, the increase in interfacial area is immense. ΔA is therefore the most significant term in the above equation and results in a positive figure for ΔG being obtained. This indicates that there would need to be an increase in the free energy. Energy will therefore be required to be applied to the system, and it can be

considered a non-spontaneous reaction. The smaller the particle size required, the higher the amount of energy required in order to achieve emulsification. Therefore it is more difficult to produce emulsions in the nano size range (micro emulsion), as opposed to a macro emulsion. Emulsions do not occur spontaneously, and there are two main methods by which an emulsion can be formed: using high speed mixers and colloid mills which require a high level of energy, and by polymerisation. There are advantages to both methods of preparation. A polymerisation reaction was carried out Obey and Vincent, where a monodisperse emulsion of PDMS in water was produced from the polymerisation of dimethyldiethoxysilane (DMDES) in water. The reaction was a hydrolysis base catalysed reaction, using ammonia and was carried out in either water, or water/ethanol mixtures. The effect of varying the monomer, ammonia, and ethanol volume fractions on resultant particle size was investigated, as well as the particle size obtained with various times allowed for the polymerisation process to occur. As a broad generalisation, it is acceptable to say that particle size increased as any number of the above constituents was increased [79]. This process results in monodisperse particles which is desirable for a model system, however it is not feasible to produce very large quantities of material. The benefit of using an emulsion mixer is that large batches of material can be prepared with the disadvantage being that there will be a degree of polydispersity. The size of the particles and degree of polydispersity depends upon the shear rate of the emulsion mixer, and the length of time for which mixing is carried out.

PDMS has several applications. It is an important component of silly putty, silicone caulks/sealants and adhesives, as well as silicone grease and other silicone based lubricants. It is also found in personal care products, the most common of which is probably hair conditioner where the silicone imparts a smooth, shiny appearance. PDMS can surprisingly be used in the treatment of headlice where PDMS coated headlice cannot excrete water ingested with meals, which eventually results in the fatal rupture of the stomach [80].

4.2.2 Xanthan

Microorganisms such as bacteria and fungi produce water soluble carbohydrate polymers which have a wide range of functional properties. The anionic biopolymer xanthan is produced by the bacterium *Xanthomonas* and was discovered in the 1950's, with the first industrial production in 1960. Xanthan has no known toxicity and has been approved for food use with no specified daily intake limit and is referred to as E415.

Xanthan is a high molecular weight heteropolysaccharide consisting of the sugars D-glucose, D-mannose, and D-glucuronic acid. The backbone is comprised of glucoses which form a glucose backbone via β-1,4-D-glucan links, where a link forms between carbon 1 from one molecule to carbon 4 of another. When a glucose ring is formed the hydroxyl group which is attached to carbon number 1 will either be above or below the plane of the ring. If it is in the same plane as the hydroxyl groups at carbons 2 and 4 then it is an α glucose, and if the hydroxyl group is on the opposite plane to the two there hydroxyl groups, then it is a β glucose. Therefore in order for β glucose monomers to form a chain every second glucose unit must be inverted [81]. The structure of Xanthan is shown in figure 4.2. The linear sequence of the units is referred to as the primary structure of the protein.

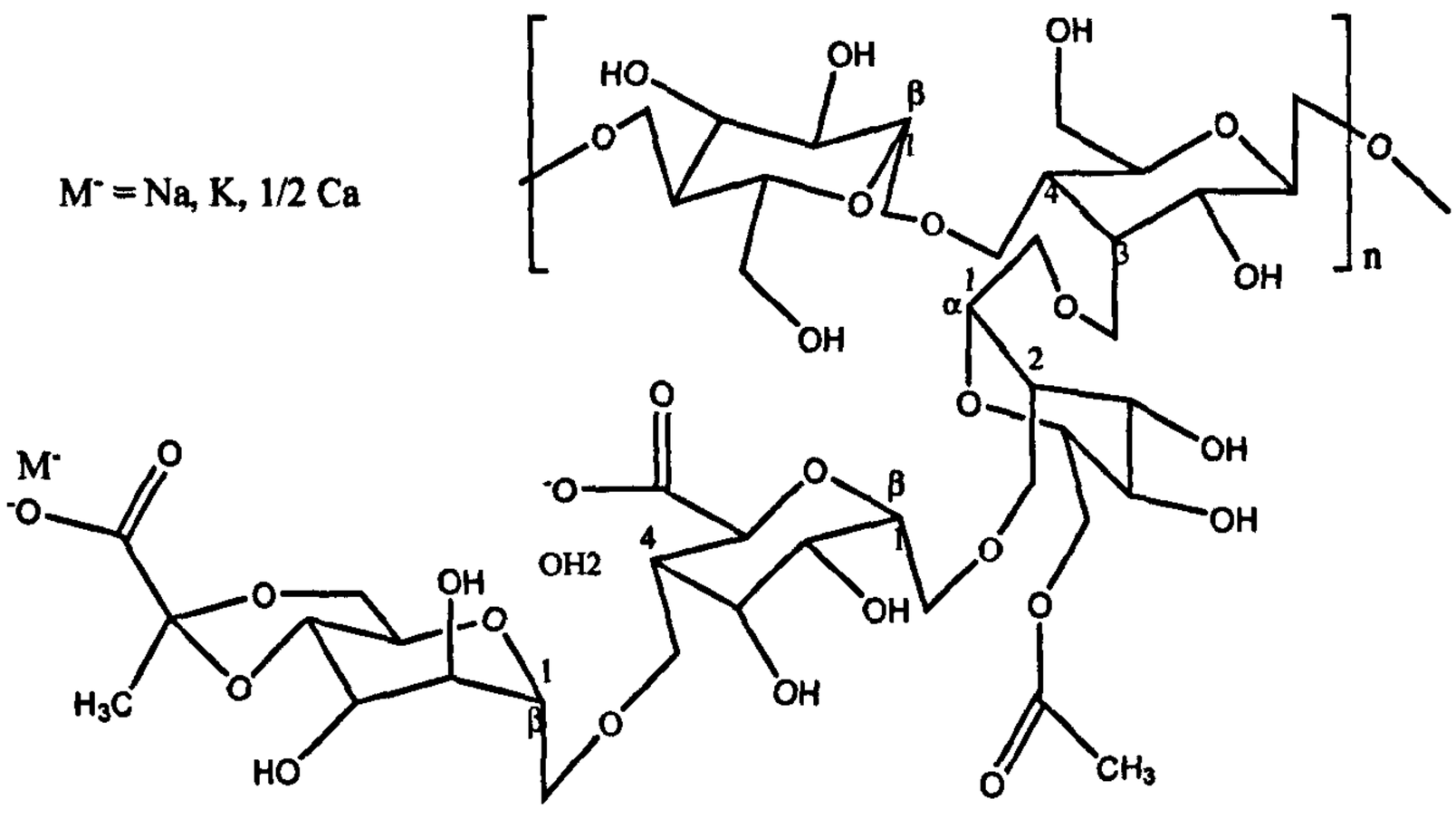

Figure 4.2: Structure of Xanthan.

The secondary structure of a polymer is determined by the shape that the backbone of the molecule assumes as a result of hydrogen bonds between atoms on the backbone. The two most common secondary structures are the α-helix and the β-pleated sheet. An α-helix retains is shape by the intramolecular hydrogen bonds, and the helical structure imparts some elasticity to the polymer. A β-pleated sheet is a result of polymers bonded side by side by intermolecular hydrogen bonds [81]. Xanthan may exist in either an ordered (helix) or disordered (coil) conformation, where transformation from the ordered to disordered state can be achieved by decreasing the salinity or increasing the temperature above the characteristic 'melting' temperature, T_m [82]. The ordered conformation can be native or renatured. Native xanthan refers to xanthan that has not undergone any heat treatment. When xanthan is heated an order→disorder transition occurs whereby helical structures become coils. Upon cooling, the helical structure is reformed, resulting in renatured xanthan where the viscosity of renatured xanthan is higher than that of native xanthan. The transition from native to renatured is therefore an irreversible process. X-ray scattering results indicate that the ordered conformation of native xanthan is a right-handed helix with a five-fold symmetry with a pitch of 4.7nm and a diameter of 1.9mm [83]. The ideas of a single helix and a double/multiple helix have been suggested with the idea of a double helix being the most preferred by authors. The helix is held together by noncovalent bonds and can be described as a rigid rod.

The molecular weight of xanthan is generally reported to be between 4 and 12 $x10^6$ g mol^{-1}. Measurement of the molecular weight is difficult due to the high molecular weight, the presence of aggregates and the stiffness of the molecule. Xanthan exhibits a varied rheological behaviour where it can be a Newtonian or shear-thinning (pseudoplastic) solution, or a gel depending upon solution properties such as the concentration of xanthan and salts. Xanthan's viscosity increasing property is its most important, and calculation of solution viscosities is important. As the viscosity of a xanthan solution is dependant upon the solution parameters, it is better to express the viscosity of xanthan in terms of intrinsic viscosity, which corresponds to the hydrodynamic volume of the polymer chain in a solvent. It

is usually obtained by measuring the viscosity of a number of xanthan solutions at very low concentrations (Newtonian liquids), where the overlap between the hydrodynamic volume of individual polymer chains is negligible and applying the equations of Huggins and Kraemer:

$$\eta_{sp}/C_p = [\eta] + \lambda_H[\eta]^2 C_p \tag{4.4}$$

$$\ln(\eta_r)/C_p = [\eta] + \lambda_K[\eta]^2 C_p \tag{4.5}$$

where:

$$\eta_r = \eta/\eta_0 \tag{4.6}$$

$$\eta_{sp} = (\eta - \eta_0)/\eta_0 \tag{4.7}$$

η_{sp} is the specific viscosity, η is the solution viscosity, η_0 is the solvent viscosity, η_r is the relative viscosity, and λ_H and λ_K are constants [84].

Determining the radius of gyration of xanthan is important as the size of the molecule sets the range of any depletion attractions, and will also govern when systems move from a dilute, through semi-dilute to concentrated polymer regime. The conformation of the molecule will play a role in determining the polymer overlap concentration when systems move from a dilute to semi-dilute regime. For example, from [85] C* for a random coil is calculated by:

$$C^* = 2^3 M_w/(N_A\langle R\rangle^3) \tag{4.8}$$

and for a wormlike chain, C* is calculated by:

$$C^* = 2^{3/2} M_w/(N_A L^{*3}) \tag{4.9}$$

where

$$L^* = (\rho L)^{3/2} \tag{4.10}$$

and for a rod, C* is calculated by:

$$C^* = 2^{3/2} M_w/(N_A L^3) \tag{4.11}$$

where M is the molecular mass, $\langle R \rangle$ is the root-mean-square end-to-end distance of the macromolecular coil at infinite dilution, N_A is Avogadro's number, L* is the effective length, and L is the real length. Using the physical end to end length of the molecule is not ideal as it is often difficult to measure. A more straight forward approach would be to use the radius of gyration, r_g which is more easily measured by several experimental methods. Using r_g , the calculation for the overlap concentration becomes:

$$C^* = 3M/(N_A 4\pi r_g^3) \tag{4.12}$$

r_g and $\langle R \rangle$ are closely related, as shown below:

$$r_g^2 = \frac{\langle R^2 \rangle}{6} \tag{4.13}$$

The r_g depends on both the chain length and the shape of the molecule. It is calculated from the mean square distance of the monomers from the polymer center of gravity, and as seen in equation 4.13 it is much smaller than the value for the mean-square end-to-end distance. This relationship holds true for highly flexible chains, but as chains become less flexible, the r_g increases as the polymer is not able to be so tightly coiled. However, xanthan is an especially inflexible polymer due to the bulky side chains, and exists as a rod structure rather than a coil, and so more complicated analysis is required in order to determine.

Xanthan has a wide variety of uses in both the food and technological industries. It is used to make a drilling fluid which is often used when drilling for oil and

natural gases. Rock which is excavated during drilling needs to be brought to the surface and increasing the viscosity of drilling fluid ensures that particles do not settle to the bottom of the well, or bore hole. Its shear thinning properties enables the drilling fluid to be easily removed. Xanthan is usually the preferred choice over other thickeners as very low concentrations are required in order to see a noticeable viscosity increase, meaning that there is less product that has to be purchased, transported and used. By adding 0.5% to water the viscosity is increased by a factor of 100,000 at low shear rates, but at high shear rates this factor is reduced to only 10 [86]. Xanthan has uses in the paint preparation industry as a thickener in non-drip paints, and a stabiliser in emulsion paints [87]. It also has numerous food uses such as a thickener for jams and sauces, a binding agent for people who are following a gluten free diet to bind and thicken gluten free ingredients, and imparting a creamy consistency in foods such as ice-cream to make them more enjoyable to eat. The life span of beer foams are enhanced by xanthan since they are often destroyed by trace amounts of surfactant left behind on glasses. Many food items such as milk, cream and mayonnaise are oil-in-water emulsions and margarine and low-fat spreads are water-in-oil emulsions. Emulsifiers are required in order to stop coalescence of droplets, but emulsion systems are potentially unstable because droplets tend to settle under gravity. Adding a stabiliser such as xanthan extends the shelf life of colloidal foods by increasing the viscosity of emulsions, reducing droplet movement and slowing down the process of creaming or sedimentation [88]. At higher concentrations, a colloidal gel is formed which exists for a finite period and prevents colloids from sedimenting or creaming. Many personal care products also require xanthan, the most common of which is probably toothpaste, where it is added to increase the viscosity of the paste and its shear thinning properties allow it to be easily squeezed from the tube. Agricultural industries utilise it for use in pesticides and herbicides where the formulations are oil in water emulsions with an active ingredient contained within the emulsion droplets. The droplets are stabilised against sedimentation/creaming, therefore extending the shelf life of the products, as in the cases of oil in water food emulsions. The uses of xanthan detailed here is not an exhaustive list, merely a summary to demonstrate its varied

applications [89].

4.2.3 Preparation of a model PDMS emulsion system

A model oil in water emulsion system was prepared where the oil droplets were formed from silicone oil (Dow Corning 200 10cSt). The refractive index of the silicone oil was reported by the manufacturer to be 1.399. This value was confirmed in the lab with an Abbe refractometer. The refractive index of water at $20°C$ is 1.330 and so in order for a refractive index match of the silicone oil to be obtained, the de-ionised water was mixed with 1,2-ethanediol (ED). In order to determine the correct mass fraction of ED to use, five solutions were prepared which had differing mass fractions of ED. At a refractive index of 1.399, the required mass fraction of ED was calculated to be 0.66 from figure 4.3.

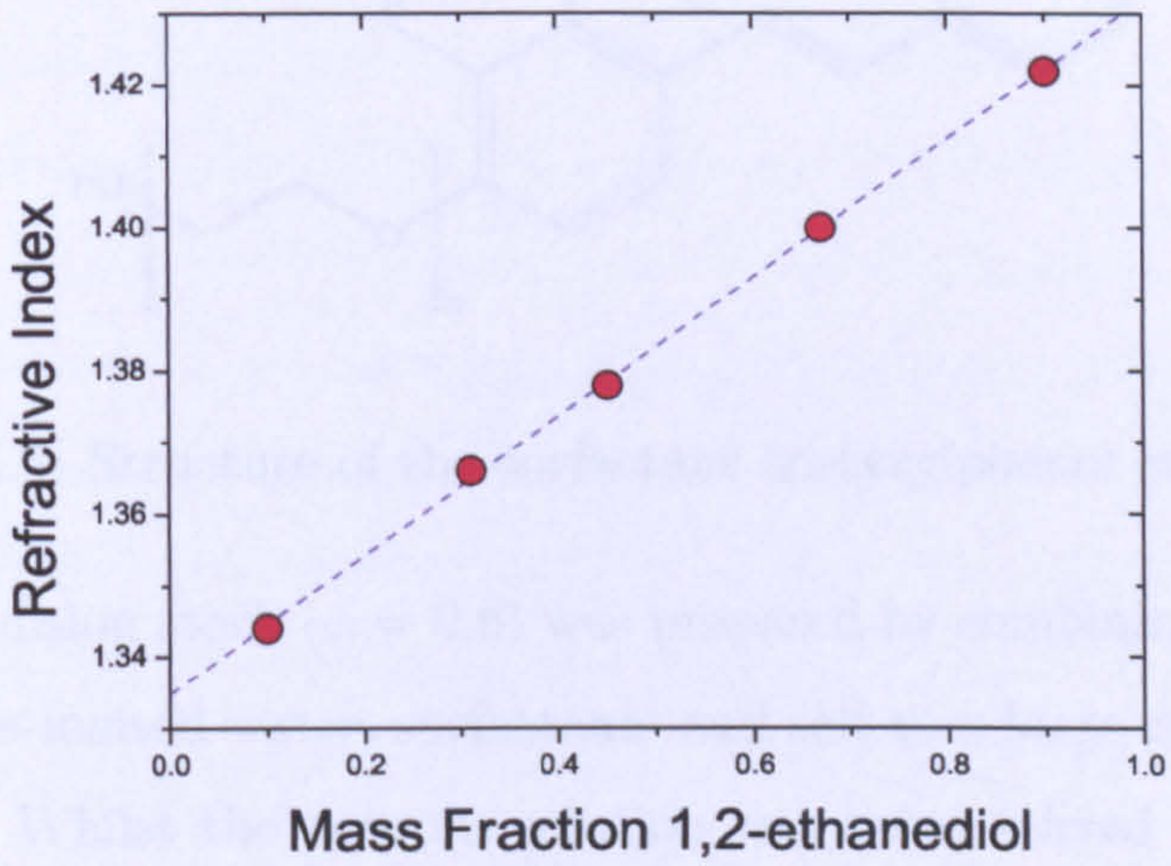

Figure 4.3: Plot showing the measured refractive index of a range of solutions with varying compositions of 1,2-ethanediol and H_2O. The measurements were obtained using an Abbe refractometer

Given that the system is representative of a real life emulsion system which is polydisperse, and that large quantities of material is required, the model system was produced using a rotor-stator. The system was stabilised against coalescence

by the addition of the two non-ionic surfactants synperonic PE/P103 (figure 4.4) and tristyrylphenol ethoxylate (TSPE)(figure 4.5) and the surfactant Na-AOT. The Na-AOT also helped to increase the repulsion between colloids by the addition of a slight negative colloidal charge.

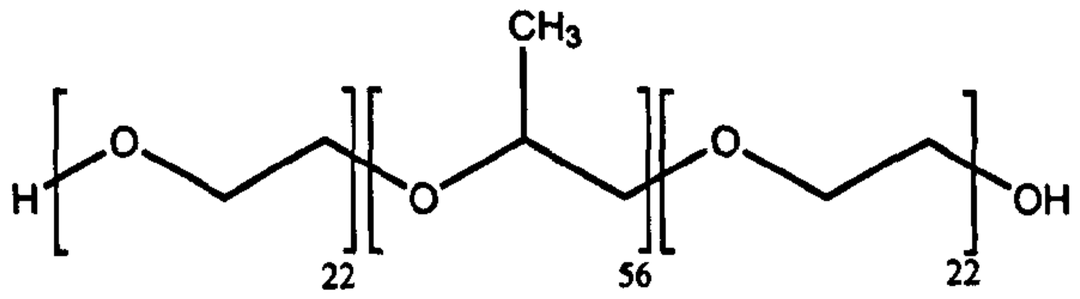

Figure 4.4: Structure of the surfactant synperonic PE/P103.

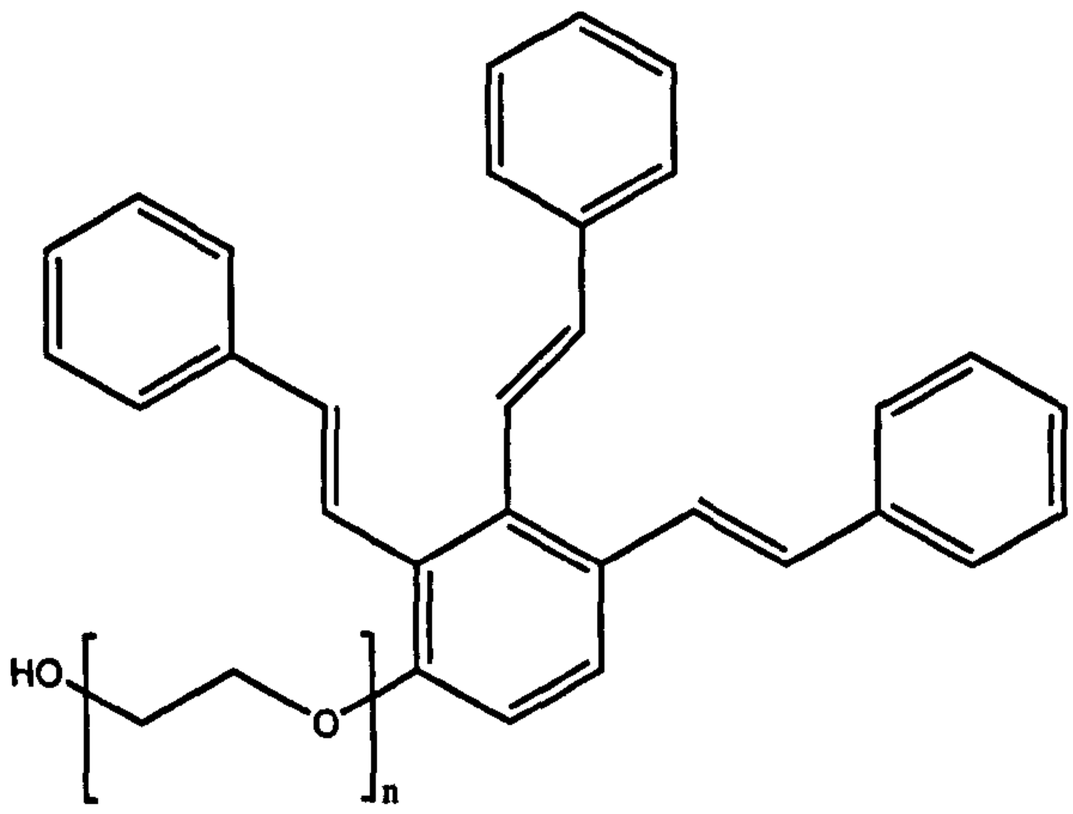

Figure 4.5: Structure of the surfactant tristyrylphenol ethoxylate.

To begin, an emulsion stock ($\phi = 0.6$) was prepared by combining the appropriate masses of ED, de-ionised water, surfactants and salt in a large container and mixing thoroughly. Whilst the aqueous solution was being stirred with an emulsion mixer, the PDMS oil was slowly added over a period of 3 hours. The mixture was left to cool at intervals throughout the mixing in order to prevent overheating and evaporation. A few drops of formaldehyde was added to prevent bacterial growth.

In order to simplify sample preparation, a total of four different stock solutions (including the emulsion stock detailed above) were prepared so that that dependant upon the sample parameters, appropriate masses of each stock could be added and mixed. The three other stock solutions comprised: a RI matched ED/H_2O solution,

a fixed concentration of xanthan (Kelco - used as supplied, without purification or heat treatment) dispersed in RI matched ED/H_2O solution, and a fixed concentration of Rhodamine B in RI matched ED/H_2O (0.09 gL^{-1}) solution. The addition of a water soluble dye enables the colloid rich phase to be differentiated from the index matched aqueous phase by eye.

4.3 Characterisation of the model system

The size and polydispersity of the PDMS drops were determined by Dynamic Light Scattering to be 316 ± 11nm, and 0.17 ± 0.07 respectively. The measurements were carried out using a Malvern 4800 autosizer, at 90 degrees with a wavelength of 532nm. The RI matched ED/H_2O solution had a viscosity of 5.47 mPa.s ± 0.009 mPa.s as determined by capillary viscometry, a refractive index of 1.399 and a density of 1.083 g cm^{-3} ± 0.005 g cm^{-3}. Density measurement were carried out using Gay-Lussac bottles which were first calibrated with de-ionised water using an average of three measurements. A further three measurements were taken for each solution and an average of the three was used to determine the final densities and errors. The density of PDMS oil was determined to be 0.939 g cm^{-3} ± 0.006 g cm^{-3} which differed from the figure quoted by the manufacturer of 0.933 g cm^{-3}. Throughout the course of the experiments the density of the PDMS was assumed to be the measured value of 0.939 g cm^{-3} ± 0.006 g. The densities of the Xanthan and Rhodamine B stocks were assumed to be equal to that of the pure ED/H_2O mix, given the negligible masses of Xanthan and Rhodamine in the stock solutions.

Xanthan

The weight averaged and number averaged molecular weights of xanthan were determined by GPC to be 4.66 x 10^6 and 3.4 x 10^6 respectively. The measurements were carried out by Rapra. However, determining r_g of xanthan is most crucial as this allows the phase behaviour of the colloid-polymer system to be mapped, and the range of attraction to be calculated. There have been several reported values for xanthan r_g in water. Light scattering measurements of Bhat et al give a measured

r_g of xanthan in water of 230nm and a resulting C* value of 0.130 gL^{-1} where it had a molecular weight of 4 x 10^6 g mol^{-1} [90]. r_g and C* values of 264nm and 0.0862 gL^{-1} respectively have been reported by Koenderink et al for xanthan in water [91].

There are no reported size measurements for xanthan in mixtures of water and ED and both experimental and theoretical routes were used in order to determine its radius in solution. To begin, the intrinsic viscosity of xanthan is calculated from viscosity measurements of solutions with varying polymer concentrations, in the RI matched H_2O / ED mixture. The specific viscosity (η_{sp}) of each xanthan solution is calculated from the efflux time of pure solvent (t_1) and the efflux time of the polymer solution (t_2) as follows:

$$\frac{t_1 - t_2}{t_2} = \eta_{sp} \tag{4.14}$$

the reduced viscosity, η_{red} of each solution is then calculated as:

$$\frac{\eta_{sp}}{C_p} = \eta_{red} \tag{4.15}$$

A plot of η_{red} V xanthan concentration yields a straight line plot where the y intercept is equal to the polymer intrinsic viscosity, and the slope of the plot is represented by:

$$d(\eta_{red})/d([C_p]) = K'[\eta]^2 \tag{4.16}$$

where K' is a Mark-Houwink constant [92, 93]. The molecular weight of xanthan can be calculated using two Mark-Houwink constants, K' and a, which are specific for every polymer-solvent combination and are related to the intrinsic viscosity as follows:

$$[\eta] = K'M^a \tag{4.17}$$

where M is the viscosity average molecular weight. The value of a depends upon the solvent. When a polymer is dispersed within a theta solvent, a is equal to 0.5, but a typical value for a good solvent is 0.8. The value of a increases above 0.8 if the polymer is semi−flexible, and for polymer rods the value of a can be as high as 2.0.

The statistics of the chain conformation of xanthan can be characterised by the Unperturbed Wormlike Chain theory where a freely rotating chain consists of N segments of length a, linked at an angle of ψ [94]. It is assumed that the chain is not perturbed by volume exclusion. The important parameters of the wormlike chain are the contour length L and the persistence length q. The mean-square end-to-end distance $<R^2>$ and the mean-square radius of gyration $\langle S^2 \rangle$ are represented by:

$$< R^2 >= 2q_pL - 2q_p^2(1 - \exp^{-L/q_p}) \tag{4.18}$$

$$< S^2 >= (q_pL/3) - q_p^2 + (2q_p^3/L)[1 - (q_p/L)(1 - \exp^{-L/q_p})] \tag{4.19}$$

The persistence length q_p is related to the Kuhn statistical segment length λ^{-1} where $q = (2\lambda)^{-1}$.

Xanthan is a polydisperse polymer in which there exists a distribution of the polymer contour length. This distribution has an effect on the the calculated radius of gyration of the polymer. The effect has been quantified by Schmidt [95]and results in an expression for the radius of gyration as follows:

$$< R_g^2 >= \frac{m_p + 2}{6y_p\lambda} - \frac{1}{4\lambda^2} + \frac{y_p}{4(m_p + 1)\lambda^3} - \frac{1}{8m_p(m_p + 1)\lambda^4}\left(y_p^2 - \frac{y_p^{m_p+2}}{(y_p + 2\lambda)^{m_p}}\right) \tag{4.20}$$

where $y_p = (m_p+1)/L$ and $m_p=1/(M_w/M_n-1)$.

Light scattering measurements of aqueous xanthan solutions performed by Coviello et al show that it can be modelled as a worm-like chain [96]. Their calculations give a Kuhn segment length (λ^{-1}) of 255nm, a diameter (d) of 2.2nm and a mass per unit contour length (M_L) of 1830 daltons nm^{-1} for a xanthan solution with salt concentration 100mM. Similar values in the high salt limit of $\lambda^{-1} = 212$nm, (d) = 2.2nm and $M_L = 1940$ nm^{-1} were calculated from intrinsic viscosity measurements by Sho et al [97] and when the salt concentration was decreased to 5mM they calculated an increased λ^{-1} of 240nm indicating a stiffer molecule.

The mass per unit contour length and the chain diameter are a function of the molecular structure and dictated by the backbone of the structure. It is therefore reasonable to assume that any change in these values is negligible as ED is added to the system. It is for this reason, and the fact that the calculations were performed using intrinsic viscosity measurements that the M_L value of 1940 nm^{-1} and the diameter value of 2.2nm as determined by Sho et al [97]are used to calculate the radius of gyration of xanthan in ED/H_2O. Using the measured molecular weight of $M_n = 3.44 \times 10^6$ and a measured intrinsic viscosity of xanthan in water of $[\eta] = 5040$ g cm^{-3}, the Kuhn segment length was calculated to be $\lambda^{-1} = 233$nm. This calculated value of λ^{-1} is in excellent agreement with the figure of 240 nm reported by Sho et al [97]. The same values of molecular weight, diameter, and unit contour length were used to calculate the Kuhn segment length of Xanthan in ED/H_2O with a measured intrinsic viscosity of $[\eta] = 2320$ g cm^{-3}, the Kuhn segment length in ED/H_2O was calculated to be $\lambda^{-1} = 98$nm. This gives a resulting calculation for the radius of gyration of $r_g = 185$nm. From $\lambda^{-1} = 98$nm, a polydisperse hydrodynamic radius of $r_h = 87$nm is calculated.

Dynamic light scattering measurements were carried out on dilute suspensions of xanthan in ED/H_2O in order to confirm the calculated value for the hydrodynamic radius. The diffusion coefficient D, is calculated at a number of angles for a fixed concentration of xanthan using Stokes-Einstein equation:

$$D = \frac{k_B T}{6\pi\eta r_h} \tag{4.21}$$

where k_B is Boltzmann's constant, T is the absolute temperature, η is the viscosity and r_h is the hydrodynamic radius. A total of five different polymer concentrations were measured, each at five different scattering angles and the results of which are shown in figure 4.6.

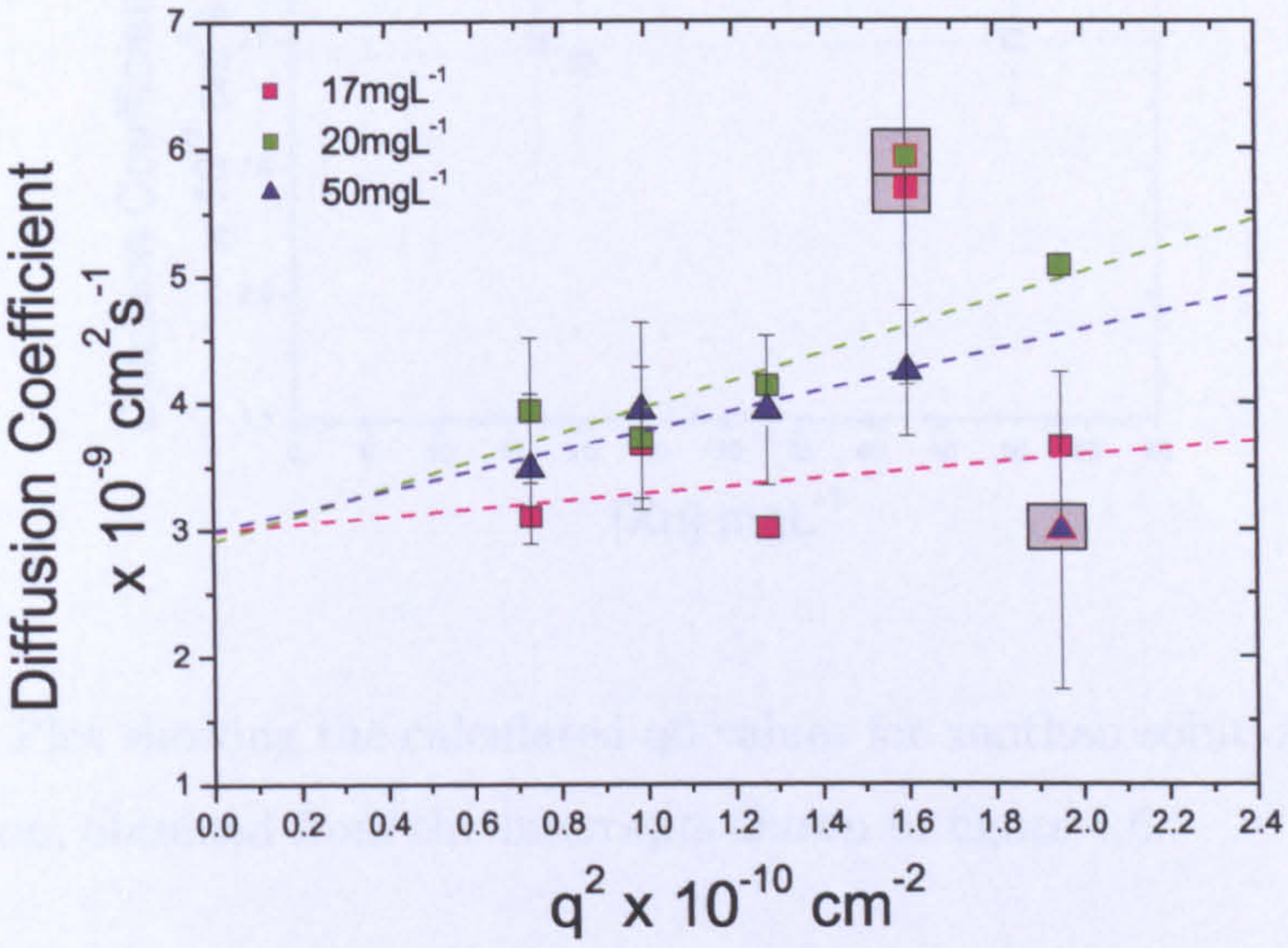

Figure 4.6: Plot showing the calculated Diffusion constant at different scattering angles for xanthan solutions of varying concentration. The gray squares indicate data points which were excluded when calculating a linear fit at each polymer concentration.

It is clear from looking at figure 3.6 that this experimental method has not been able to produce a reliable value for q=0 at each concentration. This is due to the fact that xanthan aggregates causing measurement difficulties. In order to attempt to retrieve some data from these measurements the data points shown encased in grey squares have been excluded when adding a straight line fit. The two data sets

at 35 mgL^{-1} and 65 mgL^{-1} have been completely excluded from the calculations. The q=0 value for each of the remaining three data sets, which is equal to the Y intercept, was obtained and plotted as a function of polymer concentration. A straight line was fitted to the three data points (see figure 4.7) and the translational diffusion coefficient at zero concentration, D_0 which is the intercept of the line, was found to be $2.93 \pm 0.075 \times 10^{-9}$ cm^2s^{-1}.

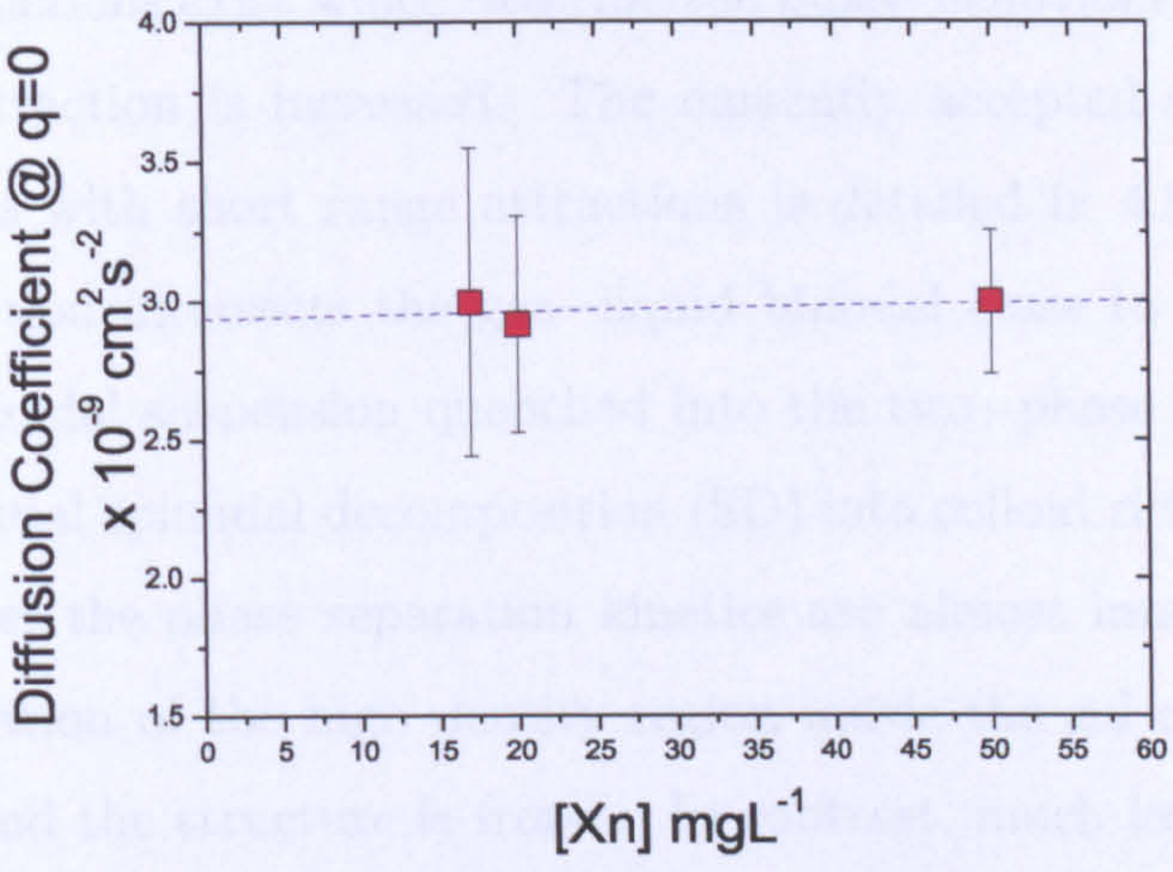

Figure 4.7: Plot showing the calculated q0 values for xanthan solutions of varying concentration, obtained from the intercepts shown in figure 4.6.

Taking the calculated value of D_0, the hydrodynamic radius of xanthan is calculated to be 138 ± 4 nm from equation 4.22.

$$r_h = \frac{k_B T}{6\pi\eta D_0} \tag{4.22}$$

In order to move from a value of r_h to r_g a ratio of $r_g / r_h = 2.17$ is used [96]. This value was reported by Coviello et al who produced a static Zimm plot to determine r_g of native xanthan and a dynamic Zimm plot to determine r_h of native xanthan. The measured r_g is therefore 299 ± 8 nm, which is 50% higher than the calculated value. The measured value for r_h of 138 ± 4 nm is about 60 percent higher than the calculated value of 87nm. This is partly due to the experimental

difficulties encountered whilst attempting to perform the measurements. A similar discrepancy has also been reported by Coviello et al [96] and so it is assumed that the experimental value for r_h is acceptable, although the calculated value of 87 nm shall be taken as the actual value in all future calculations.

4.4 Phase Behaviour of the model system

Theoretical predictions exist which describe the phase behaviour of systems as the range of the attraction is increased. The currently accepted state diagram for colloidal systems with short range attractions is detailed in 4.8(a). The attractive glass transition intersects the gas–liquid binodal close to the critical point (circled). A colloidal suspension quenched into the two–phase gas–liquid region undergoes an initial spinodal decomposition (SD) into colloid rich and colloid poor regions. However the phase separation kinetics are almost immediately arrested as the concentration of the high density region inside the gel crosses the attractive glass line and the structure is frozen. In contrast, much less is known about gelation with long range attractions. Theoretical work suggests that increasing the range of the attraction has a number of effects on the phase behaviour, which are sketched schematically in figure 4.8(b): first, the region of gas-liquid separation, which is metastable at small ξ, should increase in stability relative to the glass line, and second the gas-liquid boundary should become more sharply curved. Thus at large ξ one imagines there should be a range of compositions (hashed in 4.8(b)) at which spinodal decomposition will progress to full phase separation without being arrested, presumably without gelation. Still deeper quenches could generate kinetic arrest. Experimental studies on systems with long range attractions also suggest that phase separation can occur without becoming dynamically arrested. A system of colloidal silica spheres and poly(dimethylsiloxane) with a size ratio $\approx$ 1 was studied by Verhaegh et al [98], who observed a fluid-fluid phase separation progressing via spinodal decomposition without any dynamic arrest.

In an ideal system the depletion polymer would be monodisperse but this is rarely

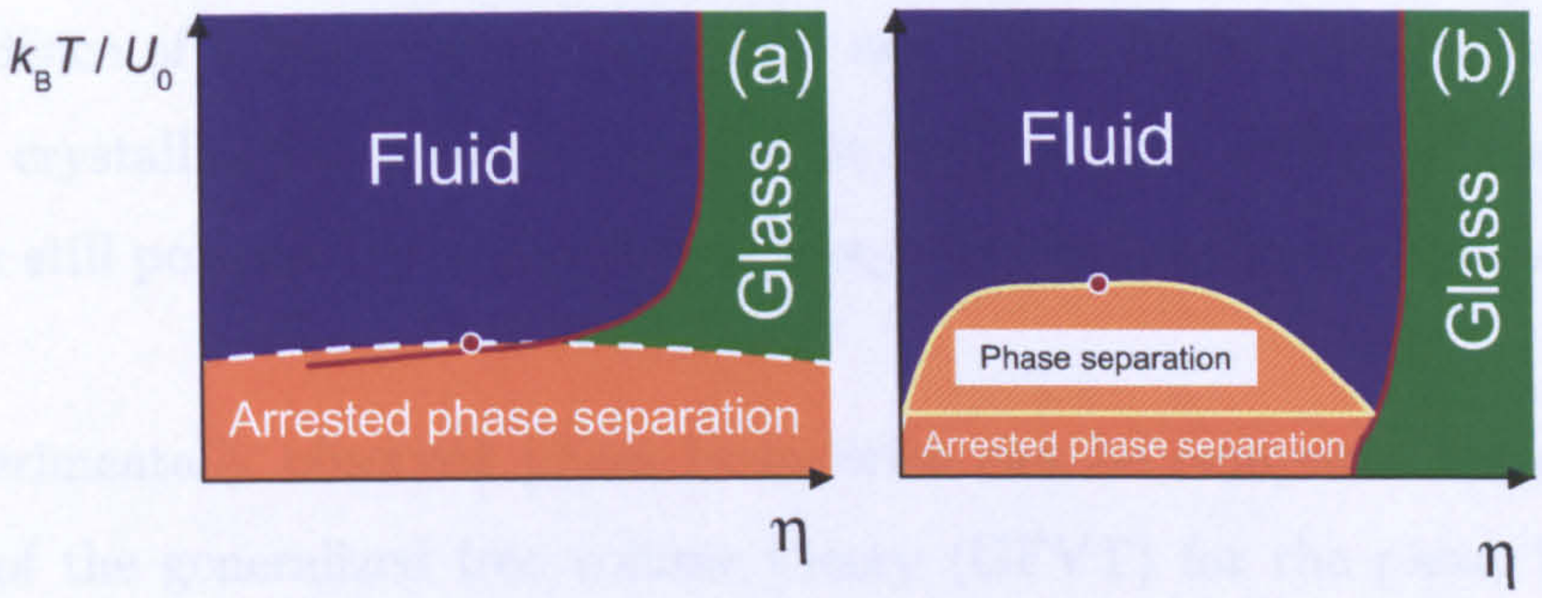

Figure 4.8: Schematic diagram which illustrates the effect of increasing the range of the attractive interactions upon the relative positions of the liquid-gas coexistence line and the glass line in a system of hard spheres of radius a with a square well attraction of width ξ and depth U_0. In (a), where the attraction is short-ranged, the glass line intersects the binodal just below the critical temperature while (b) illustrates the case for a long-ranged attraction.

ever the case for technological polymers. The concentration and size of the depletion polymer set the strength and the range of the depletion attraction respectively. When the depletion polymer has a significant size distribution, there are likely to be polymer chains which are larger than the mean polymer size. This will have the effect of simultaneously increasing the attractive range and decreasing the strength of the attraction. Recently it has been shown that the polydispersity of the depletion polymer in a colloid-polymer mixture will effect the phase separation and gelation [20]. However, this size dependence is not applicable in the semi-dilute regime where polymers overlap and so will have no effect on the determined phase diagram.

In order to confirm that the prepared samples lie within the unstable region of the phase diagram, the stability of a range of colloid-polymer mixtures was investigated, using the confocal microscope. The range of the attraction is $\xi = 0.62$ and the resulting phase diagram is shown in figure 4.9. A stable one phase fluid (circles) is found for samples with low polymer concentrations. As the polymer concentration is increased a gas−liquid (GL) phase separation is observed (crosses). There

is no evidence of a gas–crystal (GC) line, nor a gas–liquid–crystal coexistence region as crystallisation is suppressed due to the size distribution of the colloids. At higher still polymer concentrations non-equilibrium gelation is observed.

The experimentally observed phase boundaries can be compared with the predictions of the generalized free volume theory (GFVT) for the phase behaviour of hard-sphere colloids and non-adsorbing excluded-volume polymer chains [11]. Comparison with experimental and simulation data have revealed GFVT provides a near quantitative description of the colloid-polymer phase diagram for $\xi = 1$ [99]. The GFVT predictions for the phase boundaries at the experimentally measured size ratio $\xi = 0.62$ in a good solvent are shown by the solid lines in figure 4.9. The agreement between the calculated GL binodal and experiments is good, with the vast majority of the experimental two-phase samples lying above the GFVT binodal, confirming that the experimental system may be accurately approximated by a simple mixture of hard spheres and non-adsorbing polymer chains.

A number of different samples at fixed ϕ and varying C_p have been prepared throughout this research. From equations 1.21 and 1.22 the depletion potential at contact in units of k_BT is calculated to be in the range 5.24 for the lowest C_p and 9.64 for the highest C_p as detailed in table 4.1. It is generally accepted that values of less than ≈ 10 can be considered as weakly attractive systems. Throughout this thesis samples are referred to by the concentration of polymer in the total aqueous phase rather than the free volume concentration, so that samples with 0.533, 0.586, 0.638, 0.742, 0.846, 0.951 and 1.055 gL^{-1} xanthan in the free volume are referred to as 0.5, 0.55, 0.6, 0.7, 0.8, 0.9, and 1.0 gL^{-1} respectively.

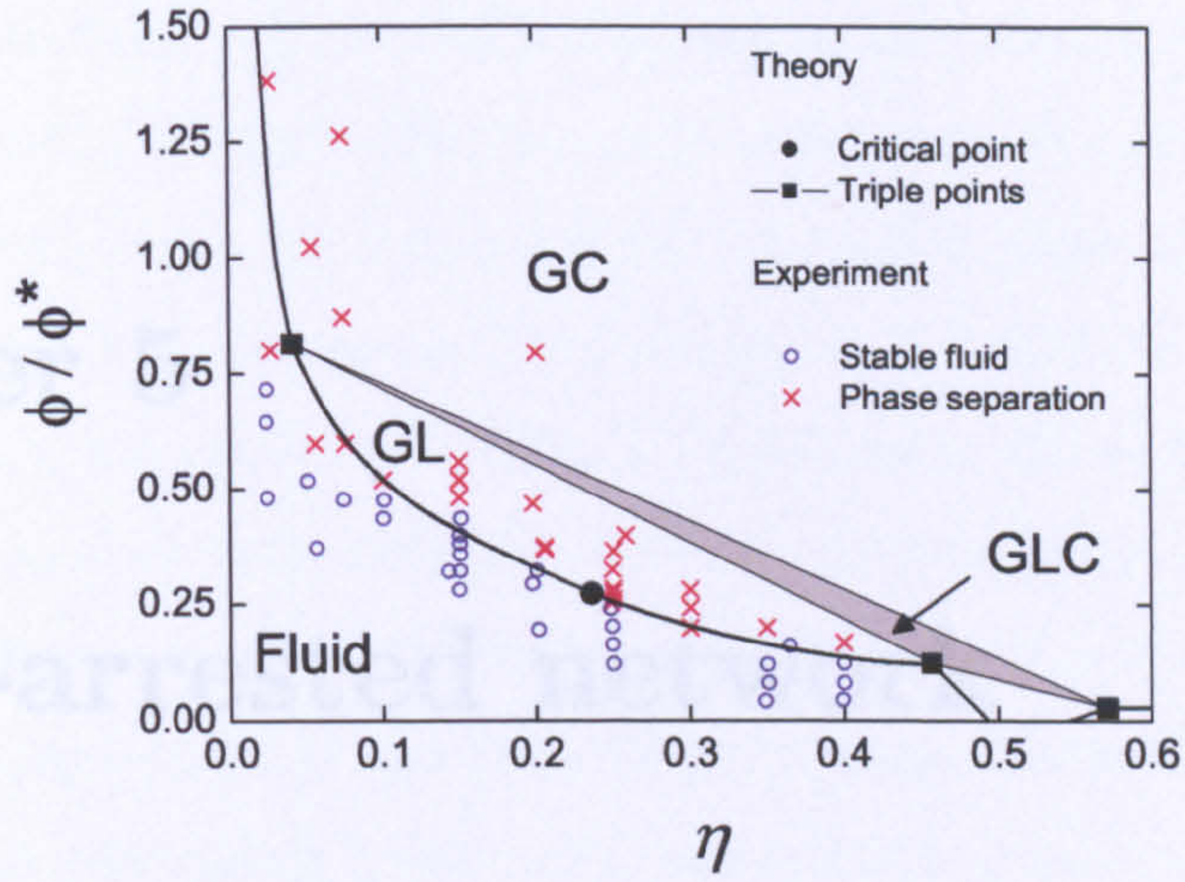

Figure 4.9: Phase diagram of the colloid−polymer mixture where $\xi = r_g / a = 0.62$. Experimental observations are indicated by the open crosses and circles. The solid curve represents the fluid−crystal, gas−liquid and gas−crystal binodals as calculated from GFVT for $\xi = 0.62$. The theoretical prediction for the critical point is shown by the filled circle while the filled squares indicate the compositions of the coexisting gas, liquid and crystal phases in the triple point triangle.

Table 4.1: Details of colloid-polymer mixtures studied. The table shows the concentration of polymer in the free volume (C_p /gL^{-1}), the reduced polymer concentration C_p /C_p * and the depletion potential at contact in units of ($-U_0/k_BT$) as calculated from equation 1.22.

C_p /gL^{-1}	C_p /C_p *	$-U_0/k_BT$
0.533	2.05	5.242
0.586	2.26	5.695
0.638	2.46	6.144
0.742	2.87	7.033
0.846	3.29	7.911
0.951	3.70	8.782
1.055	4.11	9.646

Chapter 5

A non-arrested network

5.1 Introduction

The phase separation of colloidal systems with short range attractions has been well documented in recent years. Colloidal suspensions with short range attractions display a variety of dynamically arrested states such as repulsive and attractive glasses [100], gels [101] and disconnected glassy clusters [102]. The phase separation is controlled by two key parameters, which are the strength of the depletion attraction, U, and the colloidal volume fraction ϕ. In the low ϕ limit where the strength of attraction is extremely high irreversible 'bonds' or attractions are formed between colloids which leads to diffusion limited cluster aggregation and irreversible fractal gels. In the opposite extreme where U is low, as ϕ is increased the local colloidal density continues to increase until the colloids become arrested in a glassy state. These two extremes are well understood, but it is the colloidal systems which lie between the two extremes which are more difficult to characterise since there are several parameters which have been shown to affect the phase separation behaviour, such as the range of the depletion attraction where more compact clusters are formed in the presence of a long range attraction, and in the presence of a short range attraction the clusters formed are more branched and fractal like [103].

There is a wealth of information available regarding the phase behaviour of colloidal systems with short range attractions, however, systems with long range attractions

have not been as thoroughly characterised despite their industrial importance. Here an oil-in-water emulsion system with a polymer-colloid size ratio of 0.62 is studied using Laser Scanning Confocal Microscopy, in order to probe the phase separation behaviour of a long range attractive system. The initial phase separation and the evolution of the resulting gel network is followed from t_0, and 2D Fourier Transforms of the micrographs are calculated and used to determine the characteristic domain radius as a function of both time and polymer concentration. It is conclusively shown that phase separation occurs via a mechanism that is reminiscent of classical spinodal decomposition as in the case of short range attractions, and that the characteristic domain radius grows with time until a critical length is reached. Beyond this critical length, the domain radius grows in a more accelerated and erratic manner. Critically, the domain radius growth never plateaus confirming that the system never experiences a period of dynamic arrest, contrary to the observations of short range attractive systems [101, 104–106].

5.2 Microscopic analysis of the gel network

To begin to probe the structure and ageing of the transient network a microscopic analysis is fundamental. The phase separation of a colloidal emulsion system is able to be observed with the use of Laser Scanning Confocal Microscopy. The aqueous continuous phase is labelled with the fluorescent dye Rhodamine-B so that the colloids appear as dark voids in the micrographs. Preliminary tests on the Rhodamine B dye confirm that there is little photobleaching within the time frame of the experiments, and that it can be excited using a 543 nm wavelength He-Ne laser. The mean particle diameter is almost at the detection limit of the microscope so that due to size polydispersity, not all individual particles are sufficiently large to be observed. Aggregates can be readily observed and thus samples are prepared which lie well within the gelation boundary. Network formation begins immediately upon cessation of homogenisation.

Samples are prepared by mixing together the requisite masses of colloid and poly-

mer stock dispersions with a solution of the fluorescent dye rhodamine-B, before finally diluting with the ED/H_2O solution. The samples had a fixed volume fraction of colloids of $\phi = 0.2$, a salt concentration of 3 mM L^{-1}, and a rhodamine-B concentration of 0.02 gL^{-1} in the continuous phase.

To minimise sample age it is essential that imaging is commenced as soon as possible after homogenisation. There are steps which can be taken in order to achieve this, one of which is to use predetermined settings for the amplitude offset and gain, based on the optimum settings used when imaging previous samples. Another step is to ensure that laser scanning is commenced prior to the sample being added to the confocal cell, with the sample cell already fixed in the correct position on the microscope stage. As a result, the first micrograph obtained is blank since the sample has yet to be added to the cell, and the second image is of the sample which has very recently been added to the cell, ultimately allowing imaging to commence within 5 seconds of the end of homogenisation. This method has the disadvantage that the quality of each micrograph is slightly reduced as software parameters cannot be optimised for each specific sample. Once mixed the sample is added to the confocal cell to a total height of 5mm, the height of which has been previously marked on the cell. Each scan was programmed to take 3 seconds at a resolution of 1024 x 1024 pixels, and a new scan was started every 5 seconds.

5.3 Phase Separation

Dynamic arrest occurs when the local colloid density in a colloidal system crosses the glass transition boundary, and colloidal particles are restricted to their position within a fixed cage of neighbours. The colloids still retain a certain degree of freedom and are able to exchange positions with neighbouring colloids even though there may not be any noticeable changes in the network structure. An arrested network can occur due to either a localized increase in the colloidal volume fraction, an increase in $-U_0/k_BT$, or both. An arrested system is evident by the zero

growth rate of the characteristic domain radius. The time in which it takes a colloidal system to form a gel network and become dynamically arrested will vary depending upon parameters such as particle size and C_p . Lu et al, for instance, report arrest occurring at t $\approx$ 10,000 seconds in a system with low colloid volume fraction ($\phi = 0.045$) and a polymer concentration of 3.31 gL^{-1} in a short ranged attractive system [101]. Network arrest can occur over large timescales and so when determining the point of arrest a suitably large time frame must be examined.

5.3.1 Microscopic analysis of early stage of network ageing

To pinpoint the onset of dynamic arrest three samples were prepared with 0.6, 0.7 and 1.0 gL^{-1} of depletion polymer (xanthan) and micrographs were obtained at very early times, with the first being at $t \approx 5$ seconds. A selection of the micrographs is shown in figure 5.1, with the first micrograph being obtained at a sample age of 5 seconds and the second being obtained at a sample age of 120 seconds. The micrographs obtained show that at a sample age of 5 seconds a network is already formed with the thickness of the network chains being of order 1 particle diameter. The networks are extremely fine and homogenous throughout the full image, with a pattern reminiscent of spinodal decomposition. At a sample age of 120 seconds each sample shows a network which has noticeably coarsened, although this is most clear in sample A, C_p 0.6 gL^{-1} xanthan. As C_p is increased the degree of coarsening decreases where network strands are finer, a direct result of higher polymer concentrations resulting in stronger depletion effects.

The static structure factor S(q) is determined from each micrograph obtained. A feature of spinodal decomposition is the development of a peak in the structure factor at a finite scattering vector q_{max} , where q_{max} is inversely proportional to the characteristic domain size. As spinodal decomposition progresses q_{max} narrows and moves to smaller q indicating a growing domain size, and the structure factor $S(q_{max}, t)$ increases. The calculated values of the domain radius, R_c as a function of time is shown in figure 5.2. The logarithm of the integrated q_{max} peak intensity

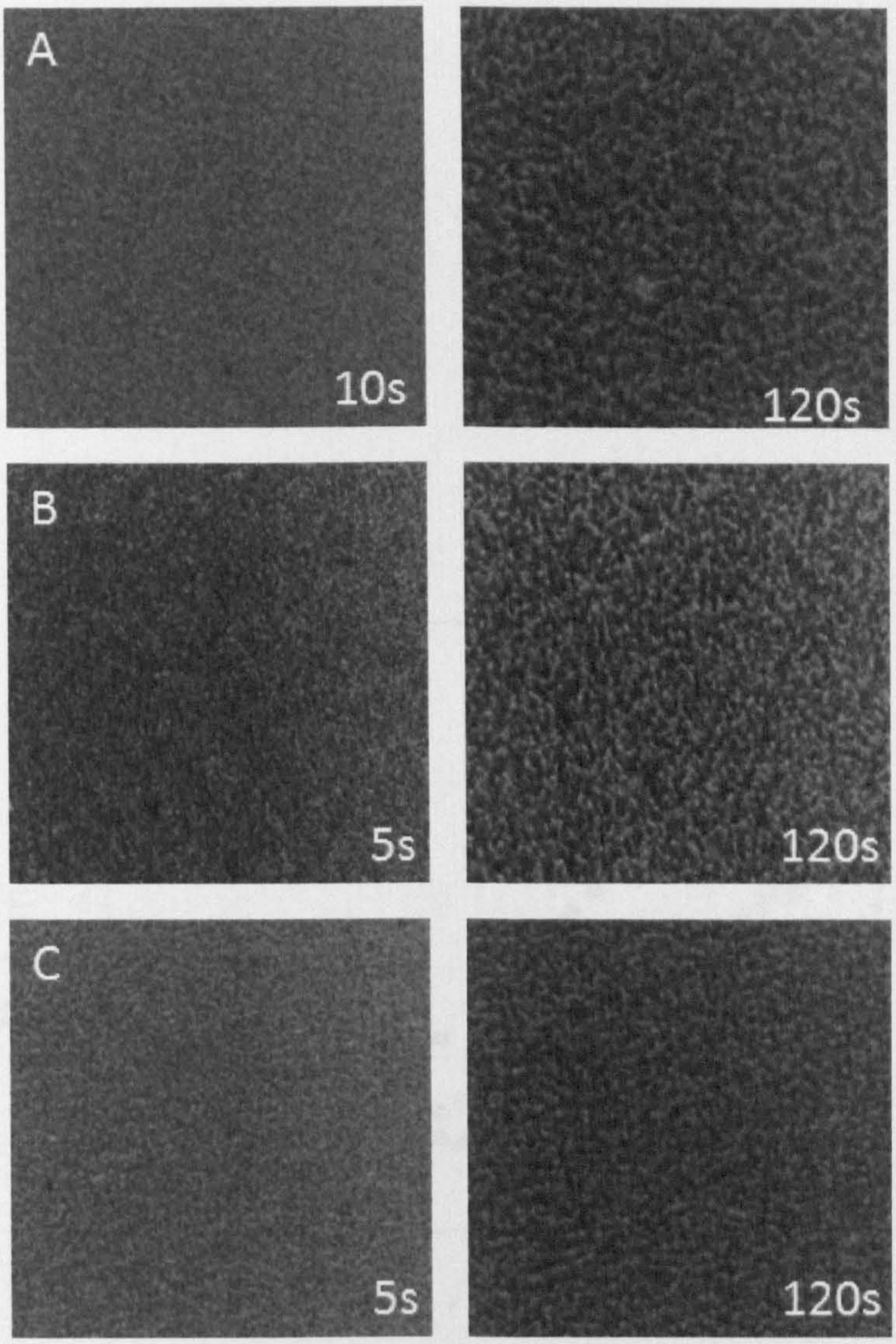

Figure 5.1: Confocal micrographs obtained during the very early stages of phase separation at a height of 2mm from the base of samples with initial height of 5mm. A = 0.6 gL^{-1} , B = 0.7gL^{-1} , and C = 1.0gL^{-1} . The images on the left were obtained after 5s and show an extremely fine and homogenous network already present in each sample. The images on the right were obtained after 120s and show coarsening over this time interval, with the samples with lower polymer concentration coarsening to a higher degree. Each micrograph has dimensions of 146 x 146 μm.

is also shown in figure 5.3 and is a clear indication that the phase separation occurs

via a spinodal-like decomposition route.

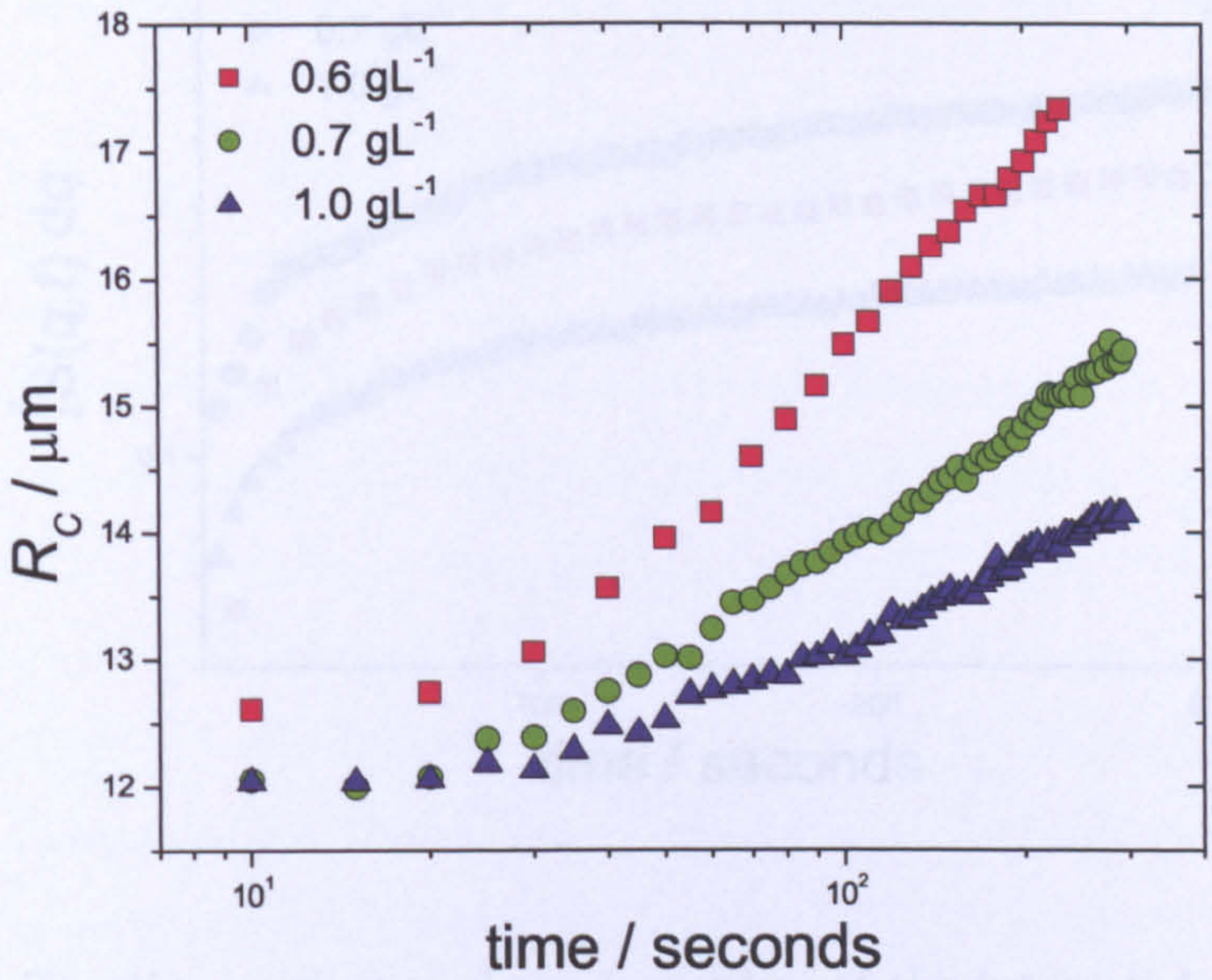

Figure 5.2: Plot of the characteristic domain radius of samples with 0.6 gL^{-1} (red squares), 0.7 gL^{-1} (green circles) and 1.0 gL^{-1} (blue triangles) xanthan at early times. The samples had initial heights of 5mm and images were obtained 2mm from the base of the sample. There is no growth of the characteristic domain radius observed prior to t $\approx$ 20 seconds at each polymer concentration.

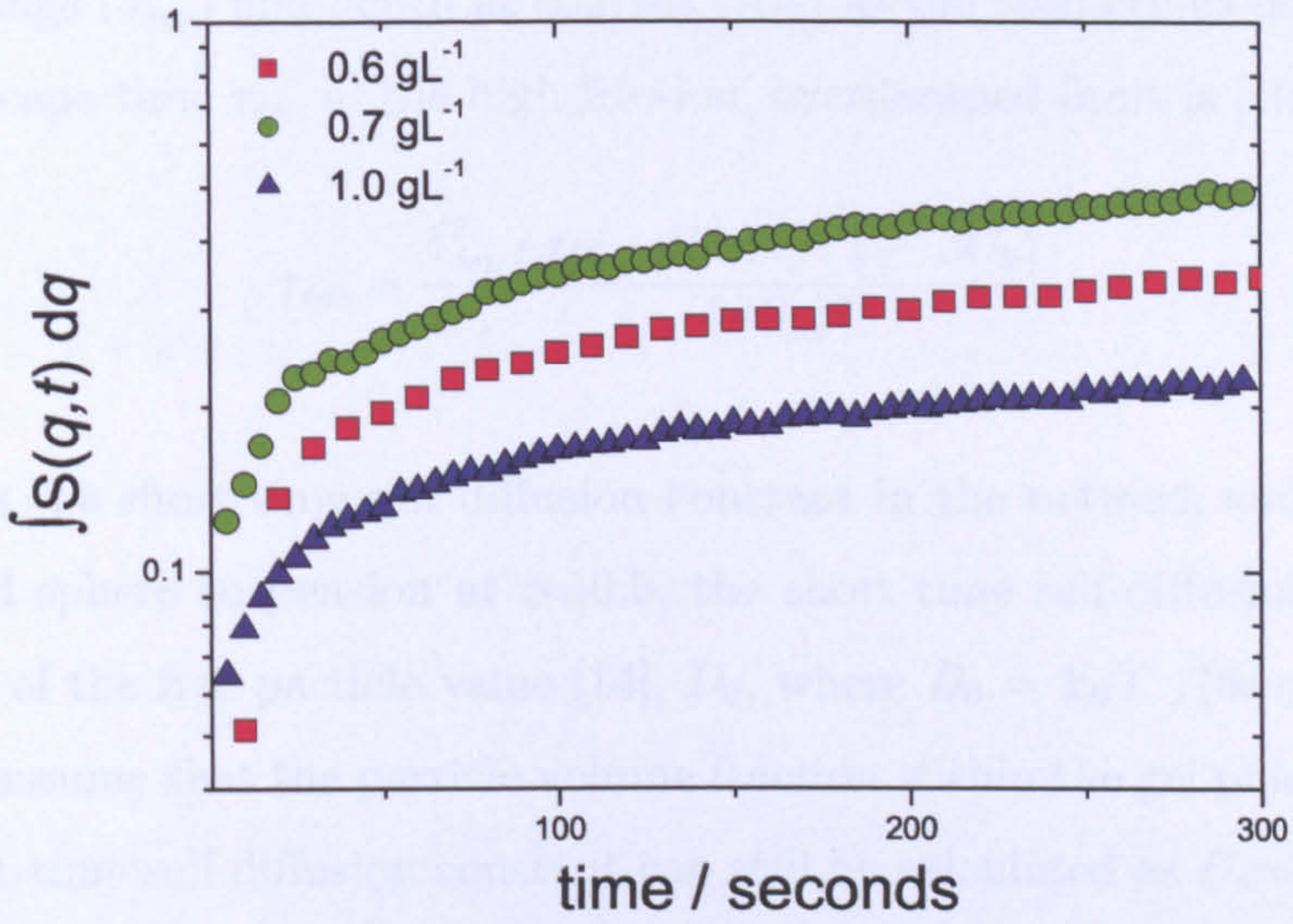

Figure 5.3: The time evolution of the logarithm of the integrated peak intensity I(t)of samples with 0.6 (red squares), 0.7 (green circles) and 1.0 (blue triangles) gL^{-1} Xanthan at early times. The samples had initial heights of 5mm and images were obtained 2mm from the base of the sample. The overall magnitudes for each data set are affected by the detector gain settings

The bond lifetime

The time in which a particle remains in a fixed position surrounded by the same nearest neighbours until it moves to a different position is referred to as the bond lifetime,τ_{esc}, and is determined by the depletion potential at contact. τ_{esc} dictates both the onset of network coarsening and the rate at which it occurs. In order to calculate τ_{esc} for each sample, it is assumed that it equals the mean-first passage Kramers escape time for a Brownian particle confined by a ramp potential with the same range (δ_{dep}) and depth at contact ($-U_0$) as the predictions of GFVT. The Kramers escape time τ_{esc} in the high friction, overdamped limit is [107]:

$$\tau_{esc} = \frac{\delta_{dep}^2}{D_s} \frac{exp(-\beta U_0) - (1 - \beta U_0)}{(\beta U_0)^2} \tag{5.1}$$

where D_s is the short-time self diffusion constant in the network and $\beta = 1/k_BT$. In a hard sphere suspension at ϕ=0.5, the short-time self-diffusion constant is about 20% of the free particle value [14], D_0, where $D_0 = k_BT\ /(6\pi\eta a)$. It is reasonable to assume that the particle volume fraction within the gel phase is 0.5, and so the short-time self diffusion constant can still be calculated as D_s=0.2D_0. Using the GFVT predictions the bond lifetime varies from 5 s for a sample with $C_p = 0.6$ gL^{-1} xanthan $\approx$ 40 seconds for the sample with 1.0 gL^{-1} xanthan.

The calculations of τ_{esc} for each sample indicate that coarsening begins between sample ages of 5 seconds and 40 seconds depending upon C_p , and from figure 5.2 it is clear that coarsening commences on a timescale comparable to that of the calculated τ_{esc} values.

5.3.2 Microscopic analysis of intermediate stage of network ageing

A study of the early stage of phase separation revealed that there is no network arrest and that the network is continually ageing. It is possible that the network may become arrested at much later times, and so the intermediate stage of ageing is

studied for evidence of spinodal decomposition ceasing due to arrest of the network. A range of samples was prepared with $\phi = 0.2$, and C_p at 0.5, 0.55, 0.6, 0.7, 0.8, and 1.0 gL^{-1} xanthan and LSCM micrographs were obtained at set time intervals for each sample. Each micrograph was then used to calculate the R_c at each time interval as a function of C_p . A selection of the micrographs obtained can be seen in figures 5.4 to 5.9 and a plot of the corresponding growth of R_c as a function of time is shown in figure 5.11(see following section for further discussion).

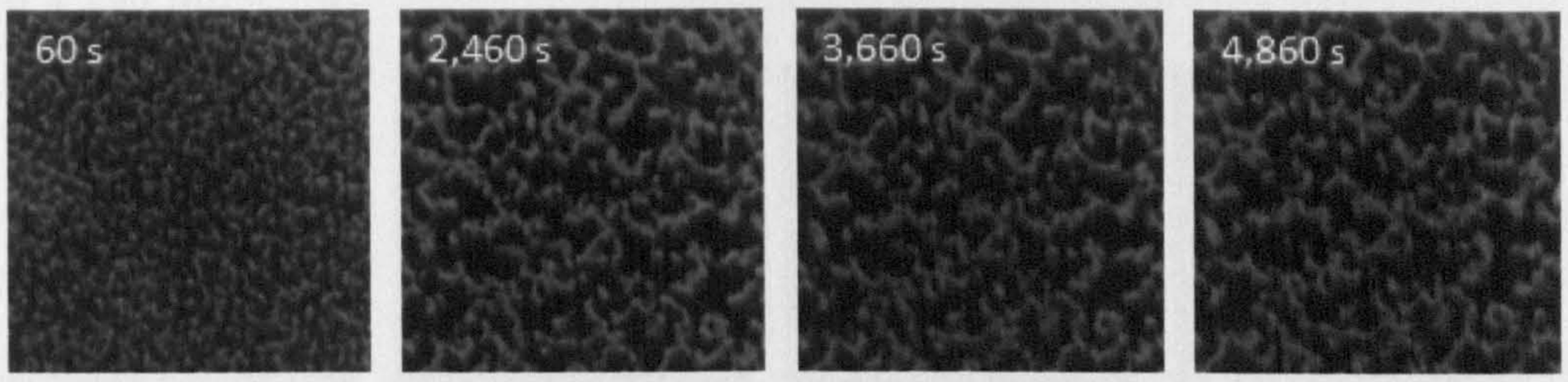

Figure 5.4: Confocal micrographs taken during the delay time of a sample with 0.5 gL^{-1} xanthan and an initial height of 5mm. Each micrograph has dimensions of 146 x 146 μm

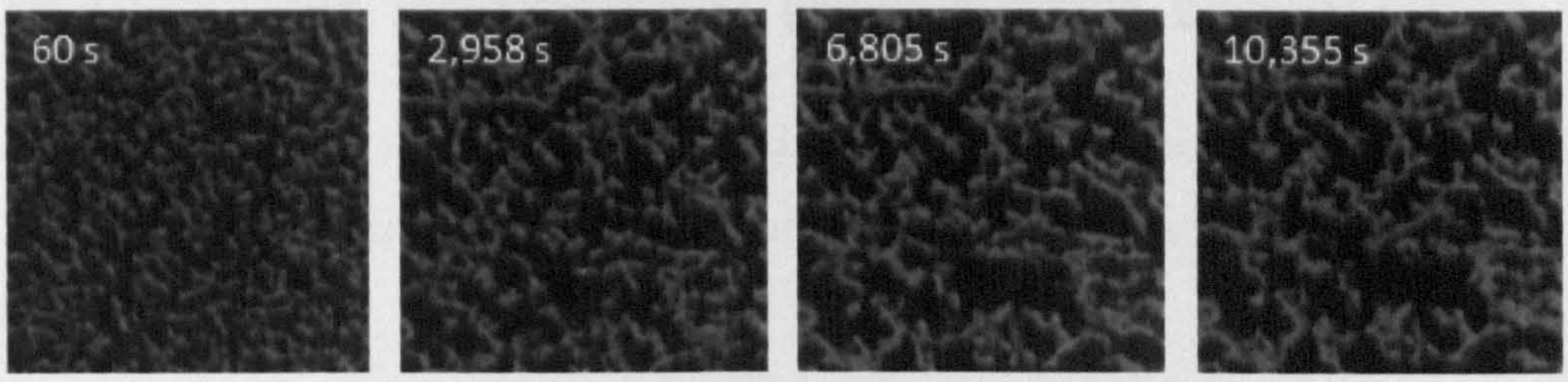

Figure 5.5: Confocal micrographs taken during the delay time of a sample with 0.55 gL^{-1} xanthan and an initial height of 5mm. Each micrograph has dimensions of 146 x 146 μm

The images shown in figures 5.4 to 5.9 were selected at random from micrographs obtained during the initial power law growth regime of each sample. Each set of images shows a network that is steadily and homogeneously coarsening with time. The effects of increasing C_p are obvious from the images with coarsening occurring at slower rates with increasing C_p . This is even clearer from examining the domain radius growth for each sample. Figure 5.10 shows that R_c increases continuously in

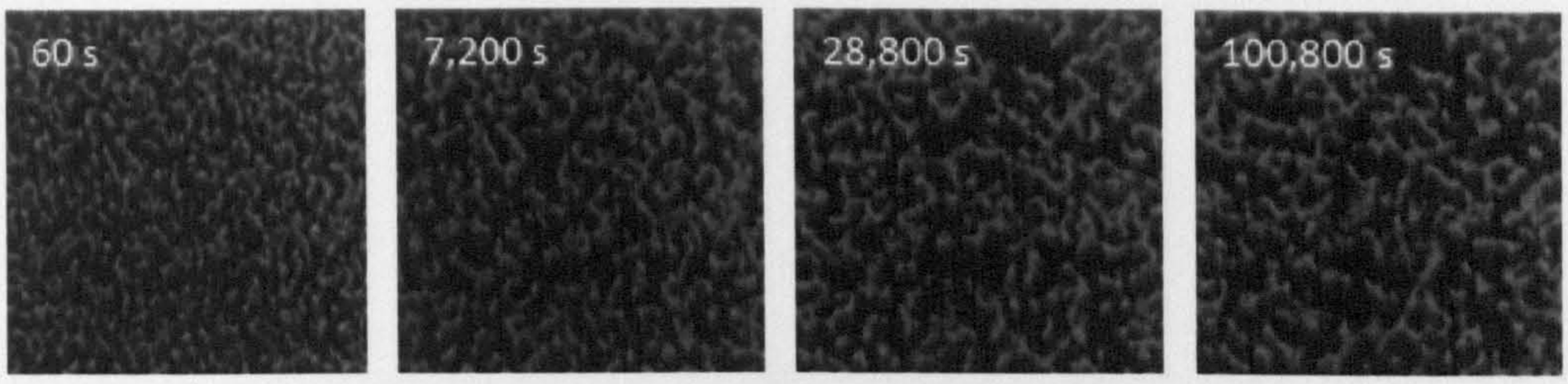

Figure 5.6: Confocal micrographs taken during the delay time of a sample with 0.6 gL^{-1} xanthan and an initial height of 5mm. Each micrograph has dimensions of 146 x 146 μm

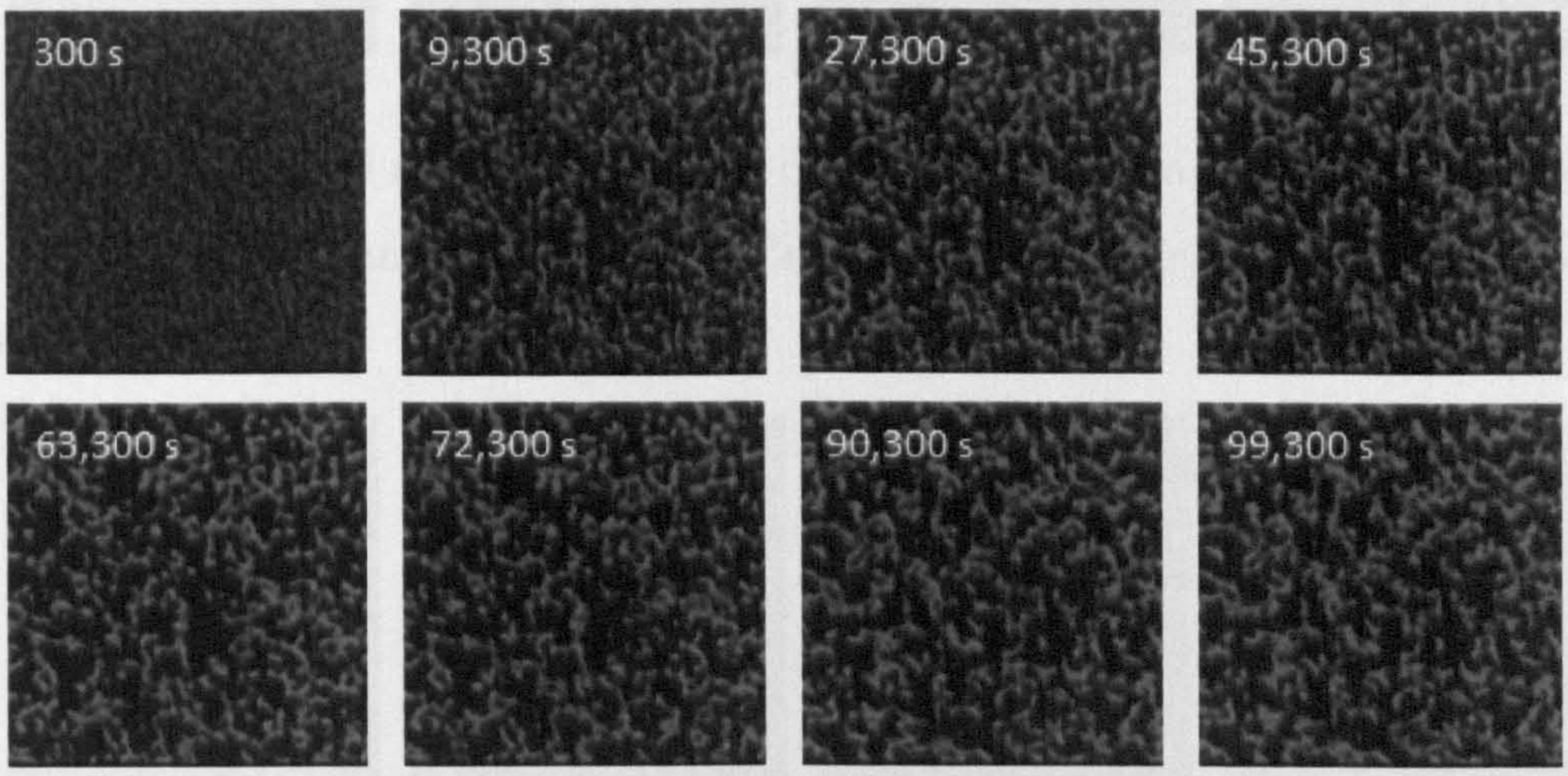

Figure 5.7: Confocal micrographs taken during the delay time of a sample with 0.7 gL^{-1} xanthan and an initial height of 5mm. Each micrograph has dimensions of 146 x 146 μm

time according to the approximate power law $R \sim t^{\alpha}$, where α is a strong function of quench depth.

The growth of R_c shown in figure 5.10 reveals that there is no apparent dynamic arrest, which would be evident by a zero growth rate of R_c . It appears the samples investigated here do not go through the usual route of an arrested gel state. One explanation for this is that the long range of the attraction prevents the formation of a truly high density phase. The colloids do not become jammed and the network is prevented from becoming arrested. At first glance the findings of Lu

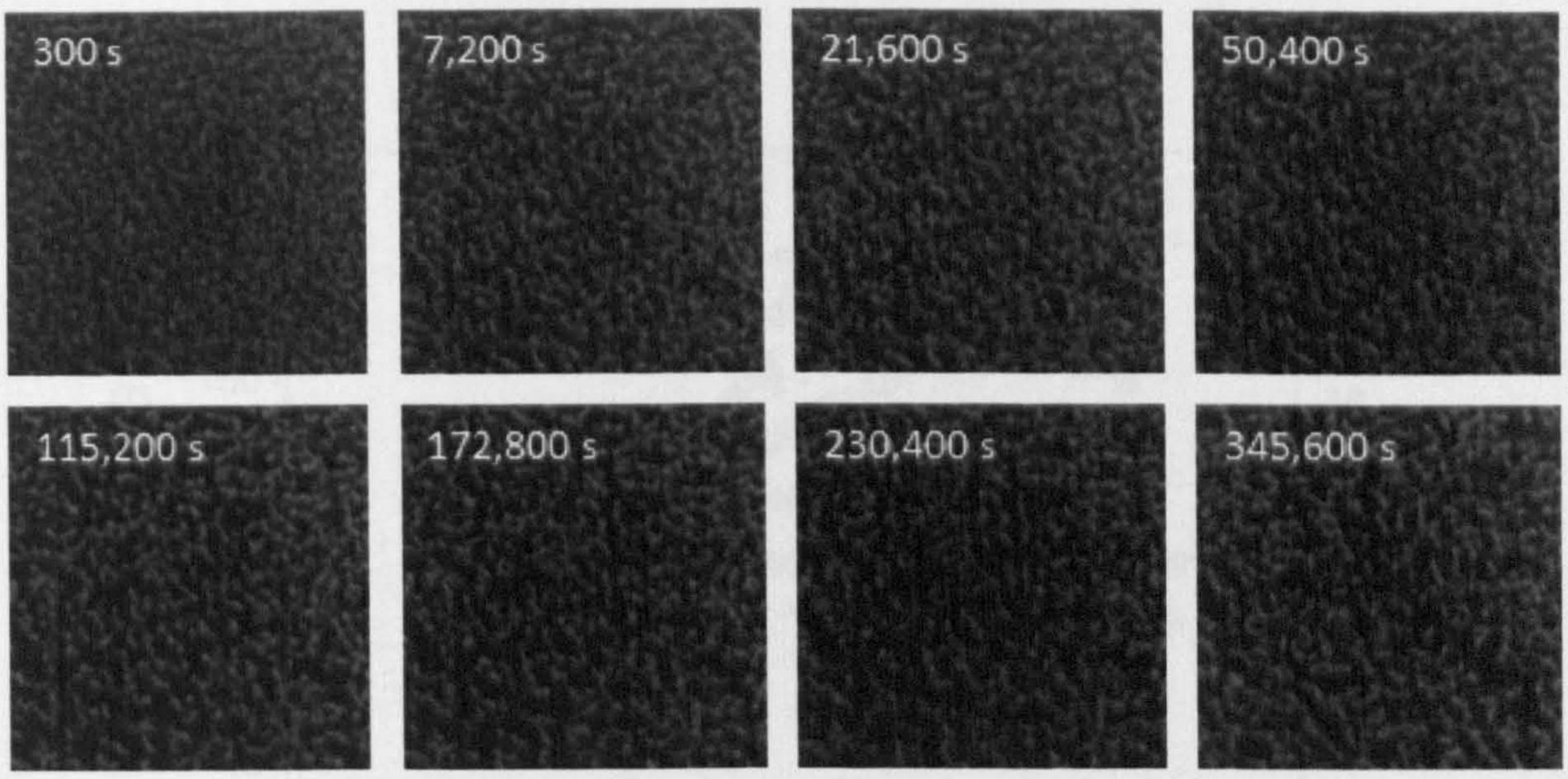

Figure 5.8: Confocal micrographs taken during the delay time of a sample with 0.8 gL^{-1} xanthan and an initial height of 5mm. Each micrograph has dimensions of 146 x 146 μm

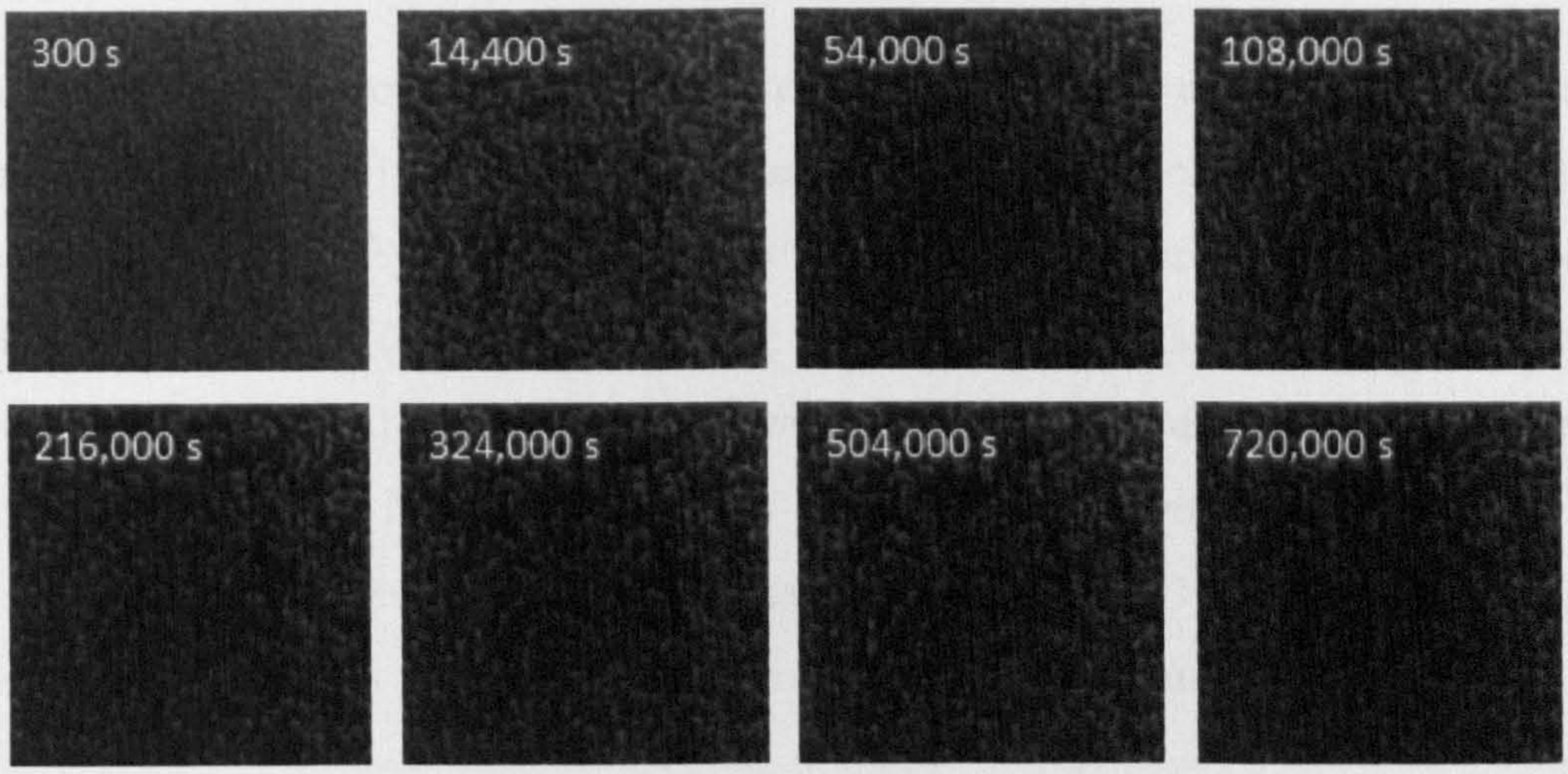

Figure 5.9: Confocal micrographs taken during the delay time of a sample with 1.0 gL^{-1} xanthan and an initial height of 5mm. Each micrograph has dimensions of 146 x 146 μm

et al [103] would seem to contradict this idea. Experiments were performed using PMMA colloidal systems where depletion attractions were induced by the addition of polystyrene. They reported that in case where the range of the attraction was long, that the colloidal clusters observed were denser than those produced by

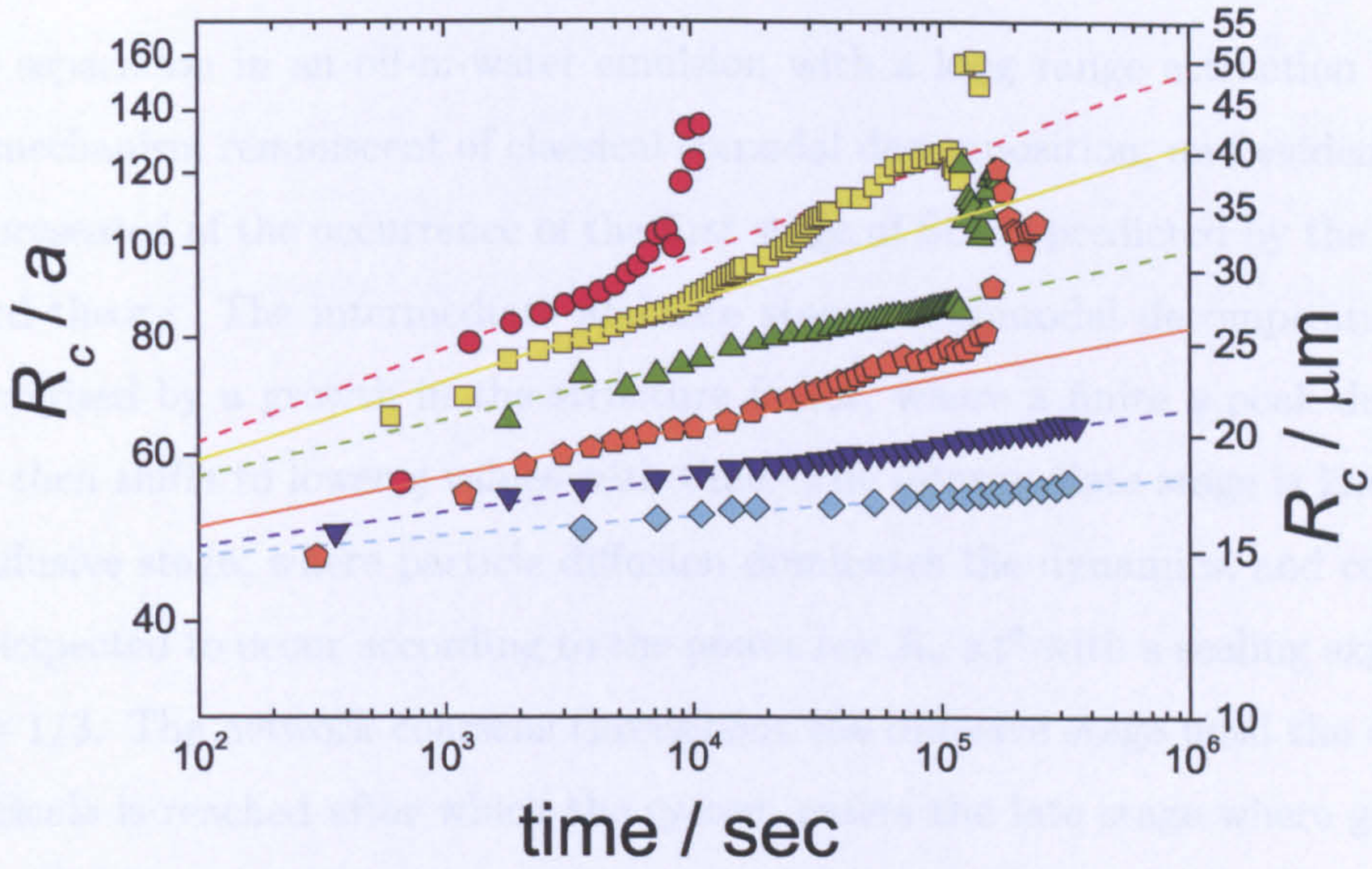

Figure 5.10: The growth of the characteristic domain size as a function of time for samples with an initial height of 5mm and a range of polymer concentrations as follows: 0.5 gL^{-1} (red circles), 0.55 gL^{-1} (yellow squares), 0.6 gL^{-1} (green triangles), 0.7 gL^{-1} (orange pentagons), 0.8 gL^{-1} (blue triangles), and 1.0 gL^{-1} (turquoise diamonds) xanthan. The power law fits are calculated using the early points of each plot. Network collapse is assumed to be occurring at the point of deviation from the linear fits, and for samples at 0.8 and 1.0 gL^{-1} xanthan, no network collapse was observed in the duration of the experiment.

shorter-ranged attractions. The ranges quoted were ξ=0.15 for the long range attraction and ξ=0.02 for the short range attraction. Although there is no precise threshold for an attraction to be considered long range, ξ=0.15 is assumed to be more consistent with a short range attractive system and so no conclusion can be drawn about 'true' long range systems.

5.3.3 Spinodal coarsening

Phase separation in an oil-in-water emulsion with a long range attraction occurs via a mechanism reminiscent of classical spinodal decomposition, and evidence has been presented of the occurrence of the first stage of SD as predicted by the Cahn-Hilliard theory. The intermediate and late stages of spinodal decomposition are characterised by a growth in the structure factor, where a finite q peak develops which then shifts to lower q values with time. The intermediate stage is known as the diffusive stage, where particle diffusion dominates the dynamics, and coarsening is expected to occur according to the power law $R_c \propto t^{\theta}$ with a scaling exponent of $\theta = 1/3$. The network coarsens throughout the diffusive stage until the critical lengthscale is reached after which the system enters the late stage where gravitational effects dominate and flow is observed within the system. During this stage the scaling exponent increases to $\alpha = 1$. The scaling exponent is calculated from each plot shown in figure 5.10 by fitting the data with the following growth law:

$$R_C(t) = R_0 t^{\theta} \tag{5.2}$$

with a scaling exponent θ and a temperature-independent prefactor R_0. The effective temperature, T_{eff} is related to the thermal energy by $T_{eff} = k_B T\ /(-U_0)$, and the exponent is calculated from the fit of the data, the results of which are shown in table 5.1.

Table 5.1: Calculated T_{eff} and θ values for samples with varying [Xn]

[Xn] gL^{-1} $^{-1}$	T_{eff}	θ
0.5	0.196	0.100
0.55	0.182	0.086
0.6	0.167	0.061
0.7	0.147	0.056
0.8	0.130	0.036
1.0	0.106	0.021

The first observation from table 5.1 is that the scaling exponent of $\theta = 1/3$ is never witnessed. Secondly, and more importantly, the scaling exponent is actually temperature dependent, and decreases with T_{eff}. To examine the temperature dependence of θ in greater detail, a plot of $1/\theta$ against $1/T_{eff}$ is prepared (see figure 5.11). The resulting linear plot suggests the simple functional dependency:

$$\theta(T_{eff}) = \left(A + \frac{\varepsilon}{T_{eff}}\right)^{-1} \tag{5.3}$$

Linear regression yields A=-36 and ε=8 for the data plotted in Fig 5.11. The dependency on T_{eff} suggests that the ageing dynamics are controlled primarily by thermal fluctuations, rather than being stress driven as has been reported previously to be the situation in irreversible gels and jammed systems [108, 109]

In the classical spinodal decomposition of gas–liquid phase separation, the scaling exponent θ is independent of T_{eff}. During the intermediate stage $\theta = \frac{1}{3}$ and during the late stage $\theta = 1$. Here θ is found to not only be T_{eff} dependant, but also to be much smaller than is seen in classical spinodal decomposition. It is most likely that this is a result of the presence of a gel network, however, a study of an emulsion system of xanthan and casein with a colloid-polymer size ratio of 2.3 reports experimental evidence of the three separate stages of spinodal decomposition, and find expected scaling exponents of $\alpha = 0.28$ at the intermediate stage and $\theta = 0.98$ at the late stage [90]. This is a system which also has a long range attraction and is in the semi dilute regime, but with a lower colloid volume fraction of ≈ 0.03. Due to the low colloid volume fraction the systems studied by Bhat et al only just lie within the two phase region, and so is not diredctly comparable to the systems studied here which have a large quench depth.

The scaling exponent can be affected by hydrodynamic effects, which would not be evident in samples with low volume fractions. Dhont performed extensive calculations for the intermediate stage of spinodal decomposition which accounted for hydrodynamic effects. He found that the scaling exponent lies between 0.2 and 1.1,

with the exact exponent being governed by the importance of the hydrodynamic effects for each system [110]. The scaling exponents calculated here still fall far below this range. The mechanism of phase separation therefore differs from the classical spinodal decomposition of binary liquids.

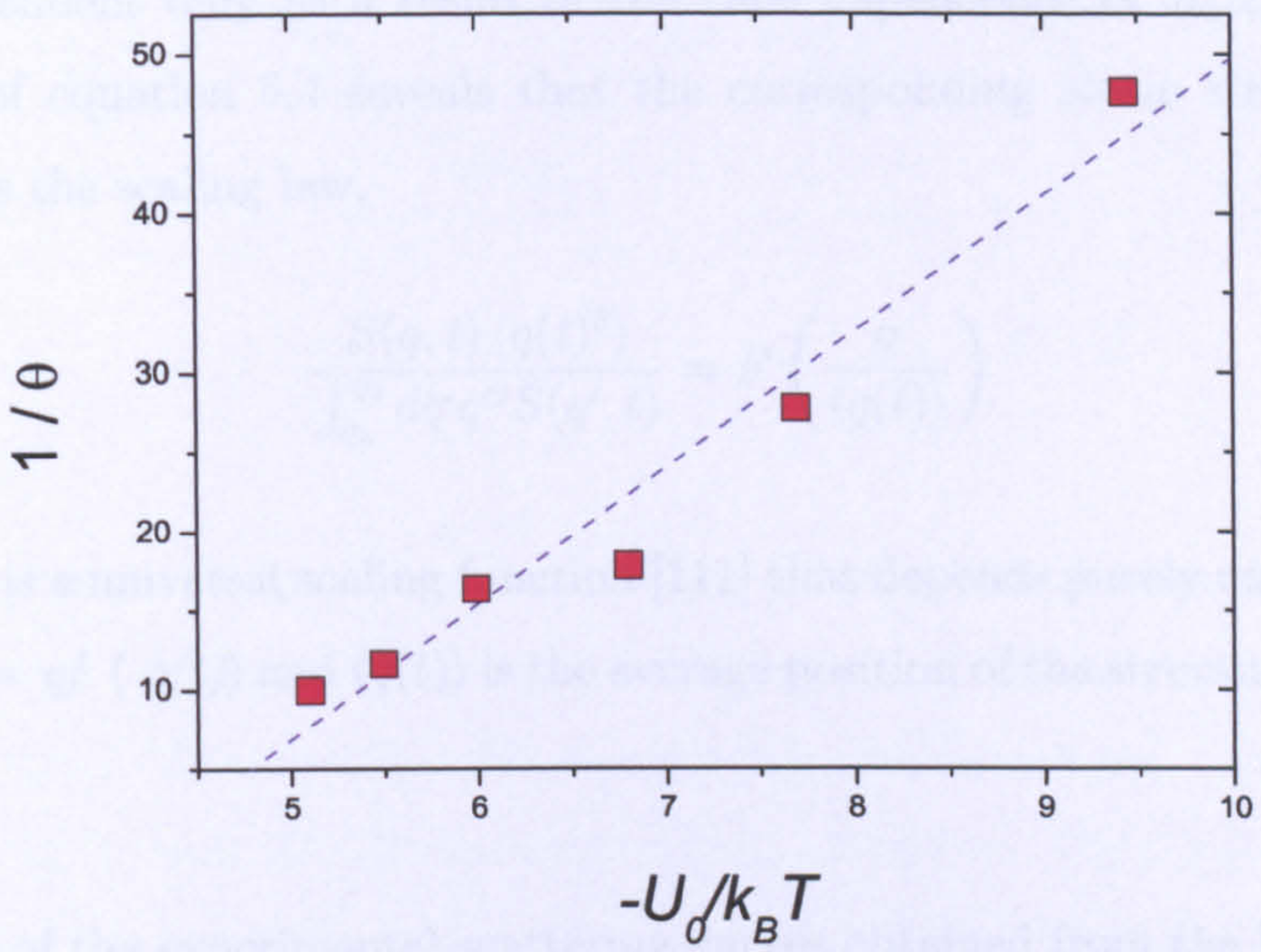

Figure 5.11: Measured scaling exponent for a range of polymer concentrations. During the intermediate stage of spinodal decomposition the scaling exponent is normally a fixed value of 1/3, but here the scaling exponent is far below this value and is also temperature dependant.

5.3.4 Dynamical scaling

The colloidal network structure, or domain pattern can be clearly observed in LSCM micrographs particularly when the network has aged somewhat. If the domain pattern at any two points in time are statistically identical, with the only difference being a change in scale, then dynamic scaling of the structure factors should occur. The phase separation may then be described with a single time-

dependent parameter, the domain size $R_c(t)$. The inhomogeneities in the particle number density at the point $\boldsymbol{r}$ with respect to the average number density $\bar{\rho}$, $\delta\rho(\mathbf{r},t) = \rho(\mathbf{r},t) - \bar{\rho}$ are then a function of the single length $\mathrm{R_c(t)}$, so that the ratio:

$$\frac{\langle \delta\rho(\mathbf{r},t)\delta\rho(\mathbf{r}',t)\rangle}{\langle \delta\rho^2(\mathbf{r},t)\rangle} = f\left(\frac{|\mathbf{r}-\mathbf{r}'|}{R_c(t)}\right) \tag{5.4}$$

is time-dependent only as a result of the time dependence of $R_c(t)$. A Fourier transform of equation 5.4 reveals that the corresponding static structure factor $S(q,t)$ obeys the scaling law,

$$\frac{S(q,t)\,\langle q(t)^3\rangle}{\int_{q_1}^{q_2} dq' q'^2 S(q',t)} = F\left(\frac{q}{\langle q(t)\rangle}\right) \tag{5.5}$$

where $F(x)$ is a universal scaling function [111] that depends purely on the wavevector ratio $x = q/\ \langle\ q(t)\rangle$ and $\langle q(t)\rangle$ is the average position of the structure factor peak [111].

A selection of the experimental scattering curves obtained from the Fourier transform of LSCM images, are shown in figure 5.12. While there is statistical scatter because of the finite size of the images used, the peaks in the structure factors clearly move to smaller q and grow in intensity with t. Fig. 5.12 (b) shows a test of dynamic scaling in the late stages of ageing ($t > 2$ hours). Dynamic scaling holds well confirming that the microstructure of the gel may be described by a single age dependent length $R_c(t)$. Dynamical scaling of the collapse of gels has been observed by Kilfoil et al [47]

5.4 Summary

It has already been shown that phase separation in a system with long range attractions does not always become interrupted by dynamic arrest [43, 98]. Here a microscopic analysis of samples with long rang attractions has been undertaken, and study of the phase behaviour has confirmed that all samples lie far beyond the

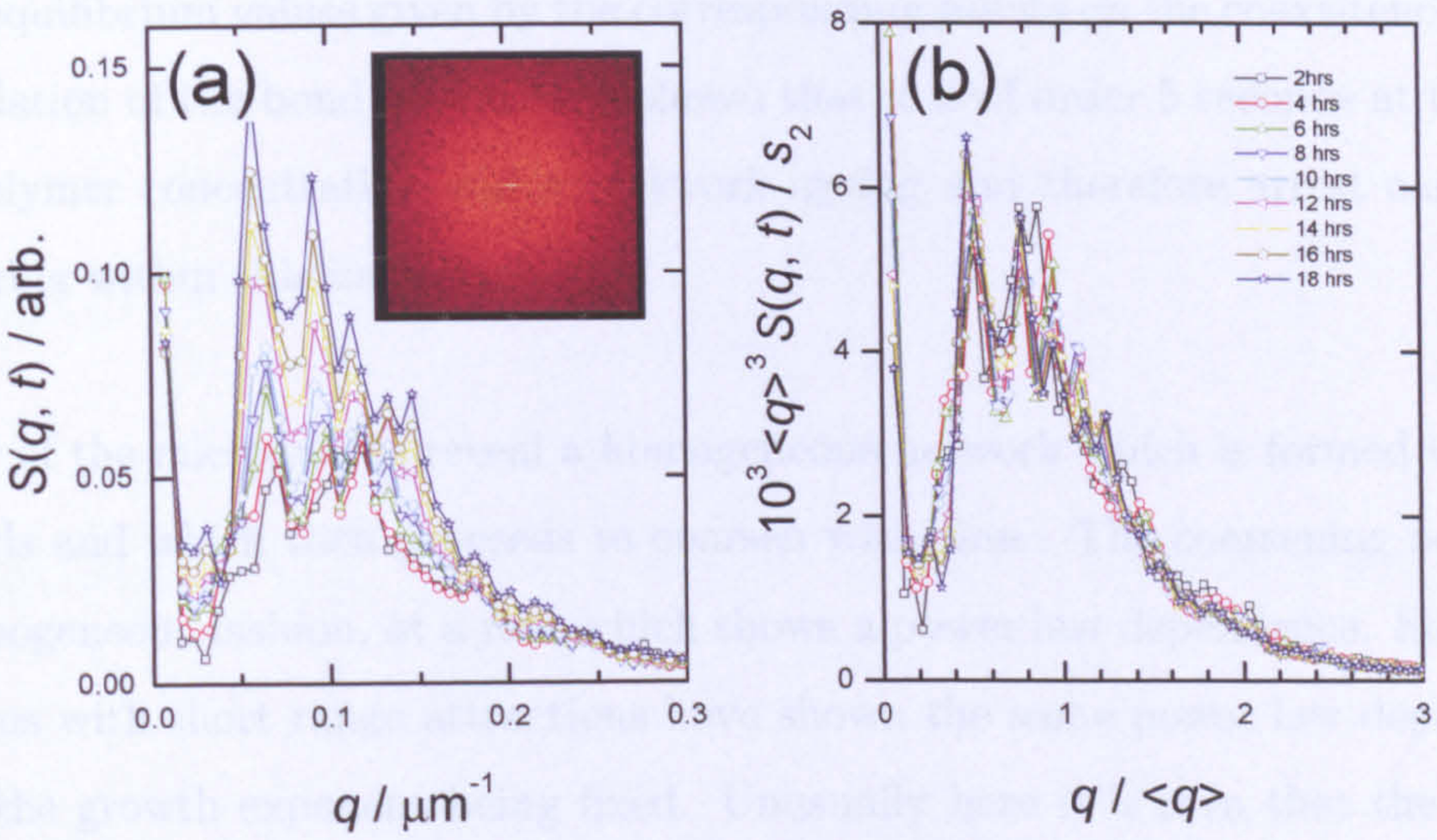

Figure 5.12: (a) Radially-averaged scattering peaks obtained from the ageing of a gel formed at a polymer concentration of $C_p\ /C_p\ * = 2.38$. Curves are labeled by the time elapsed after mixing using the symbols detailed in (b). The inset shows an example of the raw two-dimensional Fourier-transform. (b) Dynamic scaling of the data shown in (a). The normalising factor $s_2 = \int dq' q'^2 S(q',t)$ was calculated in the interval $0.02\ \mu m^{-1} < q < 0.4\ \mu m^{-1}$.

gas liquid coexistence line. All samples were prepared with identical colloid volume fractions and *h(0)* with C_p being the sole variable. Images of the ageing samples were obtained using LSCM from a fixed position within the sample, at a height of 2 mm from the internal base.

The method of analysis has allowed images to be obtained at sample ages of $t \approx$ 5 seconds. Laser scanning confocal micrographs were used to calculate R_c where plots of R_c as a function of time showed that there is no period of dynamic arrest. Instead, the systems are continually ageing until such time that the gel network fails. The zero growth rate of the characteristic domain radius at early times is predicted by the Cahn-Hilliard regime, where the amplitude of the colloidal density

fluctuations increases with time until the low and high density values have reached their equilibrium values given by the corresponding points on the coexistence curve. Calculation of the bond lifetime has shown that it is of order 5 seconds at the lowest polymer concentration and so network ageing and therefore arrest cannot be occurring within this initial period.

Study of the micrographs reveal a homogeneous network which is formed within 5 seconds and which then proceeds to coarsen with time. The coarsening occurs in a homogeneous fashion, at a rate which shows a power law dependence. Studies of systems with short range attractions have shown the same power law dependence with the growth exponent being fixed. Unusually here it is seen that the growth exponent α is not fixed, but is actually dependant upon the effective temperature, T_{eff}. The mechanism of phase separation therefore differs from the classical spinodal decomposition of binary liquids.

Chapter 6

Ageing of the colloidal network

6.1 Introduction

The addition of a non-adsorbing polymer to a colloidal system can have one of several effects. To begin, there is no observable difference to the system if the polymer is at infinite dilution. At still low concentrations of polymer the rate of sedimentation is decreased due to the increase in viscosity of the solution. Once the polymer concentration is increased again, it is observed that creaming or sedimentation occurs at an increased rate compared to a system without any polymer. This is due to the formation of colloidal aggregates which have a larger effective size compared to an individual colloid. The settling velocity of a particle or aggregate depends upon the diameter of the particle as detailed by Stokes law [68]. Once the concentration of polymer is increased further a more surprising observation is that settling of the colloidal particles is either abated or completely delayed for a period of time. This period of time, the delay time τ_D, where sedimentation is delayed is of great interest in commercial colloidal products [112–115]. As discussed previously there exists many commercial colloidal dispersions which require the colloids to remain dispersed relatively evenly throughout the system, rather than sedimenting and forming a dense colloidal layer which can often make it difficult for the particles to be redispersed. The polymer allows the particles to defy gravitational effects by causing the colloids to form a space-spanning network, or colloidal gel, as a result of depletion interactions. The resulting gel however, appears to have a finite

lifespan [51, 53, 58, 112] which so far is unable to be quantified. This phenomenon is widely observed in dispersions with short range attractions and yet the reasons for the break down of the gel network still remains a mystery. The period of stability cannot be defined by a general rule as parameters such as colloid volume fraction, polymer-colloid size ratio, and concentration of depletion polymer all play a key role in dictating the behaviors observed. Other parameters such as the initial height of the sample, and the shape of the sample container have also been shown to have an affect on τ_D. There is little published research discussing the effect of these parameters on systems with long range attractions, but it is assumed that the effects will be analogous to those of short range attractive systems.

The data presented in the previous chapter shows how the colloidal network does not become arrested. The network continually coarsens until such a point that it experiences a catastrophic failure, and begins to collapse. LSCM has been used to quantify the degree of coarsening exhibited by the network during the delay period, and the first instance of network collapse. However, once the collapse process has commenced, the LSCM cannot be used for data acquisition, since the network is moving and each micrograph will represent different portions of the network. A macroscopic approach is adopted, and sedimentation profiles are produced of sedimenting samples.

Two key observations result from this study. Firstly, there is no obvious presence of large scale channel formation or network rearrangement, and secondly, there is experimental evidence for two different ageing processes which depend upon the physical size of the sample. Where the initial height is large, the network shrinks heterogeneously, with localised areas of the network experiencing greater rearrangements than others. The inhomogeneities in the samples with large initial heights appear randomly placed. However, when the initial height of the sample is small the network appears to shrink homogeneously with time. From studying the growth of the characteristic domain radius, it is clear that the coarseness of the network is dependent upon C_p , where higher concentrations yield less coarse

networks which coarsen at a slower rate. The steady coarsening continues until a critical length is reached after which the domain radius grows in an extremely erratic manner. It has been suggested previously that a network will only start to collapse once the gravitational stress exceeds the yield stress of the network [55]. However, here it is shown how the gravitational force does not actually play a critical role in this process since the systems have very low yield stresses when compared to the gravitational stress.

6.2 Increasing network elasticity

Rheological measurements were performed periodically on a sample from t_0 and continued until the network had completely collapsed. The elastic and viscous modulii were measured by applying an oscillatory stress of 0.0025 Pa at a frequency of 0.5 Hz, and measuring the strain response. The rheological measurements were kindly carried out by Malcolm Faers, at Bayer CropScience, Germany. Measurements were carried out with the sample contained in a clear vial allowing the height of the colloid rich layer to the followed simultaneously . The sample was not held permanently in the rheometer, instead the vial was loaded onto the rheometer and the vane lowered into it each time a measurement was taken. The design of the vane limited disruption to the network. The collapse profile and corresponding measurements for G′ and G″ are shown in figure 6.1.

Oscillatory measurements performed during the delay period show that the colloidal network behaves as an elastic solid, indicating a high level of connectivity throughout the network. Initially the elastic modulus G′ is greater than the viscous modulus G″ and surprisingly it increases throughout the delay time. This increasing elastic modulus indicates a network which is increasing in connectivity, and so it is counterintuitive that the network would even begin to break down. At the point at which the network begins to collapse, there is a corresponding but minimal decrease in G′ after which it is quickly recovered and G′ then continues to grow steadily as the volume fraction of the colloid rich phase increases.

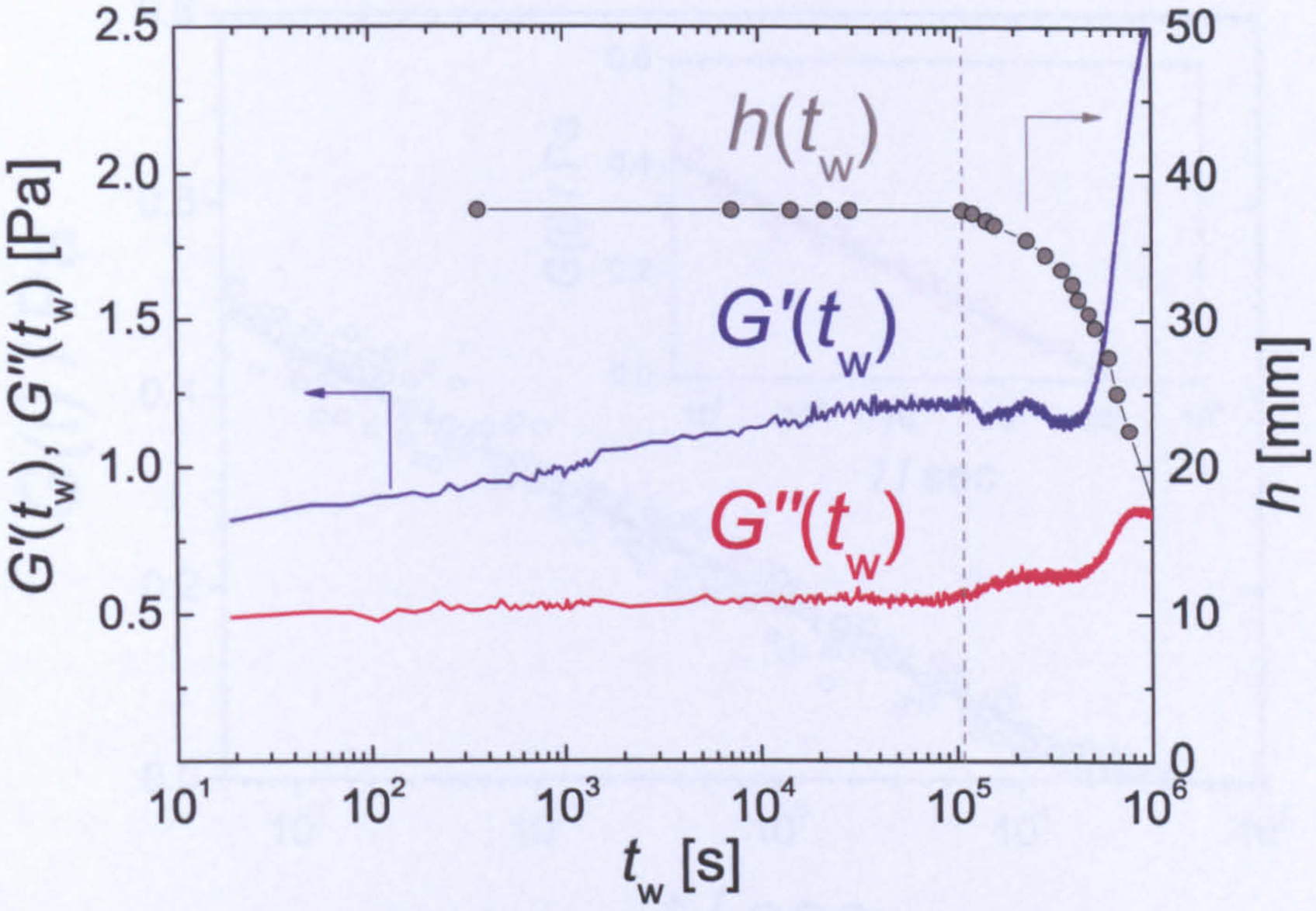

Figure 6.1: Plot showing the elastic modulus (G'), viscous modulus (G") and collapse profile (grey data points) of a sample (ϕ = 0.2, 0.9 = C_p xanthan, h(0) = 37.5mm). Here, the elastic modulus is greater than the viscous modulus and increases throughout the delay time. The height of the colloid rich phase is shown on the right hand vertical axis.

The increasing elastic modulus indicates a network which has an increasing solid-like nature, however the long time behaviour of the gel is best characterised using a stress relaxation test where a step strain of $\gamma = 0.015$ is applied at $t = 0$ seconds and the time dependant stress is recorded. Figure 6.2 shows the decay of the stress relaxation modulus $G(t)$ at two different quench depths. Both examples show a full decay to zero, confirming the true liquid−like nature of the networks.

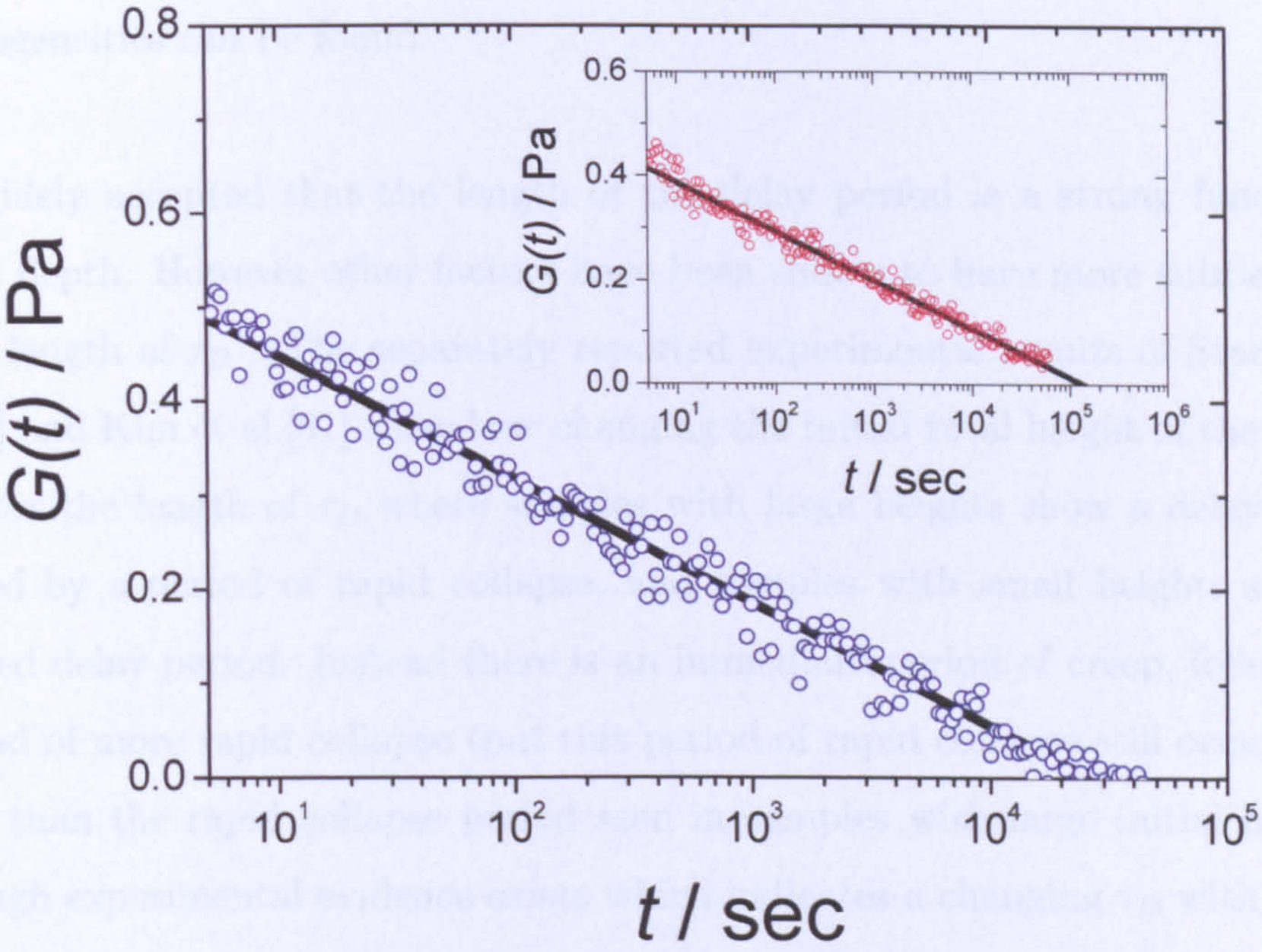

Figure 6.2: Plots showing the stress relaxation modulus G(t) of samples with C_p $/C_p * 3.17$ (blue data set) and C_p $/C_p * 3.97$ (red data set).

6.3 Network evolution

It has been suggested by Tanaka et al [63] that coarsening of a colloidal gel network is a result of self generated mechanical stress. The stress comes from particles moving to more favourable positions so that the number of nearest neighbours increased, reducing the interaction energy. These movements occur at the expense of particles with fewer nearest neighbours, and so thinner chains of the network structure are broken, as other chains coarsen. The network will relax into a lower energy state. The simulations also state that the energy required for a particle to overcome an energy barrier is reduced when the particle is under stress, ie, is part of a thin chain of the network structure which will break, allowing for coarsening of other chains. The areas of inhomogeneity are a result of internal stresses building within network which eventually lead to its failure. By following the microscopic

time evolution of the networks, it is hoped that evidence of these stress induced inhomogeneities can be found.

It is widely accepted that the length of the delay period is a strong function of quench depth. However other factors have been shown to have more subtle effects on the length of τ_D . The separately reported experimental results of Starrs et al [58, 59] and Kim et al [61] show how changing the initial total height of the sample will alter the length of τ_D where samples with large heights show a delay period followed by a period of rapid collapse, and samples with small heights show no observed delay period. Instead there is an immediate period of creep, followed by a period of more rapid collapse (but this period of rapid collapse still occurs more slowly than the rapid collapse period seen in samples with large initial heights). Although experimental evidence exists which indicates a changing τ_D with sample size there has not been a detailed study undertaken, therefore an extensive study of τ_D as a function of initial height and C_p was carried out in order to gain a more complete understanding.

6.3.1 Height dependant network evolution

The effect of altering sample size on network ageing is investigated for systems with long range attractions. A sample is prepared ($\phi = 0.2$, $C_p = 0.6$ gL^{-1})and added to the confocal cell to an initial height of 15mm. The specially constructed confocal microscope cell is fixed to a low profile manual linear translation stage so that the sample can be moved in a vertical direction and be imaged throughout its entire height. The sample cell is moved in 1mm increments and a micrograph is obtained after each position change. This process is repeated at different time intervals so that the evolution of the network can be recorded. The main disadvantage of this method is that it is almost impossible to return to the exact same point within the sample once it has been moved. Figure 6.3 shows a selection of these images, and the measurement refers to the distance from the base of the sample at which the image was obtained.

The first column of images labelled 0 hrs shows how the network appears almost homogeneous throughout its full height. At a distance of 1mm from the base the network has a very fine and uniform appearance, which becomes marginally coarser as you move up to 4mm. The coarseness and homogeneity remain almost constant throughout the rest of the height of the sample. The second column of images was taken after 3 hours, and shows how there are areas within the network which show significant change in structure while other areas remain relatively unchanged. The most noticeable changes have occurred at a height of 10mm with network chains being much thicker, and large voids are forming within the network. This area of the network is ageing at a faster rate than is occurring at heights of 4mm and 13mm. The final column of images was taken after 6 hours and shows a further but marginal degree of ageing throughout the full height. In order to determine whether there are in fact height dependant ageing mechanisms, a further sample was prepared ($\phi = 0.2$, $C_p = 0.6$ gL^{-1}) and placed in the confocal cell to a total initial height of 5mm, with micrographs being obtained at 1mm height intervals over a period of time. The micrographs shown in figure 6.4 were obtained when the sample was 18 hours old. It is clear that the sample with the small initial height *h(0)* ages very differently when compared to the sample with the large *h(0)* sample. At times as early as 3 hours the large *h(0)* sample shows considerable changes and heterogeneity, compared to the small *h(0)* sample which still shows a homogeneous network throughout its full height at a sample age of 18 hours, clear evidence of ageing mechanisms which are dependant upon the physical size of the sample.

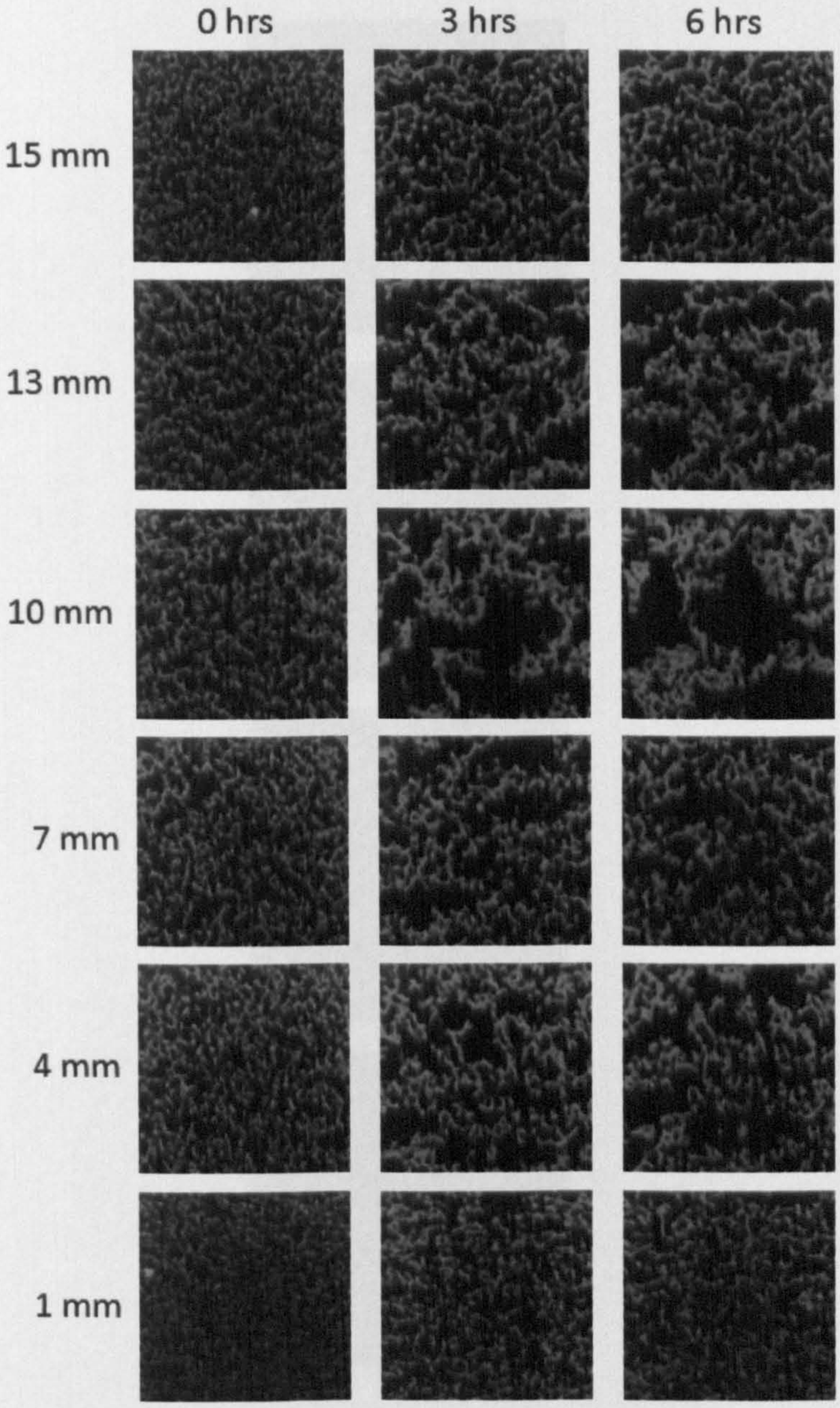

Figure 6.3: Confocal microscope images taken at different heights within a sample with 0.6 gL^{-1} xanthan, and an initial height of 15mm, at varying times after initial mixing. Each micrograph has dimensions of 146 x 146 μm. The measurements on the left denotes the distance from the base of the sample at which the image was obtained. The inhomogeneities which appear with time are evident in the second two columns of images and are most obvious at a height of 10mm

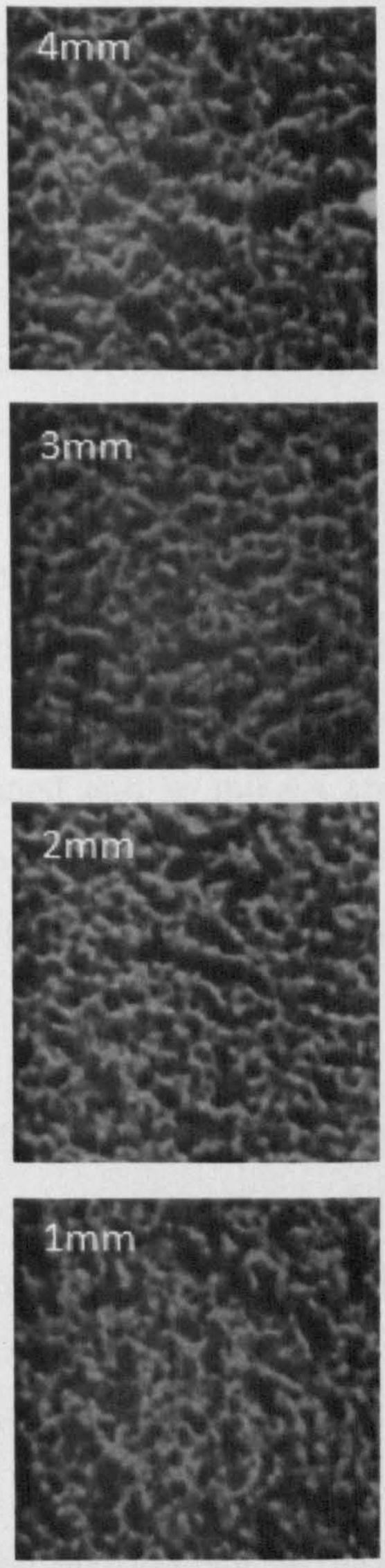

Figure 6.4: Confocal microscope images taken at different heights within a sample of $\phi = 0.2$, $C_p = 0.6$ gL^{-1} and h(0) = 5mm after 18 hrs. Each micrograph has a size of 146 x 146 μm. The sample details are the same as shown in figure 6.3, it is only the height of the sample which has been altered. The network remains homogeneous even after 18 hrs, while inhomogeneities were present after 3 hours in the sample with initial height of 15mm.

6.3.2 Comparison of network ageing in large and small height samples

Evidence has been presented for the existence of two different microscopic ageing processes which depend upon the physical size of the gel. Correlations between the two ageing processes were investigated by studying the growth of the characteristic domain radius as a function of time at large and small $h(0)$ ($\phi = 0.2$, $C_p = 0.6$ gL^{-1}). Images are obtained at fixed distances from the base of the sample. For a sample which shows homogeneous coarsening the position of the fixed height is unimportant as it is assumed that the measurements are representative of the whole network. When a sample has a large initial height there will be portions of the network which have undergone a greater degree of coarsening. The location of these areas cannot be defined and so images are obtained at a fixed distance of 10mm from the base of the sample. Images are taken 2mm from the base of samples with small initial heights. A selection of the images obtained is shown in in figures 6.5 and 6.6 respectively.

The characteristic domain radius of each network was calculated from the resulting power spectrum, however, each spectrum shows evidence of the presence of background noise. This effect could have been reduced by increasing the image size from 1024 x 1024 pixels to 2048 x 2048 pixels, but this was not feasible given the length of time required to produce an image at this resolution. R_c is only able to be calculated from images in which there is a continuous gel network throughout the full image, as no useful information can be obtained from images which show a completely disconnected structure. This point is illustrated in figures 6.7 and figure 6.8. The inset of each figure shows the complete set of power spectra for the micrographs shown in figures 6.5 and 6.6. The q position of the peak denotes the size of the domain radius, with an increasing peak height indicating an increasing domain size. No observable peak means that there is no continuous structure to measure. The main plot in each figure shows only the power spectra which have a definite peak. In the small height sample the network persists for a longer period

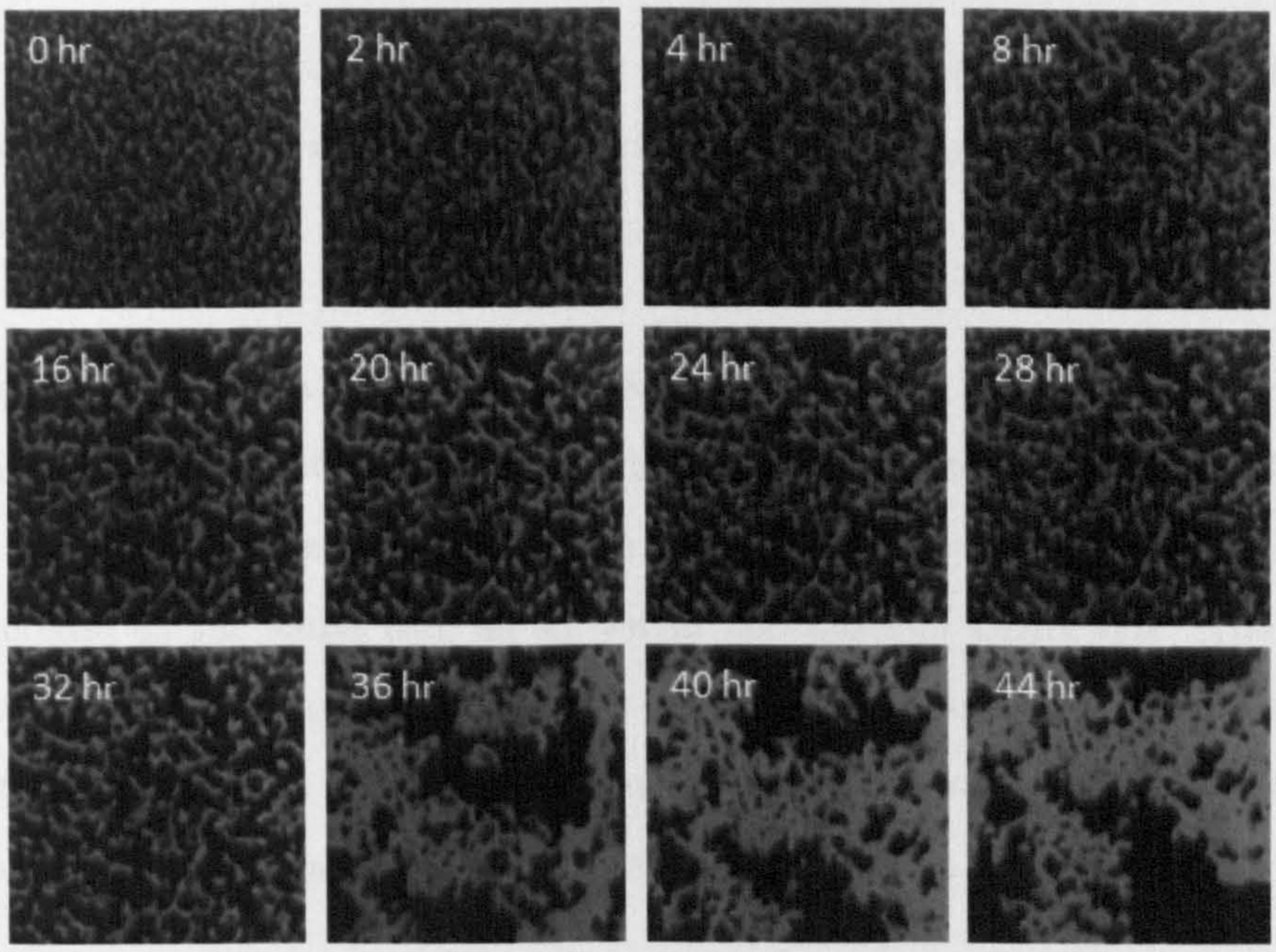

Figure 6.5: Confocal microscope images taken at a fixed height of 2mm from the base of a sample with 0.6 gL^{-1} xanthan, and initial height of 5mm. Each micrograph has the dimensions 146 x 146 μm.

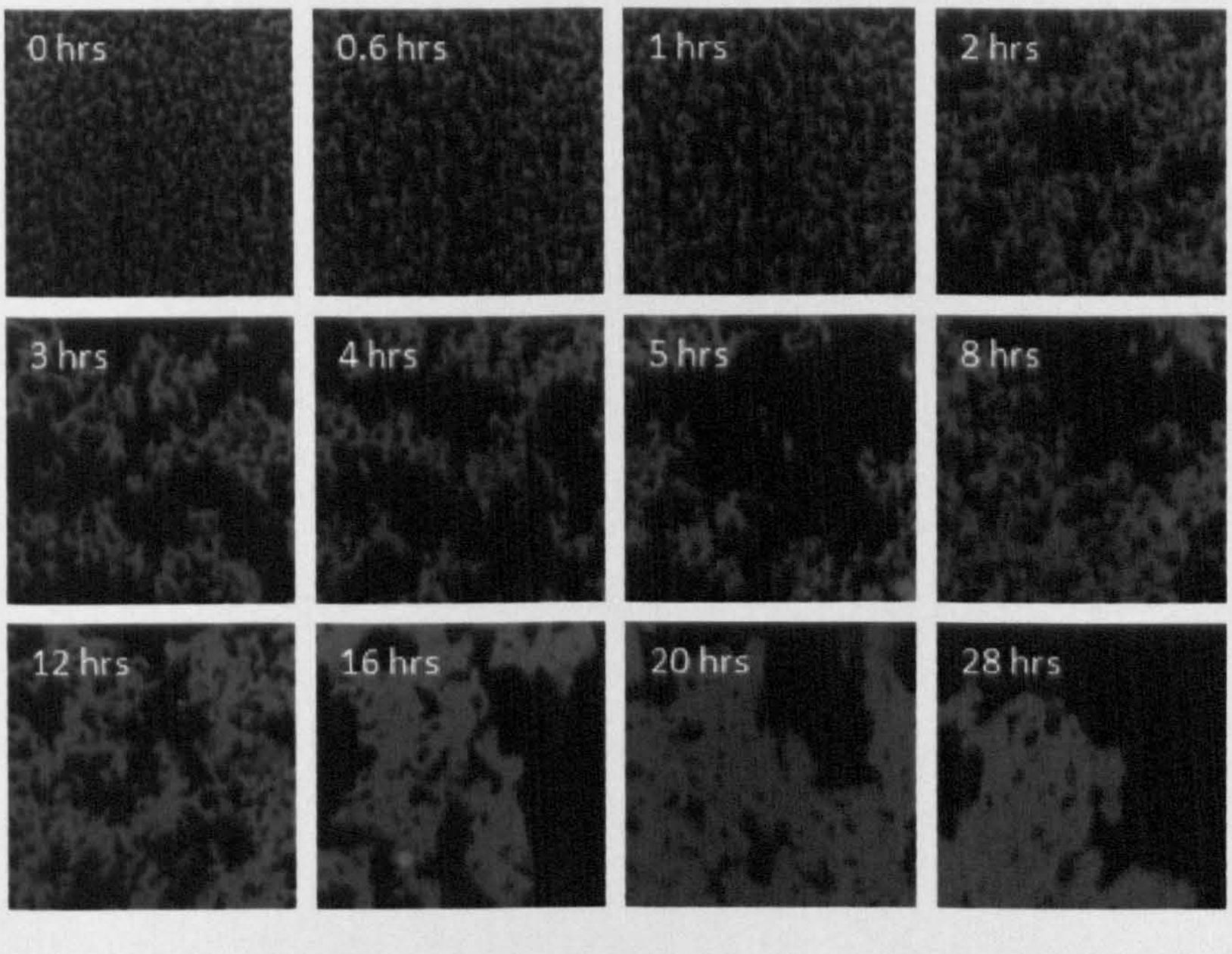

Figure 6.6: Confocal microscope images taken at a fixed height of 10mm from the base of a sample with 0.6 gL^{-1} xanthan, and initial height of 15mm. Each micrograph has the dimensions 146 x 146 μm.

of time and power spectrums are shown up to a sample age of 28 hrs. However, the network in a tall height sample becomes more disconnected after only 1 hour and has a much shorter lifespan.

Comparison of the data obtained at fixed heights within samples with small and large initial heights show that initially, both networks are formed with the same domain radius size. For a period of time of order 1 hour the networks domain radii increase at the same rate as shown in the plots in figure 6.9. The dashed red line represents a linear fit on the log-log plot of the first three data points for the large height sample. After the 1 hour period, the domain radius of the large height sample increases at a much more rapid rate and in a non-predictable fashion.

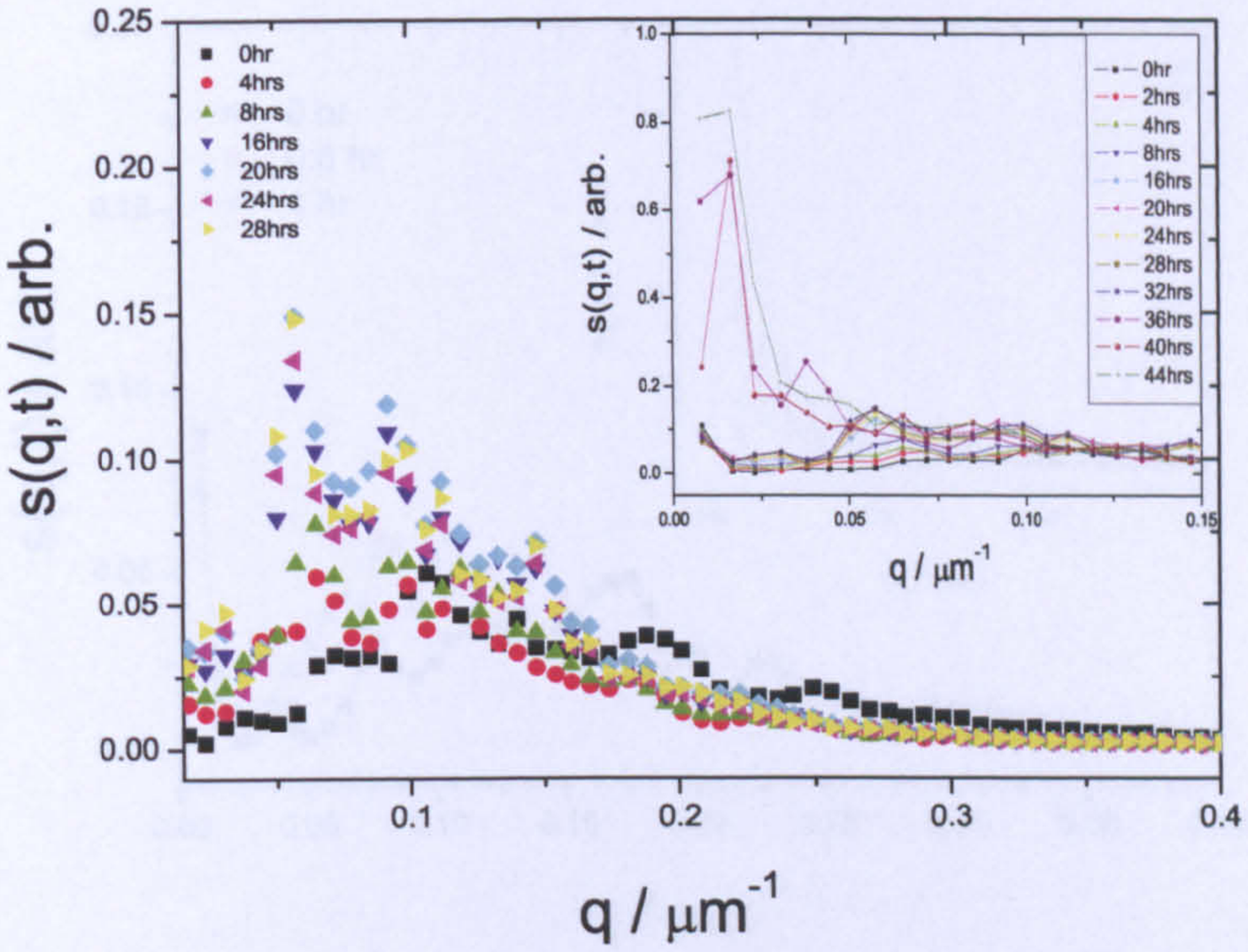

Figure 6.7: Power spectra of LSCM images taken at a fixed height of 2mm from the base of a sample with initial height of 5mm, and polymer concentration of $0.6 gL^{-1}$. The inset plot shows the power spectrums obtained for each of the images in figure 6.5 and the main body of the figure shows only the power spectrums which have a definite peak, from which a characteristic domain radius can be determined. The continuous network persists for approximately 28 hours before showing sign of collapse.

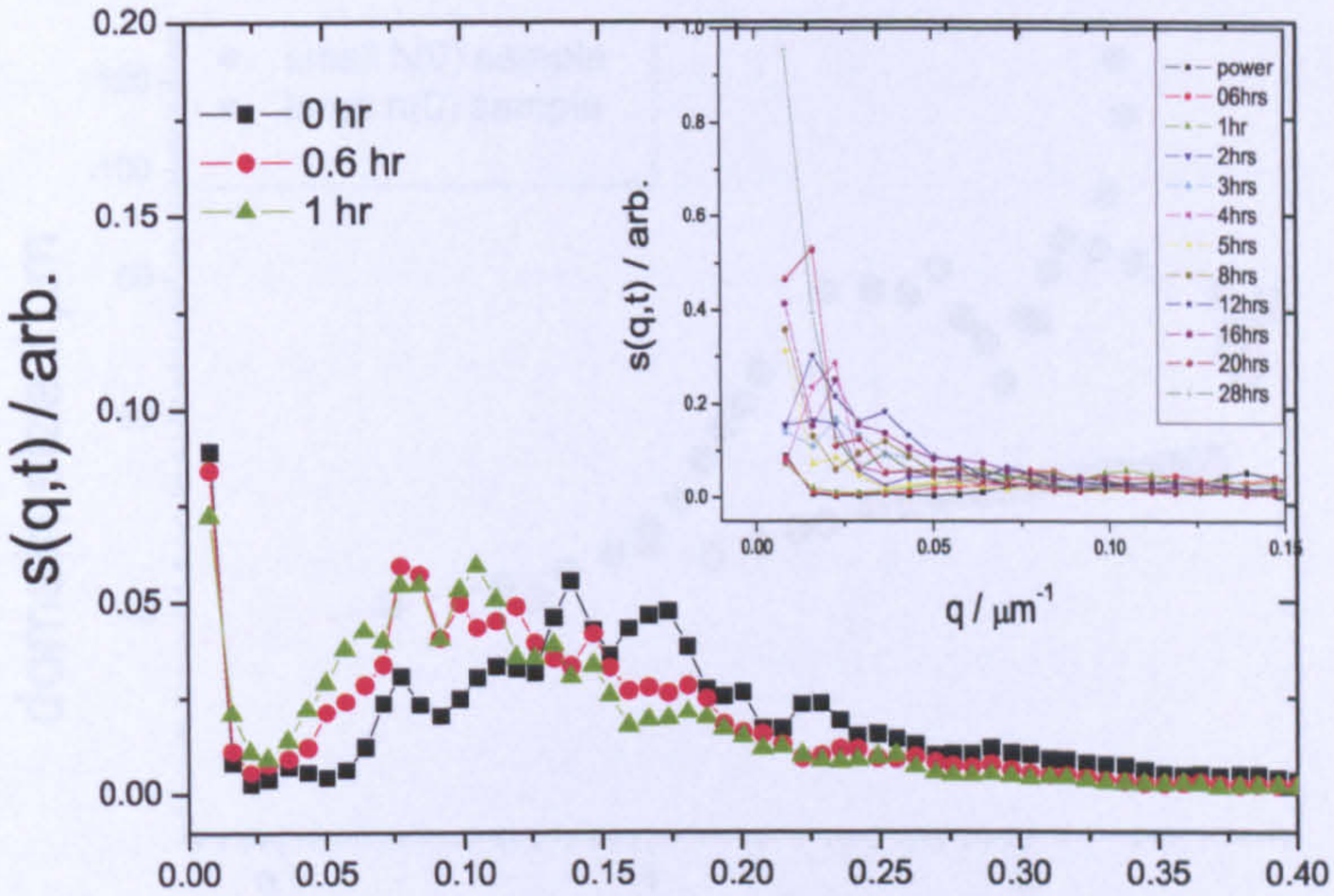

Figure 6.8: Power spectra of LSCM images taken at a fixed height of 10mm from the base of a sample with initial height of 16mm, and polymer concentration of 0.6gL^{-1} . The inset plot shows the power spectrums obtained for each of the images in figure 6.6 and the main body of the figure shows only the power spectrums which have a definite peak, from which a characteristic domain radius can be determined. The continuous network only persists for approximately 1 hour before showing sign of collapse.

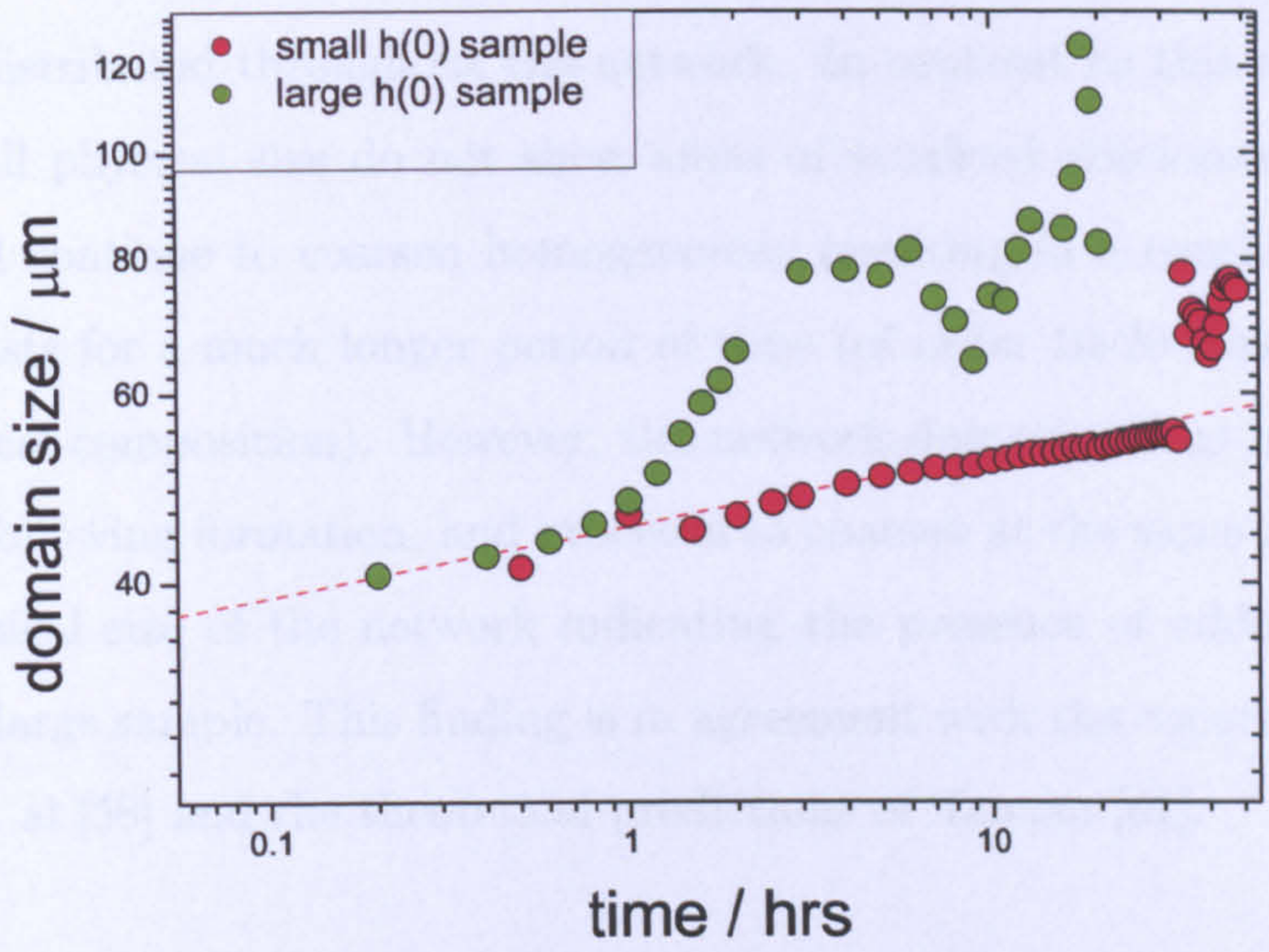

Figure 6.9: Plot showing the increasing domain size of samples with a large initial height (green circles) or small initial height (red circles),each with polymer concentration of $0.6 \mathrm{gL}^{-1}$. The dashed line represents a linear fit (on a log-log plot) of the first 3 points from the sample with large initial height. The characteristic domain radius is initially of equal size in each sample, but in the large height sample it quickly deviates from the steady growth exhibited by the small height sample and grows in an unpredictable pattern.

A quantitative microscopic analysis has enabled the coarsening patterns in samples with both large and small initial heights to be determined and comparisons to to be made. There is a clear difference in the coarsening patterns where samples with a large physical size (in this instance, a large initial height) show a heterogeneous coarsening with localised areas of the network coarsening at a much faster rate. These areas of localised accelerated coarsening show both an increase in the domain radius as well as a breakdown of the continuous network, and appear to be randomly distributed throughout the network. In contrast to this samples which have a small physical size do not show areas of localised accelerated coarsening, and instead continue to coarsen homogenously resulting in a continuous network which persists for a much longer period of time (of order 10-20 times for samples with identical composition). However, the network domain radius is identical immediately following formation, and proceeds to coarsen at the same rate regardless of the physical size of the network indicating the presence of additional stresses within the large sample. This finding is in agreement with the experimental results of Starrs et al [58] and the theoretical predictions of Tanaka [62].

6.4 The Critical Length

There is a finite period of time for which small height samples coarsen with a predictable behaviour after which comes a point where coarsening becomes erratic. This degree of erratic behaviour is difficult to quantify since it is likely that the micrographs obtained are of different areas of the gel network due to movement of some network areas. However what is clear from figure 5.10 is that there is a C_p dependent factor which denotes the end of the predictable behaviour. The six samples which were previously prepared in order to study the growth of R_c can be subdivided into two categories: those in which the domain radius growth deviates from the plotted linear regime, and those that do not. The two samples with the highest concentration of depletion polymer (C_p /C_p * 3.70 and 4.11) fall into the latter category and within the time frame of the experiment as determined by eye,

there was no microscopic evidence for the commencement of a collapse process. In contrast, all other samples exhibit a change where the domain radius initially grows linearly over a period of time (when data is plotted on a log-log plot), and then deviates from this pattern and either grows at an increasing rate with time, or increases very suddenly. It is expected that the structural changes being measured at the point of deviation relate to the onset of the collapse process, and so this point is referred to as the microscopic delay time, τ_{mD}. The measured values of τ_{mD} as determined from figure 5.10 for each sample are detailed in table 6.1. At 0.55 gL^{-1} xanthan τ_{mD} is more difficult to determine given that there is no sudden increase in the R_c . There are two points at which the data points seem to be deviating from the straight line, one at 12,600 seconds, and the other at 20,400 seconds. The former value is assumed to be the actual deviation point here since it is the first instance of deviation.

Table 6.1: Calculated τ_D for samples of fixed *h(0)* and varying [Xn]

[Xn] gL^{-1}	τ_{mD} / s
0.5	5,460
0.55	12,600
0.6	122,400
0.7	152,400

A noticeable change in the gel network structure is expected for samples that have exceeded the microscopic delay time. However micrographs obtained both before and after τ_{mD} reveal that the gel network has not undergone any severe structural changes, and there is no colloidal boundary visible to the naked eye shortly after this point. This is demonstrated in the micrographs in figure 6.10 which show images obtained both before (selected at random) and after τ_{mD} . In each instance in figure 6.10 the left hand micrograph which was obtained well within the observed τ_D , shows a homogeneous and delicate gel network structure. All samples show evidence of a coarsening network. The two samples with the lowest C_p show that

the network has indeed coarsened shortly after τ_{mD} that, as evident by the thicker network strands and increasing size of the network voids. The most significant changes are seen in the sample at 0.6 gL^{-1} , where the network has coarsened significantly when compared to 0.5 and 0.55 gL^{-1} . As a result of this coarsening large network voids appear. Finally there is evidence of network coarsening in the sample at 0.7 gL^{-1} and the formation of a void to the left of the micrograph. The coarsening does not seem as advanced when compared to the other samples but this is a direct result of the dominance of the strength of the depletion attraction. It has been shown by Poon et al in their dark field imaging of sedimenting samples that large structural changes obviously occur towards the end of the delay time, specifically, that large channels are formed in the center of samples [116]. They suggest that the formation of channels is vital as it allows for fluid flow to occur, without which, the network is unable to restructure. Here there is no such behaviour observed. It is possible that channel formation is occurring outside of the scanned area. At each polymer concentration a number of samples were prepared, and in each case there was no evidence of large channel formation, and so it is concluded that network voids rather than large scale channels are being formed.

The large scale channels observed by Poon et al at the onset of collapse suggests that the porosity of the network and subsequent fluid flow through the network are key factors in the ageing process. One hypothesis is therefore that in order for major restructuring of the gel network to occur, that the network characteristic domain radius must first reach a critical size, whereby materials become more porous. A critical length (l_c) of $\sim 2\pi$ multiplied by the capillary length, l_{cap} , was reported by Aarts et al [117] as a result of their investigation of a fluid-fluid phase separation in a colloid polymer mixture, which is calculated as follows:

$$l_{cap} = \sqrt{\frac{\gamma}{g\Delta\rho}} \tag{6.1}$$

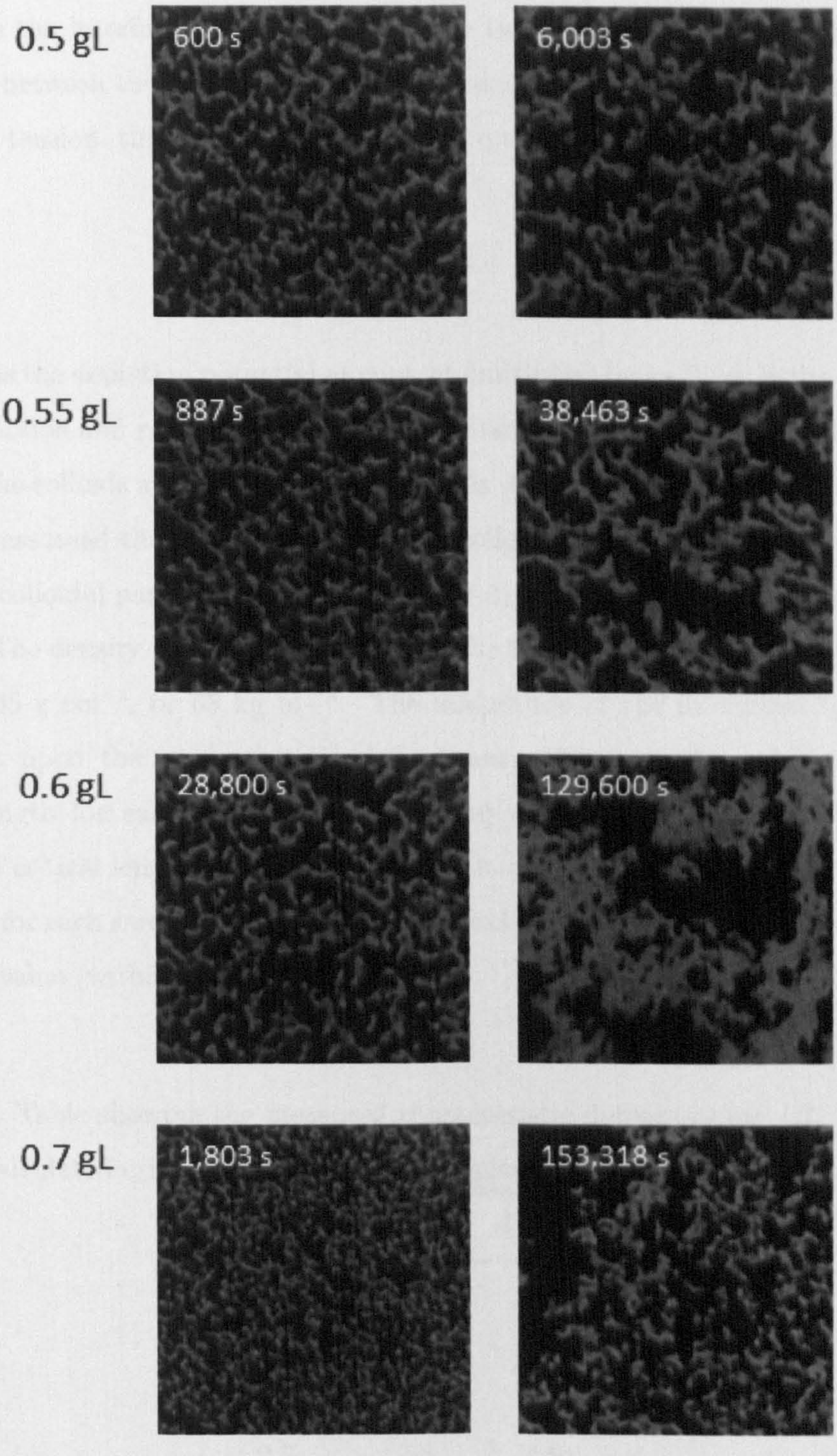

Figure 6.10: Micrographs taken before and after τ_D as detailed in table 6.1 at a range of polymer concentrations. The right hand column shows images taken during the collapse process, and how the network still remains relatively intact. Each micrograph has dimensions of 146 x 146 μm .

where γ is the interfacial tension between the two liquids, and $\Delta\rho$ is the density difference between the two. In order to determine an estimate for the value of the interfacial tension, the following expression as quoted by Bailey et al [43] is used:

$$\gamma = \frac{U_0\phi_c}{(2r_h)^2} \tag{6.2}$$

where U_0 is the depletion potential at contact multiplied by k_BT , ϕ_c is the colloidal volume fraction and r_h is the colloidal hydrodynamic radius. The density difference between the colloids and the continuous phase is -0.13 $\pm$ 0.01 g cm^3, where $\Delta\rho = \rho_c$ - ρ_s. It is assumed that the gas phase of the colloidal system is almost completely devoid of colloidal particles, and therefore $\phi \approx 0$, whereas in the colloid rich phase $\phi \approx 0.5$. The density difference, $\Delta\rho$ between the two phases is therefore calculated to be 0.065 g cm^{-3}, or 65 kg m$-^3$. The magnitude of the interfacial tension is dependent upon the concentration of depletion polymer, and so the calculated critical length for each sample will be slightly different. Table 6.2 details the calculated critical lengths and the characteristic domain radius, R_c at the point of deviation for each sample. The two values at each concentration are are essentially the same value (within 10%).

Table 6.2: Table showing the measured characteristic domain radius (R_c) at τ_{mD} and the calculated critical length (l_c) for samples of varying [Xn]

[Xn] gL^{-1}	R_c/ μm	l_c / μm
0.5	29	26
0.55	28	26
0.6	28	28
0.7	26	29

The values of the domain radius at the onset of the microscopic delay time for samples at 0.8 and 1.0 gL^{-1} xanthan were unable to be determined since the time frame

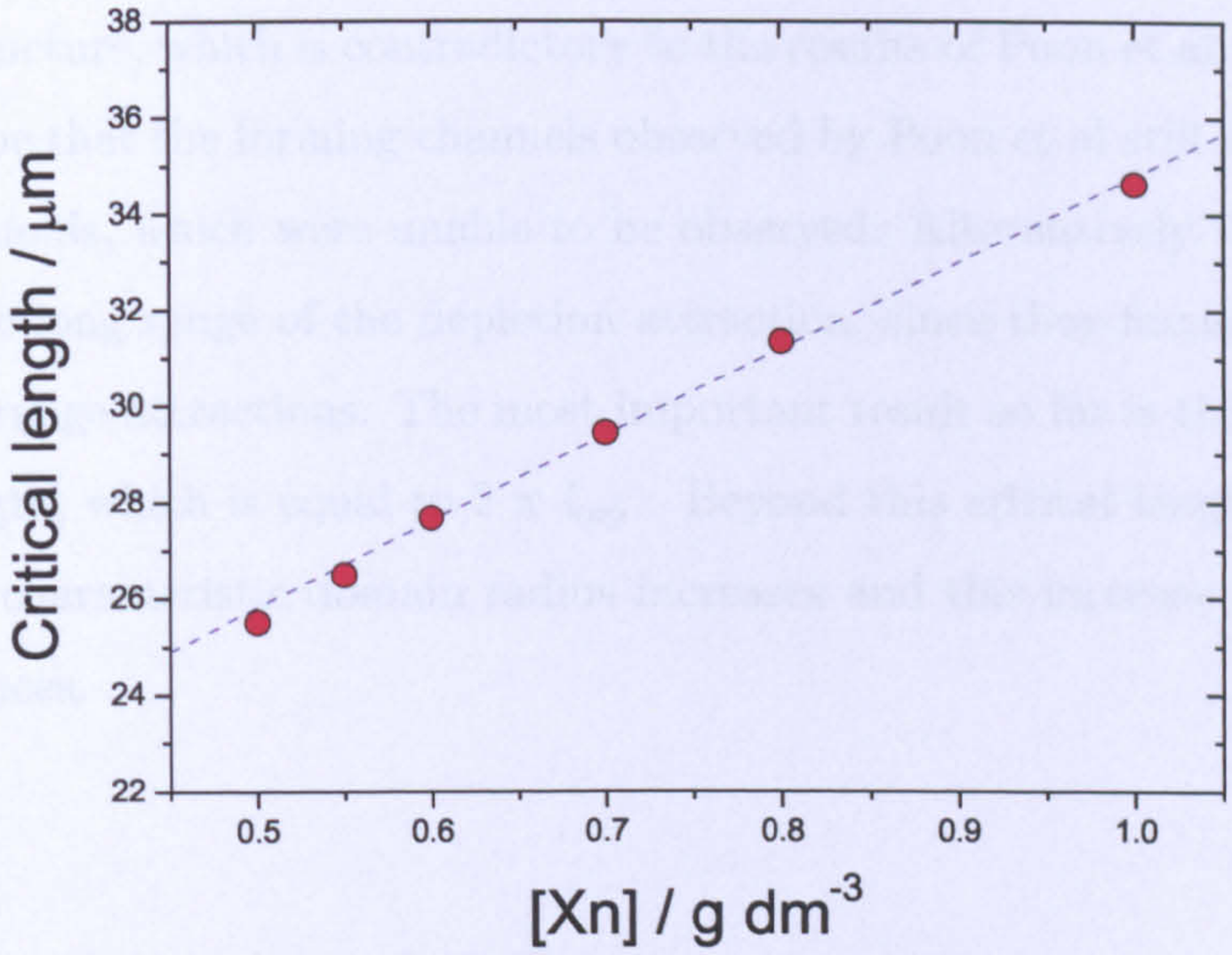

Figure 6.11: Critical length as a function of polymer concentration. The data points at 0.8 and 1.0 gL^{-1} xanthan were calculated assuming that the capillary length is equal to the critical length, using equation 6.1.

of the experiments were unable to capture the onset of the collapse process. From table 6.2 it is clear that the values of the critical length (where materials become more porous) and the domain radius for each sample at the microscopic delay time can be considered as equal. Using equations 5.1 and 5.2, the l_c can be calculated instead of measuring the domain radius at τ_{mD} since they are apparently equal in value. The values were calculated to be 31μm and 35μm respectively, showing that l_c increases with polymer concentration (see figure 6.11), which is expected since the interfacial tension is dependent upon the strength of the depletion potential at contact.

So far it has been shown that the gel networks of small height samples coarsen in a linear pattern when the characteristic domain radius plotted as a function of polymer concentration on a log-log plot, and that the rate of this coarsening is governed by the strength of the depletion potential. Towards the end of the microscopically

observed delay time and into the collapse regime there is little change noted in the network structure, which is contradictory to the results of Poon et al. One explanation could be that the forming channels observed by Poon et al still contained high levels of colloids, which were unable to be observed. Alternatively this could be a result of the long range of the depletion attraction, since they focused on systems with short range attractions. The most important result so far is the presence of a critical length, which is equal to $2\ \pi\ l_{cap}$. Beyond this critical length, the growth rate of the characteristic domain radius increases and this increase is dramatic in some instances.

6.5 Gravitational Effects

Gravity is important in any system which is not density matched, and can have several effects. Most obviously gravity will dictate whether the colloids or any non-density matched particle which are large enough not to be dominated by Brownian effects will cream or sediment. It is also possible that it can interfere with gelation where at extremely low ϕ a system can be prevented from forming a network due to colloids sedimenting before gelation can complete [118]. It is often thought that a gel network undergoes a rapid collapse regime once the gravitational stress exceeds the compressive yield stress of the network so that it can no longer support its own weight, and when the gravitational stress is less than the compressive yield stress then the network shrinks in a homogeneous fashion at a uniform rate [51].

Rheology is the study of the deformation of matter which results when a force is applied to it. The type of matter will result in different observations, for example, when a force is applied to a liquid the liquid will flow but, when stress is applied to a solid the solid will deform by a fixed amount and return to its original form once the force is removed. Rheology can be interpreted in terms of the properties of the network structure where a colloidal system can behave as a viscous liquid, an elastic solid or a viscoelastic solid/liquid. The yield stress of a network through-

out its lifetime is able to be determined by using vane rheology and is equal to the amount of stress which must be applied to a system before it begins to flow, rather than exhibit solid behaviour. If the gel network is sufficiently rigid it will behave as a solid. Under shear it will have a yield stress and an elastic modulus. In compression it will have a Compressive Yield Stress that supports its weight.

The gravitational stress is highest at the top of the emulsion sample where the full weight of the network exerts the most force due to gravity, and is calculated as follows:

$$\sigma_g = \Delta\rho g h_0 \phi_0 \tag{6.3}$$

In gel networks with short ranged attractions, the delay time has a strong dependence on σ_g. For example, σ_g can be increased by changing the density difference between the colloid particles and the continuous phase, or by applying an external shear stress. The calculated values for σ_g range from 1.27 Pa at 5mm to 16.31 Pa at 64mm. A stress sweep measurement was carried out in order to determine the yield stress value of two samples with different polymer concentrations. In a stress sweep measurement a shear stress is applied and the resulting shear rate is determined. From these two figures the instantaneous viscosity of the sample can be calculated, since $\eta = \sigma/\text{shear rate}$. Rheological measurements show that for a sample which has an initial height of 40mm, that the initial yield stress is of order 0.01 Pa as demonstrated in figure 6.12, but the calculated gravitational stress is of order 10 Pa. It is clear that for the samples investigated here that the measured yield stress during the delay time is less than the gravitational stress and so it expected that particle creaming is occurring at this point. However, this is not the case. From equation 6.3 it is shown that the highest point of the network experiences the greatest level of gravitational stress as a result of the buoyant stress of the entire network below this point. In the scenario of the delay time being controlled by the balance of the yield stress and gravitational stress it would be expected that the delay time is therefore height dependant, and increases as the initial height of

the sample decreases. Experimental observations which investigate both the effect of the polymer concentration and the initial height of the sample show this to be false. Instead there is no height dependence of the delay time, and it increases with increasing polymer concentration as expected (figure 6.13).

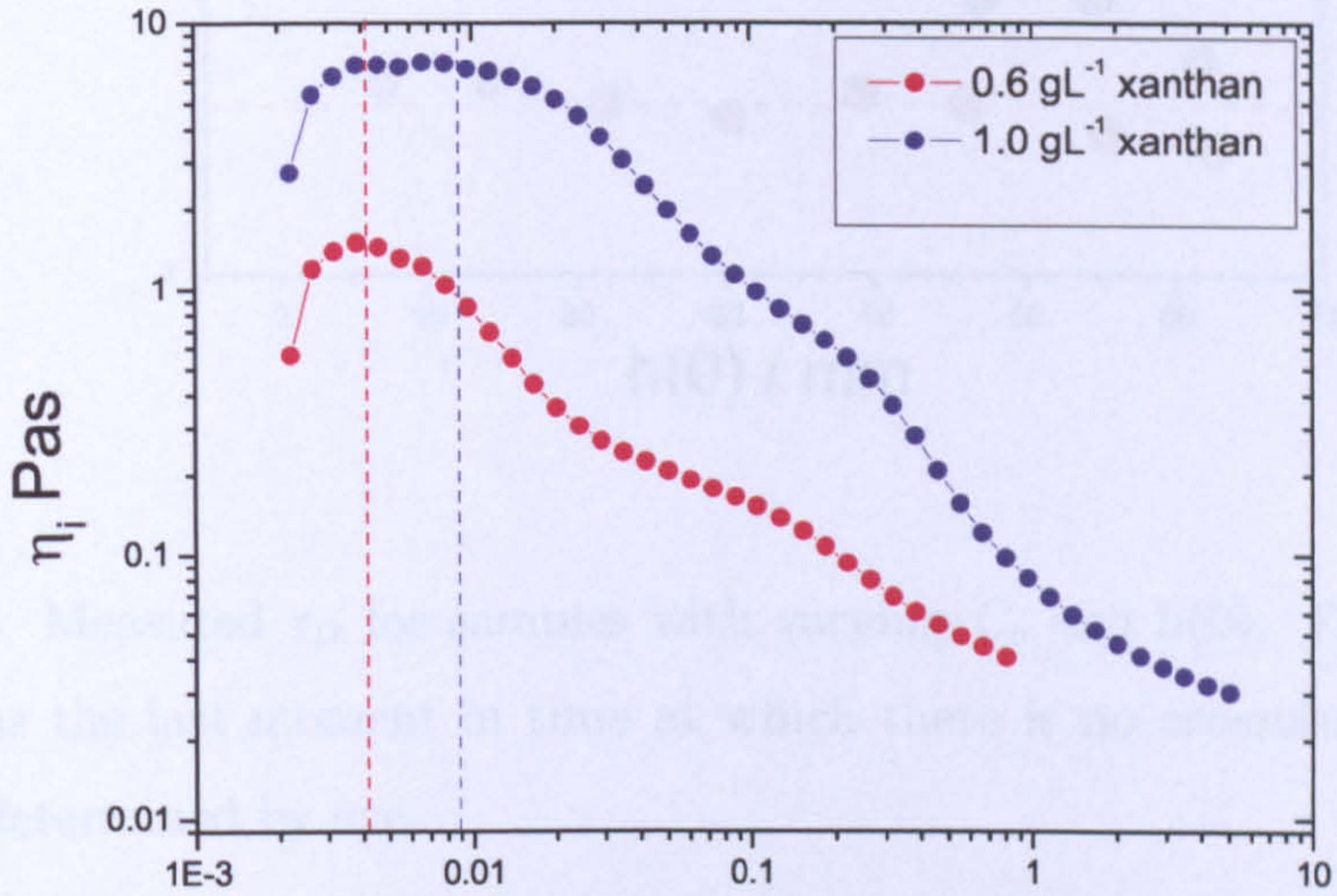

Figure 6.12: Stress sweep measurements of two samples with different amounts of depletion polymer. The instantaneous viscosity, η_i is plotted as a function of the shear stress, σ The decrease in the measured viscosity relates to the onset of network yielding. The red dashed line indicates the onset of yielding in the sample with 0.6 gL^{-1} xanthan and the blue line represents the onset of yielding in the sample with 1.0 gL^{-1} xanthan. Both samples here have a very weak structure with a yield stress that is below 0.1 Pa. The data was obtained during the delay time for each.

From figure 6.13 it can be seen that for all C_p except 0.7 gL^{-1} that there is no effect of *h(0)* on τ_D , and at 0.7 gL^{-1} , τ_D decreases with increasing *h(0)* . Since this pattern contradicts the data at all other C_p , it is assumed that there is no real height effect at 0.7 gL^{-1} . Accordingly all data sets have been fitted to a straight

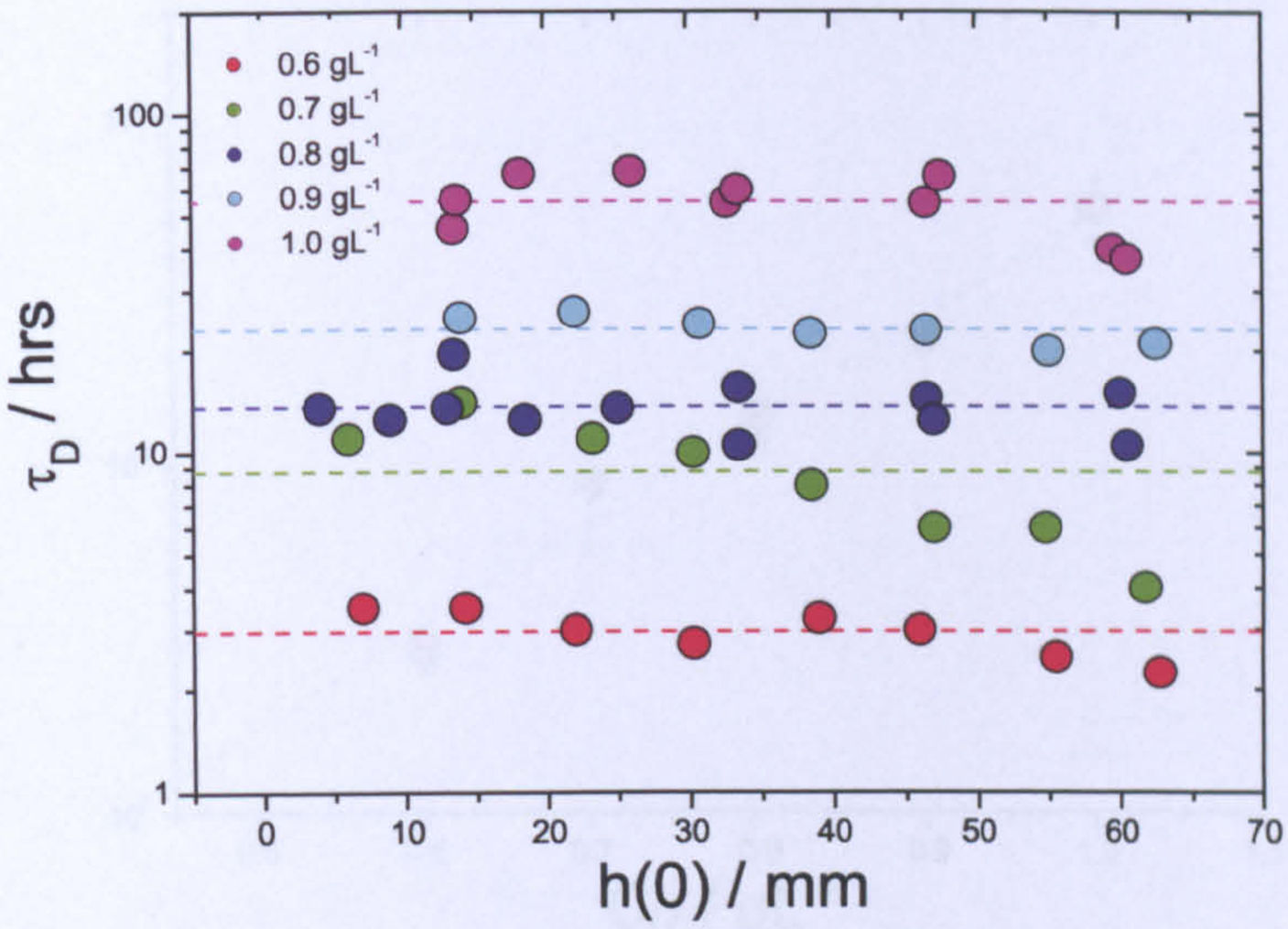

Figure 6.13: Measured τ_D for samples with varying C_p and h(0). The delay time is defined as the last moment in time at which there is no creaming of the bulk sample as determined by eye.

line of zero gradient in order to determine the average τ_D at each C_p . The rate at which the network is able to rearrange is controlled by C_p , and so it is expected that τ_D also depends upon C_p . Figure 6.14 is a plot of the average τ_D at each C_p and shows that this is indeed the case. These data are similar to the findings of Starrs et al [58] which showed that τ_D was independent of height effects at large initial heights in short range attractive systems.

6.5.1 Further study of τ_D

A comprehensive study of the effect of C_p and initial height on the delay time has revealed that the time before which the gel yields is independent of *h(0)* , in contrast to what is seen for short-range gels (see figure 6.14 for data). When discussing the origins of the delay time it has been shown that wall friction can play a role, where solid friction between the container wall and network causes some of the weight of the network to be supported by the walls. Altering the material from

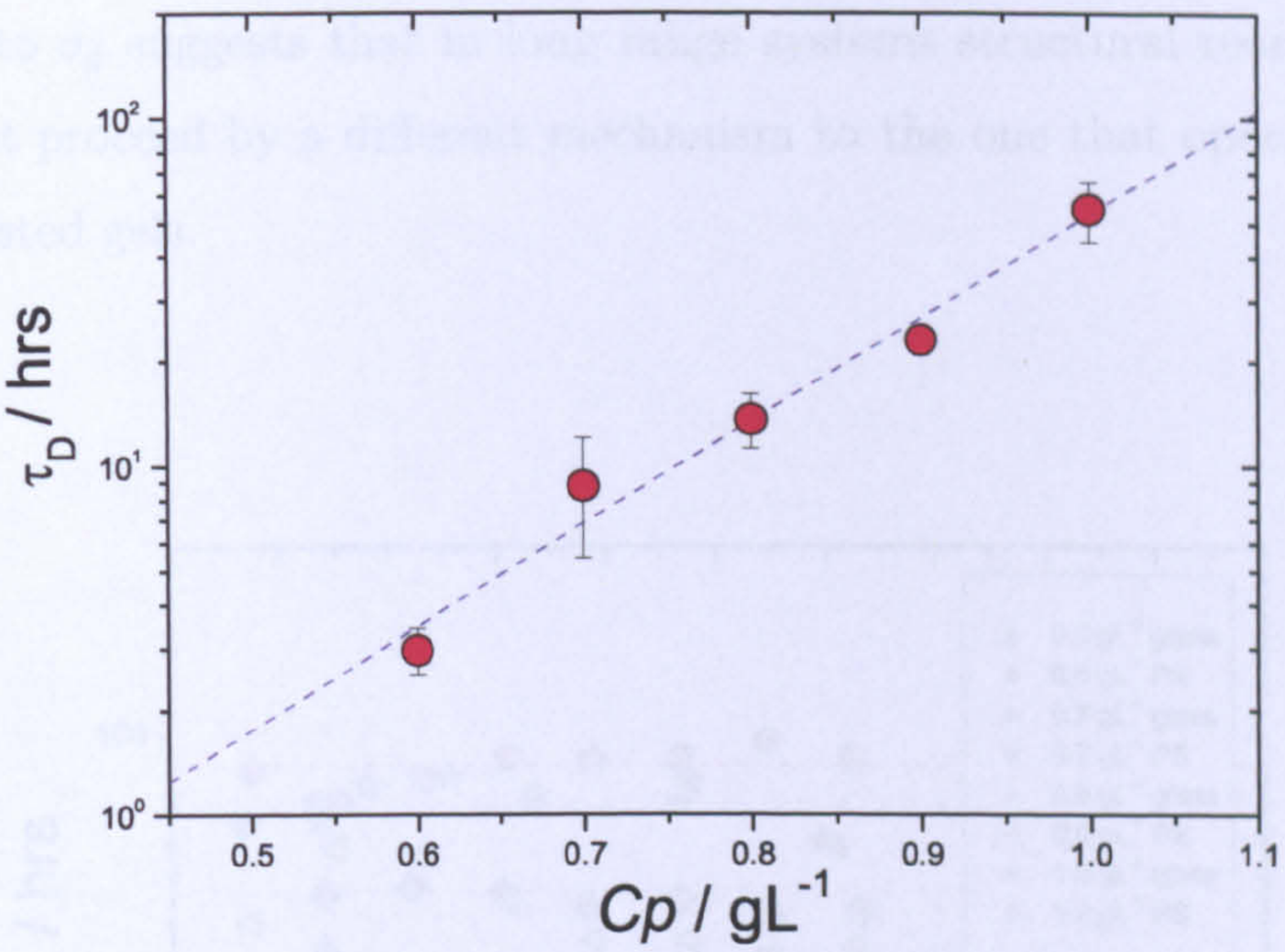

Figure 6.14: Plot showing the average τ_D as shown in figure 6.13 for samples with polymer concentrations in the range 0.6 to 1.0 gL^{-1} xanthan.

which the container was made was shown to alter the timescales for collapse. In order to determine whether wall friction is important within systems with long range attractions, some of the experiments were repeated using cylindrical poly(styrene) cells in place of glass cells to alter the degree of wall adhesion. Samples were prepared at varying C_p and $h(0)$ and added to cylindrical polystyrene vials with an internal diameter of 15mm and τ_D was determined. The results are in excellent agreement with the data obtained in the glass vials, demonstrating that wall friction is unimportant in these systems (figure 6.15). All data sets in figure 6.15 have been fitted with straight lines of zero gradient, since it has previously been decided that there is no effect of $h(0)$ on τ_D .

Changing the applied stress by altering the initial height of the sample does not alter τ_D . Instead τ_D is independent of the applied stress (in this instance it is a gravitational stress). This rules out the possibility that the delay time seen before the gel collapses is due to rearrangements induced by external stress since a de-

crease in τ_D would be expected as the stress is increased. The insensitivity of the delay time to σ_g suggests that in long range systems structural reorganization of the gel must proceed by a different mechanism to the one that operates in short-ranged arrested gels.

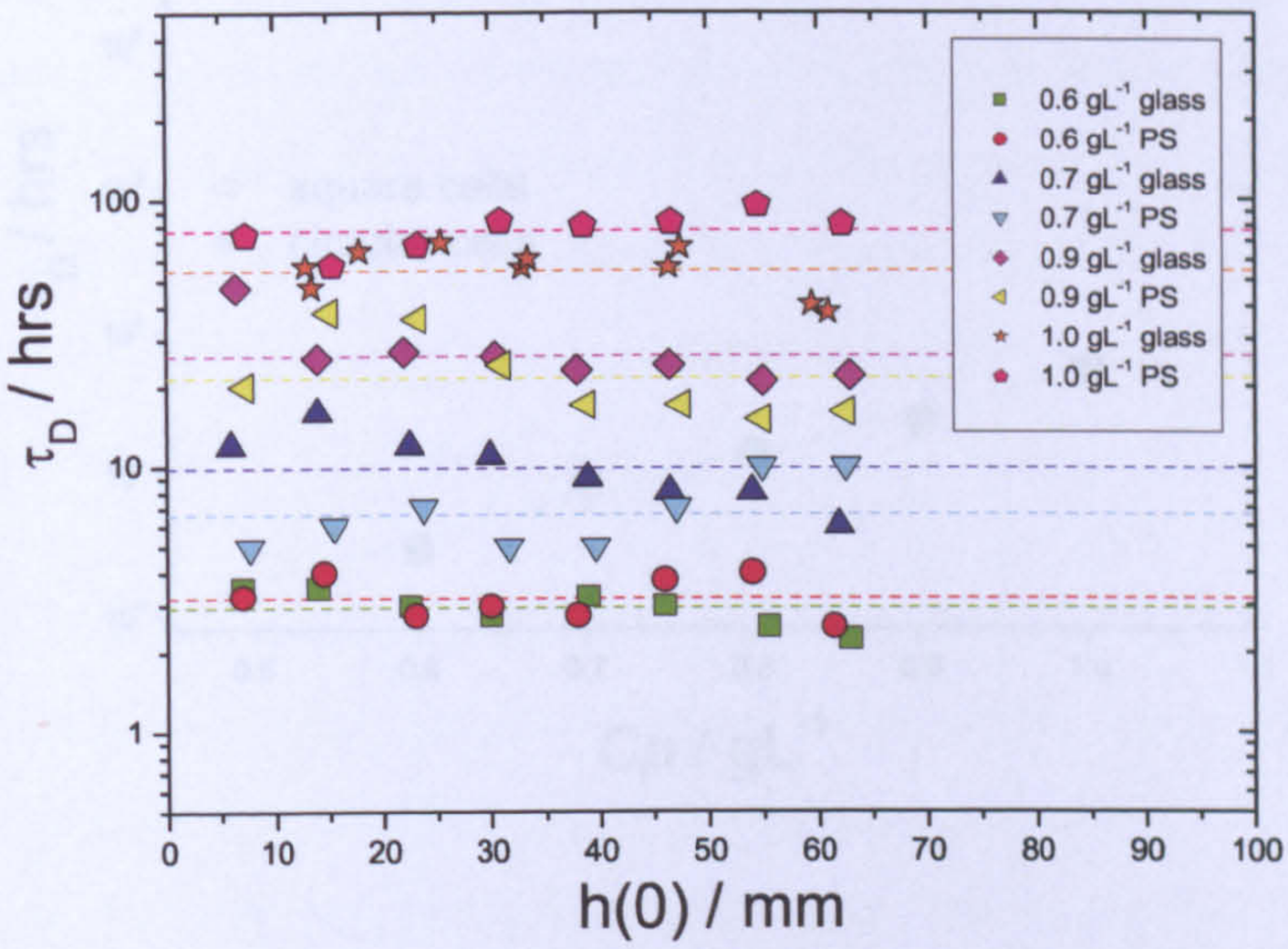

Figure 6.15: Plot showing the measured delay times for samples with identical compositions and comparable initial height, in both glass and polystyrene tubes. The glass tubes had an internal diameter of 17mm, and the PS tubes had an internal diameter of 15mm. In each case there is little difference between the delay times in glass and PS tubes at each polymer concentration.

The final parameter of interest is whether changing the shape of the container has any effect on τ_D . Samples were added to glass square cells which had an internal length of 13mm and τ_D was determined. This size of cell resulted in the circumference of the glass vial and glass square cell being the same, and the surface area of the base of the containers to be different. The results of the two experiments are shown in figures 6.15 and 6.16. From figure 6.16 it is obvious that changing from a cylindrical vial to a square cell drastically alters the measured τ_D values.

Each data set has been fitted with a straight line of an equal gradient of 2.95 hrs /gL^{-1} confirming that τ_D is still dependent upon C_p to the same extent, but that there exists a prefactor to the power law.

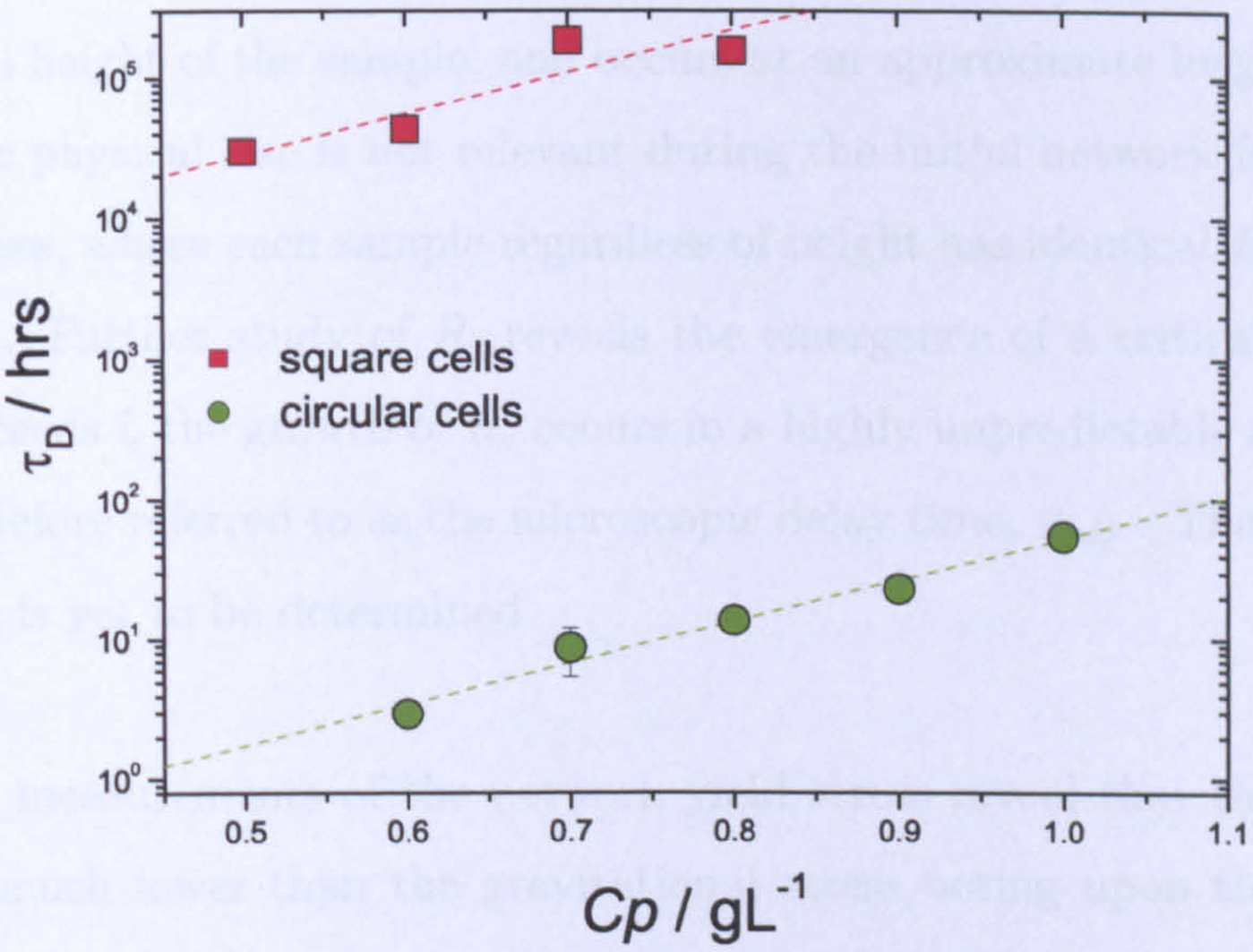

Figure 6.16: Plot showing the delay times of samples with identical composition which here studied in both square and cylindrical tubes. Each data point represents the average delay time taken from samples with a range of initial heights.

6.6 Summary

Confocal microscopy and rheology have been used to probe the microscopic ageing process of a gel network prior to the collapse process occurring in an attempt to better understand the causes of sudden network collapse. Rheological measurements have revealed that the gels behave as visco-elastic materials with solid like behaviour. The elastic modulus exceeds the viscous modulus and continues to increase throughout τ_D . What is perhaps most surprising is that there is only a relatively small drop in G′ at the point of network collapse, which is recovered quickly as the network collapses and increases in local colloid density.

The physical size of the network is a key factor in determining how a network will collapse. Microscopic imaging of the network reveals a physical size threshold above which the network collapses in an inhomogeneous process but collapse occurs homogeneously if the network size is below this threshold (where the threshold refers to the initial height of the sample, and occurs at an approximate height of 12mm). However the physical size is not relevant during the initial network formation and ageing process, where each sample regardless of height has identical R_c and growth rates of R_c . Further study of R_c reveals the emergence of a critical length (l_c). Once R_c exceeds l_c the growth of R_c occurs in a highly unpredictable manner. This point is therefore referred to as the microscopic delay time, τ_{mD} . The link between τ_{mD} and τ_D is yet to be determined.

Rheological measurements of the network yield stress reveal that the yield stress is actually much lower than the gravitational stress acting upon the network at its highest point. In this circumstance it would be expected that the network has insufficient connectivity and would therefore begin to collapse immediately. This however is not the case as the network is resistant to gravitational effects for a finite period of time, indicating that the application of external stresses is unimportant in the process of network ageing in long range attractive networks.

Chapter 7

Collapse of the colloidal network

The particles in a colloidal gel network are constantly rearranging as a result of weak inter particle attractions and a space spanning network with a weak C_p dependant yield stress persists for some time. Eventually the structural integrity of the network is lost and the network collapses to form a dense sediment. This process, particularly in short range attractive systems has been the focus of much research [51, 58, 116]. A universal process for network collapse does not seem likely especially considering the different behaviours which have been observed, for example the network may or may not exhibit a delay period [49, 50]. There has also been a variety of collapse features presented: firstly the network reduces in height linearly with time [61], secondly it may show a period of slow linear collapse (creep) followed by a period of slightly increased but still linear collapse [47, 48, 56], or it may collapse with a non-linear rate [112]. The differences are a result of changes in key parameters such a physical size, ξ, and C_p . Although this provides a very limited picture of the collapse of short range attractive systems, still less is known about the collapse of long range attractive systems.

There are experimental and theoretical reports that state that the physical size of a sample can have an effect on the network collapse process [58, 59, 61, 62]. Tanaka et al report the presence of two distinct collapse processes which are separated by the viscoelastic length ξ_{ve}, where $\xi_{ve} = (2\eta L/\phi^2)^{1/2}$ where L is the size of the system. When the size of the system is less than ξ_{ve} the network shrinks

homogeneously. Once $\xi_{ve}$is exceeded the sample exhibits a heterogeneous collapse, where localised areas of the network show greater degrees of collapse than other areas [62]. Time lapse video imaging is used to analyse network collapse by following the height of the network over time. Results have so far shown that there is a clear height dependant network ageing process with large *h(0)* samples exhibiting localised heterogeneities. The initial height of a sample is also shown to affect the collapse of the network where small *h(0)* samples reduce in height linearly over time and large *h(0)* samples at a rate which is well described by the expression $h(t-\tau_D)/h(0) \sim \exp\left((t-\tau_D)/\tau_C\right)^{\beta}$ where τ_c is a collapse time characteristic of each individual sample. $\beta \approx 1.5$ when *h(0)* is large, independent of C_p and is evidence that gravitational stress does not play a significant role in the network collapse. The precise location of the crossover point from linear to accelerated collapse is not certain, although it occurs when $h(0) = 10 \longrightarrow 15$mm.

7.1 Concentration dependent network collapse

The simplest way in which to investigate the collapse process is by direct observation to produce sedimentation profiles, where the height of the colloid rich phase is recorded as a function of time. This uncomplicated technique has previously been used to investigate the effect of altering a variety of parameters on the collapse process [58, 59, 116, 119]. The amount of published data is unfortunately limited with respect to long range attractive systems, and so a clear picture of what is occurring during gel collapse is yet to be determined. In continuation of the findings presented in the previous two chapters, a comprehensive study of the effect of altering the initial height of the sample and the polymer concentration on the collapse process is presented.

The effect of altering C_p on the collapse process is studied by preparing samples with varying C_p in the range 0.6 to 1.2 gL^{-1} ($U_0/k_BT \approx 6 \longrightarrow 11$)with the same nominal initial height. Using a CCD camera an image of the samples is recorded

every 5 minutes and then used to create a creaming profile where the height of the colloid rich phase is plotted as a function of time. The raw data can be seen in figure 7.1 which shows how the profile at each concentration has the same characteristic shape and the only difference between them is a shift along the X axis as C_p is increased.

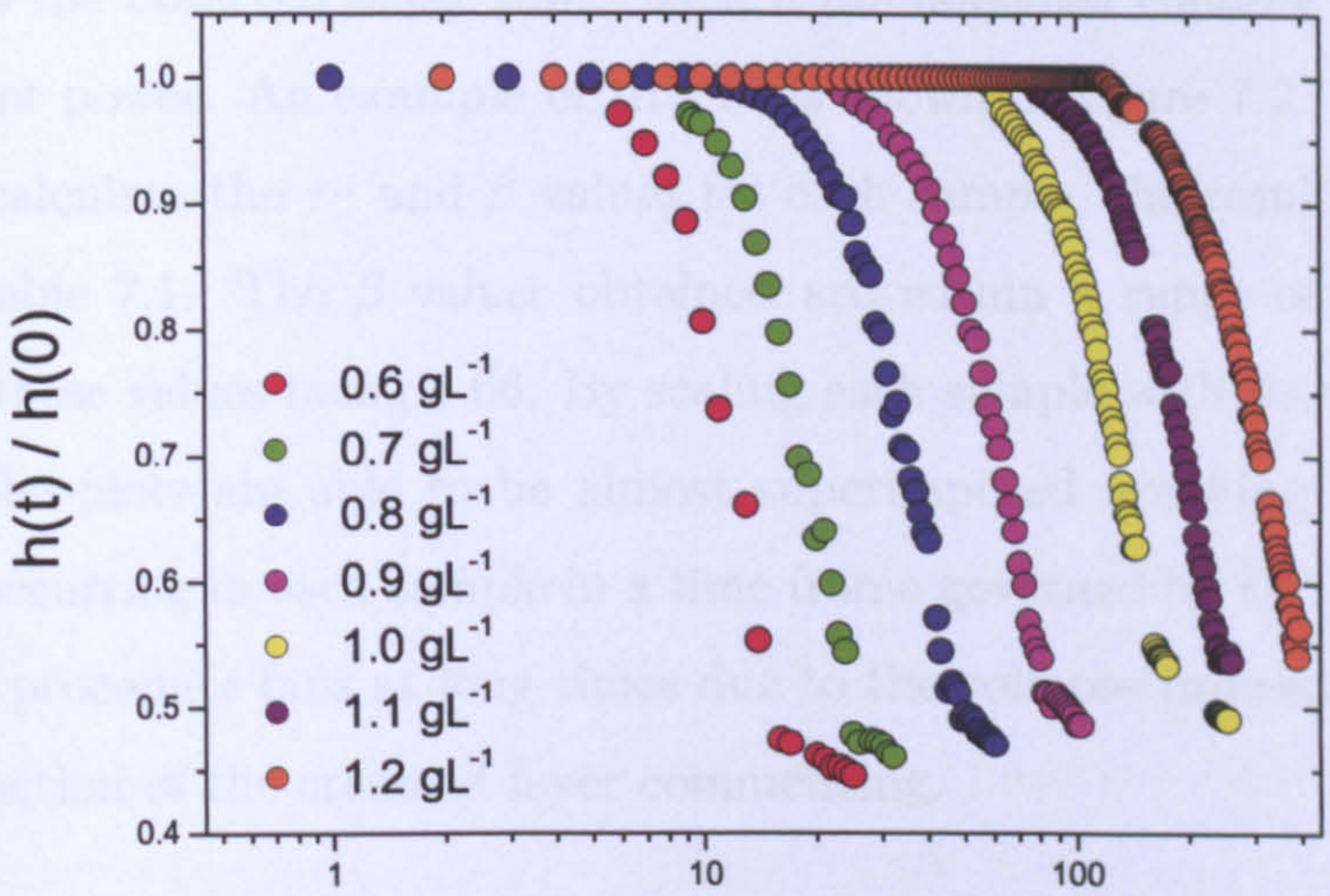

Figure 7.1: Sedimentation profiles of samples with varying polymer concentrations. Here the concentration of polymer has been varied in the range 0.6 to 1.2 gL^{-1}Xn. The heights have been normalised against the initial height for each sample so that the profiles can be compared. The initial heights of each sample were comparable and in the range 37 - 39.75 mm.

To allow the collapse processes to be directly compared, the observed delay time of each sample is deducted from the time at any given point, and so a plot of normalised height versus time minus the observed delay time (t - τ_D)is produced. From figure 7.1 it is clear that the colloid rich phase does not decrease in height linearly with time, as observed by Starrs et al [58]. Instead it decreases in height with an increasing rate. By fitting each data set with a stretched exponential

containing a variable exponent power, a numerical comparison of the data becomes possible. The collapse regime of each data set is therefore fitted with a stretched exponential decay where higher exponent powers indicate faster rates of decay, as follows:

$$h(t)/h(0) = \exp^{-((t-\tau_D)/\tau_C)^{\beta}} \tag{7.1}$$

where τ_D is the observed delay time, τ_C is a fundamental collapse time and β is the exponent power. An example of this fit is shown in figure 7.2. This equation is used to calculate the τ_C and β values for each sample, the results of which are shown in table 7.1. The β values obtained are within a range of 25% with the average of these values being 1.66. By scaling each sample with its own calculated τ_C value, the plots are able to be almost superimposed implying that the same process is occurring in each sample in a time frame governed by C_p (see figure 7.3). The fitting procedure fails at long times due to the collapse process ending, and a slow compaction of the creamed layer commencing.

Table 7.1: Calculated τ_C and β, for samples of fixed h(0) and varying [Xn]

[Xn] gL^{-1}	h(0) / mm	τ_C / hrs	β
0.6	39.5	12.14	1.84
0.8	38.75	43.50	1.84
0.9	38	74.7	1.62
1.0	37	146.93	1.49
1.1	39.75	222.42	1.64
1.2	38.25	377.04	1.54

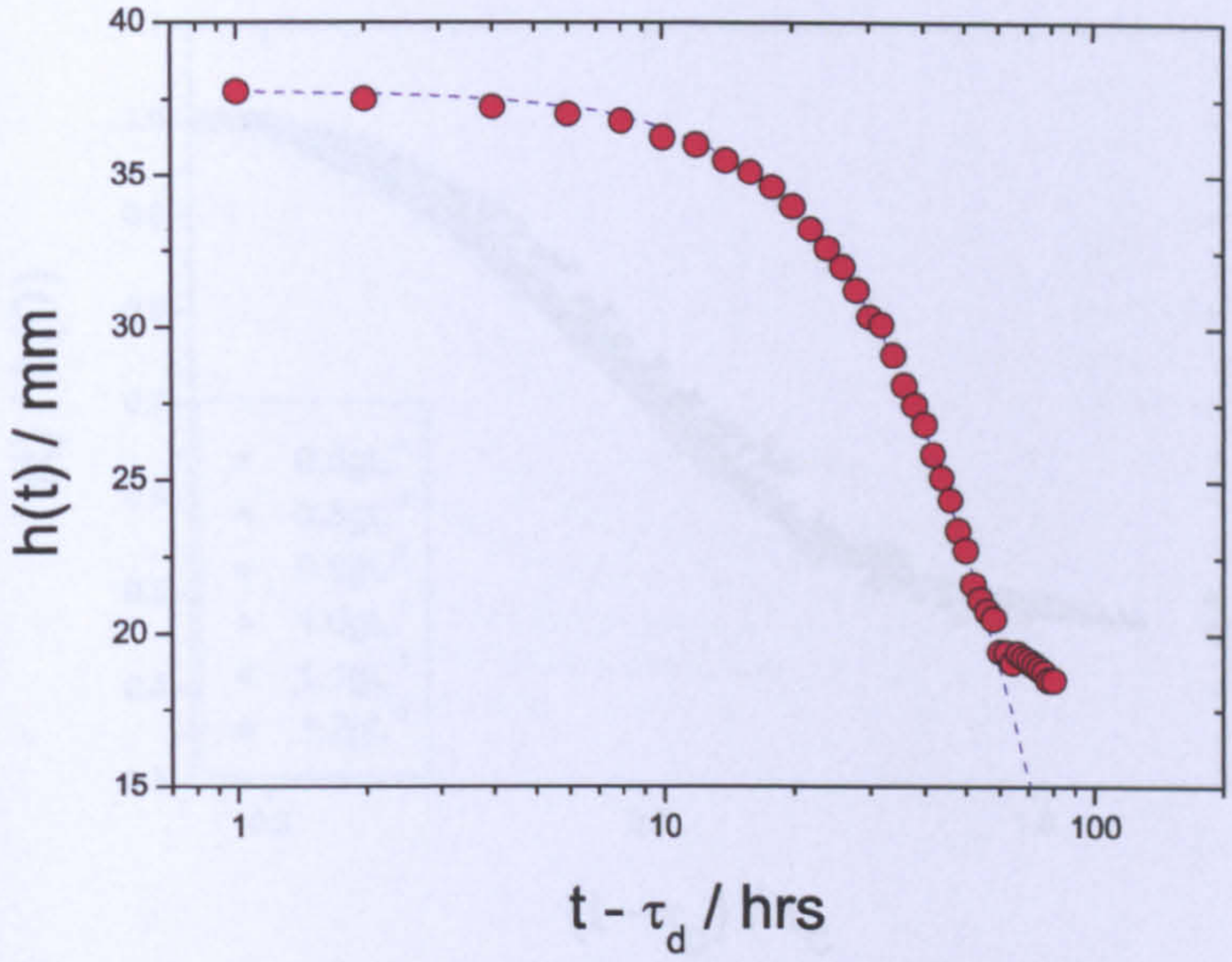

Figure 7.2: A single sedimentation profile shown on a semi-log plot. The measured delay time has been deducted from the time at any given point so that the plot represents only the collapse portion of the profile. The blue dashed line represents the compressed exponential fit.($C_p = 0.9$ gL^{-1}, h(0) = 38mm)

7.2 Height dependent network collapse

In the previous chapters evidence was presented which showed a clear height dependence of the network ageing process, and a height independence of the length of τ_D . The collapse process is studied in order to determine whether it is affected by altering the height of the sample. The effect of altering *h(0)* on the collapse process of emulsion systems is investigated by preparing a large sample with a fixed colloid volume fraction of 0.2 and a fixed non-adsorbing polymer concentration of 0.9 gL^{-1} in the continuous phase ($U_0 \approx 8.5\ k_BT$). The sample was then decanted into a total of 8 vials each with a different volume, to allow for a variety of initial heights in the range 6mm up to 62mm (from the internal base of the cell to the top of the meniscus) to be studied. The glass sample vials were cylindrical in shape with an internal diameter of 17mm and a flat base. Samples were prepared by mixing to-

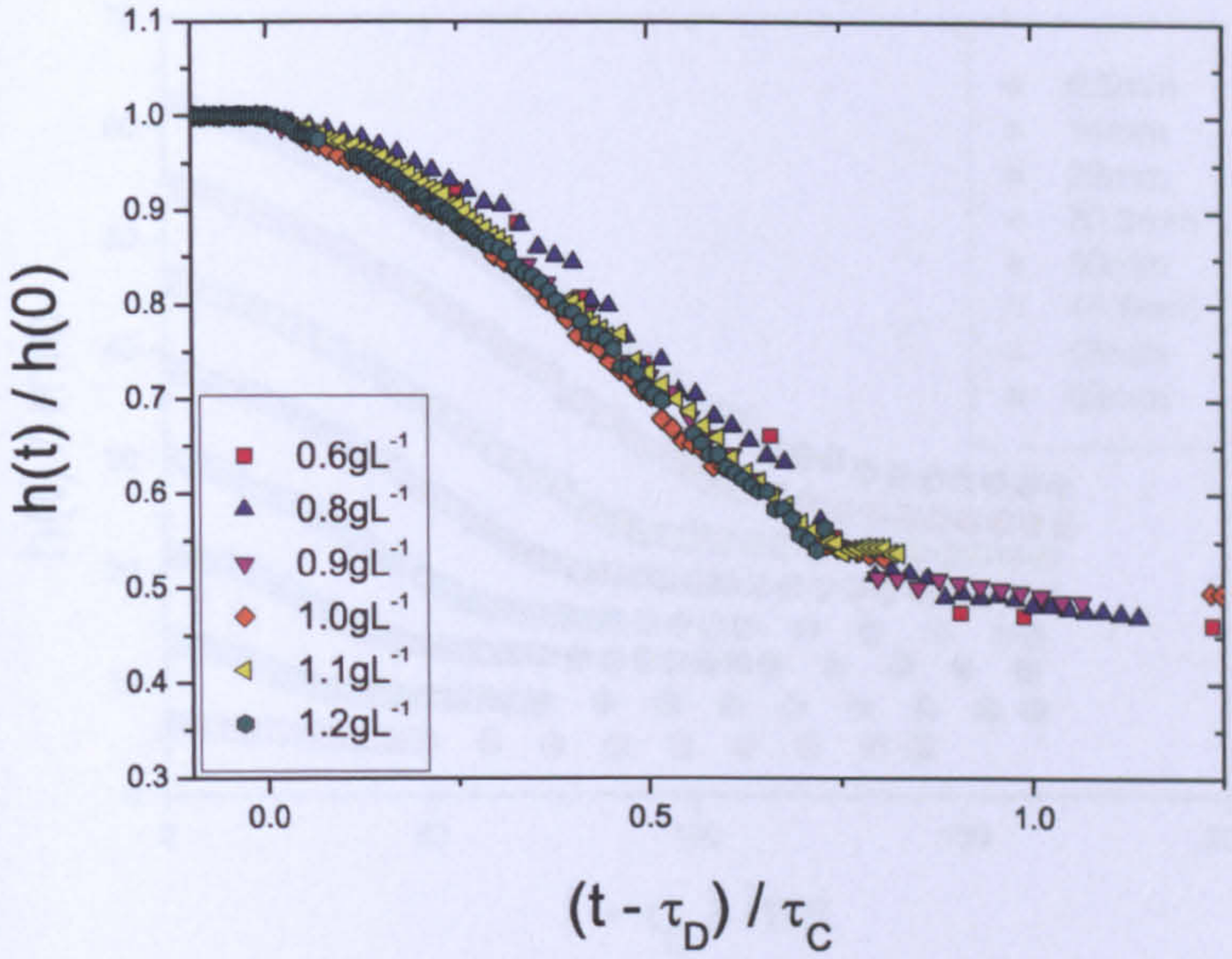

Figure 7.3: Sedimentation profiles of samples with varying polymer concentrations and the same initial heights. The heights have been normalised against each samples initial height, and the data for each sample has been scaled by its calculated τ_C value.

gether appropriate masses of polymer stock solution, ED/H_2O, and dyed ED/H_2O for 3 hours using a magnetic stirrer. The appropriate mass of PDMS stock was then added to this solution and stirred for 10 minutes at 100rpm. This speed of mixing was selected as it was the fasted speed possible which did not introduce any air bubbles which were visible by eye. The introduction of air bubbles has been shown to have an effect on the collapse process and so it is important that these are minimized [117]. The samples were then poured into the vials, and imaging was commenced. The resulting creaming profiles are shown in figure 7.4.

Once again it is apparent from figure 7.4 that the colloidal rich phase decreases in height at an increasing rate. It is not clear however that this is the case for samples with small initial heights since the total distance travelled by the network boundary may only be represented by approximately 12 pixels. A numerical analysis of the

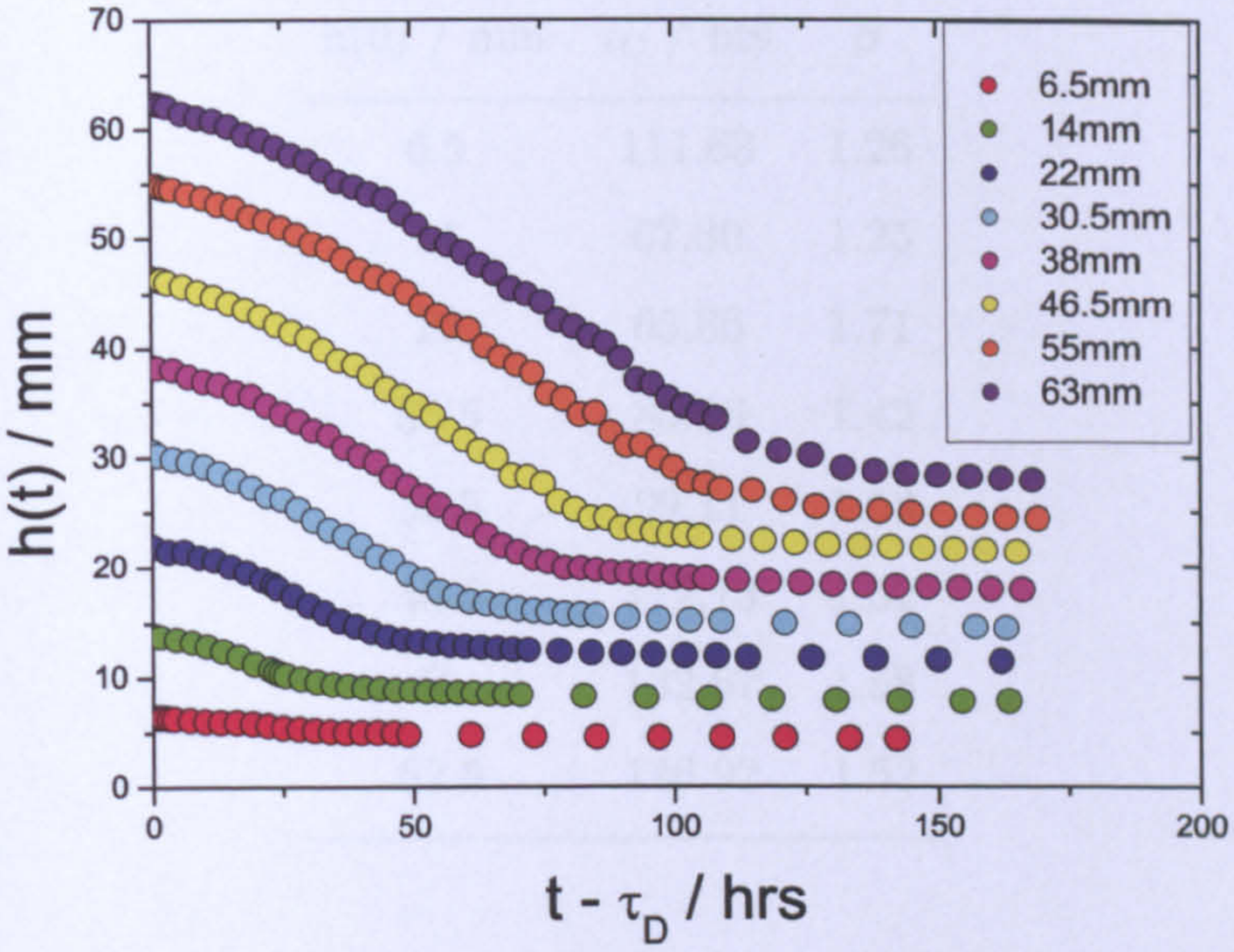

Figure 7.4: Sedimentation profiles of samples with identical composition of 0.9 gL^{-1}, but varying initial heights in the range 6.5 - 63 mm. The delay period has been excluded so that the collapse portion of the data is directly comparable.

data will allow for direct comparison of all data sets and so the values of β and τ_C are calculated for each sample for comparison, a summary of which is detailed in table 7.2.

The values in table 7.2 show that the fundamental collapse times are increasing with sample height, except in the case of the smallest sample. Where the same physical process is responsible for network collapse, an increase in τ_c is expected as there is an increasing distance over which the colloids must travel in order for the gel network to be completely compacted. The presence of height effects are evident when studying the smallest sample of h(0)= 6.5mm where the large value of τ_c indicates a collapse process which is occurring on a much slower timescale. This bears resemblance to the results of Starrs et al [59] who observed slower rates of collapse in samples with small heights and large widths.

Table 7.2: Calculated τ_C and β, 0.9 gL^{-1} Xanthan

h(0) / mm	τ_C / hrs	β
6.5	111.63	1.26
14	67.30	1.25
22	65.86	1.71
30.5	85.96	1.42
38.5	99.11	1.53
46.5	112.73	1.52
55	132.67	1.58
62.5	146.92	1.52

7.2.1 Extended study of height effects on network collapse

The data which has been presented thus far is limited in its ability to prove the presence of a height effect on the collapse process. The increased value of τ_c at a height of 6.5mm indicates a height dependence and so the quantity of data was increased in order to confirm this observation. The experiments were repeated using a range of polymer concentrations (0.6, 0.7, 0.8, and 1.0 gL^{-1} xanthan) with a range of initial heights being studied at each C_p . There is often an error associated with the preparation of collapse profiles making it difficult to reproduce a collapse profile even with identical sample compositions. The process was repeated for a number of samples in order to confirm the level of reproducibility of the experiments. Should the reproducibility be low, a much larger amount of data would be required in order to determine average behaviors. The tallest three samples at 1.0 gL^{-1} were duplicated, as well as the tallest sample at 0.8 gL^{-1} and the results show an excellent level of reproducibility. The resulting creaming profiles are shown in figure 7.5.

The individual profiles in figure 7.5 have decay plot shapes similar to those observed at 0.9 gL^{-1} . A numerical analysis is carried out by again calculating β and τ_C using equation 4.1 the results of which are are detailed in tables 7.3 to 7.6.

A

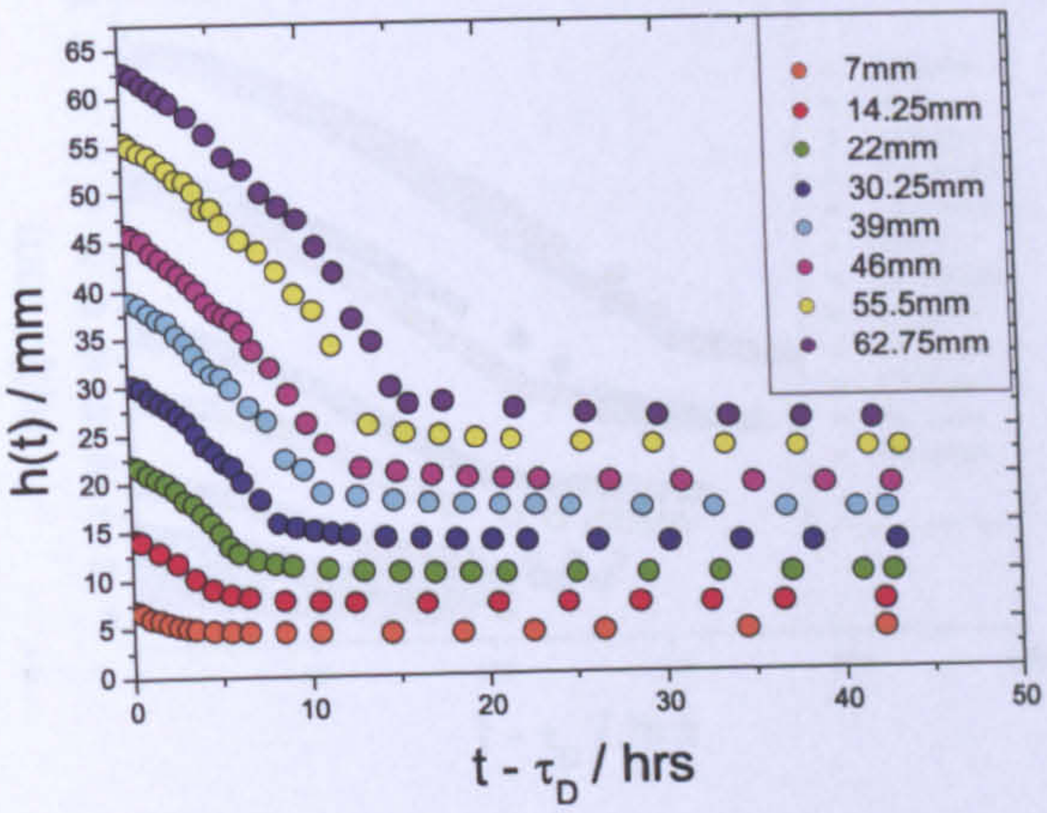
h(t) / mm
t - τD / hrs
7mm
14.25mm
22mm
30.25mm
39mm
46mm
55.5mm
62.75mm

B

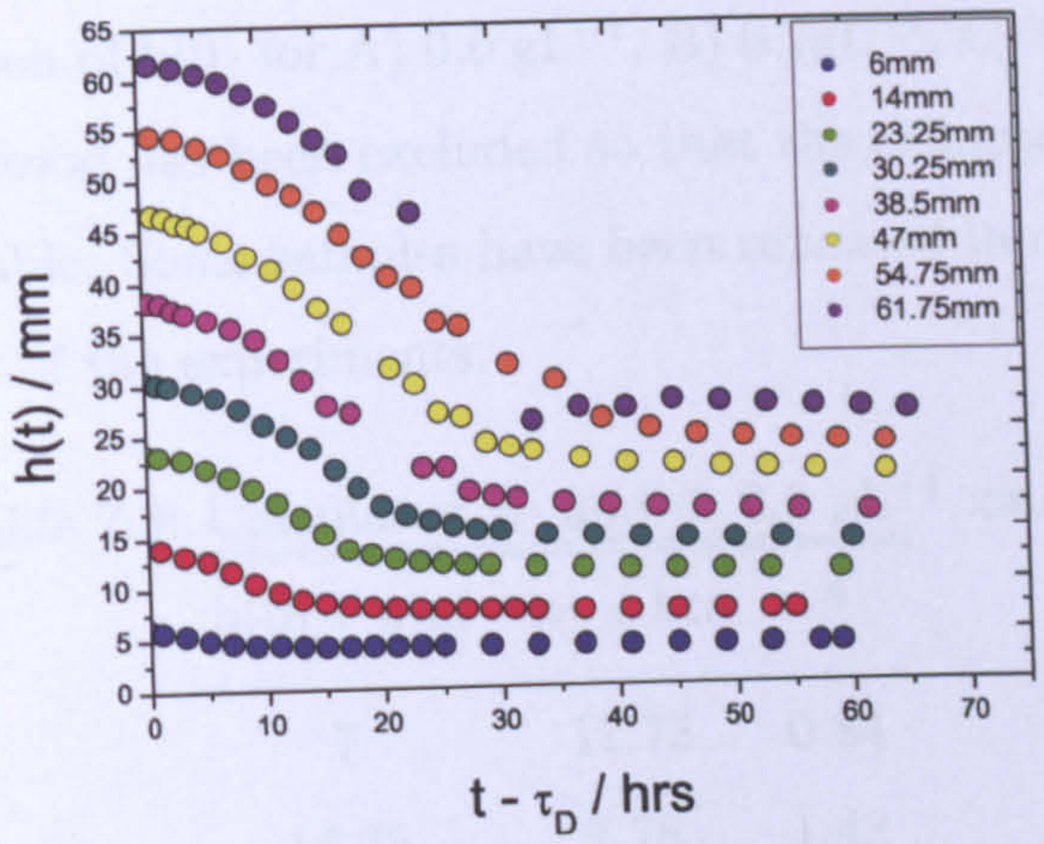
h(t) / mm
t - τD / hrs
6mm
14mm
23.25mm
30.25mm
38.5mm
47mm
54.75mm
61.75mm

C

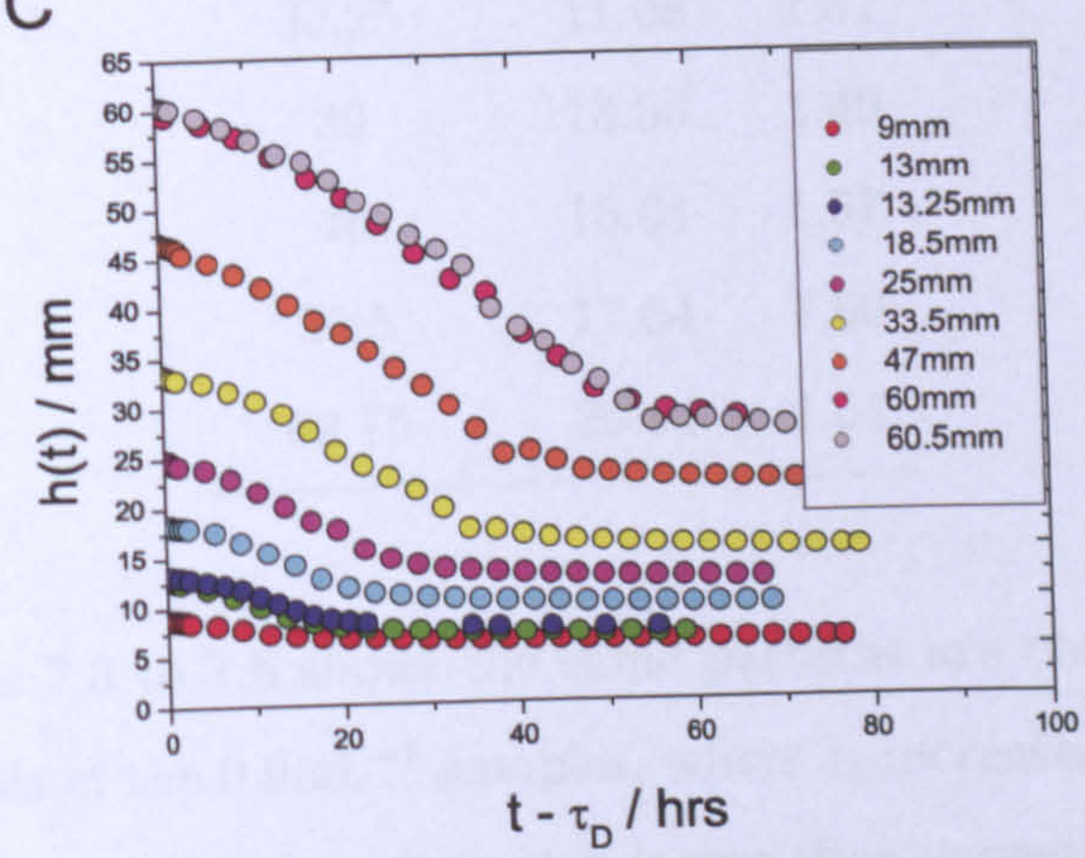
h(t) / mm
t - τD / hrs
9mm
13mm
13.25mm
18.5mm
25mm
33.5mm
47mm
60mm
60.5mm

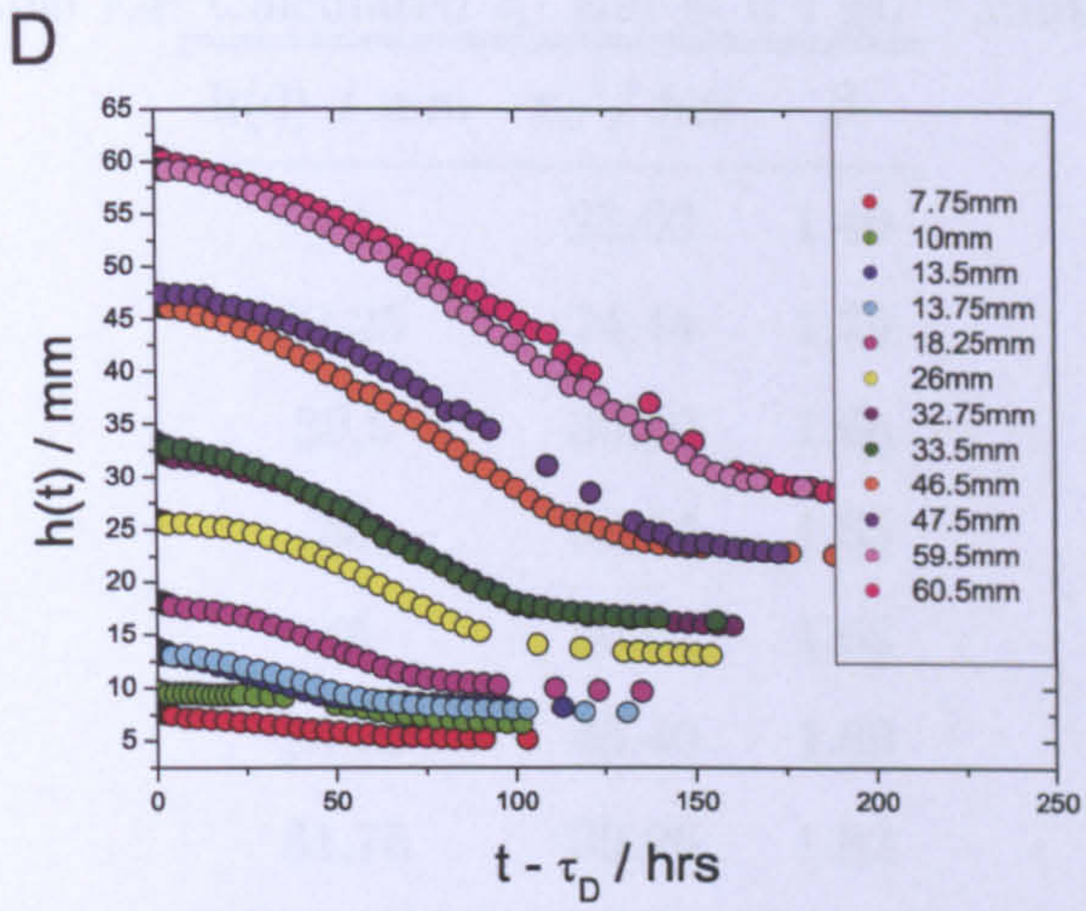

Figure 7.5: Sedimentation profiles obtained showing the height of the continuous network as a function of h(0) for A) 0.6 gL^{-1}, B) 0.7gL^{-1}, C) 0.8 gL^{-1}, and D) 1.0 gL^{-1}. The delay period has been excluded so that the collapse portion of the data is directly comparable. Some samples have been repeated in order to demonstrate the reproducibility of the experiments.

Table 7.3: Calculated τ_C and β, 0.6 gL^{-1} xanthan

h(0) / mm	τ_C / hrs	β
7	11.73	0.84
14.25	7.78	1.42
22.5	9.01	1.56
30.25	11.08	1.57
39	13.56	1.49
46	15.01	1.51
55.5	17.64	1.60
62.75	20.84	1.51

A review of tables 7.3 to 7.6 shows the same patterns are observed as previously seen in the analysis of the 0.9 gL^{-1} samples, where τ_c increases with sample height except for small height samples where it is larger than expected. Samples with an

Table 7.4: Calculated τ_C and β, 0.7 gL^{-1} xanthan

h(0) / mm	τ_C / hrs	β
14	21.62	1.40
23.25	24.44	1.79
30.5	30.50	1.66
38	32.44	1.65
46	36.07	1.68
54.75	43.40	1.69
61.75	39.96	1.82

Table 7.5: Calculated τ_C and β, 0.8 gL^{-1} xanthan

h(0) / mm	τ_C / hrs	β
4	39.49	0.86
9	66.21	0.93
13	33.52	1.15
13.25	30.08	1.60
18.5	33.92	1.55
25	38.92	1.45
33.5	38.92	1.72
33.5	46.04	1.60
46.5	54.71	1.56
47	58.72	1.34
60	65.46	1.57
60.5	64.88	1.65

increasing rate of network collapse are evident by β values greater than 1. When $\beta = 1$, the rate at which the height of the colloid rich phase decreases in height is linear over time.

A plot of β as a function of h(0) and C_p reveals a trend where two different values

Table 7.6: Calculated τ_C and β, 1.0 gL^{-1} xanthan

h(0) / mm	τ_C / hrs	β
7.75	208.18	0.88
8	194.10	1.09
13.5	104.12	1.22
13.75	125.75	1.13
18.25	108.75	1.58
26	121.59	1.93
32.75	138.33	1.61
33.5	135.88	1.53
46.5	160.57	1.57
47.5	175.96	1.77
59.5	200.53	1.58
60.5	211.99	1.61

for β emerge. At small h(0) β is close to 1, and at large h(0) β is close to 1.5, quantitatively confirming that there are two different collapse processes occurring. Figure 7.6 is a plot of all β values obtained as a function of both C_p and h(0) and shows the emergence of the two β values. Where β is close to 1 at small h(0), a plot of h(t) versus log (t-τ_D) yields a straight line in the collapse regime, and so this collapse process is referred to as linear collapse. Where β is close to 1.5 a plot of h(t) versus log (t-τ_D) yields an exponential decay pattern with an increasing rate of collapse with time. This process is referred to as accelerated collapse. It is therefore concluded that the network collapse process, as well as network ageing route is indeed height dependant. There does not seem to be a point where there is a precise crossover from the linear collapse regime to the accelerated collapse regime. Instead there is a region where the crossover occurs, which is in the region of $h(0) = 10 \longrightarrow 15$mm. It is not likely that this region is able to be further reduced by producing additional creaming profiles and so this is not attempted.

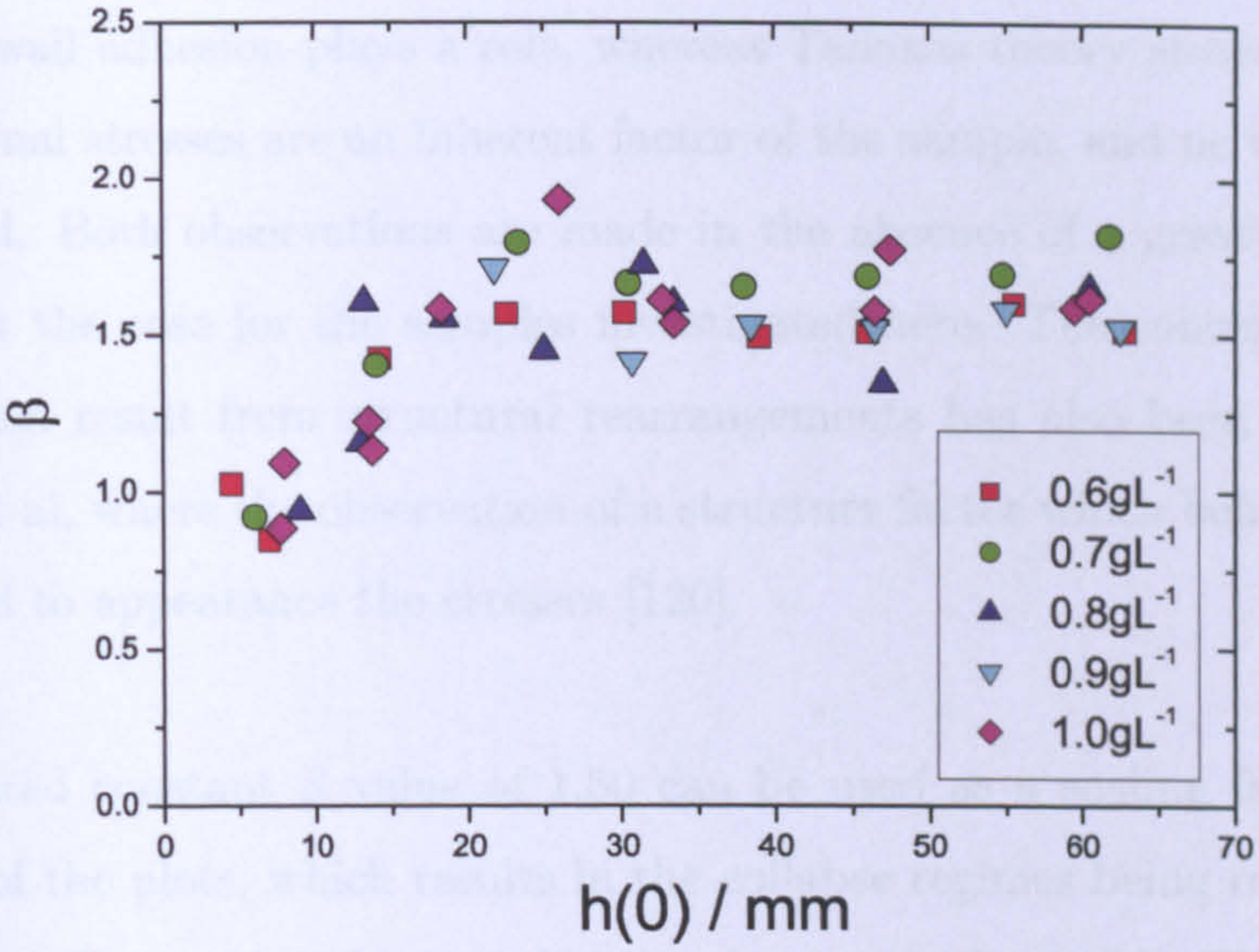

Figure 7.6: Plot of β as a function of C_p and $h(0)$.

7.3 Collapse rates in large height samples

A review of all data obtained so far shows that the average β value of all samples undergoing accelerated collapse is 1.58 ± 0.15. This value is comparable to the scaling factor of $^{3/2}$ which was reported by Cipelletti et al [108] who followed the dynamic structure factor of gels using multispeckle dynamic light scattering. The system investigated was an index matched colloidal polystyrene, with aggregation being induced by the addition of salt. Any behaviour witnessed was therefore as a result of internal forces and restructuring, rather than gravity. Their model and experiments suggest that there is restructuring within the gel, which leads to the breaking of inter-cluster bonds and allowing for the decay rate to increase. Cipelletti et al conclude that adhesion to the cell walls prevents the gel from shrinking continuously and uniformly with time. Instead, shrinking occurs locally resulting in regions of deformity. The concept of areas exhibiting localised shrinkage is something which can also be described by Tanaka's internal stress theory which states that inhomogeneities are due to particle rearrangements. Although the two theo-

ries predict the same behaviour, the origins of this behaviour is different. Cipelletti states that wall adhesion plays a role, whereas Tanakas theory states that the localised internal stresses are an inherent factor of the sample, and no outside forces are observed. Both observations are made in the absence of a gravitational field, which is not the case for the samples investigated here. The concept of internal stresses which result from structural rearrangements has also been discussed by Bouchard et al, where the observation of a structure factor which behaves as $(q\tau)^{\frac{3}{2}}$ is attributed to appearance the stresses [120].

The calculated constant β value of 1.50 can be used as a scaling factor to scale the X axis of the plots, which results in the collapse regimes being represented by straight lines. The results of this scaling can be seen in figure 7.7. The linear slope of each plot within the accelerated collapse regime now appears to be fixed when C_p is constant. The gradient of the straight line is calculated for each sample at a fixed polymer concentration, and then the average figure is obtained. This average gradient figure is used to fit a straight line to the collapse regime in plots of h(t) versus t-$\tau_D^{3/2}$, as shown by the dashed lines in figure 7.7.

The effect of altering C_p can be observed by plotting the average gradient at each concentration as a function of C_p (see figure 7.8) and it is observed that the rate of collapse decreases exponentially as the concentration of polymer increases.

A

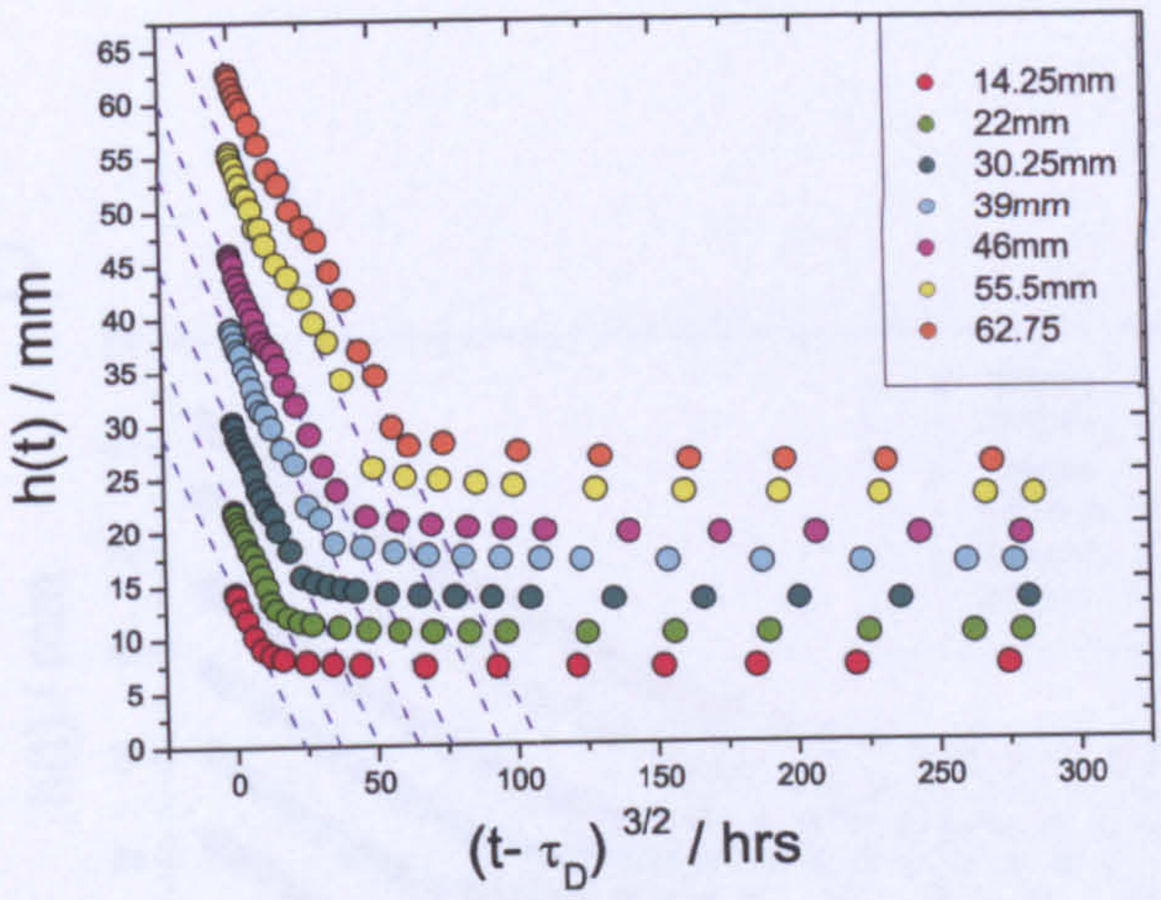
h(t) / mm
(t- τD) 3/2 / hrs
14.25mm
22mm
30.25mm
39mm
46mm
55.5mm
62.75

B

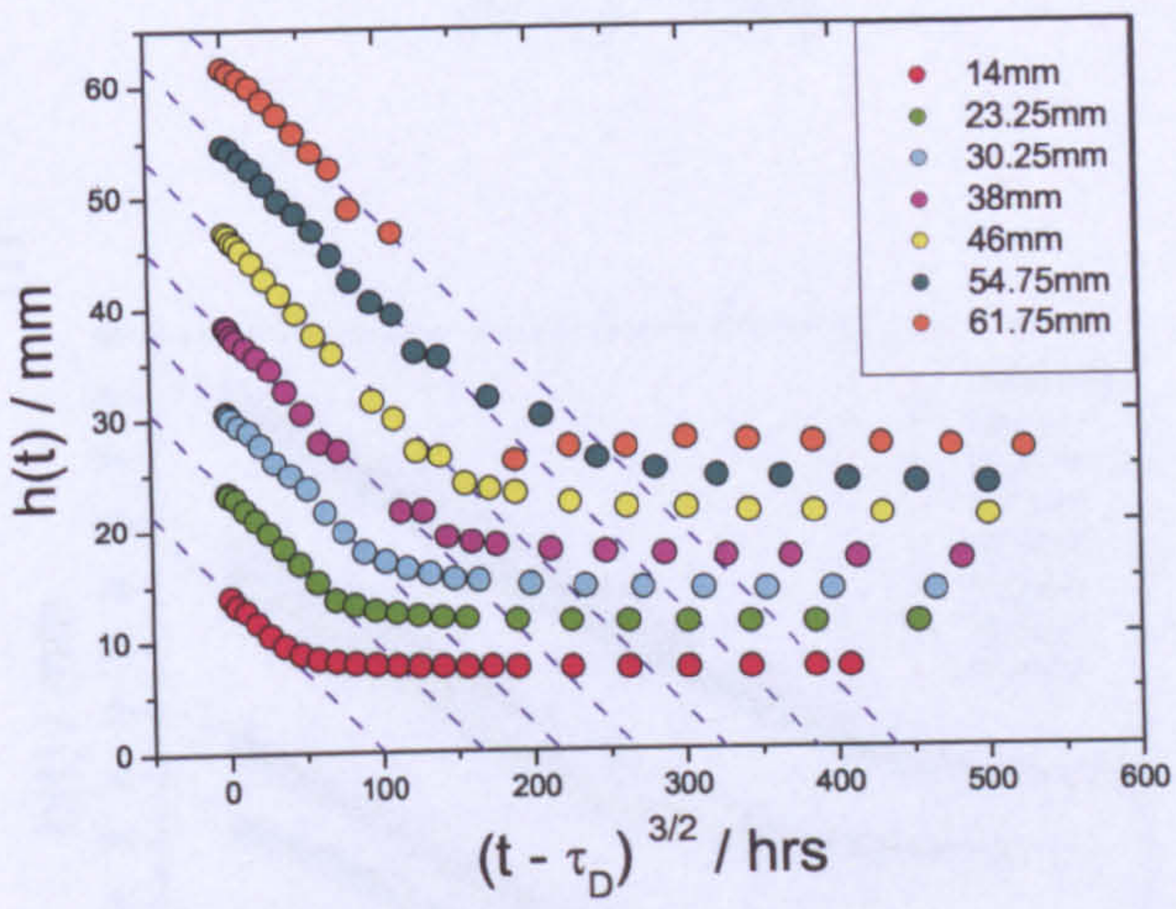
h(t) / mm
(t - τD) 3/2 / hrs
14mm
23.25mm
30.25mm
38mm
46mm
54.75mm
61.75mm

C

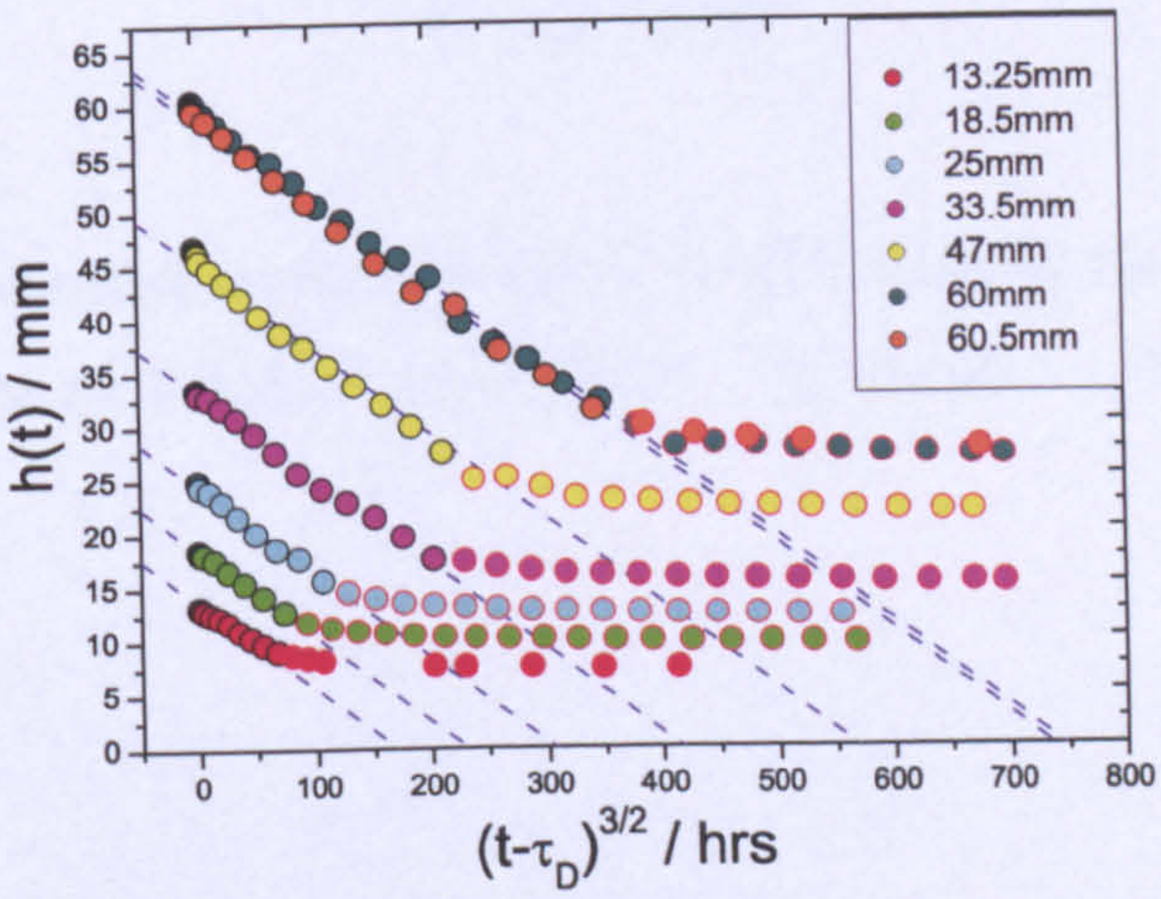
h(t) / mm
(t-τD)3/2 / hrs
13.25mm
18.5mm
25mm
33.5mm
47mm
60mm
60.5mm

D

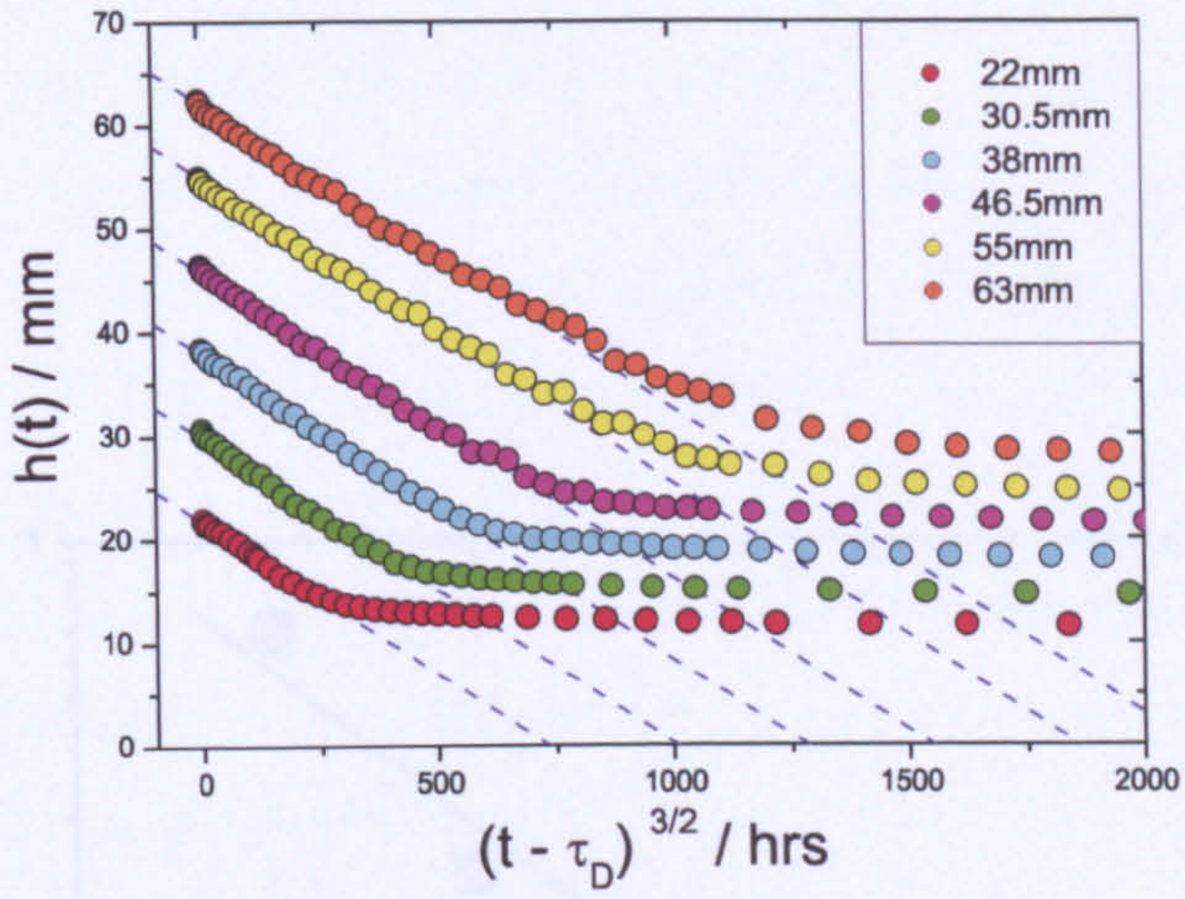

E

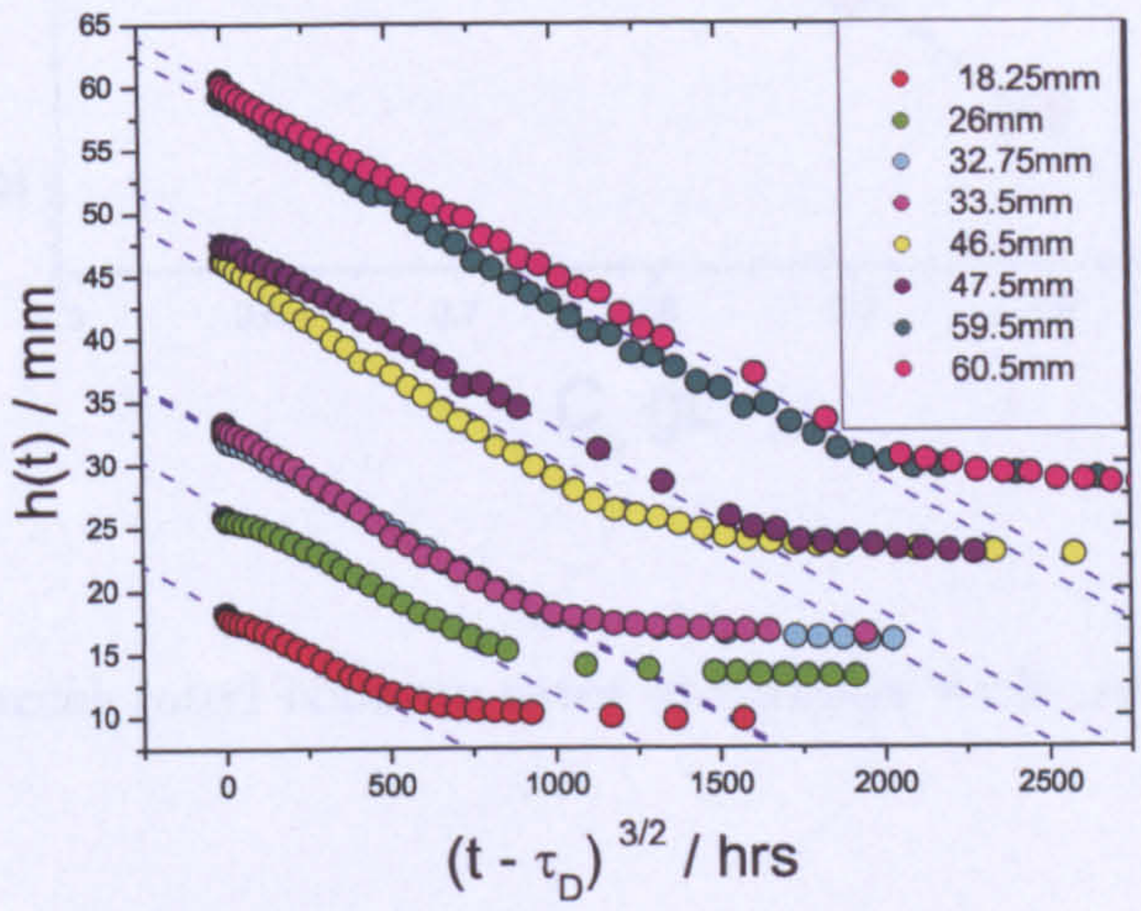

Figure 7.7: Sedimentation profiles of h(t) V (t-$\tau_D^{3/2}$) showing the linear fits of the collapse regimes for A) 0.6 gL^{-1} , B) 0.7gL^{-1} , C) 0.8 gL^{-1} , D) 0.9, and E) 1.0 gL^{-1} xanthan.

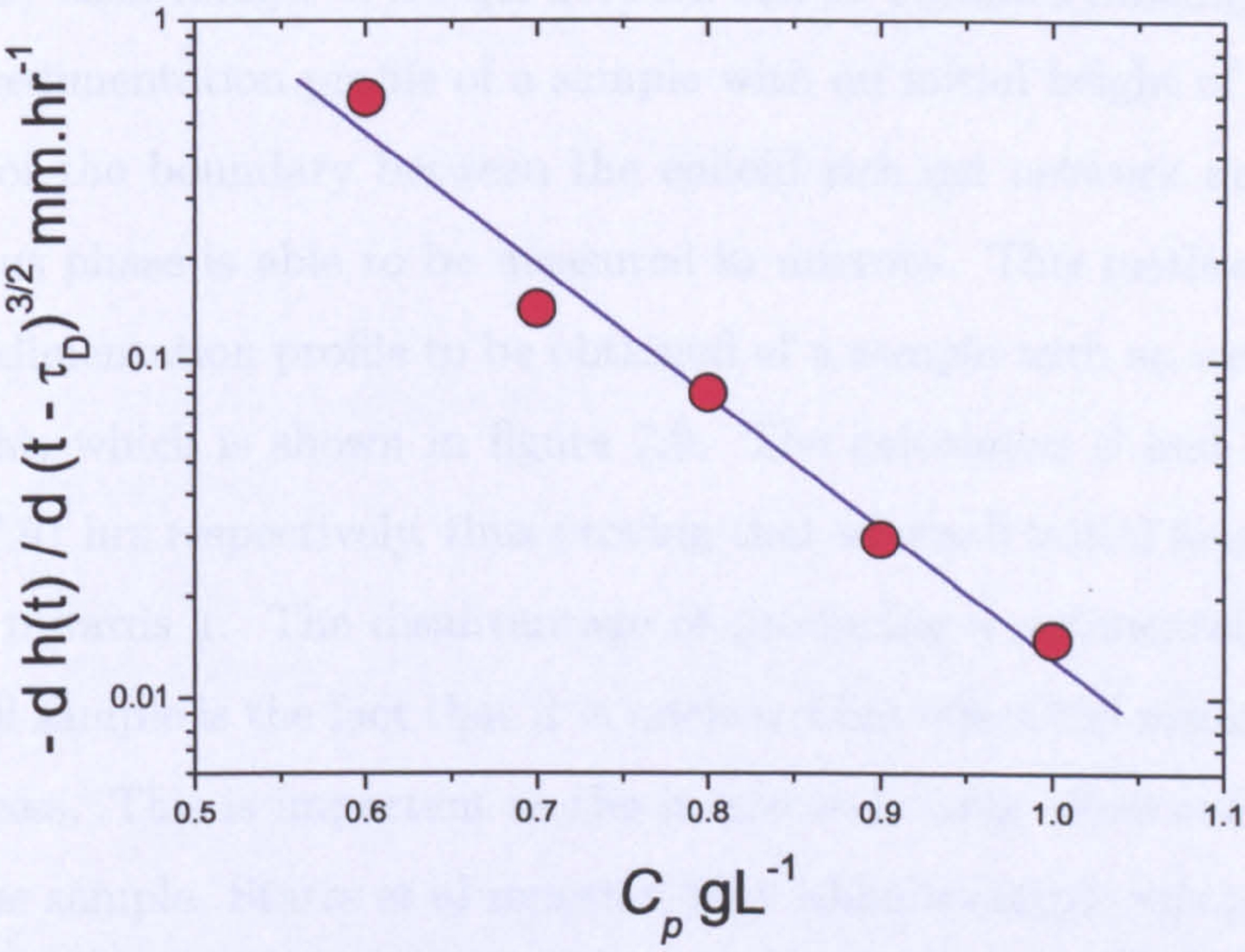

Figure 7.8: The accelerated collapse rates of samples with varying polymer concentration.

7.4 Collapse rates in small height samples

When looking at the β values in figure 7.6 it is plausible to assume that the values for β do not decrease to a value of 1 as the height is decreased, instead it continues to fall below 1. A failure of the video microscopy method is that the maximum resolution is 0.25mm per pixel, depending on how close the samples are to the camera. This means that it would be extremely difficult to produce accurate sedimentation profiles of samples with very small initial heights. As noted previously it is impossible to obtain single particle resolution on the laser scanning confocal microscope. However very clear images of the gel network can be obtained making it possible to produce a sedimentation profile of a sample with an initial height of 720μm . The movement of the boundary between the colloid rich gel network and the colloid poor aqueous phase is able to be measured in microns. This method has allowed a precise sedimentation profile to be obtained of a sample with an extremely small initial height, which is shown in figure 7.9. The calculated β and τ_C values are 1.05 and 47.91 hrs respectively, thus proving that at small initial heights the value of β tends towards 1. The disadvantage of producing a sedimentation profile of such a small sample is the fact that it is unclear what effect the meniscus will have on the process. This is important as the meniscus is large when compared to the height of the sample. Starrs et al reported that when a sample was produced with a large enough width that no meniscus was present, that the delay time of a sample was affected [58]. No comment was made as to whether the absence of a meniscus affected the collapse process.

7.5 Summary

A detailed analysis of the macroscopic collapse of colloidal gels with long range attractions as a function of C_p and *h(0)* has been undertaken by means of time lapse video imaging. Initially the effect of altering quench depth is studied by preparing samples with varying C_p at fixed *h(0)* and comparing the resulting network collapse profiles. The profiles have a characteristic shape and by scaling each curve by its

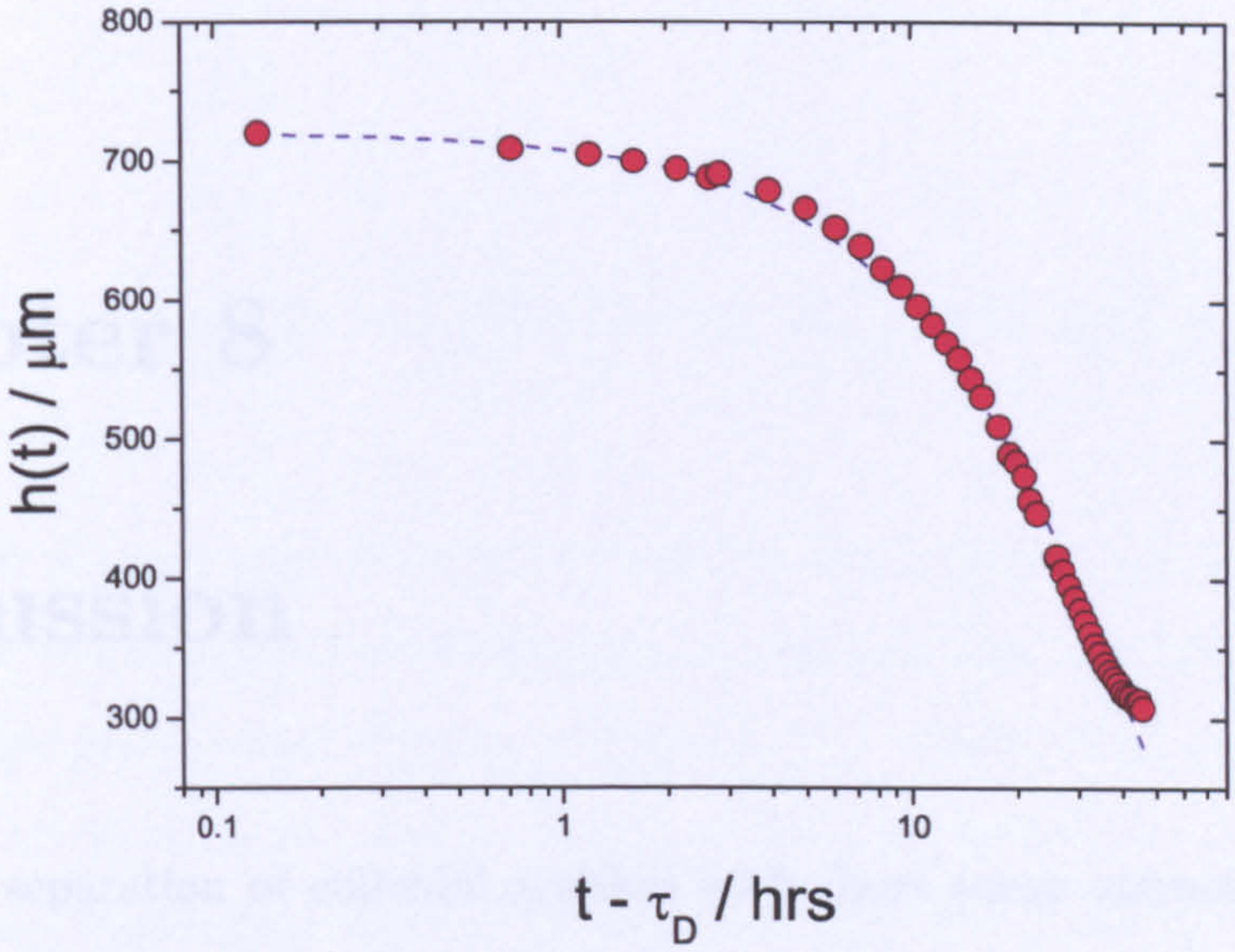

Figure 7.9: Sedimentation profile obtained of a sample less than 1mm high using the confocal microscope.

calculated τ_c value they are able to be superimposed, indicating a universal collapse process.

As observed during the delay phase direct comparison of the collapse profiles has determined that the collapse process is clearly dependant upon the physical size of the sample, where the colloid rich phase of a large *h(0)* sample reduces at a rate which is well described by the expression $h(t-\tau_D)/h(0) \sim \exp\left((t-\tau_D)/\tau_C\right)^{\beta}$ where $\beta \approx 1.5$. When *h(0)* is small the network collapses linearly where $\beta \approx 1$, reminiscent of the collapse of strong gels. The location of the crossover point from linear to accelerated collapse is unclear, although it occurs when the initial height is in the range $10 \longrightarrow 15$mm.

When $\beta \approx 1.5$, plots of *h(t)* versus $(t-\tau_D)^{\frac{3}{2}}$ yield linear rates of collapse where the rate is independent of *h(0)* but is a strong function of C_p . Higher C_p results in slower rates of collapse due to an increase in the strength of the attraction.

Chapter 8

Discussion

The phase separation of colloidal systems with short range attractions has been well documented in recent years [58, 61], but much less is known of long range attractive systems. In this thesis the ageing and collapse of long range colloidal gels have been extensively studied as both a function of polymer concentration and initial height using a combination of laser scanning confocal microscopy (LSCM), time lapse video imaging and rheology. The aim of this work has been to clarify the differences between short and long–range systems and so to understand the mechanism of gel collapse.

The work in this thesis has focused on the initial delay period, where the space spanning network persists, and the time required for the network to lose its integrity and to collapse into a dense sediment. The following sections detail the key findings of this research:

8.0.1 Lack of dynamical arrest

In chapter 5 the early stages of phase separation and network ageing was studied using LSCM. The characteristic domain radius was calculated from the structure factor of each micrograph resulting in a quantitative description of the networks. Up to sample ages of order the bond life-time there is no increase in R_c but an increasing intensity indicates a spinodal–like mechanism of phase separation. The

network does not become arrested at any point and network ageing is able to proceed in full.

8.0.2 Different ageing processes at small and large length scales

The microscopic ageing of networks throughout the entire delay time was studied in chapter 6 as functions of both the polymer concentration and the initial sample height. Rheological measurements describe a network which increases in elasticity throughout the delay time, while at long time stress relaxation measurements reveal the ultimately liquid-like nature of the network. LSCM was used to follow the ageing of networks with two different initial heights (5mm and 15mm) by repeatedly imaging the full height, at intervals of 1mm, as a function of time. Whilst initially both networks form homogeneous networks of identical domain size, localised areas of inhomogeneities appear as a result of advanced coarsening within the large *h(0)* network. From LSCM images these inhomogeneities occur randomly within the sample but always separated from the immediate vicinity of the top and bottom of the cell. Large scale structural rearrangements which result in the formation of large channels are not observed at any point.

Network coarsening proceeds until the domain radius reaches a critical length, where the critical length, $l_c \approx 2\pi$ multiplied by the capillary length, l_{cap} . Beyond this critical length coarsening proceeds in a much more erratic and unpredictable manner as expected for the onset of network collapse. The age of the sample at the point when l_c is reached is therefore identified as the microscopic delay time.

By increasing the initial height of the sample the gravitational stress at the top of the network is increased. The resulting delay time is independent of the initial height while the gravitational stress increases by approximately one order of magnitude from 5 mm to 65 mm in the experimental samples.

8.0.3 Different collapse processes in the small and large height gels

Chapter 7 presents a study of the collapse process using time lapse video imaging so that the bulk of the network could be observed. The most striking observation of this study is that the nature of the collapse is clearly dependent upon the physical size of the sample. For large samples the gel reduces in height at a rate which is well described by the expression $h(t-\tau_D)/h(0) \sim \exp\left((t-\tau_D)/\tau_C\right)^{\beta}$ with $\beta \approx 1.5$. The rate of collapse is independent of initial height but is a strong function of polymer concentration. When the initial height is small the network collapses linearly and $\beta \approx 1$, reminiscent of the collapse of strong gels.

8.1 Proposed mechanism for network collapse

A fundamental question in determining the mechanism responsible for network collapse is whether the stresses which result in collapse have external origins, or whether they are intrinsic to the system. By altering the initial sample height the maximum amount of gravitational stress acting upon each sample has been altered. The collapse of strong gels results when the gravitational stress exceeds the sum of the network yield stress and the frictional stress, and occurs poroelastically with the height of the network decreasing linearly with time [55]. Gels with a weaker strength of attraction do not exhibit the same behaviour and it has been proposed that gravity does not play a key role in the collapse process [52].

The delay time is independent of the initial height, at least within the height range investigated here. This is contrary to the findings of Evans et al [59] who report a clear height dependence of τ_D if the initial height is less than 5 mm, but no height dependence if the sample heights exceed 5 mm. The clear lack of height effects on τ_D suggests that gravitational stress is not a key parameter in the collapse of these networks. The dynamical scaling shown in chapter 5 is evidence that the same microscopic mechanism is occurring throughout the collapse process but on

a timescale which is governed by C_p . The confocal images in chapter 6 reveal that network inhomogeneities appear within samples with large initial heights, which are referred to as micro–collapses. The location of the micro–collapses tends to be deep within the network away from its edges, and they appear randomly distributed. The accelerated collapse which is observed in these large height samples indicates an additional stress within the networks originating from the micro–collapses, which is not present in samples with small *h(0)* and it is this additional stress which is responsible for the collapse behaviour observed in samples with large *h(0)* . A universal mechanism is therefore proposed which accurately describes the ageing and collapse of colloidal gel networks with long range attractions, which accounts for both the linear and accelerated collapse processes observed.

8.1.1 The origin of micro–collapses

The particles in a gel network are constantly rearranging as the system attempts to phase separate into its component parts. As a result of these rearrangements internal stresses are built up within the network resulting in the microscopically observed inhomogeneities. Consider a single chain of particles in which two particles move from their current positions to form an attractive bond with each other. The left hand particle imposes a force on the left hand side of the chain, $+f_0$ and the right hand particle imposes an equal and opposite force on the right hand side of the chain, $-f_0$. A local force dipole is created at the point of the new particle–particle bond with an intensity μ. The fluid pressure P at the force dipole increases rapidly, while at a distance from the dipole stress center there is negligible change in the fluid pressure. This fluid pressure gradient drives a fluid flow through the porous network, and as fluid is expelled from the area of the stress dipole the surrounding network deforms and more of the stress is borne by the network rather than the fluid (see figure 8.1). Fluid flow occurs until the pressure gradient is zero and the gel relaxes so that the applied stress is everywhere balanced by the elastic stress in the network. Ultimately there has been an increase in the local colloid volume fraction.

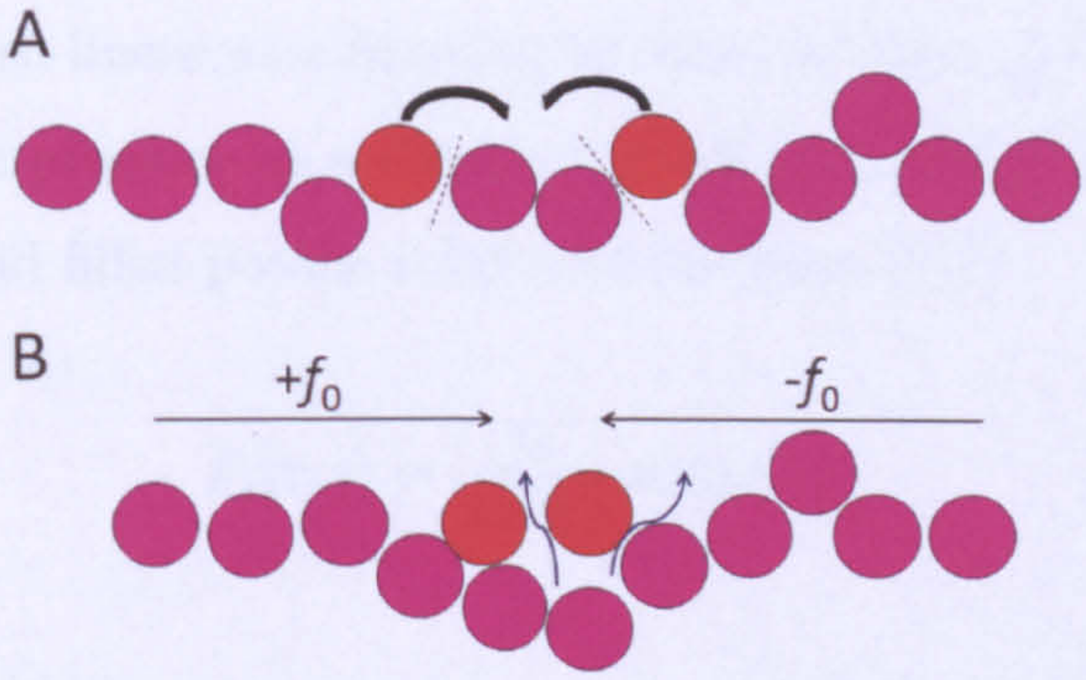

Figure 8.1: Schematic representation of the creation of a network force dipole. A: Two particles in a single chain (coloured orange) move to new positions in the chain and form an attractive bond. B: As a result of the new bond, a force is imposed on both the left hand side of the chain, $+f_0$ and the right hand side of the chain, $-f_0$. A fluid pressure gradient causes fluid to be expelled from the surrounding area, and the orange particles now have an increased number of nearest neighbours.

The timescale on which this balancing of forces occurs is determined by a diffusion constant, D_g and the deformation of the network occurs over a length scale $\approx \sqrt{D_g t}$ in a time t, where D_g is calculated as [121]:

$$D_g = \frac{Kk}{\eta_L(1-\phi)} \tag{8.1}$$

where K is the bulk modulus of the network, k is the permeability of the network, and η_L is the viscosity of the continuous phase. The elastic modulus of the gels was measured as $K \approx 10$ Pa, the permeability of the networks is estimated from literature values as $\mathrm{k} \sim 10\mathrm{a}^2 \approx 10^{-12}$ m^2, and measurements of the low shear viscosity gives $\eta_L \approx 0.1$ Pas giving an overall gel diffusion constant of $D_g \approx 10^{-10}$ m^{2}s^{-1}.

For an accurate description of network collapse it must be considered in 3D. The stress dipole center is considered to be an origin from which the stress extends outwards radially in a completely symmetrical pattern. At very short times the network is uncompressed and so the permeability is constant at each point. The bulk shrinkage of an unconstrained network is linear and so it is assumed that the

dipole intensity is also linear as a function of time, so that $\mu(t) = \mu_0 t$. It has been shown that the pore pressure at a distance of r from a single continuous point of compression in a fluid filled porous solid is of the form [122]

$$P_s(r,t) = \frac{Q}{4\pi D_g r}\text{erfc}(\xi/2) \tag{8.2}$$

where Q is proportional to μ_0, erfc is the complimentary error function and $\xi = r/(D_g t)^{\frac{1}{2}}$. As t $\rightarrow$ 0, erfc$(\xi/2) \rightarrow 0$ and the pressure is 0. At longer times the fluid is able to flow away from the stress origin and the pressure wave extends out to a maximum distance of $6(D_g t)^{\frac{1}{2}}$. As t $\rightarrow \infty$, erfc$(\xi/2) \rightarrow 1$ and the pressure field approaches the pure $1/r$ elastostatic solution expected for a continuous dipole source.

The velocity at which the network interface moves is controlled by the total pressure gradient at the bottom of the network, and the expression for the pressure gradient is:

$$-\partial_z P(t) \underset{t \gg \lambda^2/4D_g}{\approx} \frac{\rho Q}{4\lambda^2 \pi^{\frac{3}{2}} D_g^{\frac{1}{2}}}\sqrt{t} \tag{8.3}$$

where ρ is the number per unit length of stress dipole centers, λ is a distance from the network edge within which stress dipole centers do not occur. The derivation of this expression is detailed in appendix I. The micro–collapses first appear within the delay time after a period of hours, which is comparable to the delay time and so the time t available for the propagation of the pressure wave in Eq. 8.3 is $\tau = t - \tau_D$. Combining the expression in 8.3 with Darcy's law $-\partial_z P = \frac{\eta(1-\phi)}{k}(v - \partial_t w)$, yields:

$$\Delta h(t) = \left[\frac{\rho k Q}{4\eta(1-\phi)\lambda^2 \pi^{\frac{3}{2}} D_g^{\frac{1}{2}}}\right]\tau^{\frac{3}{2}} \tag{8.4}$$

It is assumed that the flow of liquid through the porous network ultimately determines the rate of its collapse, and that $t \gg \lambda^2/4D_g$. This expression is in excellent agreement with experimental data presented here, where the key exponent of $\frac{3}{2}$ is observed in samples which exhibit accelerated collapse.

For samples with small initial heights which instead exhibit a linear collapse, the description of the collapse is altered. Here, there are no dipole stress centers and therefore no pressure gradients driving fluid flow. Instead networks shrink poroelastically where the network decreases in height linearly with time, as observed in the collapse of strong gels [55].

8.1.2 The origin of the delay time

It is clear that the extent of the delay time is not affected by a change in the applied gravitational stress, since τ_D does not change with $h(0)$. The only clear observation is that τ_D is a strong function of C_p. Figure 5.10 shows that the domain radius of samples with small initial heights increases in size with a power law dependence until such a point that it becomes erratic and can no longer be predicted. The onset of this unpredictable behaviour, referred to as the microscopic delay time τ_{mD}, occurs when a critical length l_c is reached. The critical length is equal to the domain radius size at the point of τ_{mD}.

It is proposed here that the permeability of the networks is the controlling factor for determining τ_D. The permeability of a material describes its ability to transmit fluid through the void spaces. However, the dimensions of the void spaces dictate the permeability of a material. Fluid flows more readily through larger voids and so for two networks with identical volume fractions of colloids and voids, the network with larger void dimensions (domain radius size) will have a greater permeability and experience greater fluid flow [123]. It is therefore proposed that network coarsening is initially inhibited by the inability of fluid to be expelled from the network, as particles try to increase their number of nearest neighbours and phase separate. Coarsening progresses gradually until the critical length is reached at which point

fluid flow occurs more readily allowing for a greater degree of coarsening to occur and ultimately, network collapse.

The macroscopic delay time for samples studied using LSCM was unable to be accurately determined since the sample cell was largely obscured by the cell holder. However a reasonable assumption is that the value of τ_D is some multiple of τ_{mD} and that as in the case of τ_{mD} , there is a specific critical length which is required in order for appreciable fluid flow and subsequent network collapse to occur.

At first glance it might be assumed that the appearance of network micro–collapses which are observed within the delay time of samples with large initial heights suggests a slightly different coarsening process during τ_D . However it is argued that the micro–collapses actually play no role in determining the length of τ_D . The micro–collapses occur at random positions which are usually located within the bulk of the network away from the top and bottom edges of the network as shown in figure 6.3. In order for a network to reduce in height it must have a certain level of permeability at the top and bottom of the network in order for fluid to be easily expelled. Therefore, although the localised micro–collapses have increased permeability, the network cannot shrink macroscopically until the total permeability of the network and hence the domain radius size/critical length, reaches the necessary value.

The study by Gopalakrishnam et al show that increasing either the colloid volume fraction or the range of the attraction results in an increase in the delay time [60]. These observations support the proposal that the delay time is determined by the change in network permeability where a specific level of permeability is required in order for collapse to occur. One drawback of their study is that the polymer concentration is expressed as a function the total volume of the continuous phase, rather than as a free volume concentration. In this situation an increase in the delay time would be expected as the free volume available to the polymer is decreased, resulting in an effective increase in the strength of the attraction. However,

assuming a constant free volume polymer concentration, it is expected that as the volume fraction of colloids is increased, that there is a corresponding decrease in the initial void size. Therefore in order for a specific permeability to be obtained the network must undertake a much greater number of network rearrangements, which has a time cost. When the range of the attraction is increased particles are able to experience an attraction over a greater distance. In this circumstance the particles which make up a gel network may have a lower local colloid volume fraction when compared to networks with a much smaller range of attraction, resulting in the networks containing a greater amount of space around each particle. Ultimately the total network volume which is comprised of the particles and their surrounding liquid increases with the attractive range, and results in the initial void spaces being smaller. This process can be considered as an effective increase in colloid volume fraction, and once again, the time required for a specific permeability to be reached is increased.

Essentially, the permeability at the bottom of the network (or top of the network in the case of sedimenting systems) determines the length of the delay time where a system specific critical length/domain radius is required. Once this value is reached the networks begin to collapse with a mechanism that is determined by the initial height of the sample. The permeability is a function of colloid volume fraction, viscosity of the continuous phase, and pore size, and the time in which optimum permeability is achieved is dependent upon C_p .

8.2 Future work

The argument for the origins of the delay time rests upon the assumption that an ultimate domain radius size must be reached throughout the full network height, most importantly at the network top and bottom in order for network shrinkage to occur. In order to obtain unequivocal evidence for this argument it is necessary to simultaneously measure the network coarsening up to the point of network collapse, and determine the macroscopic delay time by eye. It would be most useful to follow

network coarsening close to the bottom of the network where the supernatant layer begins to grow.

The interesting feature of accelerated collapse exhibited by samples with large initial heights appears to be specific to systems with long range attractions, where the networks do not become arrested. It would be interesting to determine the crossover point from long range to short range attractions by systematically decreasing the range of the attraction and determining whether the same accelerated collapse feature can be observed until such a point that networks become arrested, or whether different collapse behaviours are observed as the attractive range is decreased.

Bibliography

[1] B. J. Ford. Brownian movement in clarkia pollen: A reprise of the first observations. *The Microscope*, 40:235–241, 1992.

[2] D Shaw. *Introduction to Colloid and Surface Chemistry.* Butterworth-Heinemann Ltd, 1992.

[3] B. Derjaguin. On the repulsive forces between charged colloid particles and on the theory of slow coagulation and stability of lyophobe sols. *Transactions of the Faraday Society*, 35:203–215, 1940.

[4] E Verwey and E Overbeek. *Theory of the stability of lyophobic colloids.* Elsevier, 1948.

[5] T Tadros. *Colloid Stability: The role of surface forces - Part 1.* Wiley-VCH, 2007.

[6] H. Lekkerkerker, W. Poon, P. Pusey, A. Stroobants, and P. Warren. Phase behaviour of colloid + polymer mixes. *Europhysics Letters*, 20:559–564, 1992.

[7] S. Asakura and F. Oosawa. Interaction between particles suspended in solutions of macromolecules. *Journal of polymer science*, 33:183–192, 1958.

[8] A. Vrij. Polymers at interfaces and the interactions in colloidal dispersions. *Pure and Applied Chemistry*, 48:471–483, 1976.

[9] W. G. Hoover and F. H. Ree. Melting transition and communal entropy of hard spheres. *Journal of Chemical Physics*, 49:3609–3617, 1968.

[10] A. P. Gast, C. K. Hall, and W. B. Russel. Polymer-induced phase separations in nonaqueous colloidal suspensions. *Journal of Colloid and Interface Science*, 96:251, 1983.

[11] G. Fleer and R. Tuinier. Analytical phase diagrams for colloids and non-adsorbing polymer. *Advances in colloid and interface science*, 143:1–47, 2008.

[12] F. Moreno and P. Sollich. Equilibrium phase behavior of polydisperse hard spheres. *Physical Review Letters*, 91:68301, 2003.

[13] S Farr and R Groot. Close packing density of polydisperse hard spheres. *The Journal of Chemical Physics*, 131:244104, 2009.

[14] P. Pusey. *Liquids, freezing and glass transition.* North Holland, 1991.

[15] P. Pusey and W. van Megen. Phase behaviour of concentrated suspensions of nearly hard colloidal spheres. *Nature*, 320:340, 1986.

[16] P. G. Bolhuis and D. A. Kofke. Monte carlo study of freezing of polydisperse hard spheres. *Physical Review E*, 54:634, 1996.

[17] M. Fasolo and P. Sollich. Fractionation effects in phase equilibria of polydisperse hard-sphere colloids. *Physical Review E*, 70:41410, 2004.

[18] W. Schaertl and H. Sillescu. Brownian dynamics of polydisperse colloidal hard spheres: Equilibrium structures and random close packings. *Journal of Statistical Physics*, 77:1007–1025, 1994.

[19] R Farinato and P Dubin. *Colloid-Polymer Interactions.* Wiley, 1999.

[20] J. J. Lietor-Santos, C. Kim, M. L. Lynch, A. Fernandez-Nieves, and D. A. Weitz. The role of polymer polydispersity in phase separation and gelation in colloid-polymer mixtures. *Langmuir*, 26:3174, 2010.

[21] S Yang, H Tan, and D Yan. Effect of polydispersity on the depletion interaction in non-adsorbing polymer solutions. *Physical Review E*, 75:061803, 2007.

[22] W. C. K. Poon, A. D. Pirie, M. D. Haw, and P. N. Pusey. Non-equilibrium behaviour of colloid-polymer mixtures. *Physica A*, 235:110–119, 1997.

[23] W. Poon, A. Pirie, and P. Pusey. Gelation in colloid-polymer mixtures. *Faraday Discussions*, 101:65, 1995.

[24] C. Allain, M. Cloitre, and M. Wafra. Aggregation and sedimentation of colloidal suspensions. *Physical Review Letters*, 74:1478, 1995.

[25] H Sedgwick, S Egelhaaf, and W Poon. Clusters and gels in systems of sticky particles. *Journal of Physics: Condensed Matter*, 16:S4913, 2004.

[26] T. A. Witten and L. M. Sander. Diffusion limited aggregation: A kinetic critical phenomenon. *Physical Review Letters*, 47:1400, 1981.

[27] W. Poon and M. D Haw. Mesoscopic structure formation in colloidal aggregation and gelation. *Advances in Colloid and Interface Science*, 73:71–126, 1997.

[28] D. A. Weitz and M. Oliveria. Fractal structures formed by kinetic aggregation of aqueous gold colloids. *Physical Review Letters*, 52:1433, 1984.

[29] R. Jullien and M. Kolb. Hierarchical model for chemically limited cluster-cluster aggregation. *Journl of Physics A: Mathematical and General*, 17: L639, 1984.

[30] P. B. Warren and R. C. Ball. Anisotropy and the approach to scaling in monodisperse reaction-limited cluster-cluster aggregation. *Journal of Physica A: Mathematical and General*, 22:1405, 1989.

[31] S Tang, J Preece, C McFarlane, and Z Zhang. Fractal morphology and breakage of dlca and rlca aggregates. *Journal of Colloid and Interface Science*, 221:114–123, 2000.

[32] M. D. Haw, M. Sievwright, W. C. Poon, and P. N. Pusey. Cluster-cluster gelation with finite bond energy. *Journal of colloid and interface science*, 62: 1, 1995.

[33] A. Coniglio, A. de Arcangelis, E. Del Gado, A. Fierro, and N. Sator. Percolation, gelation and dynamical behaviour in colloids. *Journal of Physics: Condensed matter*, 16:S4831, 2004.

[34] E. Zaccarelli. Colloidal gels: equilibrium and non-equilibrium routes. *Journal of Physics: Condensed Matter*, 19:323101, 2007.

[35] Peter Lu. *Gelation and Phase Separation of Attractive Colloids.* PhD thesis, Harvard University, 2008.

[36] E. Zaccarelli and W. Poon. Colloidal glasses and gels: The interplay of bonding and caging. *Proceedings of the National Academy of Sciences of the United States of America*, 106:15203, 2009.

[37] L. Kaufman and D. Weitz. Direct imaging of repulsive and attractive colloidal glasses. *Journal of Chemical Physics*, 125:074716, 2006.

[38] F. Sciortino. Disordered materials: One liquid, two glasses. *Nature materials*, 3:145, 2002.

[39] R. Courtland and E. Weeks. Direct visualization of ageing in colloidal glasses. *Journal of Physics: Condensed Matter*, 15:s359, 2002.

[40] L. Cipelletti and L. Ramos. Slow dynamics in glasses, gels and foams. *Current Opinion in Colloid & Interface Science*, 7:228, 2002.

[41] H. Tanaka. Viscoelestic phase separation (review article). *Journal of Physics: Condensed Matter*, 12:R207–264, 2000.

[42] J Cahn. Phase separation by spinodal decomposition in isotropic systems. *Chemical Physics*, 42:93–99, 1965.

[43] A. E. Bailey, W. C. Poon, R. J. Christianson, A. B. Schofield, A. B. Gasser, V. Prasad, S. Manley, P. N. Segre, L. Cipelletti, W. V. Meyer, M. P. Doherty, S. Sankaran, A. L. Jankovsky, W. L. Shiley, J. P. Bowen, J. C. Eggers, C. Kurta, T. Lorik, P. N. Pusey, and D. A Weitz. Spinodal decomposition

in a model colloid-polymer mixture in microgravity. *Physical Review Letters*, 99:205701, 2007.

[44] J Mark, K Ngai, W Graessley, L Mandelkern, E Samulski, J Koenig, and G Wignall. *Physical Properties of Polymers.* Cambridge University Press, 2004.

[45] H. Tanaka, S. Jabbari-Farouji, J. Meunier, and D. Bonn. Kinetics of ergodic-to-nonergodic transitions in charged colloidal suspensions: Aging and gelation. *Physical Review E*, 71:021402, 2005.

[46] H. Tanaka, J. Meunier, and D. Bonn. Nonergodic states of charged colloidal suspensions: Repulsive and attractive glasses and gels. *Physical Review E*, 69:031404, 2004.

[47] M. Kilfoil, E. Pashkovski, J. Masters, and D. Weitz. dynamics of weakly aggregated colloidal particles. *Phil. Trans. R. Soc. Lond. A*, 361:753–766, 2003.

[48] C. Derec, D. Senis, L. Talini, and C. Allain. Rapid settling of a colloidal gel. *Physical Review E*, 67:62401, 2003.

[49] L Cipelletti, C Ligoure, and J Condre. The role of solid friction in the sedimentation of strongly attractive colloidal gels. *Journal of Statistical Mechanics: Theory and Experiment*, 2:02010, 2007.

[50] J. Y. Huh, M. L. Lynch, and E. M. Furst. Microscopic structure and collapse of depletion-induced gels in vesicle-polymer mixtures. *Physical Review E*, 76: 051409, 2007.

[51] S. Manley, J. Skotheim, J. Mahadevan, and Weitz. D. Gravitational collapse of colloidal gels. *Physical Review Letters*, 94:218302, 2005.

[52] J. J. Leiter-Santos, C. Kim, M. L. Lynch, A. Fernandez-Nieves, and D. A. Weitz. The role of polymer dispersity in the phase separation and gelation in colloid-polymer mixtures. *Langmuir*, 26:3174–3178, 2010.

[53] J. Lietor-Santos, C. Kim, P. Fernandez-Nieves, and D. Weitz. Gravitational compression of colloidal gels. *The European Physical Journal E*, pages 159–164, 2009.

[54] G. Brambilla, S. Buzzaccaro, R. Piazza, L. Berthier, and L. Cipelletti. Highly nonlinear dynamics in a slowly sedimenting colloidal gel. *Physical Review Letters*, 106:118302, 2011.

[55] R. Buscall and L. White. The consolidation of concentrated suspensions. *Journal of the Chemical Society, Faraday Transactions*, 83:873, 1987.

[56] D. Senis, L. Gorre-Talinia, and C. Allain. Systematic study of the settling kinetics in an aggregating colloidal suspension. *The European Physical Journal E*, 4:59, 2001.

[57] A. Michaels and J. Bolger. Settling rates and sediment volumes of flocculated kaolin suspensions. *Industrial and Engineering chemistry fundamentals*, 1: 24–33, 1962.

[58] L. Starrs, W. Poon, D. Hibberd, and Robins M. Collapse of transient gels in colloid polymer mixtures. *Journal of Physics: Condensed Matter*, 14:2485–2505, 2002.

[59] R. Evans and L. Starrs. Emergence of a stress transmission length-scale in transient gels. *J. Phy. Condensed Matter*, 14:2507–2529, 2002.

[60] V. Gopalakrishnam, K. Schweizer, and C. Zukoski. Linking single particle rearrangements to delayed collapse times in transient depletion gels. *Journal of Physics: Condensed matter*, 18:11531–11550, 2006.

[61] C. Kim, Y. Liu, A. Kuhnle, S. Hess, S. Viereck, T. Danner, T. Mahadevan, and D. Weitz. Gravitational stability of suspensions of attractive colloidal particles. *Physical review letters*, 99:028303, 2007.

[62] H. Tanaka. Viscoelastic model of phase separation in colloidal suspensions and emulsions. *Physical Review E*, 59:6842–6853, 1999.

[63] H. Tanaka and T. Araki. Spontaneous coarsening of a colloidal network driven by self generated mechanical stress. *Europhysics Letters*, 79:58003, 2007.

[64] A Clarke and C Eberhardt. *Microscopy techniques for materials science.* Woodhead Publishing Limited, 2002.

[65] W Amos, J White, and M Fordham. Use of confocal imaging in the study of biological structures. *Applied Optics*, 26:3239–3243, 1987.

[66] I. Morrison and S. Ross. *Colloidal Dispersions.* Wiley, 2002.

[67] B. Berne and R. Pecora. *Dynamic Light Scattering.* Wiley, 1976.

[68] P. Bartlett, T. Cosgrove, S. Davis, J. Eastman, J. Estoe, R. Hughes, J. Reid, P. Reynolds, R. Richardson, J. Riley, J. van Duijneveldt, and B. Vincent. *Colloid Science.* Blackwell Publishing, 2005.

[69] R. Hunter. *Foundations of Colloid Science.* Oxford University Press, 2001.

[70] E. Gopal, T. Hanai, J. Kitchener, and P. Mussellwhite. *Emulsion Science.* Academic Press, 1969.

[71] S Sahin and S Sumnu. *Physical properties of foods.* Springer, 2006.

[72] T Tadros. *Rheology of Dispersions: Principles and applications.* Wiley-VCH, 2010.

[73] J Goodwin and R Hughes. *Rheology for Chemists.* The Royal Society of Chemistry, 2000.

[74] C. Servais, H. Ranc, S. Sansonnens, S. Ravji, A. Romoscanu, and A. Burbidge. 3rd international symposium on food rheology and structure. In *Rheological Methods for multiphase materials*, 2003.

[75] R Chhabra and J Richardson. *Non-Newtonian fow and applied rheology: engineering applications.* Elsevier, 2009.

[76] J Steffe. *Rheological methods in food process engineering.* Freeman Press, 1992.

[77] Walter Noll. *Chemistry and technology of Silicones.* Academic Press, 1968.

[78] A Colas, J Siang, and K Ulman. Silicones in pharmaceutical applications. Dow corning website.

[79] T. Obey and B. Vincent. Novel monodisperse 'silicone oil' / water emulsions. *Journal of Colloid and Interface Science*, 163:454–463, 1994.

[80] I. Burgess. The mode of action of dimethicone 4 percent lotion against head-lice, pediculus capitis. *BMC Pharmacology*, 9, 2009.

[81] N. Campbell and J. Reece. *Biology.* Benjamin Cummings, 2002.

[82] I. Capron, G. Brigand, and G. Muller. About the native and renatured conformation of xanthan exopolysaccharide. *Polymer*, 38:5289–5295, 1997.

[83] R. Moorhouse, M Walkinshaw, and S Arnott, editors. *Extracellular microbial polysaccharides.* American Chemical Society, 1977.

[84] K Born, V Langendorff, and P Boulenguer. *Biopolymers Volume 5. Polysaccharides I.* Wiley, 2004.

[85] Q. Ying and B. Chu. Overlap concentration of macromolecules in solution. *Macromolecules*, 20:362–366, 1987.

[86] P. Sandford and A. Laskin. *Extracellular microbial polysaccharides.* American Chemical Society, 1977.

[87] R Poulenc. Use of xanthan gum in water-based paints. *Pigment and Resin Technology*, 16:7–11, 1987.

[88] M Garvey. The impact of colloid science. *Chemistry World*, 2, 2003.

[89] J Rockey G Higton M J Waites, N Morgan. *Industrial Microbiology: An Introduction.* Wiley-Blackwell, 2001.

[90] P. Schurtenberger, S. Bhat, and R. Tuinier. Spinodal decomposition in a food colloid-biopolymer mixture: evidence for a linear regime. *Journal of Physics: Condensed matter*, 18:L339–L346, 2006.

[91] G. Koenderink, D. Aarts, V. Villeneuve, A. Philipse, R. Tuinier, and H. Lekkerkerker. Morphology and kinetics of phase seperating transparent xanthan-colloid mixtures. *Biomacromolecules*, 4:129–136, 2003.

[92] B Jonsson, B Lindmand, K Holmberg, and B Kronberg. *Surfactants and Polymers in Aqueous Soution.* Wiley, 1998.

[93] J Goodwin. *Colloids and Interfaces with Surfactants and Polymers.* Wiley, 2009.

[94] Hiroshi Fujita. *Polymer solutions.* Elsevier, 1990.

[95] M. Schmidt. Effect of molecular weight distribution on rg of wormlike chains. *Macromolecules*, 17:553–560, 1984.

[96] T. Coviello, K. Kajiwara, W. Burchard, M. Dentini, and V Crescenzi. Solution properties of xanthan.1. dynamic and static light scattering from native and modified xanthans in dilute solutions:. *Macromolecules*, 19:2826–2831, 1986.

[97] T. Sho, T. Sato, and T. Norisuye. Small effect of ionic strength on persistence length. *Biophysical Chemistry*, 25:307–313, 1986.

[98] N Verhaegh, J van Duijneveldt, J Dhont, and H Lekkerkerker. Fluid-fluid phase separation in colloid-polymer mixtures studied with small angle light scattering and light microscopy. *Physica A*, 230:409–436, 1996.

[99] R. Tuinier, P. Smith, W. Poon, S. Egelhaaf, D. Aarts, H. Lekkerkerker, and G. Fleer. Phase diagram for a mixture of colloids and polymers with equal size. *EPL*, 82:68002, 2008.

[100] D. Kleshchanok, A. Meijer, A. Andrei, V. Petukhov, A. Portaleb, and H. Lekkerkerker. Attractive glass formation in aqueous mixtures of colloidal gibbsite platelets and silica spheres. *Soft Matter*, 7:2832–2840, 2011.

[101] P. Lu, E. Zaccarelli, F. Ciulla, A. Schofield, F. Sciortino, and D Weitz. Gelation of particles with short-range attraction. *Nature*, 453:499–504, 2008.

[102] C. Klix, C. Royall, and H. Tanaka. Structural and dynamical features of multiple metastable glassy states in a colloidal system with competing interactions. *Physical Review Letters*, 104:165702, 2010.

[103] P. Lu, J. Conrad, H. Wyss, A. Schofield, and D. Weitz. Fluids of clusters in attractive colloids. *Physical Review Letters*, 96:28306, 2006.

[104] J. C. Conrad, H. M. Wyss, V. Trappe, S. Manley, K. Miyazaki, L. J. Kaufman, A. B. Schofield, D. R. Reichman, and D. A. Weitz. Arrested fluid-fluid phase separation in depletion systems: Implications of the characterisitc length on gel formation and rheology. *Journal of Rheology*, 54:421–438, 2010.

[105] E Zaccarelli, P Lu, F Ciulla, D Weitz, and Sciortino. Gelation as arrested phase separation in short-ranged attractive colloi-polymer mixtures. *Journal of Physics: Condensed Matter*, 20:494242, 2008.

[106] M Lee and E Furst. Response of a colloidal gel to a microscopic oscillatory strain. *Physical Review E*, 77:041408, 2008.

[107] P Smith, G Petekidis, S Egelhaaf, and W Poon. Yielding and crystallization of colloidal gels under oscillatory shear. *Physical Review E*, 76:041402, 2007.

[108] L. Cipelletti, S. Manley, R. Ball, and D. Weitz. Universal aging features in the restructuring of fractal colloidal gels. *Physical Review Letters*, 84:2275–2278, 1999.

[109] L Cipelletti, L Ramos, S Manley, S Pitard, and D Weitz. Universal non-diffusive slow dynamics in aging soft matter. *Faraday Discussions*, 123:237, 2003.

[110] T. Gibaud and P. Schurtenberger. A closer look at arrested spinodal decomposition in protein solutions. *Journal Physical Condensed Matter*, 21:322201, 2009.

[111] J. Dhont. Spinodal decomposition of colloids in the intial and intermediate stage. *Journal Chemical Physics*, 105:5112, 1996.

[112] A. Parker, P. Gunning, and M. Ng, K. and. Robins. How does xanthan stabilise salad dressing? *Food Hydrocolloids*, 9:333–342, 1995.

[113] T Tadros, editor. *Colloids in Agrochemicals.* Wiley-VCH, 2009.

[114] T Tadros, editor. *Colloids in Cosmetics and Personal Care.* Wiley-VCH, 2008.

[115] E Dickinson and P Walstra, editors. *Food Colloidsand Polymers: Stability and Mechanical Properties.* The Royal Society of Chemistry, 1993.

[116] W. Poon, L. Starrs, S. Meeker, A. Mousaaid, R. Evans, P. Pusey, and M. Robins. Delayed sedimentation of transient gels in colloid-polymer mixtures: dark-field observation, rheology and dynamic light scattering studies. *Faraday Discussion*, 112:143–154, 1999.

[117] D. Aarts, R. Dullens, and H. Lekkerkerker. Interfacial dynamics in demixing systems with ultralow interfacial tension. *New Journal of Physics*, 7:40, 2005.

[118] S. W. Kamp and M. L. Kilfoil. Universal behaviour in the mechanical properties of weakly aggregated colloidal particles. *Soft Matter*, 5:2438–2447, 2009.

[119] R. Tuinier and A. Kruif. Phase separation, creaming, and network formation of oil-in-water emulsions induced by an exocellular polysaccharide. *Colloid and Interface Science*, 218:201–210, 1999.

[120] J. Bouchard and E. Pitard. Anomalous dynamical light scattering in soft glassy gels. *The European Physical Journal E*, 6:231–236, 2001.

[121] G Charras, J Yarrow, M Horton, and L Mahadevan. Non-equilibriation of hydrostatic pressure in blebbing cells. *Nature*, 435:365, 2005.

[122] J Rudnicki. Fluid mass sources and point forces in linear elastic diffusive solids. *Mechanics of materials*, 5:383, 1986.

[123] *Ward's - Porosity and permeability of soils model. Users guide.*

Appendix A

Sudden collapse of a colloidal gel

Sudden collapse of a colloidal gel

Paul Bartlett,[1,*] Lisa J. Teece,[1] and Malcolm A. Faers[2]

[1] *School of Chemistry, University of Bristol, Bristol BS8 1TS, UK.*
[2] *Bayer CropScience AG, 40789, Monheim am Rhein, Germany*

(Dated: Printed: September 23, 2011)

Metastable gels formed by weakly attractive colloidal particles display a distinctive two-stage time-dependent settling behavior under their own weight. Initially a space-spanning network is formed that for a characteristic time, which we define as the lag time τ_d, resists compaction. This solid-like behavior persists only for a limited time. Gels whose age t_w is greater than τ_d yield and suddenly collapse. We use a combination of confocal microscopy, rheology and time-lapse video imaging to investigate both the process of sudden collapse and its microscopic origin in an refractive-index matched emulsion-polymer system. We show that the height h of the gel in the early stage of collapse is well described by the surprisingly simple expression, $h(\tau)/h_0 \sim \exp[-(\tau/\tau_c)^\beta]$, with h_0 the initial height, $\tau = t_w - \tau_d$ the time counted from the instant where the gel first yields, and $\beta \approx 1.5$. We propose that this unexpected result arises because the colloidal network progressively builds up internal stress as a consequence of localized rearrangement events which leads ultimately to collapse as thermal equilibrium is re-established.

PACS numbers: 82.70.Dd, 83.50.Fc, 05.40.+j

I. INTRODUCTION

Soft materials such as colloidal suspensions and emulsions form a remarkably rich variety of non-ergodic states [1–3] – examples of which are familiar to us in our daily life in products as diverse as foodstuffs, surface coatings, fabric conditioners, and pesticides. Out-of-equilibrium phases occur when suspensions are quenched deep into a region of thermodynamic phase separation. Unable to phase separate, amorphous solids form which are mechanically rigid but without the long-range translational order characteristic of crystalline solids. Slow relaxation dynamics prevents the system from reaching their underlying global equilibrium configurations so these amorphous solids evolve slowly in a complex energy landscape with a high number of local minima and as a result display glassy dynamics with a rich phenomenology of effects such as aging, non-linear responses, and spatial and temporal dynamic heterogeneities.

One of the most dramatic macroscopic manifestations of aging is the phenomenon of sudden network collapse in gels. Gels consist of a network of particles linked together by long-lived attractive bonds. Sedimentation or creaming of the particles within a gel imposes a buoyant stress on the network. Weak gels, where the strength of the attractive potential at contact U_c is only a few k_BT, show a very unusual mechanical response. Initially, the gel behaves as a solid but after a finite lag time τ_d, the gel yields and catastrophically collapses. Sudden or 'delayed' network collapse is observed in a wide variety of materials [4–13] and seems to be ubiquitous at small U_c/k_BT. However, while sudden collapse has been attributed to channel formation within the gel [9, 10], the microscopic processes operating have never been fully established. A better microscopic understanding of the origin of sudden gel collapse is important not only because the distinctive settling behavior is intriguing from a scientific viewpoint but also because a quantitative prediction of gel stability is a critically important issue in the formulation and manufacture of many commercial products.

The aim of this paper is to report a detailed experimental study of the stability of gels under gravitational stress. We use a colloidal suspension of nearly monodisperse emulsion drops of radius a suspended in an index-matched mixture of solvents, which has been well characterized elsewhere [14]. Gelation is induced by long-range attractive depletion forces. Using time-lapse video imaging we measure the dependence of the height h of a gel upon its age t_w, counted from the moment when the gel was formed. No macroscopic sedimentation is observed initially but after a period of latency the gel undergoes a rapid collapse as the system separates into colloid-rich and colloid-poor phases. We investigate the collapse dynamics as a function of the strength $-U_c/k_BT$ of the attractive interactions and the initial height h_0 of the gel. Remarkably we find that when collapse starts the change in the height of the gel $\Delta h = h_0 - h$ follows a simple universal dependence on t_w which is independent of the initial height h_0 of the gel. The observation of height-independent collapse is surprising and contrasts with the marked height dependence seen in short-range gels studied to date [10, 15, 16]. Using a combination of rheology, confocal microscopy and time-lapse video imaging we speculate that the collapse of the gel network occurs via a spatially heterogeneous process of localized 'micro-collapses' which leads to a build up of internal stress within the gel.

The paper is organized as follows: Section II discusses the preparation of the emulsion gels studied and the experimental techniques used. Section III details experi-

* Corresponding author:P.Bartlett@bristol.ac.uk

mental results from both macroscopic and microscopic measurements on the settling behavior of suspensions of attractive particles. The interpretation of the results in terms of internal stress relaxations is discussed in Sec. IV before we summarize our main findings in Sec. V.

II. MATERIALS AND METHODS

A long-range attractive interaction was induced between emulsion colloids by polymer depletion. The emulsion consisted of poly(dimethyl siloxane) drops dispersed in a solvent mixture of 1,2-ethane diol (ED) and water (mass fraction of ED = 0.59). The solvent composition was adjusted to closely match the refractive index of the emulsion to minimize van der Waals attractions between drops and to enable confocal imaging to be conducted deep within the sample. A particle radius of $a = 316 \pm 11$ nm and a size polydispersity of 0.17 ± 0.07 was determined from dynamic light scattering measurements. The thickness of the polymeric stabilizing layer surrounding each emulsion drop was evaluated by centrifuging a suspension and equating the packing fraction of the sediment to the jamming density of a hard sphere system with the same polydispersity [17]. This procedure gave a layer thickness of $\approx 7 \pm 1$ nm. The density mismatch between emulsion drops and the continuous phase is $\Delta\rho = -130 \pm 10$ kg m^{-3}. To induce a depletion interaction, we added the non-adsorbing anionic polymer xanthan (Kelco, $M_w = 4.66 \times 10^6$ g mol^{-1}). The polymer radius of gyration was determined as $r_g = 194 \pm 10$ nm by light scattering and viscometry. The strength of the depletion attraction generated is a function of the polymer concentration and its range is controlled by the relative size $r_g/a = 0.62 \pm 0.04$ of the polymer and particle. The polymer concentration is quoted here in terms of the dimensionless ratio c_p/c_p^*, where $c_p^* = 3M_w/4\pi r_g^3 N_A$ is the overlap concentration ($c_p^* = 0.25$ mg/ml) and N_A is Avogadro's constant. Full details of sample preparation are contained in Teece et al. [14].

To monitor the collapse of the gels we used time-lapse video recording to record images of the emulsions as they cream. A low magnification image of the settling gel was projected onto a CCD camera (Allied Vision Technologies F-080B). A regular sequence of images were captured every 20 seconds. The image series was corrected for optical distortion and non-uniformities in illumination before being calibrated using an accurate grid of lines. The images near the center of the cells were analyzed and the interface separating the upper (dark) phase from the lower (bright) phase was identified automatically using a image analysis routine. The height h of the interface was extracted as a function of time with an accuracy of about ± 0.3 mm. To aid visualization a low concentration (≈ 0.001 mg/ml) of an adsorbing black dye, Sudan black, was added. The dye preferentially partitions into the index-matched PDMS drops so that the colloid-rich phase appears dark in transmitted light. The colloid-polymer mixtures were thoroughly mixed at the start of the experiments before being loaded into cylindrical glass vials with an internal diameter of $d = 17$ mm. The cell diameter was varied between 15 – 23 mm and both cylindrical glass and poly(styrene) cells were used, with no significant change in collapse behavior. To eliminate air bubbles which lead to irreproducible settling dynamics we used a gentle slow tumbling of the sample vial to thoroughly mix the samples before observation. Repeat experiments showed that following this protocol the collapse kinetics could be measured with a reproducibility of about 10-15%.

Rheological measurements were performed at 23°C with a Bohlin HR Nano rheometer (Malvern Instruments). To study simultaneously the temporal evolution of the elastic properties and the height of the gel a novel rheometric vane experiment was developed which allowed visual observation of the gel as rheological measurements were performed. The vane was made from stainless steel and consisted of four blades (diameter 22.7 mm, height 10 mm). The vane was carefully inserted into clear polycarbonate sample vials (diameter 25 mm, height 65 mm), 10 mm below the top surface of the gel and a thin layer of silicone oil added to minimize evaporation. The vane remained inside the dense upper phase for the duration of the rheological experiments, allowing the collapse process to be continuously monitored. Oscillation measurements were performed at 0.5 Hz at intervals of 200-250 s under controlled stress conditions, within the experimentally-determined linear viscoelastic region, while the height of the gel was monitored simultaneously by time-lapse video microscopy. The absence of wall slip was confirmed by watching the movement of small air bubbles deliberately introduced into samples.

To directly probe changes in the microscopic topology of the gel during collapse we used fluorescent confocal microscopy. The continuous phase of the gel was labeled with 0.02 mg/ml of the fluorescent dye rhodamine-B which combined with the high transparency of the emulsions provided by refractive-index matching allowed high resolution optical visualization deep within the gel. A light microscope (Zeiss, Axioskop S100) was mounted horizontally on its side, at right angles to gravity, and two-dimensional fluorescent images of regions 146 × 146 μm were acquired at 543 nm. The gel was contained in a square cross-section glass vial, with an internal dimension of 13 mm, mounted on a low profile translation stage so that the gel could be imaged at different vertical positions, throughout the full 30 mm height of the sample [14]. Since the emulsion drop radius is below the optical resolution limit of the confocal microscope we can not identify individual drops. Instead, we concentrated on the larger scale structure of the gel. The bicontinuous network was identified by thresholding the confocal images to determine the location of the interface separating the (dark) emulsion phase from the (bright) continuous phase. To correct for in-plane variation in the fluorescence yield, each image was divided into 16 sub-images

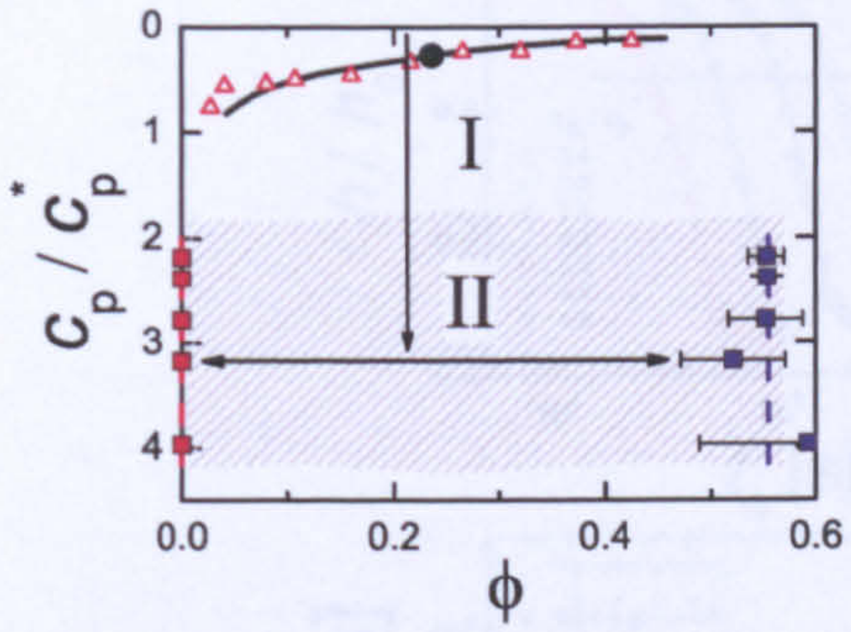

FIG. 1. (color online). State diagram showing gels studied. The solid curve corresponds to the gas-liquid binodal calculated from the generalized free volume theory [19], for a polymer-colloid size ratio $r_g/a = 0.62$. The open triangles identify the experimentally determined phase boundary. The theoretical prediction for the critical point is shown by the filled circle. The region below the coexistence line can be separated into two kinetic regimes: a region of complete demixing (I), and gelation (II). Quenched into region II, suspensions form a space-spanning network consisting of thick strands of particles. The vertical line indicates the constant colloid volume fraction gels studied ($\phi = 0.213$). The colored symbols represent estimates of ϕ for the strands of particles (blue squares) and the coexisting gas (red squares) after phase separation is complete locally. Error bars represent the age-dependent variation in ϕ from the same sample.

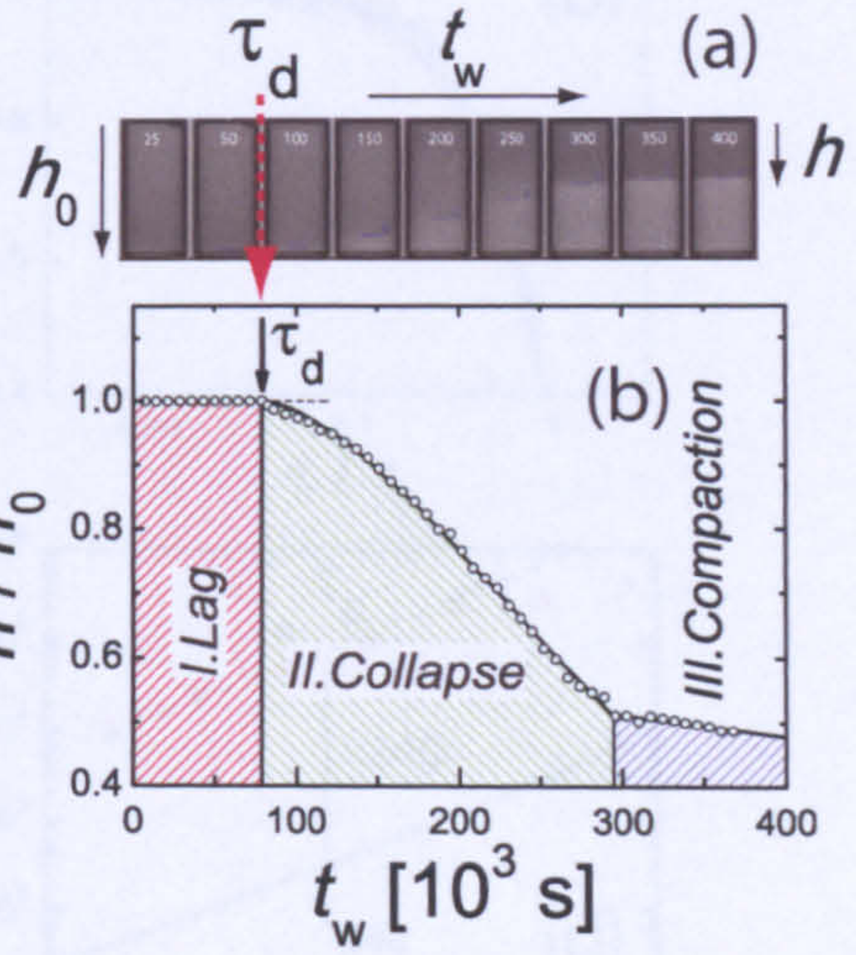

FIG. 2. (color online). Sudden collapse of a gel. (a) Time-lapse images of an emulsion-polymer mixture, with composition $\phi = 0.21$ and $c_p/c_p^* = 3.6$, as a function of the time after shaking. Each image is labelled by the time elapsed t_w, in units of 10^3 s. The initial height h_0 of the sample is 40 mm. The characteristic delay time τ_d after which the network starts to collapse is indicated by the dashed arrow. The solid line denotes the position of the interface between the upper colloid-rich and lower polymer-rich phases. (b) The normalized height h/h_0 of the gel shown in part (a) as a function of the elapsed time showing the three stages of settling characteristic of sudden collapse.

and a local threshold for each sub-image was determined using a cluster-based algorithm [18]. A careful analysis of the resulting binary images, backed up by direct observation, showed that this approach reliably located the shape and positions of the emulsion and aqueous domains.

III. EXPERIMENTAL RESULTS

A. Collapse dynamics

To begin, the phase behavior of mixtures of emulsion and polymer was investigated as a function of both the emulsion volume fraction ϕ and polymer concentration c_p/c_p^*. The state diagram plotted in Fig. 1 summarizes the results and shows the locations of a stable liquid phase, a narrow region of equilibrium gas-liquid demixing (I) and a broad zone of non-equilibrium gelation (II). The generalized free volume predictions (GFVT) [19] for a polymer-colloid size ratio $r_g/a = 0.62$ in a good solvent are shown by the solid lines in Fig. 1. The agreement between the calculated gas-liquid binodal and experiments is good confirming that the experimental system is accurately represented by a simple mixture of hard spheres and non-adsorbing polymer chains.

The sudden collapse of gels was investigated as a function of both the strength of the attractions $-U_c/k_BT$ and the initial height h_0 of the sample. In the absence of polymer, emulsions remained stable and showed no noticeable separation so the mechanical instability seen is a consequence of aggregate formation. The process of collapse is exemplified by the time-lapse CCD images reproduced in Fig. 2(a). Qualitatively we identify three distinct stages, characterized by the interface velocity $\nu = \mathrm{d}h/\mathrm{d}t_w$, where t_w is the age of the gel. During an initial lag period (I) the network of attractive particles produces a mechanically stable solid, which is capable of supporting its own weight. This regime of solid-like stability persists however only for a limited duration. On times longer than τ_d, the lag time, the network yields and a clear interface appears (identified by the solid line in Fig. 2(a)). The interface velocity ν grows smoothly as the gel shrinks and the collapse becomes progressively more rapid. This period (II) of rapid collapse terminates when phase separation nears completion and the interface approaches the final equilibrium plateau. In the final consolidation stage (III), the settling velocity drops markedly as the collapsed gel continues to slowly compress like a solid under its own weight.

The lag time τ_d is a strong function of the polymer concentration and hence the strength of depletion attractions. Fig 3(a) shows normalized sedimentation profiles

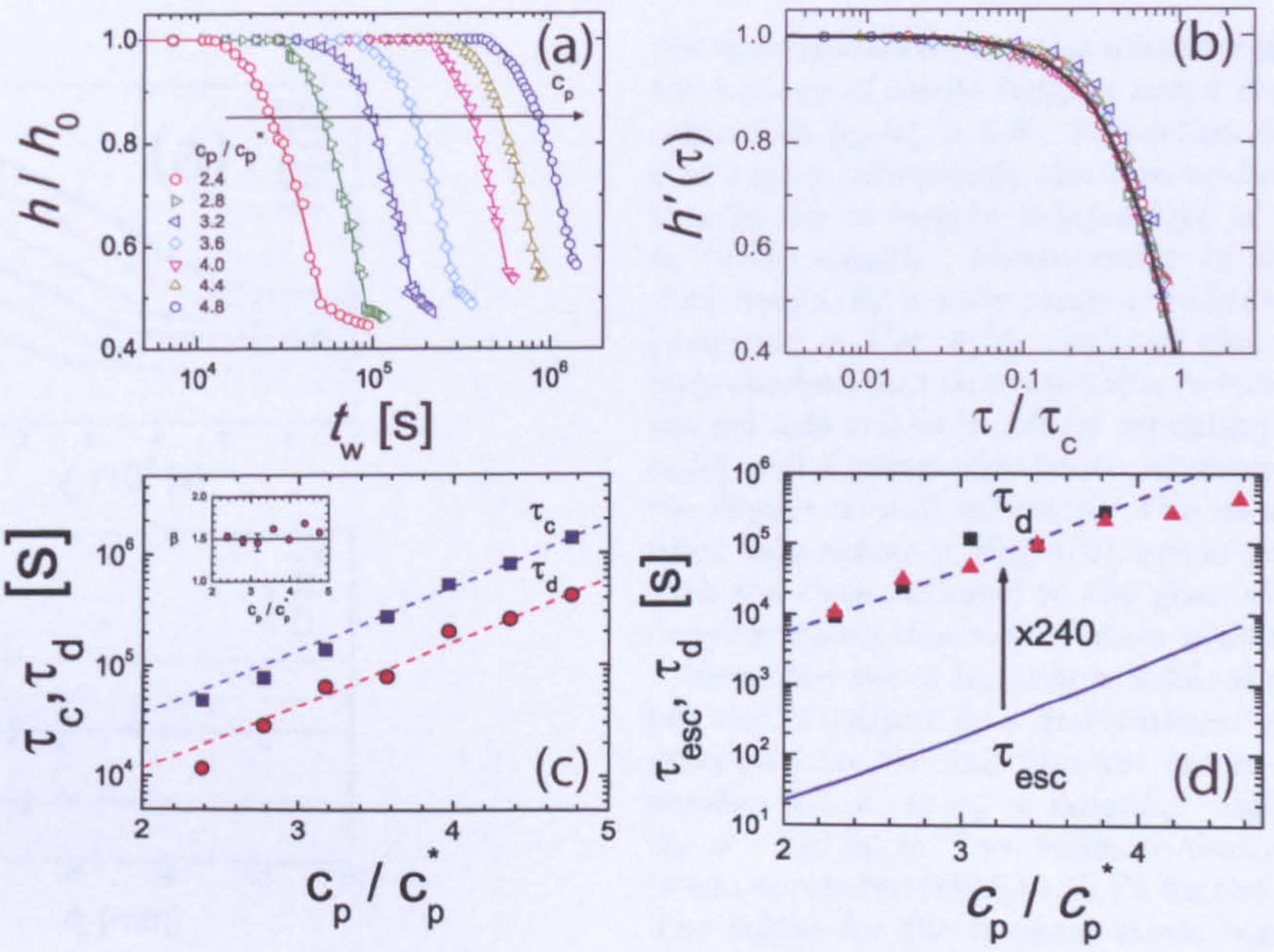

FIG. 3. (color online). Scaling of collapse dynamics at fixed height. (a) Time evolution of a gel with various polymer concentrations but the same initial height, $h_0 = 40$ mm. Only data in the lag and collapse regimes is shown for clarity. (b) The heights replotted as a function of the dimensionless time τ/τ_c where $\tau = t_w - \tau_d$ is the time elapsed after yielding. The scaling time τ_c is chosen so that the data collapses onto a single master curve. The solid line is the function, $h'(\tau) = \exp -(\tau/\tau_c)^{3/2}$. Symbols are the same as in (a). (c) Exponential dependence of characteristic times τ_c and τ_d on polymer concentration. The inset diagram shows that the height displays a compressed time-dependence with exponent $\beta \approx 3/2$. (d) Comparison between the experimentally-measured lag times τ_d (filled points) and the average lifetime τ_{esc} of an individual particle bond (solid line), as a function of polymer concentration. Lag times were measured for gels in both glass (triangles) and poly(styrene) vials (squares). The dashed line, which reproduces the experimental data reasonably well, equates to a fixed number of bond lifetimes ($\tau_d \approx 240\, \tau_{esc}$).

h/h_0 measured from gels at different polymer concentrations from $c_p/c_p^* = 2.4$ to 4.8, at a fixed initial height of $h_0 = 40$ mm. Inspection reveals two striking features. First, as reported in previous work [7, 8], τ_d grows strongly with increasing polymer concentration. Indeed the concentration dependence of the lag time is well described by the exponential relationship, $\tau_d \sim \exp(c_p/c_p^*)$, as shown in Fig. 3(c). Second, the curves of normalized interface height h/h_0 as a function of time are remarkably similar in shape when plotted in a linear-log representation. The height profile at a low polymer concentration may be mapped onto a high concentration sample by simply shifting the collapse profile to the right along the logarithmic time-axis. To explore this scaling behavior quantitatively, we focus purely on the portion of the height profile in the collapse regime and replot h/h_0 as a function of the shifted time variable $\tau = t_w - \tau_d$, the time counted from the instant when the network first yields. Fig. 3(b) demonstrates that remarkably all of the shifted data falls onto a single master curve if the normalized height $h'(\tau) = h(\tau + \tau_d)/h_0$ is plotted as a function of the dimensionless time ratio τ/τ_c where τ_c is a suitably-chosen time scaling factor. The existence of this scaling relation suggests that there is a single common mechanism governing the sudden collapse of the gel at different polymer concentrations. We shall return to this point in Sec. IV to speculate on the origin of this scaling behavior. We note that an alternative scaling law has been suggested previously by Kilfoil et al. [20]. Although this approach does yield a simplification of the settling data at a fixed height, it fails to scale data measured at *different* heights, because as we show below τ_d and τ_c show different dependencies on the initial height h_0 of the gel.

To determine the characteristic time τ_c for collapse, the shifted interface height h' was fitted to the stretched-exponential form

$$h'(\tau) = \exp[-(\tau/\tau_c)^{\beta}] \qquad (1)$$

where τ_c is a characteristic time for collapse and β is the stretching exponent. Values of β less than 1 correspond to a so-called stretched exponential while $\beta > 1$ describe a compressed relaxation. Optimum values for τ_c and β were determined from the collapse data using a non-linear regression routine. The solid lines in Fig. 3(a) are the results of fits to Eq. 1, which as can be seen describe the gel settling data accurately over a reasonable range of τ. Results for the relaxation time τ_c and the stretching exponent β are shown as a function of the polymer concen-

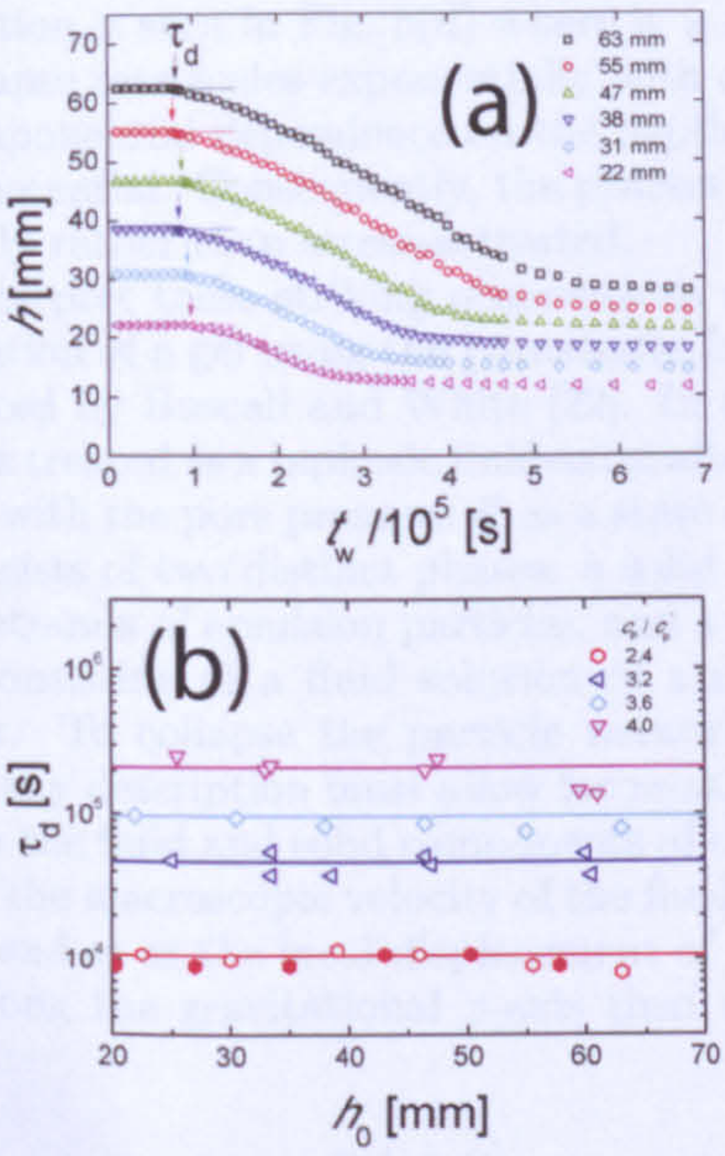

FIG. 4. (color online). Height-independent lag times. (a) Temporal evolution of a gel with different initial heights but a fixed composition, $\phi = 0.213$, and $c_p/c_p^* = 3.6$. The arrows indicate the lag time τ_d. (b) The lag time τ_d as a function of the initial height h_0 of the gel, for a number of different polymer concentrations. The open symbols denote data obtained in glass-walled cells while the filled symbols indicate measurements in poly(styrene) cells. The nature of the cell wall has no noticeable effect on the delay time measured.

tration in Fig. 3(c) and the inset diagram, respectively. Clearly, the shape of $h'(\tau)$ is inconsistent with the simple exponential dependence $\beta = 1$ identified previously in the compaction of strong gels [15, 16]. Instead the best fits to the collapse curves give $\beta \approx 1.5$, with no systematic variation with polymer concentration (inset Fig. 3(c)). The simple compressed form $h'(\tau) = \exp[-(\tau/\tau_c)^{3/2}]$ is in excellent agreement with all of the data recorded at different polymer concentrations, as shown by the accurate reproduction of the data given by the solid line drawn in Fig. 3(b).

Earlier studies [10, 21] of gel collapse have suggested that the mechanism of collapse depends sensitively on the initial height h_0 of the gel. Gels formed in short sample cells display steady or 'creeping' sedimentation where the height falls continuously with age at a rate which decays exponentially with time while taller samples show sudden collapse. To test whether this behavior is intrinsic to the long-range systems studied here we have varied the initial height h_0 and monitored the evolution of the height of the gel with time. In all the samples reported here, polymer concentration from $c_p/c_p^* = 2.4 - 4.0$ and heights $h_0 = 22 - 63$ mm, sudden gel collapse was always observed and we saw no transition to creeping sedimentation. Fig. 4(a) shows a representative set of data where the time evolution of the interface height $h(t_w)$ is plotted for a range of initial heights and a single polymer concentration ($c_p/c_p^* = 3.6$). Inspection of the data reveals that rather surprisingly the time τ_d during which the gel is solid-like is largely independent of the initial height h_0 of the sample. Measurement of the variation of τ_d with height for a wide range of polymer concentrations, presented in Fig. 4(b), confirms this observation. We have checked that this is not due to solid friction between the gel and cell wall [16] by repeating measurements at $c_p/c_p^* = 2.4$ using cylindrical poly(styrene) cells to alter the degree of wall adhesion. The results, shown as the filled data points in Fig. 4(b), are in excellent agreement with the data obtained in the glass vials (open points), demonstrating that wall friction is unimportant.

Since the gel is initially a solid, the top of the sample vial is subject to a gravitational stress σ_g, which is generated by the full buoyant stress of all of the suspension below, so $\sigma_g = \Delta\rho g\phi h_0$. Taking $\phi = 0.21$ and $\Delta\rho = -130$ kg m^{-3} we estimate that σ_g varies from between approximately 5 to 15 Pa for the heights used here. The values for the buoyant stress considerably exceeds the yield stress of the gel network, which we estimate from rheological measurements as $\sigma_y \sim 0.1$ Pa, so even while σ_g is an order of magnitude larger than the stress required to break the gel's load-bearing structure the gel does not collapse macroscopically. The insensitivity of τ_d to h_0 means we can rule out the possibility that the initial period of latency of the gel is determined purely by the breaking of single uncorrelated bonds. Collapse clearly requires a substantially larger degree of restructuring of the network than is necessary simply for mechanical yielding.

To explore the effect of height on the kinetics of collapse we focus on the initial rate of collapse of the gel. The excellent fit achieved to Eq. 1 suggests that at short-times ($\tau \ll \tau_c$) the height of the gel should follow the algebraic expression

$$h(\tau) = h_0 - A\tau^{\frac{3}{2}} \qquad (2)$$

where A is a constant scale factor. Consequently, a plot of the height of the settling gel against $\tau^{\frac{3}{2}}$ should be linear with a gradient $-A$. Figure 5 shows this expression captures well the initial height variation for gels with a wide variety of different starting heights and polymer concentrations. The gel therefore does not collapse with a fixed time-invariant velocity but rather the interface velocity $\nu = \mathrm{d}h/\mathrm{d}\tau$ behaves at short times like $\tau^{1/2}$, a behaviour which hints at a surprisingly novel mechanism of collapse. To further investigate this mechanism we have studied the dependence of the initial slope $A = \mathrm{d}\Delta h/\mathrm{d}\tau^{3/2}$ on the height and polymer content of the gel. Fig. 5(c) shows that rather remarkably, for all the gels studied, the rate of collapse A does not change with the initial height of the gel. Since the gravitational stress σ_g on the gel increases linearly with its height, this result confirms the relative unimportance of σ_g in determining the rate of collapse, at least under the conditions of our ex-

periments. The central role of thermally-induced bond dissociation is seen in Fig. 5(d) where it is revealed that the collapse rate scales exponentially with c_p, equivalent to an exponential dependence on the depth of the interaction potential. Consequently, the process of collapse is thermally rather than stress-activated.

To interpret these striking observations we model the deformation of a gel using the poroelastic formalism first introduced by Buscall and White [22]. In this approach the gel is treated as a biphasic fluid-saturated porous continuum with the pore pressure P as a state variable. The gels consists of two distinct phases: a solid phase of connected strands of emulsion particles, and a second liquid phase consisting of a fluid solution of a non-adsorbing polymer. To collapse the particle network must expel fluid so any description must allow for relative movement between the fluid and solid components of the gel. Defining v as the macroscopic velocity of the fluid flow through the gel and w as the local displacement of the solid network along the gravitational z-axis then using Darcy's law,

$$-\partial_z P = \frac{\eta(1-\phi)}{k}(v - \partial_t w), \tag{3}$$

where k is the permeability of the network, and η is the viscosity of the continuous phase. Continuity demands

$$(1-\phi)v = -\phi\partial_t w \tag{4}$$

which, since $\phi < 1-\phi$, implies that the fluid velocity $|v|$ must be small [15] in comparison to $|\partial_t w|$. Consequently, if the displacement of the gel varies as $\tau^{3/2}$ then, from Eq. 3, the pressure gradient at the top of the gel, adjacent to the interface, must be increasing as $\tau^{1/2}$. This time dependence rules out a simple compression of the gel as a consequence of gravity because the pressure gradient would then be a constant, $\partial_z P = -\Delta\rho g\phi$, and the gel would accordingly shrink linearly with time [15]. The $\tau^{1/2}$ dependence of P suggests instead a diffusive process may be responsible for the unusual collapse dynamics seen. We can however rule out a bulk diffusive process of conventional syneresis, akin to the shrinkage of a polymer gel undergoing a phase transition [23]. In this case, the contraction of the matrix as the phase separation ensues would generate an increase in P which leads to the expulsion of fluid and a shrinkage of the gel as $t^{1/2}$ [24] rather than the $t^{3/2}$ dependence seen here. Furthermore, this process would require fluid to be transported through the full length of the system so the rate of diffusion would depend on the height of the gel, which is also incompatible with our data. Clearly, a new mechanism is required to correctly explain the observed data.

B. Microstructure

Sudden collapse reflects a dramatic loss of mechanical integrity as the gel ages. To understand the origin of this mechanical failure, we first examine the evolution of the elastic properties of the gel while simultaneously recording the height of the gel. Figure 6 shows the rheology and interface height $h(t_w)$ during the settling of a representative gel. At the earliest times recorded, the sample is solid-like with an elastic shear modulus G' which is larger than the viscous modulus G''. The measurements however reveal that the elasticity of the gel far from reducing with time, as one might naively expect, actually increases continuously up to the point $t_w = \tau_d$ when the gel starts to collapse. Immediately collapse starts, G' also drops, but only by a relatively small amount (less than 10%), before finally growing steadily as the emulsion volume fraction in the upper phase increases with the onset of phase separation. Comparable measurements on a short-ranged gel ($r_g/a \sim 0.05$) have been reported [5]. We see no sign of large-scale hydrodynamic mixing, recirculation, and the development of channels which have been seen in some other studies of gravitational collapse [5, 9, 10].

While the rheological measurements provide a mechanical insight into gel settling, they do not clarify the link between the macroscopic processes of collapse and the microscopic structural reorganization occurring during aging and sedimentation. Indeed, at first sight, it seems counter-intuitive that a gel which is becoming gradually stiffer with time should ever collapse at all. To probe the link between the microscopic and macroscopic length scales, we have examined the temporal evolution of the gel microstructure using confocal microscopy. The coarsening is illustrated by the binary two-dimensional images reproduced in Fig. 7. In the rectangular cell used for imaging experiments, the delay time was measured as $\tau_d \approx 1.3\times10^5$ s so both images refer to the latency period before collapse starts. Clearly, although the gel remains mechanically stable during this period there is a slow but continuous evolution in the microscopic nature of the particle network and the system is not arrested. A closer look at the data in Fig 7 reveals that the interface between the continuous and particle phases is quite rough, suggesting that surface tension is unimportant and the dense portion of the gel is not a fluid. Direct observation show that particle diffusion is strongly suppressed and particles move infrequently between the strands of the network, indicating that the interaction network is probably glassy. The images in Fig 7 illustrate two further microstructural characteristics which will be important to our later discussion on the mechanism of network collapse. First, with time, it is evident that the thickness of the backbone of the gel grows slowly but continuously with time, a fact which probably explains the increase of G' with t_w seen in Fig. 6. Second, the thickness of the network of particle strands is not uniform. The gel contains a relatively large number of thin junction points where two or three arms (in 2D) are connected together. Simultaneous breakage of the particle bonds at these relatively weak junction points would lead to a rapid break up of the whole network.

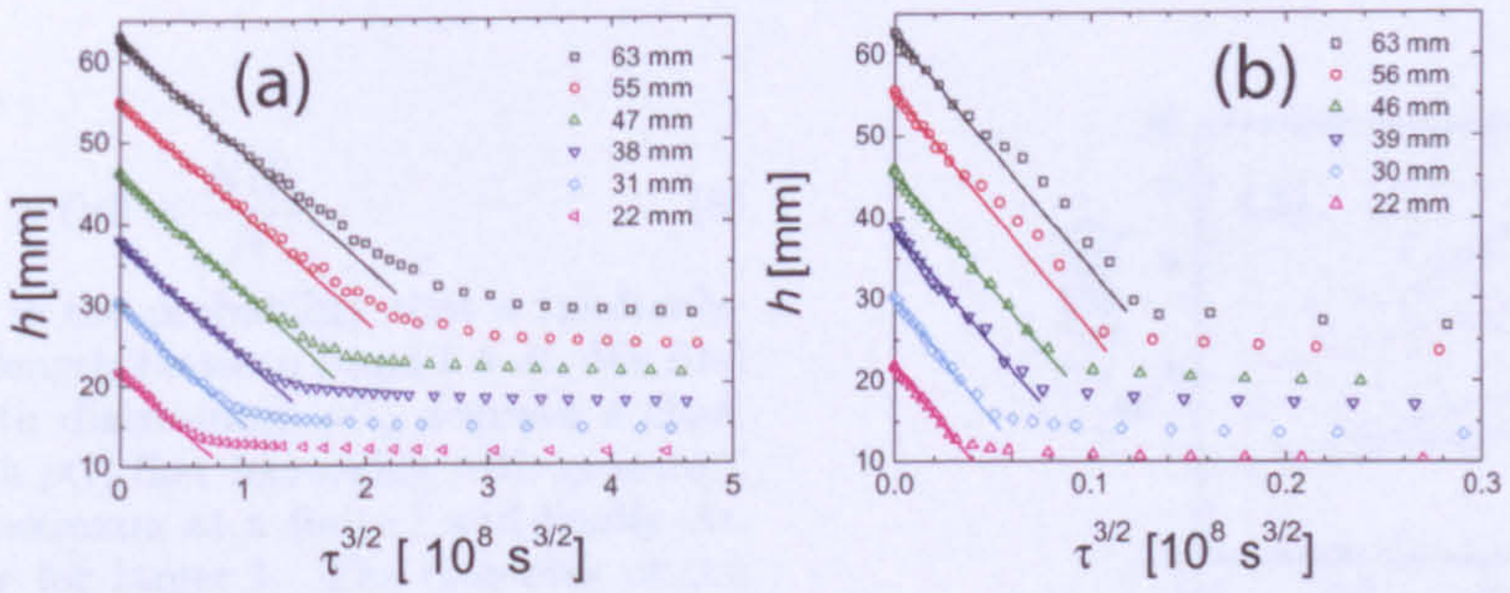

FIG. 5. (color online). Initial $\tau^{3/2}$–collapse dynamics. (a) The height h of a gel plotted as a function of the 3/2–power of the time elapsed after the gel yields, for different initial heights h_0. Curves are labelled by the initial height. The samples have fixed polymer concentration $c_p/c_p^* = 3.6$, and colloid content $\phi = 0.213$. (b) Similar time-dependent settling observed in gels with $c_p/c_p^* = 2.4$. (c) Invariance of the initial rate of collapse $A = -\lim_{\tau\to 0} dh/d\tau^{3/2}$ with the height of the gel. Curves are labelled by c_p/c_p^*. (d) Exponential dependence of A on the polymer concentration, highlighting the activated nature of the collapse process.

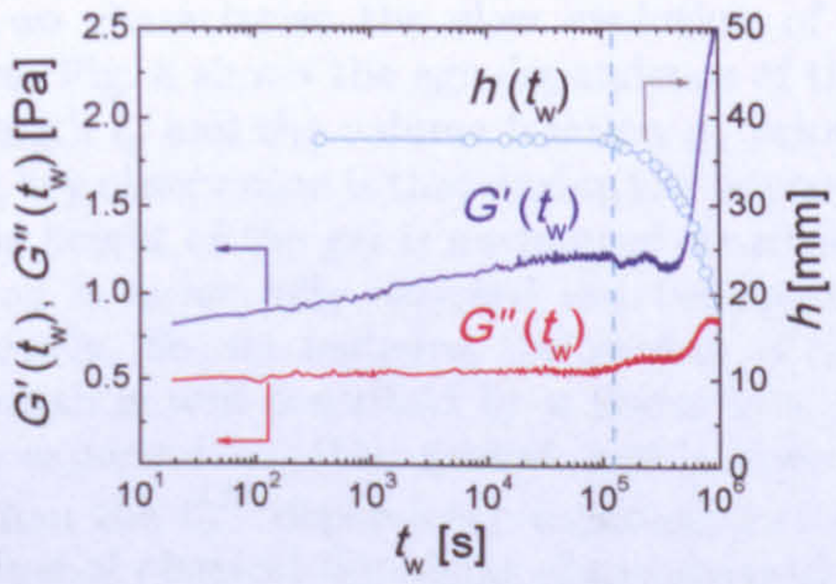

FIG. 6. (color online). Simultaneous measurements of linear viscoelasticity and height h of gel as a function of time elapsed since preparation t_w. Gel had an initial composition of $c_p/c_p^* = 3.6$, $\phi = 0.213$ and a measured delay time of $\tau_d = 1.2 \times 10^5$ s (indicated by dashed line). The elastic G' and loss G'' moduli were measured by applying a oscillatory stress of magnitude 0.0025 Pa at a frequency of 0.5 Hz and measuring the strain response. The gel stiffens continuously with age until the elastic modulus drops at $t_w = \tau_d$ as the gel begins to collapse.

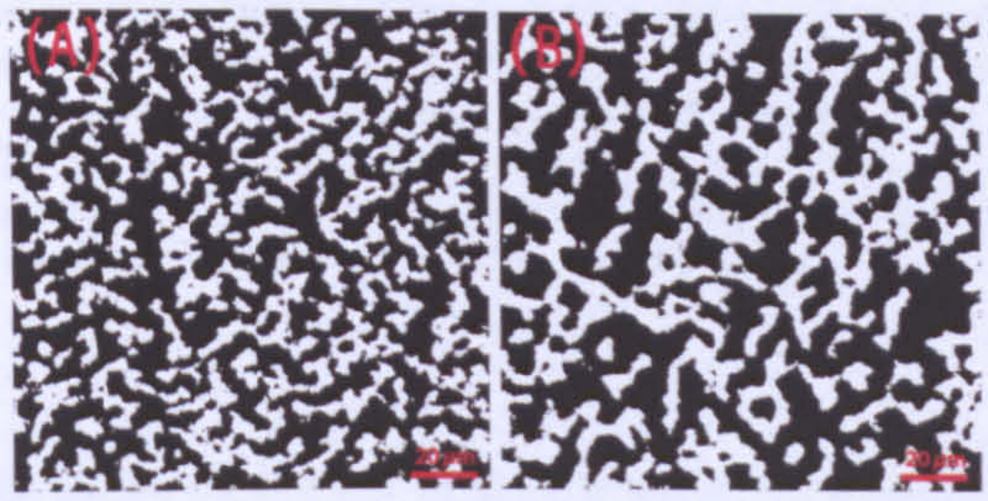

FIG. 7. Continuous coarsening of gel with age. Two-dimensional binary representation of a gel with composition $c_p/c_p^* = 2.4$, $\phi = 0.213$ after (a) 3.6×10^3 s, and (b) 1.12×10^5 s from preparation. Gravity points vertically downwards and the scale bar corresponds to 20 μm.

To quantify the change of the microstructure with time, we use chord methods developed to analyze statistically random heterogeneous materials [25]. We superimpose on the images of Fig 7 a uniform grid of horizontal and vertical lines. The two-phase interfaces divide each grid line into chords that are either inside the dense part of the network or else lie within the solvent background. We define a chord as the line segment between two consecutive intersections of the random line with the bounding two-phase interface. Focusing only on those chords that lie *within* the dense strands of the network, we count the number of chords $N(l)$ with lengths in the range l and $l + dl$. If N is the total number of chords then the degree of linear 'connectedness' of the gel may be characterized in terms of a probability density func-

tion, $p(l)$, where

$$p(l)\mathrm{d}l = \frac{N(l)}{N}. \tag{5}$$

The quantity $p(l)\mathrm{d}l$ is the probability that a randomly-chosen chord has a length between l and $l + \mathrm{d}l$. We find that the chord length distribution $p(l)$ displays a characteristic shape, with $p(l)$ first increasing with growing l before reaching a maximum at a finite l and finally decaying exponentially for larger l. The diameter of the strands of particles within the gel may be characterized either from the value at which $p(l)$ takes a maximum value or from the mean chord length l_{g}

$$l_{\mathrm{g}} = \int_0^\infty lp(l)\mathrm{d}l, \tag{6}$$

which we use here because it displays a smaller statistical error. Finally, the chord functions also provide an efficient means to estimate the volume fraction of the high density colloidal regions in the gel. If we assume the gel is isotropic and the two-dimensional images are chosen randomly then the fraction χ of the volume of the gel occupied by the dense regions is

$$\chi = \frac{1}{L}\sum_l N(l)l \tag{7}$$

where L is the total length of the original lines. The volume fraction of colloids, ϕ_{g}, in the dense regions of the gel is given by the ratio ϕ/χ, where ϕ is the initial colloid volume fraction.

Next we characterize the slow evolution of the gel structure. Fig. 8 shows the age dependence of the mean chord length l_{g} and the volume fraction ϕ_{g} prior to collapse. A key observation is that during the latency period when the height of the gel is unchanged structural reorganization is never fully arrested but continues, albeit rather slowly. So, for instance, the growth of the mean chord length is well described by a power law, $l_{\mathrm{g}} \sim t_{\mathrm{w}}^{\alpha}$, with an exponent α. The growth law is always much slower than the $t_{\mathrm{w}}^{1/3}$ dependence expected for the diffusive regime of classical liquid-gas phase separation. The growth exponent α depend rather strongly on the polymer concentration with α decreasing markedly as $c_{\mathrm{p}}/c_{\mathrm{p}}^*$ is increased. Similar slow growth has been identified previously in simulations of deep quenched Lennard-Jones systems [26] and has been interpreted as indicating that the dense domains of the gel are actually glassy. Consistent with this picture, Fig. 8(b) indicates that while the colloid volume fraction ϕ_{g} in the dense regions of the gel initially increases with the age of the gel, in all cases it eventually saturates at a plateau of ≈ 0.55, which is compatible with repulsive glass formation.

C. Origin of lag time

Having characterized the macroscopic process of collapse, we now discuss the mechanism for the initial failure

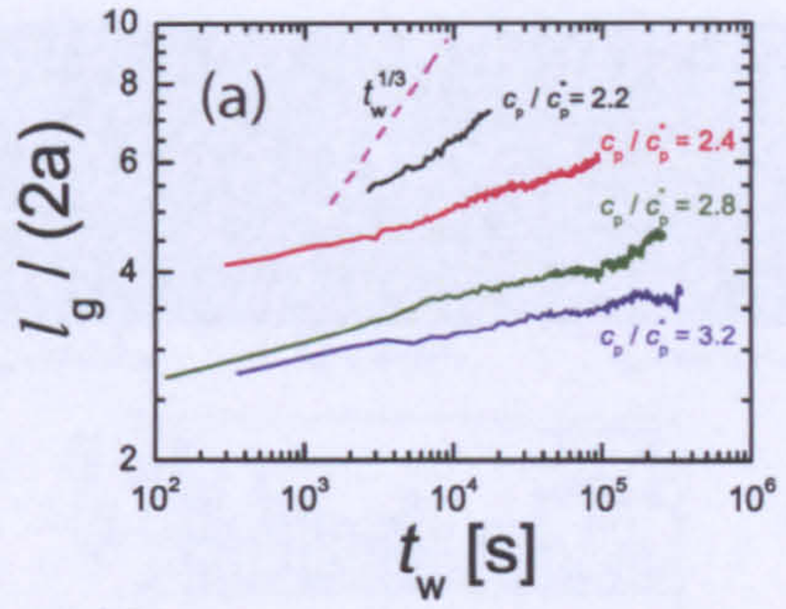

FIG. 8. (color online). Evolution of colloidal network with time. (a) Average chord length l_{g} in the colloid phase, in units of the particle diameter. The rate of increase of l_{g} is always slower than the diffusive growth, $l_{\mathrm{g}} \sim t_{\mathrm{w}}^{1/3}$ (shown by dashed line) characteristic of classical spinodal decomposition [26], and slows down considerably with increasing polymer concentration $c_{\mathrm{p}}/c_{\mathrm{p}}^*$. (b) Average colloid volume fraction ϕ_{g} within dense regions of the gel, as a function of elapsed time. The density of the particle strands within the network increases progressively with age and approaches a density characteristic of a hard-sphere glass ($\phi \sim 0.55$) at long times.

of the particle network. A gel is a metastable phase with a high free energy density whose consolidation is driven ultimately by the thermodynamic driving force for phase separation. However once a stable percolating network of strands of particles is formed the dynamics of phase separation is slowed down considerably because, as evident from Fig. 7, the strands of the network are many particles wide so large scale rearrangements of the gel require the simultaneous dissociation of all of the particle bonds within the cross-section of a strand, which will be very rare. The network accordingly lowers its free energy via a series of small-scale structural reorganizations which proceed through the rupture of essentially single particle bonds. The breakup of an energetic bond between particles, diffusion to dense region of the network, and a reformation of the broken bond allows a net increase in the number of nearest neigbouring particles with a concomitant lowering of the free energy of the system. For the network to coarsen, the system must overcome the energetic barrier associated with single bond rupture.

This could be achieved, in principle, either thermally or as a result of an applied stress. The observation that the delay time is unaffected by the initial height of the gel strongly suggests that the delay time and hence the rupture of individual bonds is controlled primarily by thermal fluctuations rather than being stress-driven.

To calculate the average lifetime $\tau_{\rm esc}$ of an individual particle bond due to thermal fluctuations, we assume that a single bond ruptures on a scale comparable to the time it takes a Brownian particle to escape from an attractive ramp potential with the same range δ/a and depth $-U_{\rm c}/k_{\rm B}T$ as the interparticle depletion potential. The mean escape time in the overdamped limit is given by the Kramers expression [27]

$$\tau_{\rm esc} = \frac{\delta^2}{D_{\rm t}} \frac{\exp(-U_{\rm c}/k_{\rm B}T) - (1 - U_{\rm c}/k_{\rm B}T)}{(U_{\rm c}/k_{\rm B}T)^2} \qquad (8)$$

where $D_{\rm t}$ is a translational diffusion constant. We estimate $D_{\rm t}$ from the short-time self diffusion constant in a hard sphere suspension at the same ϕ, which since the dense regions of the gel have a volume fraction ≈ 0.55 is about 20% of the dilute free particle limit, $D_0 = k_{\rm B}T/(6\pi\eta_{\rm L}a)$. The limiting low shear viscosity $\eta_{\rm L}$ was determined by extrapolating measurements of the steady-shear rheology of the polymer solution to a vanishing shear rate and fitting to the Martin equation,

$$\frac{\eta_{\rm L}}{\eta_0} = 1 + [\eta]c_{\rm p}\exp\left(k_{\rm H}[\eta]c_{\rm p}\right) \qquad (9)$$

which has been found to correlate well viscosity in dilute and semi-dilute polymer solutions ($c_{\rm p}/c_{\rm p}^* < 10$). Here $[\eta]$ is the intrinsic viscosity, η_0 is the viscosity of the mixed solvent, $c_{\rm p}$ the polymer mass concentration, and $k_{\rm H}$ is a constant (equivalent to the Huggins constant at low $c_{\rm p}$). Fitting data in the range $c_{\rm p} = 0.6 - 1.2$ mg/ml to Eq. 9 gave $[\eta] = 2.32$ ml/mg and $k_{\rm H} = 1.2$. The width of the depletion zone δ and the potential at contact $-U_{\rm c}/k_{\rm B}T$ were estimated using the generalized free volume theory for mixtures of hard sphere colloids and excluded-volume polymer chains, as detailed in Ref. [14]. Figure 3(d) shows a comparison between the measured delay time $\tau_{\rm d}$ and the average lifetime $\tau_{\rm esc}$ of a single particle bond, estimated from Eq. 8. The ratio of the two timescales is very nearly constant, for a wide range of polymer concentrations, with the delay time approximately 240 times the estimated Kramers escape time. This strong correlation highlights the pivotal role of spontaneous thermal fluctuations in determining the latency period of the gel.

To explore the microscopic mechanism by which thermal fluctuations lead to delayed failure we used real-space confocal imaging to follow the time evolution of the gel. Since the load-bearing nature of the network is clearly important we concentrate on changes in the connectivity of the strands of particles which constitute the gel. Figure 9(a) shows two-dimensional confocal slices taken from the same physical region within an aging gel before collapse occurs. Because of the finite bond energy, the network structure slowly but continuously evolves, with fluctuations in both the number and type of junction points.

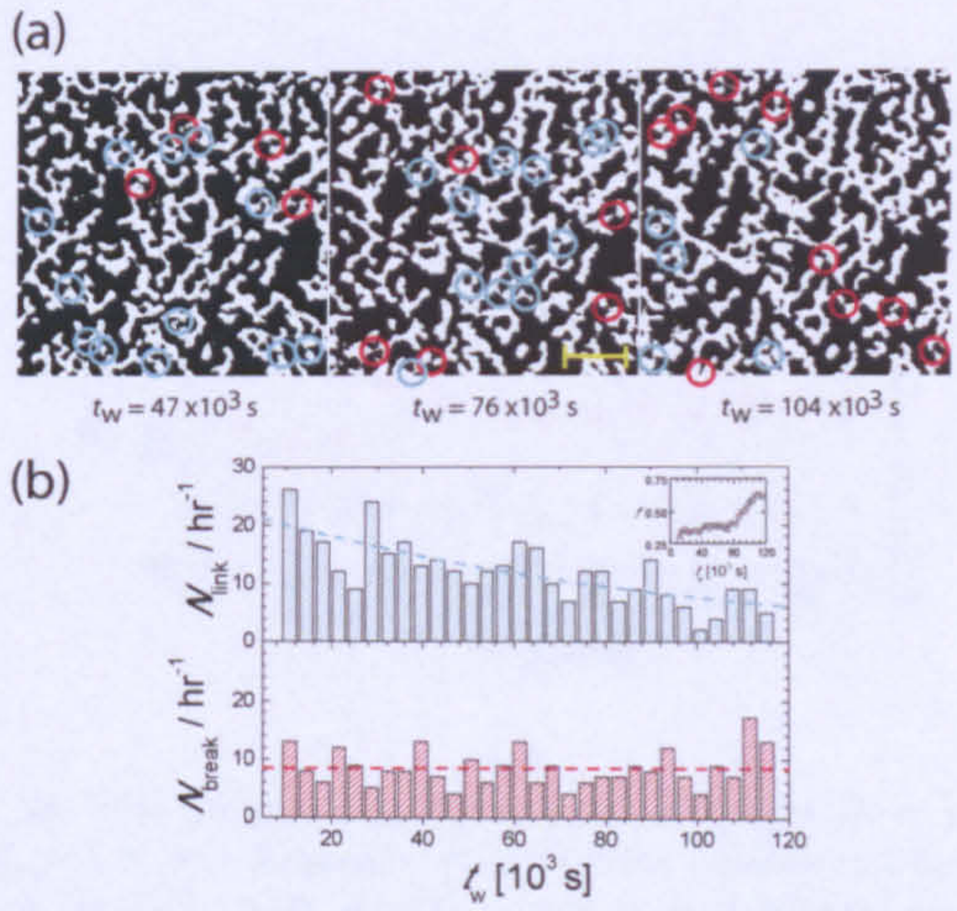

FIG. 9. (color online). (a) 2D confocal images of coarsening gel network formed at $\phi = 0.213$, and $c_{\rm p}/c_{\rm p}^* = 2.4$. The particles are shown in white. The solid (blue) circles indicate network junctions which have formed in the preceding 3600 s. The dashed (red) circles indicate positions where the network has, in the same interval, broken. The scale bar is 30 μm long. Network collapse occurs at $\tau_{\rm d} \sim 120 \times 10^3$ s. (b) The number of reassociation $N_{\rm link}$ and rupture $N_{\rm break}$ events per hour as a function of the age $t_{\rm w}$ of the gel. The dashed lines are guides to the eye. The inset shows the $t_{\rm w}$-dependence of the fraction f of rupture events.

By comparing 2D images of the fine-stranded structure of the network at hourly intervals we identified discrete strand association and dissociation events occurring over this period. Examples where the strand network is ruptured are indicated by the red dashed circles in Fig. 9(a) while the blue solid circles identify new cross-links formed by the reassociation of strands. Counting the number of reassociation $N_{\rm link}$ and rupture $N_{\rm break}$ events recorded per hour, as a function of the age of the gel, results in the data shown in Fig. 9(b). There is gradual reduction over time in the number of reassociation events $N_{\rm link}$, as the network is formed in an open high-energy state and then relaxes slowly into a lower more compact structure. Strikingly however, we see that the rate of bond rupture does not show the same slowing-down. $N_{\rm break}$ is essentially independent of age, presumably because rupture is an activated process which is dominated by the single particle bond energy barrier. The consequence of the different time dependence seen for association and rupture is that the proportion of breakage events $f = N_{\rm break}/(N_{\rm break} + N_{\rm link})$ (shown in the inset of Fig. 9(b)) grows with the age of the gel. The increasing proportion of strand ruptures ultimately leads to failure of the stress-bearing backbone of the gel and the initiation of collapse.

D. Heterogeneous aging

Work in the last decade [1, 28, 29] has shown that the slow dynamics of soft glassy materials is frequently heterogeneous in character. In materials where the elastic behavior of a material dominates over its viscous response any deformation due to a local rearrangement can propagate macroscopic distances so the size of regions which undergo correlated rearrangements can be sizeable. If this holds true in our system, then it should be feasible to see signs of the long-range distortion field generated by local rearrangement events by microscopy.

To test these ideas we have used confocal microscopy to monitor the time evolution of the network structure as a function of the vertical z-position within a gel. A series of 2D-confocal images were collected at regularly-spaced 1 mm heights from a colloid-polymer gel with a total height of $h_0 = 15$ mm. Images were acquired for ≈ 7 hours after the cessation of mixing, until the point at which gel collapse occurred. The characteristic domain size of the network $R_c(h, t_w)$ at a height h and time t_w was calculated from the static structure factor $S(q, t_w)$

$$S(q,t_w) = \frac{1}{2\pi q \Delta q} \int_{q \le |\mathbf{q}'| \le q+\Delta q} \mathrm{d}\mathbf{q}' \left\langle \tilde{I}(\mathbf{q}',t_w)\tilde{I}(-\mathbf{q}',t_w) \right\rangle \tag{10}$$

where $\tilde{I}(\mathbf{q}, t_w)$ is the two-dimensional Fourier-transform of the image intensity $I(\mathbf{r}, t_w)$ at time t_w, $\Delta q = 2\pi/W$, and W is the image width. The domain size is $R_c = \pi/\langle q \rangle$ where $\langle q \rangle = \int \mathrm{d}q \; qS(q)/\int \mathrm{d}q S(q)$. Measurements of R_c for different sample ages t_w are plotted in Fig. 10 and confirm that the aging of the gel network shows considerable spatial diversity: the domain size is large in some regions of space and small in others. Immediately after mixing, we observe the formation of a very uniform network with an average domain size of $\langle R_c \rangle = 17.5$ μm and a spatial variation of just 1.4% (standard deviation/$\langle R_c \rangle$). But after $t_w = 2$ h, while the mean size has grown only slightly to $\langle R_c \rangle = 21.3$ μm the spatial variation in R_c has increased to 3%. After 5 h, the variation in the domain size has increased still further to 9% ($\langle R_c \rangle = 26.7$ μm). Clearly the data reveals that aging of the network is heterogeneous with spatial variation increasing with sample age.

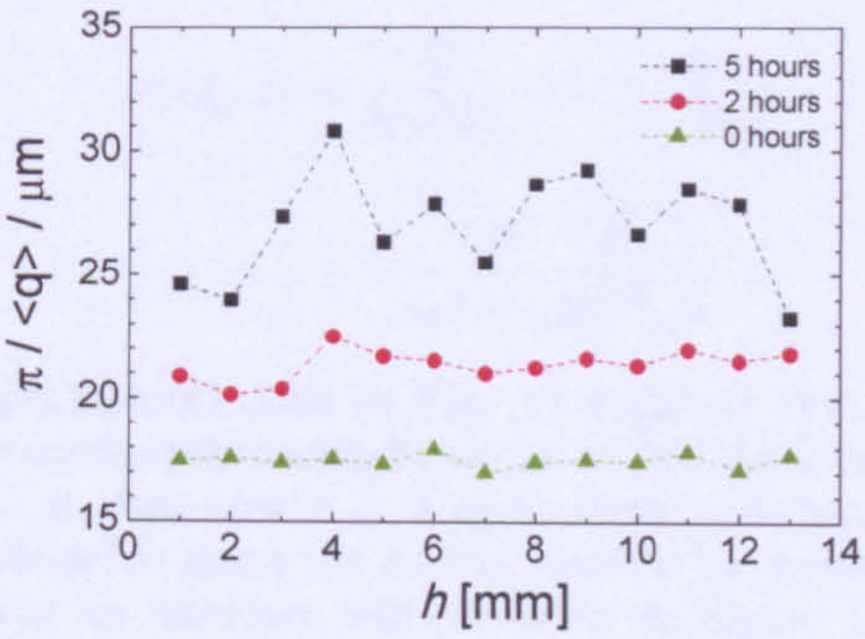

FIG. 10. The domain size R_c in a gel of height $h_0 = 15$ mm ($c_p/c_p^* = 2.4$) as a function of the distance measured from the base of the cell. Note growth seems to be hindered near the boundaries of the gel.

IV. DISCUSSION

The most striking feature of our results is the appearance during collapse of the $\frac{3}{2}$-power law dependence of the height $h(\tau)$ on the elapsed time τ. A natural question is the physical origin of this unusual behavior. We propose that the dominant mechanism for collapse is the appearance of random micro-collapsed regions throughout the gel. On a microscopic level, the basic idea is that the particles comprising the gel attract each other relatively strongly so over time the gel spontaneously restructures locally to create small regions of more dense packing. Since the collapsing particles are attached quite strongly to strands of the network as they rearrange they induce a local pressure field. This induced field, as a consequence of the poroelastic character of the gel, expands relatively slowly into the bulk of the gel. It is this long-range pressure field which we hypothesize generates the characteristic collapse dynamics evident in our experiments. Similar arguments have been invoked to account for the anomalous microscopic motion evident in dynamical light scattering of colloidal gels [28, 29] but not, as far as we are aware, for the macroscopic settling dynamics of gels. While our discussion has some features in common with the purely elastic models used previously [28, 29], we focus here on deformations at large (macroscopic) length scales where poroelastic fluid flows are important.

For the moment, we idealize the gel as a one-dimensional chain of particles. Then if two particles leaves their equilibrium positions to stick together the left-hand particle imposes a force $+f_0$ on the left part of the chain at z', while the right-hand particle imposes an equal and opposite force $-f_0$ on the right-hand side of the chain located at $z' + \delta z'$. The net effect of the rearrangement is therefore the creation of a local dipolar force $f(z', t')$ at the random position $z = z'$. The intensity of this dipolar force, the dipole moment μ, is the product of the force f_0 and the displacement vector $\delta z'$ in the limit as $\delta z' \to 0$. At the dipolar stress center the fluid pressure P rises rapidly to a high value while further away P is almost unchanged. The resulting pressure gradient drives a flow through the porous medium and as fluid exits from around the applied force the gel deforms locally and more of the load is borne by the network. Eventually, the pressure at all points reaches the same value and the gel relaxes so that the applied load is everywhere balanced by the elastic stresses in the network. The time scale for this equilibration is determined by a diffusion constant D_g, with the deformation in the gel occurring over a length scale $\approx \sqrt{D_g t}$ in a time t.

The gel diffusion constant D_g is [30, 31]

$$D_g = \frac{Kk}{\eta_L(1-\phi)}. \tag{11}$$

where k is the permeability of the network, η_L is the viscosity of the continuous phase, and K is the bulk modulus of the network. Using measurements of the low shear viscosity ($\eta_L \simeq 0.1$ Pas), the elastic modulus of the gels ($K \simeq 10$ Pa), and literature values for the permeability of similar density gels [15] ($k \sim 10a^2 \simeq 10^{-12}$ m^2) we estimate a diffusion constant in our system of $D_g \simeq 10^{-10}$ m^{2}s^{-1}. Both the pore pressure and, in general, the permeability will change with time as the gel contracts locally. However in the initial stages of collapse the gel is uncompressed, the permeability is constant, and the equations of linear poroelasticity apply [32]. The bulk shrinkage of an unconstrained gel is linear so it is natural to assume that the dipole intensity will also be a linear function of time, $\mu(t) = \mu_0 t$.

For simplicity, we first consider the isotropic deformation produced in the gel by the supposition of three continuous orthogonal stress dipole centers (a single center of compression [33]). Rudnicki [34] has shown that the pore pressure at a distance r from a single continuous center of compression in a fluid-saturated porous solid is of the form

$$P_s(r,t) = \frac{Q}{4\pi D_g r}\mathrm{erfc}(\xi/2), \tag{12}$$

where $\xi = r/(D_g t)^{1/2}$, Q is proportional to μ_0, and erfc is the complementary error function [35]. As $t \to 0$, ercf$(r/2\sqrt{D_g t}) \to 0$, and the pressure is zero. At finite times, the fluid has an opportunity to diffuse away from the origin, and the spherically symmetric pressure wave expands. In Fig. 11 we plot a time series of the spreading pressure field as it diffuses away from the origin. The length scale where the pressure is finite is controlled by fluid diffusion within the gel and is thus time-dependent. From the figure it is clear that the spatial extent of the pressure field is of order $6(D_g t)^{1/2}$. Finally, as $t \to \infty$, ercf$(r/2\sqrt{D_g t}) \to 1$, and the pressure field approaches the pure $1/r$-elastostatic solution, expected for a continuous dipole source [32].

We assume that at the start of collapse the gel contains centers of compression which are randomly distributed throughout the height of the gel, with a certain number ρ per unit length. To calculate the velocity of the gel interface $\partial_t w$ we note that, from Darcy's law (Eq. 3), $\partial_t w$ is fixed by the total pressure gradient at the bottom of the gel. If we assume that each micro-collapse contributes independently then the pressure gradient is simply the sum of the gradients generated by individual events occurring at different heights z_j within the gel. For simplicity we ignore the true vectorial nature of the problem and use a one-dimensional scalar approximation. A single center of compression located a distance z_j from the gel interface creates a pressure gradient, $\theta_j = \partial_r P_s$, which from Eq. 12 is

$$-\theta_j(z_j,t) = \frac{Q}{4\pi z_j^2 D_g}\mathrm{erfc}\left(\frac{z_j}{2\sqrt{D_g t}}\right) + \frac{Q e^{-\frac{z_j^2}{4D_g t}}}{4\pi^{3/2} z_j D_g^{3/2}\sqrt{t}}. \tag{13}$$

The experimental data in Fig. 10 suggests that micro-collapse events preferentially occur within the bulk of the gel, *i.e.* at distances $z \geq \lambda$ away from a surface. This seems plausible since the energy barrier for a rearrangement near an interface will probably be higher than for the same event in the bulk of the gel, as the strain induced by the creation of the dipole is larger. Inspection of the data in Fig. 10 suggests that λ here is of order a few millimeters. Hence, we assume that micro-collapses are uniformly distributed over the interval from $z = \lambda$ to $z = h_0 - \lambda$. The total pressure gradient at the base of the gel is therefore,

$$\partial_z P\Big|_{\text{base}} = \rho \int_{\lambda}^{h_0-\lambda} \theta(z,t)\mathrm{d}z. \tag{14}$$

Since experimentally the rate of collapse does not depend on the total height h_0 of the gel the upper limit of the integral can be extended to $z = \infty$ without significant error. After inserting Eq. 13, the resulting integral can be performed exactly with the result:

$$-\partial_z P(t) = \frac{\rho Q}{4\lambda^2 \pi^{3/2} D_g^{1/2}}\sqrt{t}e^{-\frac{\lambda^2}{4D_g t}} + \frac{\rho Q \ln\lambda}{4\pi^{3/2} D_g^{3/2}\sqrt{t}}. \tag{15}$$

In the regime where $t \gg \lambda^2/4D_g$, which from our estimates for D_g and λ equates to $t \gg 10^3$ s and holds for all but the shortest times studied, the expression for the pressure gradient simplifies to

$$-\partial_z P(t) \underset{t \gg \lambda^2/4D_g}{\approx} \frac{\rho Q}{4\lambda^2 \pi^{3/2} D_g^{1/2}}\sqrt{t}. \tag{16}$$

The confocal data, presented in Sec. III C, reveals that micro-collapses first appear in gels with an age t_w of $\approx \tau_d$ so the time t available for the propagation of the pressure wave in Eq. 16 is $\tau = t_w - \tau_d$. By combining Eq. 3, 4, and 16 we obtain

$$\Delta h(\tau) = \left[\frac{\rho k Q}{4\eta(1-\phi)\lambda^2 \pi^{3/2} D_g^{1/2}}\right]\tau^{3/2}. \tag{17}$$

where we have assumed that the flow of fluid through the network determines the initial rate of collapse, and $t \gg \lambda^2/4D_g$. This expression is in very good agreement with the experimental results where a similar exponent of 3/2 has been found, thus providing convincing evidence for our simple phenomenological model. In addition, our arguments predict that the coefficient of $\tau^{3/2}$, which we

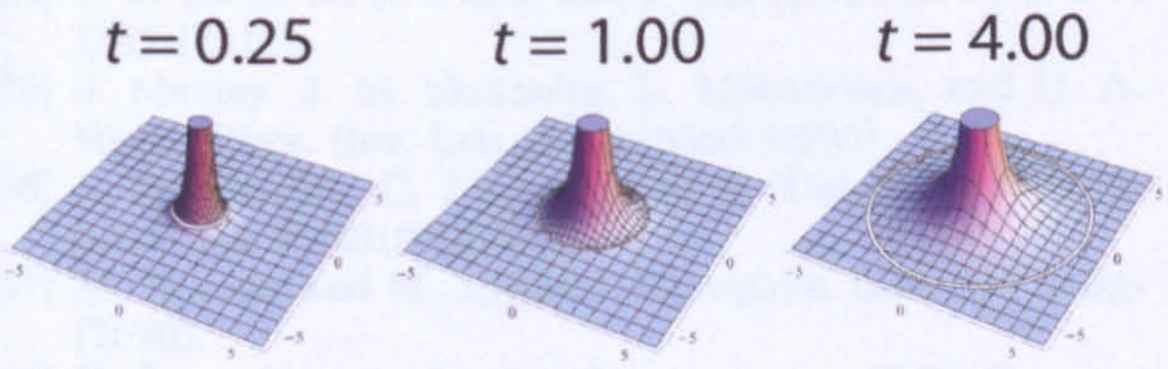

FIG. 11. An illustration of the pore pressure field generated by a continuous compression center placed at the origin of a gel. Times and distances are scaled so the diffusion constant D_g is unity. The ring of radius $r = 6(D_g t)^{1/2}$ parameterizes the spatial extent of the induced pressure field.

identify with the scale factor A in Eq. 2, should be a system constant, independent of the initial height of the gel. This agrees with the height-independence seen in the experimental data presented in Fig. 5(c). Finally, we expect that the formation of micro-collapses is thermally activated so their number density ρ will be of the form

$$\rho = \rho_0 \exp\left(-\frac{\Delta E}{k_B T}\right) \tag{18}$$

where ΔE is an energy barrier for rearrangement. Since $\Delta E/k_B T$ will scale with the strength of the interparticle potential $U_c/k_B T$ one expects that the scale factor A will depend exponentially on the interparticle potential, or equivalently the polymer concentration, in agreement with the experimental data plotted in Fig. 5(d).

V. SUMMARY

We have studied the gravitational collapse of a colloidal gel by a combination of confocal microscopy, time-lapse video imaging, and rheology focusing particularly on the effect of the initial height h_0 of the gel and the strength of attractions $U_c/k_B T$. The gels are made of emulsion drops suspended in a refractive index-matched mixture of ethylene glycol and water, with a high molecular polymer added to induce a weak long-range attraction. For all systems, the height $h(t_w)$ of the gel shows a characteristic two-step decay as a function of age t_w: for t_w less than the lag time τ_d the system resists gravity and there is no significant deformation, but for $t_w > \tau_d$ the gel abruptly yields and collapses. The change in the height $\Delta h = h_0 - h(t_w)$ of the gel during collapse has a number of distinctive features. First, we find that the initial degree of settling is well described by the expression, $\Delta h \sim \tau^{3/2}$, with τ the time counted from the moment when collapse first starts. Second, both the rate of collapse and the lag time τ_d are independent of the initial height of the gel. Microscopically, the gel consists of a network of interconnected strands of particles. Confocal microscopy reveals that continuous restructuring of this network occurs which, with increasing age, leads to the breaking of bonds between particle strands and a progressive weakening of the network. The subsequent reduction in the large scale connectivity of the network eventually triggers a macroscopic collapse. Measurement of the microscopic structure of the gel during settling show that the age-dependent changes in the network are not isotropic but are concentrated around large inhomogeneities within the sample. We hypothesize that the collapse of the gel is determined by the rate at which fluid can be expelled from the gel. A simple phenomenological model of fluid flow driven by the formation of random compression centers within the gel correctly accounts for the behavior experimentally observed.

ACKNOWLEDGMENTS

We thank C.P. Royall, R. Buscall, W. Poon, and W. Kob for helpful discussions and Leila Wannell and Humphrey Yeung for their assistance with the experiments. The work was supported by Bayer CropScience and the UK Engineering and Physical Science Research Council through the award of an Industrial Case Studentship to LJT.

[1] L. Cipelletti and L. Ramos, Journal of Physics-Condensed Matter **17**, R253 (2005).
[2] E. Zaccarelli, J. Phys.: Condens. Matter **19**, 50 (2007).
[3] F. Sciortino and P. Tartaglia, Advances in Physics **54**, 471 (2005).
[4] J. J. Lietor-Santos, C. Kim, M. L. Lynch, A. Fernandez-Nieves, and D. A. Weitz, Langmuir **26**, 3174 (2010).
[5] S. W. Kamp and M. L. Kilfoil, Soft Matter **5**, 2438 (2009).
[6] J. Y. Huh, M. L. Lynch, and E. M. Furst, Phys. Rev. E **76**, 051409 (2007).
[7] V. Gopalakrishnan, K. S. Schweizer, and C. F. Zukoski, J. Phys.: Condens. Matter **18**, 11531 (2006).
[8] T. B. J. Blijdenstein, E. van der Linden, T. van Vliet, and G. A. van Aken, Langmuir **20**, 11321 (2004).
[9] C. Derec, D. Senis, L. Talini, and C. Allain, Phys. Rev. E **67**, 062401 (2003).
[10] L. Starrs, W. C. K. Poon, D. Hibberd, and M. Robins, J. Phys.: Condens. Matter **14**, 2485 (2002).
[11] N. Verhaegh, D. Asnaghi, and H. N. W. Lekkerkerker, Physica A **264**, 64 (1999).
[12] C. Allain, M. Cloitre, and M. Wafra, Phys. Rev. Lett. **74**, 1478 (1995).
[13] A. Parker, P. A. Gunning, K. Ng, and M. M. Robins, Food Hydrocolloids **9**, 333 (1995).

[14] L. J. Teece, M. A. Faers, and P. Bartlett, Soft Matter **7**, 1341 (2011).
[15] S. Manley, J. M. Skotheim, L. Mahadevan, and D. A. Weitz, Phys. Rev. Lett. **94**, 218302 (2005).
[16] J. M. Condre, C. Ligoure, and L. Cipelletti, J. Stat. Mech. **02**, P02010 (2007).
[17] M. Hermes and M. Dijkstra, Europhys. Lett. **89**, 38005 (2010).
[18] N. Otzu, Systems, Man and Cybernetics, IEEE Transactions on **9**, 62 (1979).
[19] G. J. Fleer and R. Tuinier, Adv. Coll. Interf. Sci. **143**, 1 (2008).
[20] M. L. Kilfoil, E. R. Pashovski, J. A. Masters, and D. A. Weitz, Phil. Trans. R. Soc. Lond. A **361**, 753 (2003).
[21] C. Kim, Y. Liu, A. Kuhnle, S. Hess, S. Viereck, T. Danner, L. Mahadevan, and D. A. Weitz, Phys. Rev. Lett. **99**, 028303 (2007).
[22] R. Buscall and L. R. White, Journal of the Chemical Society-Faraday Transactions I **83**, 873 (1987).
[23] M. Doi, J. Phys. Soc. Jpn. **78**, 19 (2009).
[24] H. J. M. Van Dijk, P. Walstra, and J. Schenk, Chem. Eng. J. **28**, B43 (1984).
[25] S. Torquato, Annu. Rev. Mater. Res. **32**, 77 (2002).
[26] V. Testard, L. Berthier, and W. Kob, Phys. Rev. Lett. **106**, 125702 (2011).
[27] P. A. Smith, G. Petekidis, S. U. Egelhaaf, and W. C. K. Poon, Phys. Rev. E **76**, 11 (2007).
[28] L. Cipelletti, S. Manley, R. C. Ball, and D. A. Weitz, Phys. Rev. Lett. **84**, 2275 (2000).
[29] J. P. Bouchaud and E. Pitard, Eur. Phys. J. E **6**, 231 (2001).
[30] T. T. Tanaka, L. O. Hocker, and G. B. Benedek, J. Chem. Phys. **59**, 5151 (1973).
[31] G. T. Charras, J. C. Yarrow, M. A. Horton, L. Mahadevan, and T. J. Mitchison, Nature **435**, 365 (2005).
[32] H. F. Wang, *Theory of linear poroelasticity with applications to geomechanics and hydrogeology*, Princeton Series on Geophyiscs (Princeton University Press, Princeton, 2000).
[33] A. E. H. Love, *A Treatise on the Mathematical Theory of Elasticity* (Cambridge University Press, 1920), 3rd ed.
[34] J. W. Rudnicki, Mech. Mater. **5**, 383 (1986).
[35] M. Abramowitz and I. A. Stegun, eds., *Handbook of Mathematical Functions* (Dover, New York, 1972), ninth ed.